BURIED PIPELINE RESPONSE TO ICE GOUGING

by

© Farzad Eskandari

A Thesis submitted to the

School of Graduate Studies

in partial fulfillment of the requirements for the degree of

DOCTOR OF PHILOSOPHY

Faculty of Engineering and Applied Science

Memorial University of Newfoundland

Feburary2014

St. John's Newfoundland

ABSTRACT

Arctic region is rich in abundant discovered and undiscovered hydrocarbon resources and is an important area for energy development. In the arctic and other cold regions, subsea pipelines, which are considered to be an economical and convenient way of oil and gas transportation, are exposed to various geohazards such as pressure ridges or icebergs gouging the seabed. These floating ice masses could impose distress to the pipe through interaction with the seabed and ultimately jeopardize the integrity of the pipeline structure. To protect the pipelines the most common and efficient practice is to bury them into the seabed. Efficiency refers to both cost and performance of this method. Comparing to alternative methods, such as ice management or construction of protective structures along the length of the pipeline, trenching would be a more manageable option. In addition to protecting against ice features, trenching can help maintain the structural integrity of the pipelines against other hazards such as lateral buckling or hydrodynamic loads. Trenching is very useful to cope with uneven seabed and mitigate free spans.

As the result, finding a safe but economic burial depth to install the pipelines in the subsea is important in offshore pipeline projects. The key to determination of a safe and economical burial depth is the proper understanding of the seabed soil response to the ice gouging and accurate prediction of the sub-gouge deformation under gouging loads.

Numerical analysis could be an efficient tool to capture the seabed behaviour during the ice gouging event and simulate the sub-gouge deformations provided an appropriate soil model is applied. The soil constitutive model should be able to account for different stress paths. It should also be simple in terms of estimating input parameters with small number

of common tests. Most of the constitutive models available in commercial finite element packages do not appropriately simulate the dilative behaviour of sand. An improvement in hardening law could also enhance their accuracy in predicting soil stress-strain behaviour.

In this research, ABAQUS Explicit Finite Element (FE) software is used for numerical analyses. Some of the limitations of built-in soil constitutive models in the ABAQUS Explicit for capturing the ice gouging mechanism are shown. A variant of the Drucker-Prager Cap model is therefore proposed to capture the behaviour of sand under large deformation more realistically. NorSand plasticity model, developed on critical state framework, has shown good performance in modeling various laboratory test results of sand and has been used for a variety of geotechnical applications. In this research, the proposed Drucker-Prager Cap model as well as the NorSand critical state model have been implemented in ABAQUS Explicit using the user subroutine VUMAT and are used to simulate the seabed response to the ice gouging event within the Arbitrary Lagrangian Eulerian framework (ALE). Through the application of volume constraint method, these constitutive soil models are extended to predict the undrained behaviour of soils which is lacking in ABAQUS Explicit. The developed constitutive models are verified and validated against triaxial drained and undrained tests. The finite element simulations using these constitutive models are also validated against the centrifuge ice gouging test results.

In addition to ice gouging mechanism the effect of some of the more influential factors of this process is investigated. Through the numerical analyses it is demonstrated that: (i) the

critical stress ratio of soil directly correlates with the keel reaction forces; (ii) in a specific soil at a denser state (i.e. more dilative), larger keel reaction forces are required in order to reach the steady state condition; (iii) the higher attack angle of the keel results in the lower keel reaction forces; (iv) deeper gouges yield larger keel reaction forces; (v) it is possible to normalize the keel reaction forces based on the keel geometry and soil material properties; (vi) the developed frontal berm height consistently increases with the increasing shear strength of the soil; (vii) larger frontal berm is developed in denser soil in steady state; (viii) the increase of keel attack angle and gouging depth result in larger frontal berm height. The variation of the attack angle modifies the mechanism of the frontal berm development; (ix) smaller sub-gouge deformations are observed in denser soil; (x) the sub-gouge deformation increases in the soils with higher shear strength. The critical stress ratio is more influential for denser soils compared with the loose soils; (xi) the increase of the attack angle reduces the vertical extension of the sub-gouge deformation and (xii) as expected, the increase of the gouging depth extends the sub-gouge deformations deeper into the seabed. These results are confirmed through physical tests published in literature.

The developed numerical models are used to simulate the results of some of the physical tests of research programs that are carried out in C-CORE such as the PIRAM project. The results of numerical analyses show good agreement with results obtained from centrifuge tests. Although the proposed Drucker-Prager Cap model is able to simulate different behavior of sands but because some issues such as the effect of intermediate principal effective stress and the definition of the yield surface are better addressed in

critical state NorSand model, the latter model is found to be more preferred in the analyses of this research.

ACKNOWLEDGEMENTS

I would like to express my gratitude to my supervisor Dr. Ryan Phillips and my co-supervisor Dr. Bipul Hawlader for their support. I am very thankful for their help and recommendations during the writing of this dissertation. I would also like to sincerely thank Dr. Seshu Adluri, my supervisory member, for his valuable feedbacks and advices. This work has never been completed without his support and encouragement.

My gratitude is also extended to the staff of C-CORE. I would like to thank Mr. John Barrett for his scientific and technical assistance in this research. I am also thankful to Mr. Tony King, the Director of Ice Engineering in C-CORE, and Dr. Arash Zakeri, the former Director of Geotechnical Engineering in C-CORE, for their support and guidance.

I would like to gratefully acknowledge funding from C-CORE and its partners in the PIRAM: Pipeline Ice Risk Assessment & Mitigation Joint Industry Program including the support of Atlantic Canada Opportunities Agency, AGIP KCO, Chevron Canada Resources, ConocoPhillips Canada, ExxonMobil Upstream Research Company, Husky Energy, Shell International, Statoil and Suncor; and the technical advice from Ken Croasdale & Associates, Bold Island Engineering and Golder Associates. I would also deeply appreciate the financial support of the School of Graduate Studies, the Faculty of Applied Science and Engineering and Graduate Students' Union of the Memorial University of Newfoundland through the course this doctoral program.

Last but not the least; I am tremendously grateful to my parents for raising me with a love of science and the principle of hard work. Without their unconditional support this degree would not have been possible.

TABLE of CONTENTS

List of Figures

List of Tables

List of Abbreviations and Symbols

Abbreviations

ALE	Arbitrary Lagrangian Eulerian
CEL	Coupled Eulerian Lagrangian
CSL	Critical State Line
CSSM	Critical State Soil Mechanics
DPC	Drucker Prager Cap Soil Constitutive Model
EOM	Equation of Motion
HHT	Hubert-Hughes-Taylor
OCR	Overconsolidation Ratio
PIRAM	Pipeline Ice Risk Assessment and Mitigation
PRISE	The Pressure Ridge Ice Scour Experiment
PTL	Phase Transformation Line

Symbols

$\bar{F}_H$	Normalized Horizontal Keel Reaction Force
$\bar{\sigma'}_m$	Mean Effective Stress
$\bar{\sigma'}_q$	Deviatoric Stress
D_r	Relative Density
D_s	Gouging Depth
F_H	Horizontal Keel Reaction Force
I_1	First Stress Invariant (trace)
J_{2D}	Second Deviatoric Stress Invariant
K_{skel}	Bulk Modulus of Soil Skeleton
K_w	Pore Water Bulk Modulus
$d\varepsilon_1$	Major Principal Strain Increment
$d\varepsilon_q$	Shear Strain Increment
$d\varepsilon_v$	Volumetric Strain Increment
s'_i	Effective Stress Component
$\ddot{u}$	Acceleration
$\dot{u}$	Velocity
θ_L	Lode's Angle

$\sigma'_{m,c}$	Critical State Mean Effective Pressre
$\sigma'_{q,c}$	Critical State Deviatoric Stress
σ^*	Stress at Trial Step
σ_{ij}	Stress Components
σ_m	Mean Pressure
ψ_i	Image State Parameter
ϕ_{cr}	Critical State Internal Friction Angle
ϕ_f	Operational Friction Angle or Mobilized Friction Angle
ϕ_f	Critical State Friction Angle
ϕ'_{max}	Angle of Internal Friction at Peak Stress
ϕ_μ	Mineral to Mineral Friction of the Soil
A	Vertical Radius of the Cap in Drucker Prager Cap Model
B	Horizontal Radius of the Cap in Drucker Prager Cap Model
B	Developed Frontal Berm Height
c	Cohesion
C	Damping Matrix
d	Cohesion of the Material in Drucker Prager Model
D^p	Dilation Rate
e	Void Ratio
E	Elasticity Modulus
e_c	Critical State Void Ratio
e_{max}	Maximum Void Ratio
e_{min}	Minimum Void Ratio
G	Shear Modulus
G_s	Drucker Prager Cap Flow Rule in Shear Zone
H	Hardening Modulus of NorSand Model
I	Identity Matrix
I_D	Relative Density
I_r	Rigidity Modulus
I_R	Dilatancy Index
k	Hardening Parameter
K	Stiffness Matrix
K	Bulk Modulus
M	Critical Stress Ratio
M	Mass Matrix

M_i	Image Friction Angle
M_{tc}	Critical Stress Ratio at Triaxial Compression Condition
M_{te}	Critical Stress Ratio at Triaxial Extension Condition
N	Volumetric Coupling Coefficient
n	Increment Number
p	Mean Pressure
p^*	Trial Mean Pressure
p'	Mean Effective Stress
p_a	Evolution Parameter of Drucker Prager Cap Model
p_i	Image Pressure
q	Deviatoric Stress
q^*	Trial Deviatoric Stress
R	Overconsolidation Ratio
W	Gouging Width
Γ	Critical State Line altitude at 1kPa
γ	Transition Factor in Drucker Prager Cap Model
$\Delta\varepsilon_v$	Volumetric Strain Increment
Δu	Pore Water Pressure Increase
$\Delta\varepsilon$	Strain Increment
η	Stress Ratio
λ_c	Critical State Line Slope in Semi Logarithmic Pressure-Void Ratio Space
ν	Poisson's Ratio
ν_u	Equivalent Undrained Poisson's Ratio
χ_{tc}	Multiplier to Relate Critical State to maximum Dilatancy
$d\varepsilon_{ij}^p$	Plastic Strain Increment Components
$d\varepsilon_q^p$	Plastic Shear Strain Increment
$d\varepsilon_v^p$	Plastic Volumetric Strain Increment
$d\sigma$	Load Increment
α	Damping Factor
γ	Soil Unit Weight
δ	Kronecker Delta
θ	Material Friction Angle in Drucker Prager Model
κ	Hardening Function
ψ	State Parameter
ϕ	Internal Friction Angle of Soil

1. Introduction

1.1. General

The demand for energy resources is continuously growing. As a result, the oil and gas industry has been increasingly interested in discovery and extraction of offshore hydrocarbon resources. It is believed that over 25% of the world's petroleum reserves are located in the Arctic areas or other frozen regions (USGS study). As Figure 1-1 suggests much of the energy resources in the Arctic area are located offshore. Pipelines then play an important role in transport of oil and gas to the land as the most convenient way of transfer. However, the construction of seabed pipelines is considerably more demanding compared to those built over the land with more associated challenges. Usually pipelines are a significant component of an offshore project budget. Therefore, there is a need of constructing the pipelines more economically while maintaining the safety and functionality of the whole structure. The importance of marine pipelines in energy industry has led them to be the subject of much research aimed to improve their serviceability and reduce the construction cost.

In this research ice gouging as one of the most prominent threats to the offshore pipelines in cold areas is studied.

The Pipeline Ice Risk Assessment and Mitigation (PIRAM) project developed a set of engineering models, design procedures for implementation into industry best practices for risk mitigation and protection of pipeline infrastructure from ice keel loading. In the following chapter the PIRAM project is introduced in more detail.

The main objective of this research is the need to develop an effective stress constitutive model for sand, which is then used for simulating ice keel-soil interaction in finite element analyses as part of the PIRAM project.

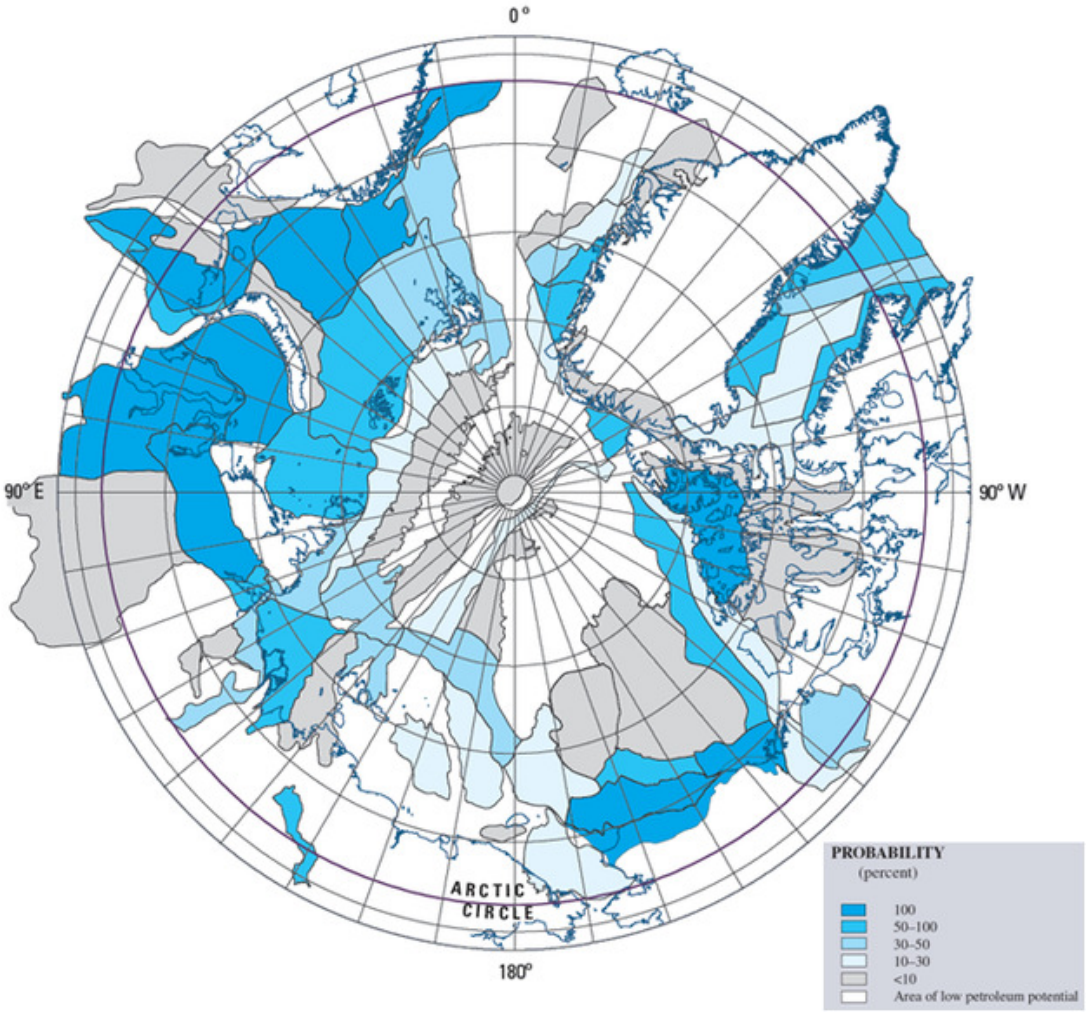

Figure 1-1 Potential Oil and gas resources in Arctic Circle (Bird et al., 2008)

1.2. Original Contributions

In this research the Drucker-Prager Cap model was improved to capture different responses of sands depending on the initial density and stress level of the soil. The proposed constitutive model addresses the issue of excessive dilation which the original

Drucker-Prager Cap model suffers. The excessive dilation is replaced by more realistic dilatancy rates through the application of dilatancy index proposed by Bolton (1986). The shear hardening law of the model which is based on soil state and a maximum allowable dilation enables the model to predict some of the dense sand behaviours such as softening. The proposed model has been implemented in ABAQUS finite element software using the user defined subroutine VUMAT in order to simulate large strain behaviour of sand during ice gouging event.

NorSand plasticity model, developed on critical state framework, has shown a good performance in modeling various laboratory test results of sand and has been used for a variety of geotechnical applications. In this research, the NorSand model has also been implemented in ABAQUS Explicit using the user defined subroutine VUMAT in order to simulate the seabed response to the ice gouging event.

In this research through the application of volume constraint method, the proposed Drucker Prager Cap model and the critical state model NorSand are extended to predict the undrained behaviour of soils.

The developed constitutive models are verified and validated against triaxial drained and undrained triaxial tests. The finite element simulations using these constitutive models are also validated against the centrifuge ice gouging test results.

1.3. Organization of the Thesis

This thesis is divided in three parts. In the literature review the geo-hazards of Arctic areas that are known to have adverse effects on the integrity and the safety of the marine pipelines are explained. In particular close attention is devoted to ice gouging and the

related implications for the buried pipeline and the seabed soil. The different methods of the study of the gouging phenomena and the recent development in this field are reviewed.

In the second part of the thesis, the soil behavior of the seabed is studied. The characteristic response of the sand under different situation is investigated. In this part of the thesis the theoretical concepts that are required to develop a constitutive model that can represent the sand behaviour are discussed. The employed constitutive models are explained in detail and their advantages are highlighted. The application of a user material model in ABAQUS Explicit is shown and the two chosen models are implemented in the VUMAT subroutines. The developed models are then verified using the laboratory triaxial tests.

In the third part of the thesis the ice gouging problem is simulated using a three-dimensional finite element model using the developed constitutive models. The features of the three-dimensional model are explained in detail and the use of particular numerical procedures is justified. Based on the implemented models a sensitivity analysis is performed to distinguish the influential parameters of the gouging event. The results of the simulations are compared with centrifuge data and the accuracy of the implemented models is assessed. The ice gouging mechanism including the keel reaction forces and sub-gouge deformations are studied.

At the end of thesis the conclusions of this study are summarized and some suggestions for future work are offered.

2. Literature Review

2.1. Marine Geo-hazards in the Cold Areas

Different kinds of geo-hazards can occur in an offshore project. The most prominent issues include earthquake, fault planes, seafloor instability, scour and sediment mobility, shallow gas, seabed subsidence, submarine slope instability, liquefaction and faulting.

Other geo-hazards exist that are specific to cold offshore areas. Some of the challenging issues in these areas are ice gouging, strudel scour, permafrost thaw, and upheaval buckling as described by Abdalla et al. (2008). In this research ice gouging is comprehensively studied.

2.2. Ice Gouging Event

2.2.1. Icebergs and Ice Ridges

Ice features that gouge the seabed are generally divided in two categories, icebergs and ice ridges. Ice ridges are formed of sea ice covers under environmental agents such as current and wind. In the east arctic and Labrador icebergs are usually observed whereas in Alaskan Beaufort sea ice ridges gouge the seabed. As the result it must be noted that each area demands specific design considerations.

Iceberg is a large mass of ice that is detached from a glacier or an ice sheet and sent off floating in the ocean. Icebergs are formed from freshwater. Therefore, about 90 percent of their volume is immersed (the keel) and the rest (the sail) floats above the water (P. Barrette, 2011). Since the ice ridges are formed from saline waters the immersed volume

is higher than that of icebergs. Gravity is the main factor that ends into the mechanism called calving through which icebergs break off the glacier. Figure 2-1 shows the separation of an iceberg from a glacier through calving.

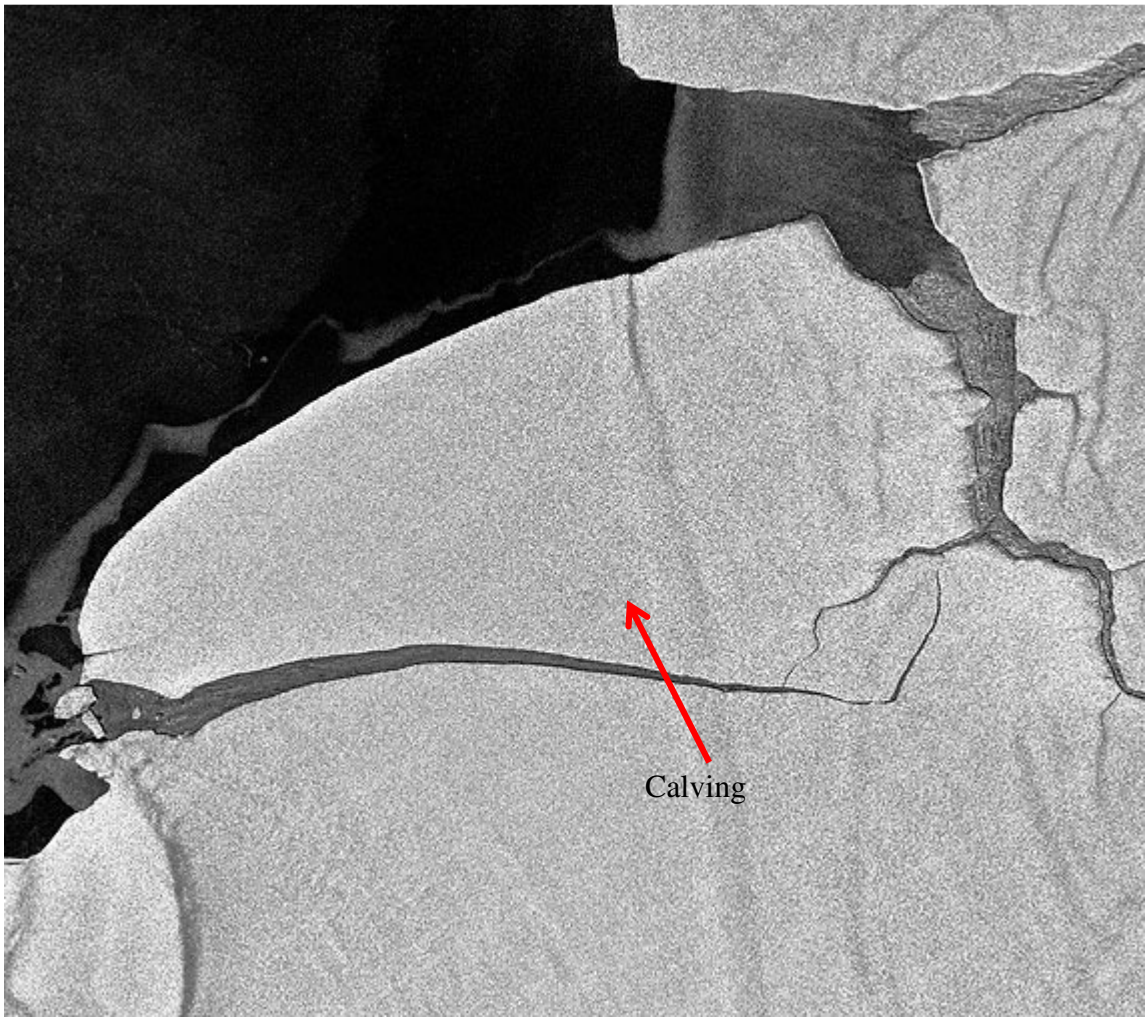

Figure 2-1 Iceberg calving from the Fimbul Ice Shelf in Antarctica

Sea ice is formed at sea by freezing the saline sea water. However, during this formation process most of the salt separates from the ice so the outcome is fresh ice that could easily float on the saline ocean water. Compared to the icebergs they are more porous and have more complex internal structures. Therefore, they are considered weaker than icebergs. In

addition the keel is weaker than the sail because of the exposure to the near melt water temperature.

Ice ridges are typically found in frozen lakes or sea ice. When two ice floes of sea ice cover collide into each other due to the wind or current forces, in the same way that plate tectonics created mountains, a ridge would be created. This ridge can be several meters above the water and tens of meters below the water. If these ridges are moved under high horizontal forces they might gouge the seabed as well.

2.2.2. Ice Gouging Mechanism

In arctic region ice gouging is the main threat to the offshore pipelines. It happens when an ice feature moves into shallower waters or approaches the shoreline. Tidal effect would also intensify the likelihood of the gouging event. When the ice feature and the seabed make contact based on the interaction of the internal and external forces several different scenario may occur. The case which is concerned to the gouging event is when the driving forces like the wind and currents are high enough to push the ice further into the soil and the ice is stronger than the soil to avoid any breakage in the keel.

The ice gouging process starts with the contact of the ice and soil followed by the ice being lifted up. The next phase is the penetration of the ice into seabed which includes vertical movement of the ice. Next step is the steady state gouging where there is no more penetration and the ice gouges the seabed horizontally at a velocity of several cm/s. This velocity depends on the seabed shear strength and environmental conditions such as wind and current. The observed drift speed of the Springdale M-29 scour in Grand Banks was reported to be around 0.5 m/s (McKenna et al., 1999).

When an iceberg comes in contact with the seabed it rotates over the point of contact to maintain the equilibrium. The angle between the seabed level and the keel is called the "attack angle". This angle is governed by local interactions between soil and ice. In Figure 2-2 a schematic view of ice gouging event is shown.

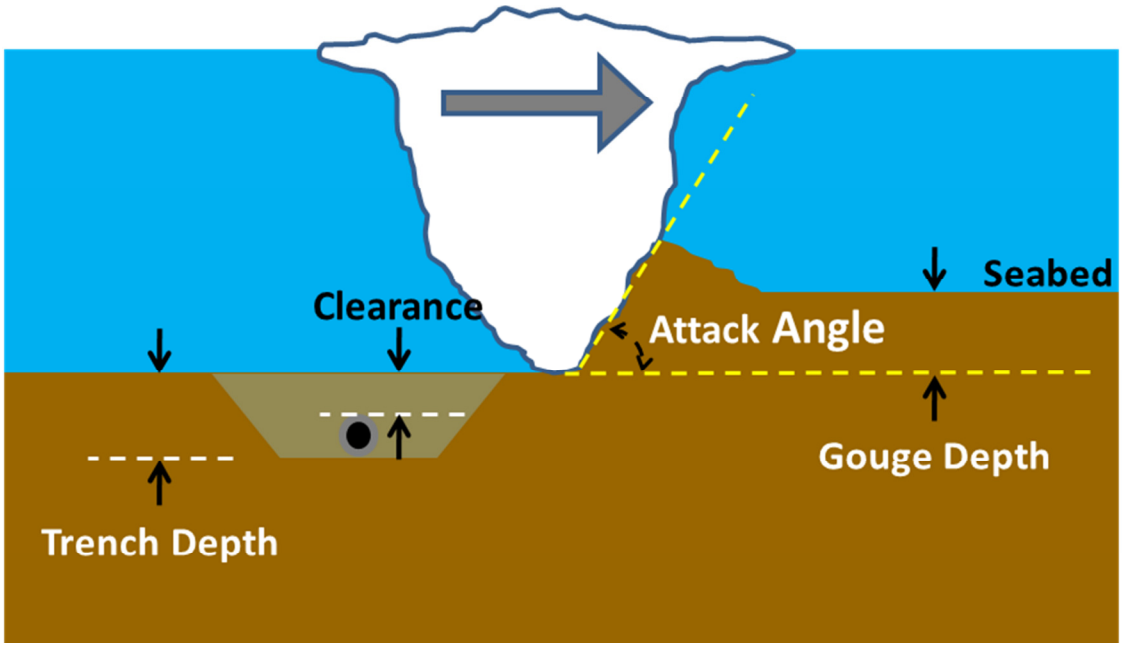

Figure 2-2 Schematic view of an ice gouging event (not to scale)

Based on studies on the gouge marks at the seafloor the geometric characteristics of the gouges have been identified. Gouges as deep as five meters have been recognized; however most of the gouges are less than one meters. Generally a gouge depth of more than two meters is considered an extreme occurrence. As an example of an extreme gouging event a 50 km long gouge in the Beaufort Sea with a maximum depth of 8.5 meters can be mentioned. This extreme event which happened in areas of water depth of 40 to 50 meters is estimated to have an age of more than 2000 years. Gouge widths could

be as low as a few meters to tens of meters wide in more extreme cases. Figure 2-3show the marks of ice gouging on the seafloor.

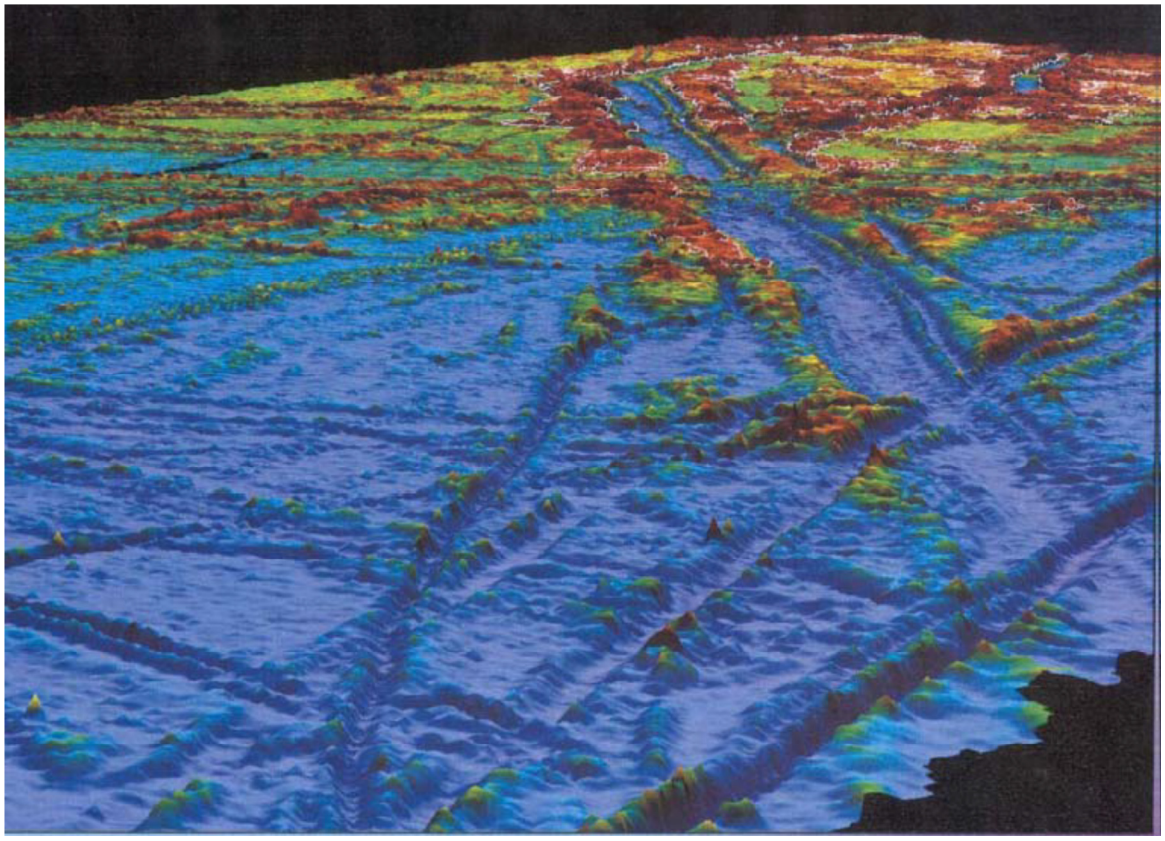

Figure 2-3 Ice gouge tracks in Canadian Beaufort Sea (S. Blasco, NRCan)

The current experience in offshore pipelines in cold areas is relatively limited. As the results very little damage to the pipelines by ice features has been documented. However some instances of these damages can be found in literature (Grass, 1984; Noble & Comfort, 1980; Vershinin et al., 2008).

2.2.3. Typical gouge geometry

It is widely agreed that the most important issue endangering the safety of offshore pipelines in cold areas is seabed gouges. The problem of ice gouging affects both the pipeline design and route selection in offshore projects.

Floating ice masses are sometimes directed into shallow water due to wind and current. These masses can cause deep gouges into the seabed when they ground in shallower waters. It is generally accepted that deeper gouges occur in relatively deeper waters of about 20 meters and in shallower waters (about 5 to 10 meters deep) smaller gouging events will happen. However, it should be considered that this notion might become misleading. The reality is the sedimentation has a strong effect on removal of the relicts of the previous gouges and in shallower waters smaller waves could initiate the sedimentation process compared to deeper waters. Figure 2-4 shows a typical relation between water depth and gouging depth based on the data obtained from Beaufort Sea. The data shown in this figure is based on the surveys in Beaufort Sea (Rearic & McHendrie, 1983).

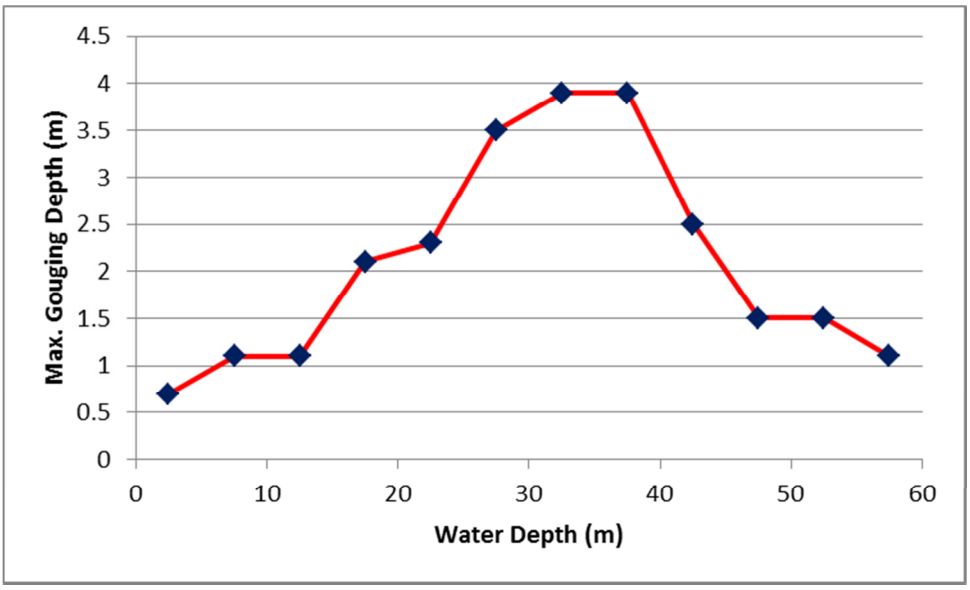

Figure 2-4 Water depth and maximum gouging depth in Beaufort Sea

In the Beaufort Sea and the Arctic Islands the gouging occurs from shore into water as deep as 50 meters. Although some gouges of around 5 meters deep have been discovered, most gouges in the seabed usually have shallower depths. Table 2-1 presents the statistical data of gouging events obtained from Alaskan Beaufort Sea (Rearic & McHendrie, 1983). Surveys show that deeper ice gouges happen in deeper waters from icebergs such as Davis Strait in Labrador Sea and the Grand Banks in southeast coast of Newfoundland.

Table 2-1 Ice gouge data from Alaskan Beaufort Sea

Water Depth (m)	No. Gouges	Gouging Depth (m)	
		Mean	Max
0 - 5	22	0.3	0.7
5 - 10	220	0.3	1.1
10 - 15	1141	0.4	1.1
15 - 20	3820	0.4	2.1
20 - 25	10250	0.4	2.3
25 - 30	6210	0.5	3.5
30 - 35	2165	0.6	3.9

Water Depth (m)	No. Gouges	Gouging Depth (m)	
		Mean	Max
35 - 40	298	0.9	3.9
40 - 45	163	0.6	2.5
45 - 50	139	0.6	1.5
50 - 55	51	0.7	1.5
55 - 60	2	1	1.1
Total	24481	0.5	3.9

Different gouge depths could be observed in various parts of cold regions, for example at Terra Nova (located in northeast Grand Banks of Newfoundland in water depths of about 95 meters), iceberg tracks are typically less than 1 meter deep.

Primarily it was hoped that the gouges that have been discovered at the seabed are the relict of the past and they do not happen contemporarily but further studies showed that even deep gouges are being formed at present (Palmer et al., 1990).

Ice gouging is an interaction event between seabed soil and the keel. If a subsea structure such as pipeline system exists in vicinity of such event it could reinforces the surrounding soil locally therefore the coupled response of the marine structure, /seabed and ice should be considered. Ice gouging can exert very large forces on the seabed and induce large plastic sub-gouge deformation.

Ice gouges usually leave very large marks on the seabed. As an example, in Terra Nova gouges of an average of 25 meters wide and hundreds of meters long have been observed (McKenna et al., 1999). Ice gouging is the result of various ice features that reach the seabed level like icebergs as shown in Figure 2-5.

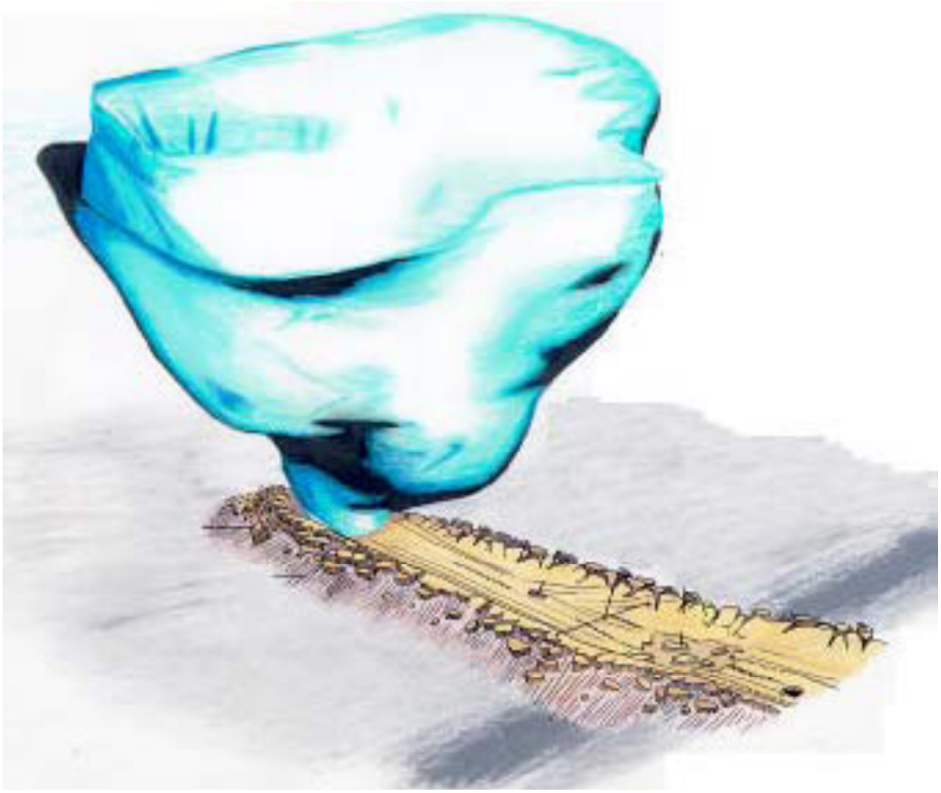

Figure 2-5 Iceberg 'Bertha' gouging the seabed in Grand Banks

2.2.4. Ice gouge – pipeline interaction

Ice gouging could pose a big challenge for pipelines in cold regions. Based on the extent of the soil deformation, the seabed is divided in three zones as shown in Figure 2-6. The zone 1 is the uppermost layer of the seabed. The ice keel induces very large deformation in this zone leading to potential failure of the pipeline system due to possible direct impact. Therefore, the placement of the pipelines in this zone should be avoided. Zone 1 extends to the base of the ice keel. Zone 2 is located below zone 1. It used to be assumed that in case the direct contact between the keel and the pipeline is avoided then the safety of pipeline is not jeopardized, therefore laying the pipeline just below the ice base or Zone 1 deemed as sufficient. However the findings of the PRISE project and the prior

studies as well, showed that Zone 2 or the intermediate zone also includes large deformations in the soil under ice gouging. The large sub-gouge deformation in the proximity of the keel could have serious consequences on the buried pipeline even without any impact between the ice and the pipe. Zone 3 is where the small strain region starts. Placement of the pipelines in this zone is safe but not economical and depending on the environmental situation it might not even be feasible. The current state of practice is to find the optimum burial depth of pipeline where all the safety provisions are met and meanwhile the construction would not be too expensive. In the past pipeline used to be trenched in a depth twice the maximum gouging depth or more (Nobahar, Kenny, & Phillips, 2007). However, further studies showed that the pipeline can experience large deformations before it fails. Since ice gouging is a displacement-controlled phenomenon it is acceptable to define an ultimate state in which the pipeline is plastically deformed yet the structural integrity is maintained. (Nobahar, Kenny, & Phillips, 2007).

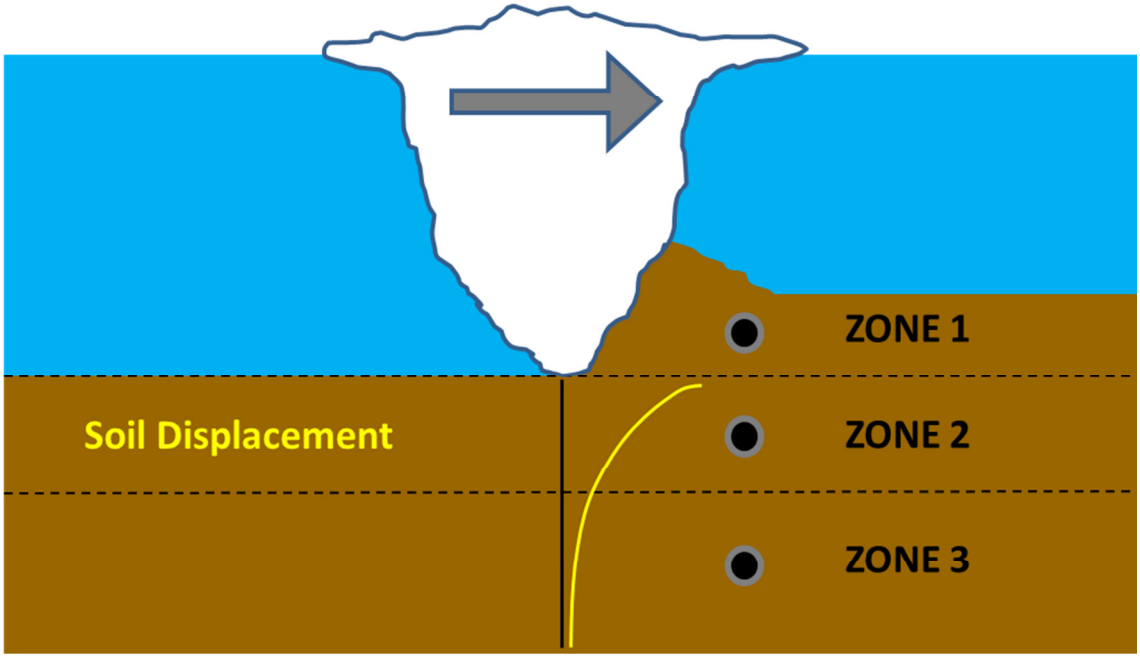

Figure 2-6 Sub-gouge deformation is divided in three zones

2.3. Offshore Pipeline Protection

The marine pipelines have to be secured against ice gouging in cold areas. There are two main methods for offshore pipeline protection: 1) shielding and 2) trenching and burial. Shielding refers to instalment of protective structures over the pipelines. These structures must resist the impact of the ice feature. These structures are mostly used for pipelines approaching the shore but the implementation of such protective shield for the whole length of the pipeline network is uneconomical (Palmer & King, 2008; Vershinin et al., 2008).

The most common method of pipeline protection is seabed trenching and pipeline burial. Currently to safeguard the offshore pipelines against the ice gouging in cold areas, trenching followed by pipe burial is recognized as the most effective method. However, the main question that should be addressed is that how deep the pipeline should be buried. Obviously the deeper the pipeline is placed the safer it is should it face a gouging event. However, trenching the seabed deeper increases the project cost dramatically.

The design method used to be the placement of the pipeline at a depth lower than the maximum anticipated gouging depth. Further investigation though, showed that large soil deformation below the gouging depth exerts high forces on the pipeline that may lead to excessive pipe displacement. As mentioned before the placement of pipeline at zone 3, where the soil deformation is essentially in small elastic range, needlessly escalates the economic cost of the project. Therefore, the challenge is to find the right depth in zone 2, as shown in Figure 2-6, where the pipeline can undergo appropriate amount of bending due to the soil deformation and yet maintains its safety and functionality. Taking

advantage of the structural ability to sustain plastic deformation provide the opportunity of reducing the project costs by embedment of shallower buried pipelines.

2.4. Previous Studies about Ice Gouging

The ice gouging problem has been studied using four different methods:

1. Field studies;
2. Simulation in laboratory;
3. Theoretical studies; and
4. Numerical analysis

For example historical events show that ice gouging causing large deformations of the soil forming trenches at seabed and pushing soil materials into berms at either side of the trench (Woodworth-Lynas et al., 1996) and numerical analyses and laboratory tests show that a mound would be formed in front of the keel and as the gouging advances the mound clears around the keel. This shows that the ice gouging phenomena is a three dimensional process in nature (Palmer et al., 1990). Palmer and Niedoroda (2005) provided comprehensive information describing ice scouring process and some unresolved question in this field.

2.4.1. Field studies

Field studies can provide precise information about ice gouging event. However, technically they involve significant operational challenges. Field studies are implemented to pursue different purposes. One of these purposes is to study a real gouging scenario in a natural environment. Such study can give valuable insight as to how the gouging

mechanism works. This kind of study includes finding an area where gouging might occur, predicting the drift path of an ice feature, instrumentation of the drift path, specification of ice feature properties and characterization of seabed soil properties. An example of natural ice gouging study was performed in 1985 on the Labrador continental shelf. The program was called the Dynamics of Iceberg Grounding and Scouring (DIGS) (Hodgson et al., 1988; Lever et al., 1991; Woodworth-Lynas et al., 1991).

Some of the offshore pipelines projects that were designed with consideration of ice scour in cold regions are North Star in Beaufort Sea in which the pipes are trenched to a depth of 2.2 meters (Lanan & Ennis, 2001), the Millennium project in Lake Erie in order to convey Canadian natural gas to the United States in which the pipes are prone to deep scours and a trench of 3.4 meters was proposed in the design (Lever, 2000), the millennium project was never built though, the Hibernia, the Terra Nova and White Rose facilities in Grand Banks of east coast of Canada and Drake F-76 pipeline which was a test project to study the feasibility of gas transmission in Canadian arctic islands. These types of projects have been implemented in other cold areas such as Kashagan field in the Caspian Sea and Sakhalin projects 1-4 in the Sea of Okhotsk (Kenny et al., 2007).

Another category of field studies deal with characterization of the real ice features. To predict the maximum gouge depth it is essential to have adequate knowledge of both soil and ice properties of a geographical location. This is particularly crucial for ice ridges which have complex internal structure (Croasdale et al., 2001; Croasdale et al., 2005; P. Liferov et al., 2002).

Another important category of field studies is seabed mapping. These studies provide an understanding of the nature of the ice gouging in an area. Important data such as gouge

depth, width, length, orientation, density and frequency could be obtained through a seabed mapping study (King, 2011).

Another subject of field studies concentrates on the gouge relicts now on land that used to be the seabed of ancient lakes or seas. These studies can provide helpful information about the sub-gouge deformation of the soil (Woodworth-Lynas et al., 1996). The sub-gouge deformation is an important parameter in assessment of the burial depth. Therefore understanding the amount or extend of soil deformation under the real gouges is a key factor in design of burial pipelines.

Field measurements data of ice gouging simulation are very limited. P. Liferov (2005) reported the results of a series of tests that measured the failure of seabed soil and ridge keel.

Because of the complexity in obtaining in situ full scale ice gouging data the small scale test and numerical analyses are being used for design purposes (P. Liferov et al., 2007).

2.4.2. Experimental Tests

The ice gouging event is a soil interaction problem that is associated with large deformations, shear bands and cracks. As the result its simulation through finite element analysis or other numerical methods poses difficulties. Therefore experimental research stands as a reliable and accurate way to understand the ice gouging process. However a real scale ice gouging experiment would be a massive and expensive project that deals with very large forces which are hard to be handled accurately. In addition it would be very difficult to measure the sub-gouge deformation due to scouring ice keels.

These issues make a real scale test project unfeasible therefore laboratory tests are executed to simulate the ice gouging phenomenon. Small scale test soil samples can be readily prepared in almost identical situations. However, very small scale laboratory tests have usually the disadvantage of misrepresentation of the real situation since the soil response under the low pressure of the controlled testing situation is considerably different of that in the field. This issue is especially crucial for cohesive soils since the stress level is relatively small comparing to the soil cohesion and the constituted mound in front of the translating keel adds to surcharge load and influence the deformational response of the soil. For sand the shear response is different at low level and high stress level as well. At high stress level because of the onset of the particles crushing the soil might tend to show cohesive behavior unlike low stress level where the sand response is chiefly frictional. In addition bigger measurement error is usually affiliated with the lab instrument at low stress levels than at higher stress levels. The centrifuge testing provides the opportunity to increase the stress level to overcome some of these problems.

The studies that employ physical modeling to examine the ice gouging event should include consideration of applying the obtained laboratory data to the actual real-scale event. This is usually achieved through scaling the dimensions, velocities and forces of the model in way that represents the original gouging event. As with many other complex phenomena a complete identical simulation is hard to reach therefore compromises should be made. It should be noted that scaling has been ignored in some laboratory programs where the main object was to validate or calibrate a numerical model (Barker & Timco, 2002, 2003; P. Barrette & Timco, 2008; Stava et al., 2008; Vikse et al., 2007); and

the other approach is using a centrifuge to simulate the high gravity (Allersma & Schoonbeek, 2005; Phillips et al., 2005; Schoonbeek et al., 2006).

Ice scour studies at C-CORE started in 1978. As the first step Gustajtis (1979) comprehensively reviewed and reported what was presented in literature about various aspects of ice scour process. During 1978 to 1990 C-CORE research was concentrated in fields such as collecting phenomenological data of ice scouring, direct observation of scours from manned submersibles, study of the relict scours in the Canadian Arctic and Lake Agassiz, Manitoba, study of small-scale iceberg gouging events in the St. Lawrence River and Laboratory modeling of the scour process. In the industry sponsored field project DIGS, the Dynamics of Iceberg Grounding and Scouring, C-CORE in association with other organizations studied the relict iceberg scours in the former seabed of glacial Lake Agassiz in south eastern Manitoba. In this onshore study scour displacements as large as 3.5 m were concluded in strong over-consolidated clay seabed (Woodworth-Lynas, 1998). In other small scale field program scours formed in St. Lawrence estuary near Montmagny, Quebec and at Cobequid Bay, Nova Scotia were the subject of research. These scours were 0.5 to 1.0 m wide and 0.15 to 0.2 m (Poorooshasb & Clark, 1990). It was concluded that in fine materials significant subscour deformations can happen while the surface deformations is relatively small.

Chari and Green (1981) conducted scouring tests in a flume 14 meters long and 4 meters wide. The study illustrated the motion of sediment ahead and below a gouge. Green and Chari (1981) buried pipes below the scour and in front of the keel and measured the pressure on the pipes. Green et al. (1983) showed that a keel with an inclination of 30 degrees in front yields about 30% increase in pressure on the pipes as compared to a keel

with vertical face. Abdelnour et al. (1981) used an 18 meters long and 6 meters wide basin and measured the pressure distribution on the soil and the keel model for different types of seabed material such as sand, silt and clay. They also examined the different cutting depth and different towing velocities. The keel was also modeled with two different shapes.

Kioka et al. (2000) and Kioka et al. (2004) have performed small and medium scale laboratory tests.

Kioka et al. (1999) conducted several tests and examined the effect of attack angle and scouring velocity. The experiments showed that the gouging force is influenced by the velocity but not by the attack angle. However the attack angle affects the scour depth and the upward displacement of the model keel increases with the decrease of attack angle (measured with respect to horizon).

Barker and Timco (2002) used ice blocks to scour a number of soils. They examined the issue of compaction and the effect of void ratio during the scour process. They tested compacted and loose sand and gravel and concluded that the forces measured during the scour of compacted soil is an order of magnitude higher than the forces measured for loose sands. Palmer (1999) earlier explained this behaviour. He concluded that following the dilation of dense sand pore water pressure may severely drop therefore the plowing force would considerably increase.

Vikse et al. (2007) performed gouging tests in which pipelines were present. They reported when the gouging element passes the pipeline it follows a cyclical motion path. They also report that the maximum pipeline deformation occur at the lower attack angles of the keel.

Paulin et al. (1991) conducted scouring tests on sand both in dry and fully saturated sediments. They modeled two angles of attack of 15 and 30 degrees. They concluded that displacements in loose sand were larger than dense sand.

Laboratory experiments using the scour tank facilities in Memorial University of Newfoundland were also performed. Clark et al. (1990) studied modeled ice scouring in very soft silt soils and Clark et al. (1994) examined the ice scouring event in sands. Although previous laboratory researches used to assume that the ice scour is dominantly a ploughing action on the seabed with negligible vertical force but the studies of the relict scours and small scale laboratory test suggested that the vertical force of the ice feature might be sufficient enough to lead to failure and displacement in the soil below the scour. This observation was used in design of these scour tests and the model iceberg was allowed to move vertically.

The experiments on soft silt soils consisted of two scour cut depth of 40 and 70 mm. Tests data recorded soil displacements as deep as 200 mm for 40 mm scour depth. For the deeper scour depth of 70 mm it appeared that the soil is completely remoulded. The overall conclusion was that the silt scours causes deep deformation.

The sand tests were performed for two sets of soil of relative density of 0 and 50 percent. Two different scour depths of 40 and 75 mm were also chosen for the tests. The test results showed that the scouring imposes soil deformation to a depth of 3 times of the gouge depth. It was observed that the horizontal component of the displacement was dominant. The variation of the attack angle was also examined in these tests and it was shown that a change in attack angle from 30 to 15 degrees would result a noticeable increase in soil disturbance and deformation beneath the scour as the force required for

scouring increases. It was reported that the most important factors controlling the subscour deformation in sand bed models are the angle of attack of the iceberg and the density of the soil. In medium to dense sands in was shown that the vertical total stress decrease and then increase upon the approach and passage of the iceberg. In addition larger deformations were reported for looser sands. As a conclusion a “safe” burial depth of one time of the scour depth below the maximum depth of scour was suggested for coarse grained soils. These tests concluded that under certain conditions both coarse and fine materials can exhibit significant sub-gouge deformations.

P. Barrette and Timco (2008) conducted an experimental program in order to study the mechanism of ice scouring of a coarse sand seafloor. They improved the test procedure of ice scouring in several aspects to remove some effects of test set-up that are not present in real situation. In this program the scouring process was modeled in a flume and real ice was used to scour the soil. The length and width of the flume were 6 and 2.6 meters respectively. The height of flume was 1.2 meters. Their observation confirms the previous suggested mechanisms of ice scouring. They found that upon the start of scouring the ice keel sinks into the seabed almost suddenly along the horizontal movement until midway where the steady movement parallel to the seabed starts. They concluded that the horizontal load also stabilizes when the steady state of ice scouring begins. They inferred that an important contributing factor of the loads exerted on the buried pipeline, especially in rubble material, is the uniformity of sediment strains and suggested that this issue be investigated more.

Centrifuge experimental testing is an important method of research in ice gouging studies. These tests allow the researchers to observe the response of the soil and pipeline as the

function of different contributing parameters and factors. Centrifuge tests are a good source of information to overcome some of the scaling problems of small scale test results to full scale conditions. Woodworth-Lynas et al. (1996) and Allersma and Schoonbeek (2005) have done such tests to examine the scaling issues that exist. Palmer et al. (2003) performed a thorough set of experiments and compared them with full scale data of buried pipelines and concluded that there are uncertainties in scaling the displacement field of the test results to full scale situation.

Schoonbeek and Allersma (2006) performed some preliminary centrifuge test on the multiple scouring as well as the scouring of the remolded soil. They tested ice scouring of the soft soil located on an over consolidated layer. This research focused on the scouring of clays.

The Pressure Ridge Ice Scour Experiment, known as PRISE, was an internationally funded, interdisciplinary project that C-CORE was also involved. The project aimed to develop the required guideline for safe design of the pipeline and other seabed installations in regions that are prone to ice scouring. PRISE included a wide range of activities such as data collecting, centrifuge and numerical modeling, model development and installation of experimental pipeline in regions affected by ice scour. Phillips et al. (2005) summarized the experimental program of the PRISE project. Figure 2-7 schematically shows a pressure ridge ice gouge event.

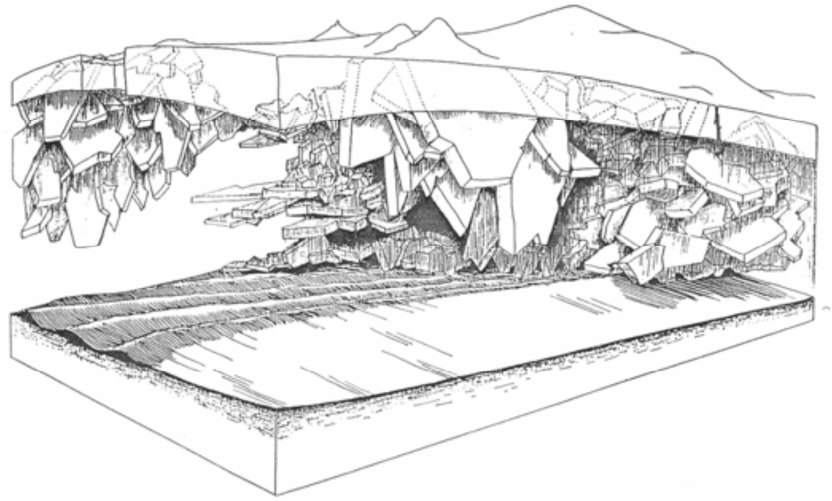

Figure 2-7 Schematic illustration of a pressure ridge

Woodworth-Lynas et al. (1998) performed a series of tests on sands and clays at scales of 1/75 and 1/150. Walter and Phillips (1998) analyzed these centrifuge tests and concluded some empirical equations to predict the forces. In their work no buried pipeline was present and the keel was modeled by a rigid indenter. The study was a part of a joint industry project called PRISE. These empirical functions (Woodworth-Lynas et al., 1996) are a valuable source of information in ice gouging event however care should be taken when they are applied to situation other than those of the tests since the soil deformation predicted using these formulas are independent from the soil properties. The result of PRISE program was published in 2005 (Kenny et al., 2005; Phillips et al., 2005).

2.4.3. Theoretical Studies

It is possible to address the ice gouging event through geotechnical theories. These theories usually consider only important aspects of a mechanism therefore they can provide simple solution as the preliminary guideline for further evaluations.

Chari (1979) studied the horizontal movement of an iceberg gouging the seabed. Considering the equilibrium of forces on the body of soil in front of the iceberg and the anticipated failure surfaces, forces on the iceberg were calculated. The momentum balance equation then is applied to predict the horizontal iceberg traveling distance. Some other researchers also followed the same method to calculated force and scour length (Kioka et al., 2000). Nilsen (2003) has summarized a detailed parametric study of these types of models that employ force equilibrium or energy balance to obtain forces and scour length. These studies provide a better understanding of the effects of kinetic energy, attack angle and other important parameters on soil deformation.

2.4.4. Numerical Analysis of Ice Gouging

Iceberg gouge models are usually categorized based on two general approaches. One approach employs a variation of plastic limit analysis. Schoonbeek et al. (2006) performed a comprehensive research based on this approach. They also discussed the construction of possible failure planes in detail to improve the estimation of the forces.

The other approach is the application of finite element method. The finite element approach has the advantage of utilizing available codes which were developed and validated to solve soil mechanics problems. It also gives the opportunity to use different type of constitutive models for various types of soils (Kenny et al., 2005).

In spite of progress in this field there are still unresolved issues. Plastic limit analysis cannot predict the distribution of the strains, stresses and void ratio. Also it is not possible to predict the deformation and stresses of the model beneath the assumed slip lines. The large deformation associated with the nature of the scour problem poses a lot of

difficulties when finite element method is applied. On the other hand the finite element methods that employ mesh reconstruction are numerically expensive and therefore their practicality is limited. Palmer and Niedoroda (2005) discussed some of the challenges that were present in modeling. However, numerical analyses are known to be a strong tool to study the mechanism of ice gouging and determine the behaviour of soil and pipeline to the scours. As an example Konuk et al. (2005) showed through numerical analyses that the deformation path of particles in sub-gouge region is elliptical as the keel pushes the soil down and advances forward. After the keel passed the soil particles recover their deformations to some extent and spring back toward their initial state but not to the exact same position which is an implication of plastic deformations.

Numerical analyses have the advantage of being able to simulate the response under different boundary conditions and loading cases or soil materials in general.

The selection of an appropriate constitutive model is essential for an accurate numerical analysis. These models should be able to account for different stress paths. They also should be simple in term of providing the input parameters with small number of common tests. In addition it is important that they are based on the realistic interpretations of material stress- strain behavior of the ice gouging event. Kenny et al. (2005) showed the finite element analysis can simulate key aspects of ice/seabed/pipe interaction adequately.

Continuum models are theoretically exact representation of the physical problem they define, however in practice they are not exact and their response depends on the constitutive model and the idealizations employed in the solution method.

Various numerical methods are introduced in literature to solve the problem of the ice gouging. Some of these methods are more popular like pure Lagrangian, updated

Lagrangian, pure Eulerian, mesh free and Arbitrary Lagrangian Eulerian. The advantage of the pure Lagrangian formulation is the precise definition of the ice-seabed interface as the nodes are fixed within a material. However as mentioned before, because of the large deformation in gouging problem that generally prevents the analysis to converge a Lagrangian reference approach may not be stable. Woodworth-Lynas et al. (1996) reported that this technique encounters convergence problems due to excessive mesh distortion that might happen in the large deformation problem of ice gouging. Konuk et al. (2005) also reported that the process of projecting the nodal values to the nodes of the new mesh in the updated Lagrangian method produces errors in the analysis. To overcome the problem of large deformation and its consequent numerical instability and to improve the results of the numerical analysis the Arbitrary Lagrangian Eulerian method is used in ice gouging finite element analysis (Jukes et al., 2008; Kenny et al., 2004; Konuk et al., 2005; P. Liferov et al., 2007; Nobahar, Kenny, King, et al., 2007). In addition to ALE, meshless method can also be used to address large deformation problem of ice gouging, however little work has been done in this regard.

To study the mechanism of ice scour problem both 2D and 3D models have been developed. However as laboratory tests have shown as the keel advances the developed mound in front of the ice feature clears away into the berms at the sides. Therefore to better simulate the ice scour phenomenon the model should be 3D in order to be capable to clear the mound in front of the keel and prevent the extra-large overburden.

During the PRISE program many researches were done to numerically simulate the ice scouring process. Q. S. Yang et al. (1993) and Poorshasb and Yang (1993) used an elastic-perfectly plastic, non-dilatant Drucker Prager model. They used small strain

formulation and modeled the pipe with beam elements. The soil was assumed to be in undrained condition. Q. S. Yang et al. (1996) back analyzed the centrifuge results for clay soil using 2D model under undrained condition. The model concluded larger results than observed in test.

Lach (1996) also used 2D model with the modified Cam Clay constitutive material. He faced limitation due to 2D simplification and excessive mesh distortions.

Phillips and Popescu (1998) performed sensitivity analyses using non-associated Mohr Coulomb plasticity model. They reported that large displacement can be achieved but this requires assigning low values for soil elastic modulus.

Konuk and Gracie (2004) proposed a 3D model applying ALE to the large deformation problem of ice scour. In this model soil material is defined as Eulerian elements and the ice indenter moves through the Eulerian mesh. The model assumes that scour reaches steady state situation before reaching to the pipe trench. The indenter is rigid. They used Cap model for the soil constitutive model. They concluded that application of the ALE numerical models could result in the burial depths half as deep as that obtained using either Winkler models or PRISE empirical equations.

Kenny et al. (2005) performed a series of numerical analyses as part of the PRISE program to characterize the subgouge deformation phenomenon under ice/soil/pipe interaction. The ice/soil/pipe interaction is decoupled into ice/soil and soil/pipe interaction and studied separately. In this study the deformation were imposed to Winkler type model according to empirical relations proposed by PRISE JIP. The Winkler type structural model simulates the response of pipeline. The ice keel is modeled as a rigid indenter without any failure surface. The gouging analyses were performed on both clay

and granular material. Using Modified Cam Clay model for clay seabed led to results in agreement with centrifuge tests however for granular material the analyses could not simulate the seabed behavior successfully.

Nobahar, Kenny, King, et al. (2007) developed 3D continuum ice/soil/pipe model using ALE feature of ABAQUS. This model was used mainly to study the pipeline buckling and local instability. In this model contact elements were used for the ice-soil interaction. The pipeline is modeled using shell elements and extended beyond the soil domain using beam elements and springs to cancel the effect of boundary condition on the pipeline. The ice was modeled as rigid indenter. To overcome the element distortion due to large deflection adaptive mesh refinement in ABAQUS explicit was used. In this study the elastic plastic Von Mises constitutive model was chosen for the soil. This study concluded that the result of Winkler models are conservative however it is noted that validation based on physical test should be performed. The result of the analyses showed that severe load on pipeline happens during the gouging process rather than a steady state deformation.

P. Liferov et al. (2007) developed a series of numerical models to analyze the different aspects of ice gouging problem of ice/soil/pipe aspect. The main goal of the study was the determination of the ice gouge depth. Semi empirical functions were derived through the extensive parametric analysis that was conducted. The interaction problem was addressed in both coupled and decoupled 3D finite element models. To deal with the large deformation problem of ice gouging event and prevent the numerical instability the analysis was performed using a finite difference method with Arbitrary Lagrangian Eulerian (ALE) formulation. The updated mesh option in PLAXIS continuously updates

the finite element mesh in updated Lagrangian analyses and is very important to overcome the large deformation issues. In their analysis the ice keel failure has been defined. For the coupled analyses the finite element software of PLAXIS and for the decoupled analyses the finite element software ABAQUS were used. This study suggested that the ice keel failure is not a stable mechanism and depends on local geometry of the keel. These local factors are usually unknown and in general ice failure should not be considered as a factor limiting the scour depth. The study proposed empirical relationships to describe ice gouging process and predict the gouge depth as a function of physical factors such as soil properties, soil stratigraphy, seabed slope, ridge dimension,, initial velocity, attack angle, keel strength, keel-soil friction and driving force.

Konuk et al. (2007) reported some challenges that are involved in numerical analyses of ice gouging event and the response of the pipeline. These challenges include proper understanding and modeling of the ice indenter, determination of the initial geometry of the ice feature that gouges the seabed, selection or development of the suitable constitutive soil model, selection of the discretization method, definition of the interface processes and contact mechanism between the ice and seabed.

Jukes et al. (2008) proposed a three-dimensional finite element model that employed a Coupled Eulerian Lagrangian (CEL) to deal with the large mesh distortion problem. In their model ice ridge movement is allowed to move in one translational direction as a steady state process. ABAQUS software 6.7 was used in this study. Lagrangian elements were used to model the pipe and ice ridge and Eulerian elements to model the soil. The ice ridge was modeled as rigid indentor and general contact with penalty based friction

was chosen to model the ice/soil interaction. The constitutive material model of Drucker Prager Cap was selected to represent the soil seabed. The study suggested that in general ice gouging event in dense soils leads to higher deformations of the pipeline. In addition higher deflections are produced in the soil as the scouring depth increases. The study also showed that under scouring phenomenon the displacement of the pipeline is not just horizontal but as the ice ridge reaches the pipeline it moves downward as the result of the increase in vertical stress and then the pipeline spring back upward as the ridge moves away. The rebound of pipeline deformation and its duration have a direct relation with the scour depth. The study reported the effect of the scour depth and soil compaction on the deflections and strains imposed on pipeline and soil through finite element analysis.

Evgin and Fu (2008) developed two models, a two-dimensional and a three-dimensional model. The goal of this study was to show the importance of employing interface elements between different materials. They also showed the advantage of using three-dimensional models over two-dimensional models. The ice is modeled as linear elastic material with high elastic properties and the soil is simulated as Cam-Clay critical state model. The study concluded that the use of interface elements reduced the amount of mesh distortion and led to less numerical instability that is usually present in ice gouging problems. The study also showed that the 3D model predicts smaller displacement than the 2D model. Although both models used a Lagrangian system but the presence of interface element are shown to have a significant role in reduction of mesh distortion and numerical instability. The 2D analyses were performed with PLAXIS and for the 3D analyses the ADINA software was used. In this study the effects of burial depth, the

shape of the ice feature and the seabed soil material properties on the pipeline stresses were examined.

Sayed and Timco (2009) proposed a 2D model to simulate ice scouring problem with a rigid moving indenter as iceberg. Their model used Particle-In-Cell (PIC) advection scheme which is suitable in large deflection problems and problems dealing with discontinuities. PIC models soil as discrete particles which behave as moving nodes that have all the information needed to solve the governing equations. In this model the soil is represented by a rigid plastic Mohr-Coulomb criterion. This is to simplify the numerical analysis since consequently there would be no need to track the elastic strains. The model assumes that the displacements in the sand occur at the critical state and the stress path from initial state to critical state is neglected. The study investigated the dependence of scour stresses on scour depth, soil properties, compaction and scour velocity. The observed result from this study was qualitatively in agreement with the PRISE displacement functions. However, a larger value of stress in the soil is predicted as the keel advances. This could be related to the physical process of ice gouging where the frontal mound is allowed to clear away to the berm which is not simulated in these 2D analyses. In this study only vertical movements of the iceberg were modeled. The results of the study showed that most of the displacement occurs over the narrow zones which are located mostly in the wedges that are formed in front of rigid indenter near the free surface. The authors concluded that numerical modeling is capable to simulate the scour process of seabed and can handle the large deformation associated to the event. Their study showed that the numerical simulation can predict distribution of stress and displacement and consider the role of material properties. The validation of the analyses

result was carried out using detailed measurements of passive earth pressure experiments. The role of internal angle of friction and soil compaction was also examined in the study.

Abdalla et al. (2009) used the Coupled Eulerian Lagrangian (CEL) method in ABAQUS finite element software to examine the ice gouging process. Their three dimensional model predicted induced stresses and strains in the pipe under ice gouging event. They validated their model by comparing the result of the subgouge soil displacement to centrifuge tests data and other FE models developed by other researchers. They proposed relations between pipeline burial depth and pipeline strains for various ratios of pipeline diameters to thickness.

Banneyake et al. (2011)used a Coupled Eulerian Lagrangian based three-dimensional model in ABAQUS to study the ice/soil/pipe interaction. In their numerical model a variation of different gouging depths, attack angles, pipe diameters, keel widths, depths of pipe placement and seabed soil type was investigated. In this study the linear Drucker Prager model and the total stress Von Mises model of ABAQUS were utilized respectively for sandy and clayey seabed. This study concludes some general observations regarding the nature of the gouging event including:

- The heights of the side berms and frontal berm are proportionately related to the gouge depth, keel attack angle and the keel width;
- The sizes of side berms are higher in sandy soil than the clayey soils;
- The larger keel attack angles result in a the scraping-like mechanism of removal of the soil which reduces the subgouge deformation;
- The larger keel width increases the subgouge deformation of the seabed; and

- The sub-gouge deformation in sandy seabed is generally greater than the sub-gouge deformation in the clayey seabed.

2.5. Ice Gouging Design Methods

With the growing energy demand drawing more attention to the offshore resources during the past recent decades many researches have been conducted to establish a methodology that addresses different aspects of the ice gouging event. These methods focus on specific issues of ice gouging such as gouging depth, gouging frequency, burial depth or other subjects of interest. Some of these methods are introduced in this section.

A comprehensive design method should include investigation of gouge widths and depths, soil properties, pipeline properties and operating conditions. Finite element analyses and physical tests can provide strain interpolation for combinations of gouge depths and widths. Statistical studies should be conducted to assess the probability of the gouging. The statistical studies of the area of interest help to determine a probability density function for gouging depths and widths. All these studies together could provide burial curves that define the failure probability as a function of burial depth for a gouging event. Depending on the target reliability these curves are used to determine the required pipe cover. Based on the industrial guidelines a return period of 1000 years of exceedance of strain criteria is usually selected. This return period will increased to 10000 years when the design relates to areas near manned structure or significant environmental damage (DNV, 2007).

Kioka et al. (2004) proposed a probabilistic model that derives the gouging depth of the ice features. The concept behind the model is that the keel ceases to scour the seabed

when the resistance mobilized by the seabed becomes high enough compared to the kinematic energy of the driving agents such as wind, current and the surrounding ice sheets. In this model the material properties are assumed constant and the physical properties of the keel such as attack angle or ice thickness are the most influential parameters of the model.

Croasdale et al. (2005) proposed a model that predicts the gouge depth. The model derives the maximum gouging depth based on soil properties and the keel physical characteristics. This model utilizes the Mohr-Coulomb for the soil constitutive model and is specifically intended for first year ridges. In this model the failure of the keel is allowed. The influential parameters of this model are soil strength, keel attack angle and ice strength.

Been et al. (2008) proposed a model that derives the sub-gouge deformation in consistence with the centrifuge or single gravity tests. This model considers the undrained shear strength, soil stiffness, gouge depth and width, keel attack angle and soil-keel interface strength. The model is solely empirical therefore it should be just applied to the test conditions on which it is based.

(King et al., 2009) proposed a study method specific to a hypothetical pipeline in offshore Newfoundland. The method studies the failure probability for burial depth of zero to four meters. Two assess the failure two limit state criteria were defined: 1) keel-pipeline direct contact and 2) pipeline compressive and tensile strains (2.11% and 2.5% respectively)

Nobahar, Kenny, King, et al. (2007) and Nobahar, Kenny, and Phillips (2007) studied the probability of failure along a hypothetical pipeline of 10 km long. In this study various ratios of diameter to wall thickness was considered. On the other hand, the undrained

properties of the soil assumed to be constant. Two limit states were defined: 1) 90% of pipe yield stress and 2) compressive strain limit of the pipe. The study shows the superiority of strain based criterion over stress based in a displacement-controlled loading.

The ICE PIPE JIP was led by DNV and thirteen other industrial entities to propose safety and practical guidelines for offshore pipeline in cold regions. These guidelines particularly address the ice gouging. Based on these guidelines a design approach is recommended that principally aims at reduction and identification of uncertainties associated with ice gouging (Davies et al., 2011).

2.6. The PIRAM Project

PIRAM, Pipeline Ice Risk Assessment and Mitigation, is one of the two projects of the program “Protection and Risk Mitigation Strategies for Subsea Infrastructure in Ice Environments”. This project is devoted to enhancement of safe, cost-efficient and reliable pipeline systems in ice environments as one of the most important elements of the offshore industry (Phillips et al., 2012). The project aims to develop a pipeline protection model which is a set of integrated engineering models capable of simulation and prediction of the interaction of ice keel with the seabed and pipelines, derive a probabilistic tool of estimation of the imposed loads and the mechanical response of the pipeline system. The pipeline protection model also evaluates the protection and risk mitigation strategies for pipeline systems. The project consists of a number of tasks which each of them is studied independently.

At the first step the interaction scenarios have been identified to define the range of engineering parameters that are to be investigated under pipeline protection framework.

Among various possible interactions, the one between ice and seabed is of special interest. Therefore, an entire task is devoted to development, calibration and validation of the three-dimensional model based on the finite element method and adaptive meshing to simulate this particular interaction. The purpose of this modeling is to estimate the seabed reaction forces, the ice keel driving forces, the ice keel stress state and the spatial extend and magnitude of the free field sub-gouge deformations during the ice/seabed interactions.

In this task the development of the soil plasticity models are further improved to address different factors contributing to the soil behaviour. These factors include non-associative behaviour, strain softening or hardening response and the negative dilation. The initiative of this research study comes from the requirements and limitations that are encountered during this task. The focus of this research is to improve the numerical simulation of the ice/seabed interaction by enhancing the constitutive models of the soil.

When the buried pipelines are studied the common practice is to separate the interaction events of the pipeline and the soil and the ice keel and the seabed. As the consequence it is assumed that the pipeline does not influence the soil failure mechanism or load transfer mechanism or the deformations of the soil but only responds according to the loadings that are exerted by the soil deformations under the gouging. To overcome these restrictions a fully coupled model is developed in PIRAM based on finite element method to account for ice/pipe/seabed interactions. This model is calibrated according to a series of centrifuge experiments conducted in C-CORE.

2.7. Recent Developments

Lele et al. (2011) describes advanced FE analysis of buried pipelines subjected to ice gouging. An advanced finite element model is presented as an alternative to the current empirical methods which are mostly Winkler type models. It was shown that the continuum approach can model the ice gouging problem more realistically. It is noted that to validate this approach, large gouging test should be performed to examine the accuracy of the model.

Sancio et al. (2011) provide an overview of unique full-scale ice-pipe sub-gouge deformation tests conducted by the Kashagan project partners. Large scale ice gouging tests were performed by towing rigid "keels" over the prepared soil and a buried pipeline. The keels were towed by bulldozer and the both sand and clay soils were used. This test program consisted of 17 tests that were completed by early 2009. The last six tests of the program included the measurement of sub-gouge deformations. Different keel shapes were used to study the ice gouging under different gouge depth to gouge width ratios. This test program emphasized on the value of carrying out large scale 1g tests and concluded that significant cost savings can be achieved for the project through the implementation of the findings of such tests. It was observed that the sub-gouge deformations are smaller than the predicted values.

Phillips and Barrett (2012) provides a review of recent development through the PIRAM project in areas such as subgouge response and physical model tests. In this paper some refinement of three dimensional continuum finite element analyses of steady state gouging and development of an effective stress plasticity model for soil are discussed.

Peek and Nobahar (2012) utilized an elastoplastic material model with the von Mises yield criterion and handled the large deformation using ALE methods combined with re-meshing and re-mapping strategies.

El-Gebaly et al. (2012) used advanced numerical methods that reduce the conservatism in the conventional numerical methods (decoupled ice-soil and pipe-soil) and studied ice gouging. The Coupled Eulerian Lagrangian (CEL) finite element method was used to compare the results with available centrifuge and full scale test data. This study concluded that the CEL analysis results in smaller sub-gouge deformations compared to the current methods.

Peek et al. (2013) model the large scale tests of Texas using a finite element model. In their model the soil was modeled as 3D continuum with Eulerian elements. In this study the large scale test on clay was modeled. The constitutive model for clay was an invariant of Von Mises yield surface with a time-dependent elastoplastic feature for calculation of yield strength. The model could capture strain hardening of the soil and stress-strain curves were obtained based on unconfined compression laboratory tests. Due to the non-uniformity of the soil in the test and simplicity of model some discrepancies were observed. However, the study concluded that theses discrepancies hardly influence the effect of gouging on the seabed.

Been, K., et al. (2013) describes the approach to pipeline design for ice load that was developed during the design of the Kashagan project in North Caspian Sea. In this design methodology, the mechanism through which the ice interacts with the buried pipe includes determination of sub-gouge deformations based on the soil properties and keel shapes and then translating the sub-gouge deformations into loads on the pipe.

Been, Peek, et al. (2013) developed new empirical relationships for sub-gouge deformation in clay. These relationships improve the previous works that were done as part of PRISE program and removed some of the conservatism that became costly in larger projects like the development of Kashagan. The new empirical relationships include data from numerical analyses, centrifuge tests and the flume tests. Unlike the PRISE program where most of the test were carried out using keels with attack angle of 15°, attack angles of 30° and 45° were considered too. The new sub-gouge deformation relationships were proposed for both clay and sand. New parameters that capture the material properties were included in sub-gouge deformations formulas which significantly improved the PRISE functions.

Fuglem et al. (2013) described methods used to determine extreme-level and abnormal – level scour dimensions required as input for determining design pipeline burial depth based on the soil conditions and pipeline configurations. These methods were used in the design of the Kashagan project. Maximum and average scour depth are significant design data in determination of burial depth.

P. D. Barrette and Sudom (2014) compiled a database of nearly 500 physical tests that were performed in order to understand the mechanism of ice gouging. The database includes different keel shapes, degrees of freedom of the keel, soil and pipe properties. In this research a number of significant issues and gaps that should be addressed in future studies are identified.

Pavel Liferov et al. (2014) assessed the effect of the key parameters involved in determination of the pipeline burial depth. The study concluded that steeper keels, keels with attach angles of larger than 30°, more likely would produce extreme gouges.

However, these steeper keels will results in lower pipeline responses. In this study the current gaps in determining the design gouging (such as gouge depth) are identified.

Eltaher (2014) identifies and discusses the gaps in the knowledge and numerical modeling of ice gouging. These shortcomings include relevant field and test data, especially test data with inclusion of pipe, lack of a unified design guideline and rational simplified models and gaps in numerical models. Soil constitutive models, numerical formulations, ice-soil interface and pipe-soil interface are among the topics that need further development in order to achieve robust numerical models.

Pike et al. (2014) highlights the areas of uncertainty that exist in the state-of-practice methodology of the design of offshore pipelines in ice gouge environments. This paper specifically focuses on the issues related to the simulations of contact mechanics and definition of interface parameters. The study concludes that the use of idealized interface conditions can provide a rational approach to establish bound estimates on contact mechanics, sub-gouge deformations, soil clearing processes and failure mechanism.

Pike and Kenny (2014) studies the interpretation of soil resistance to axial pipe movement in cohesive soil material for oblique loading. Through a sensitivity analyses, the effect of changing the interface shear stress limit and friction coefficient is examined. The study concludes that the incorporation of a shear stress limit in the definition of tangential shear behavior has a considerable effect on the axial pipeline reaction forces. A combined approach that applies a reasonable drained friction coefficient in parallel with an interface shear stress limit associated with the remolded undrained shear strength of soil is recommended for numerical simulations of oblique pipe/soil interaction in cohesive soils.

3. Critical State Soil Mechanics and Modeling of Soil Behaviour

3.1. Introduction

The critical void ratio was the subject of much research since it was first proposed by Casagrande (1936). It had been already understood that dense soils tend to dilate and loose soils contract toward failure, e.g. Reynolds (1885). Further observations showed that volumetric response of soil keeps evolving until almost a specific void ratio is developed at large strains. The fact that this void ratio distinguishes the volumetric strain behavior of soils was the reason why Casagrande named it the critical void ratio.

The critical state concept of soils was proposed by Roscoe et al. (1958). The critical state can be defined as a state where the soil tends to continue to deform in the constant stress level and void ratio. In other words the steady state of a mass of particles is a situation in which the volume of the mass, the normal effective stress, the shear stress and the velocity remain constant while the mass deforms continuously. The critical state proposed by Roscoe et al. (1958) in fact refers to Casagrande critical void ratio and defines the ultimate state of the soil if it is kept being sheared (deformed).

Conventionally, to account the influence of soil density geotechnical engineers used to assign different values of properties to the same soil depending whether the soil state is loose or dense, e.g. the same soil could have had an effective friction angle of 30 degrees in loose condition varied to 35 in denser conditions. Applying the generalized plasticity constitutive models,e.g. Pastor and Zienkiewicz (1986); Pastor et al. (1990), the same exact sand should be dealt with as different materials depending on its density and

pressure level because sand behaves differently under different states. In other words, density used to be an irrelevant parameter to the constitutive models used in soil simulation. This failure routed back to the extension of utilization of metal constitutive models to the soil. Nevertheless, changing material properties to accommodate contractive or dilative behaviour of the same soil is conceptually misleading as soil is a material that emerges over a wide range of densities while maintaining the same native characteristics.

One of the most important progresses that emerged as the outcome of the researches in this area was the advent of Critical State Soil Mechanics by Schofield and Wroth (1968). CSSM is the first systematic effective stress framework that tried to interpret the soil basic properties into engineering behaviour based on soil density.

Although clays were the main concentration of the research, but the concept of critical state of soils was also applied to sands (Stroud, 1971; Wroth & Basset, 1965). The studies on sands led to fewer successes than clays due to the complexities associated with the determination of the critical state of sands. However, the advances in laboratory techniques solved these problems.

3.2. The theory of critical state soil mechanics

The theory of critical state soil mechanics consists of two principles.

- There exists a unique locus for critical state in the void ratio-stress space.
- The soils move toward the critical state as the shear strain evolves.

The first principle suggests that in the q, p, e space, respectively deviatoric stress, mean stress and void ratio, a unique locus exist that in this region the soil can deform without

any kind of restriction while the stress level and void ratio remain constant. This locus is called critical state line. The first principle defines the critical state and confirms its existence.

The second principle can be interpreted such that the CSL portray the final position of all deforming processes of soils. Therefore, every stress path would tend to critical state with continued deformation. As noted previously, the second principle could be expressed readily by choosing a simple criterion of deviation from critical state. This criterion is the state parameter with the simplest possible form of $\psi = e - e_c$ (Been & Jefferies, 1985).

A sample of cohesionless soil can have different fabric with respect to the same void ratio or relative density. Therefore, it is widely accepted that the behaviour of sands should be represented in term of the two following factors:

- A state parameter that combines the effects of void ratio and stress level together.
- A fabric parameter that represents the arrangement of sand particles.

The state parameter which is defined as a function of void ratio and stress level should be measured according to a reference condition. Hence, it is required to determine an appropriate reference condition from a physical point of view. As an acceptable approximation it is possible to consider the critical state line in form of a unique and straight locus in $e - \ln p$ and $p - q$ spaces, at least as far as no significant particle crushing in the soil medium is caused by the applied loadings. By the term of “unique” it is intended to emphasize that the locus of this line is independent of test conditions such as sample preparation, drainage and strain rate.

For the sake of convenience in defining the critical state, this concept is originally expressed in triaxial condition. In other word, all the equations are derived in term of mean effective stress, $\bar{\sigma}'_m = \frac{\sigma'_1 + 2\sigma'_3}{3}$ and deviator stress, $\bar{\sigma}'_q = \sigma'_1 - \sigma'_3$.

The critical state is conventionally summarized in eq. 3-1 below.

$$\bar{\sigma}'_{q,c} = M\bar{\sigma}'_{m,c} \qquad \textbf{3-1}$$
$$e_c = \Gamma - \lambda_c \log \bar{\sigma}'_{m,c}$$

In Eq. 3-10, *M* is the critical stress ratio, $\sigma'_{q,c}$ is the critical deviator stress, $\sigma'_{m,c}$ is the critical mean effective stress, Γ is the critical void ratio on the CSL that corresponds to a mean effective stress of 1 kPa and finally λ_c is the slope of CSL in the $e - \ln \bar{\sigma}'_m$ space.

During the loading, the sand behaviour is a function of initial conditions or in fact initial void ratio and initial mean effective pressure. The results obtained from the laboratory tests have shown that the initial parameters of *e* and σ_m do not determine the behaviour of sandy samples decisively if they are used separately and it is the combined effect of both of these two parameters that influence the soil behaviour and establishes the initial state. Regarding the mentioned reality, Been and Jefferies (1985) represent the state parameter as the departure of current void ratio from that related to critical state at any time. This definition could be idealized mathematically as shown in eq. 3-2 below.

$$\psi = e - e_c \qquad \textbf{3-2}$$

Figure 3-1 describes the physical meaning of the state parameter ψ.

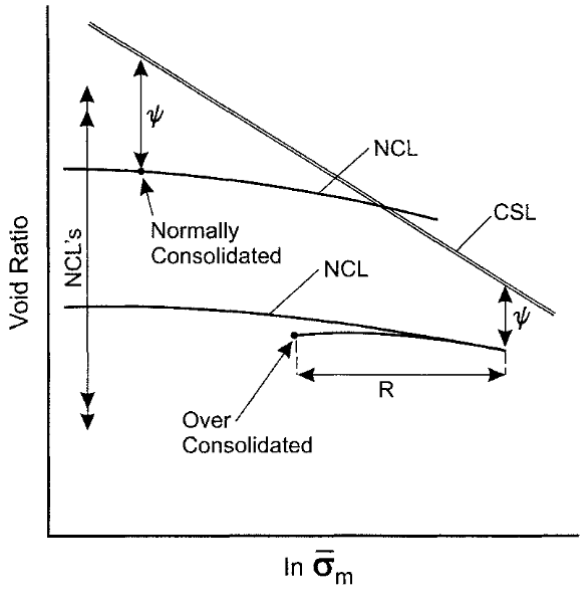

Figure 3-1 Schematic definition of state parameter ψ (Jefferies, 1993)

Note that in the Figure 3-1 over consolidation parameter *R* is also introduced. *R* determines the initial stress state of the soil with respect to the maximum over consolidation pressure that soil has ever undergone. In other word *R* is a measure of soil initial state in regard of the yield surface. ψ and *R* together define the initial state of the soil.

3.3. Uniqueness of Critical State

Some researchers used drained dilative samples, *"S" line*, and the others used the contractive undrained tests, *"F" line*, to find the CSL. The difference between "S" line and "F" line initially interpreted as an issue against uniqueness of CSL. If the CSL is to be adopted as the reference structure for state of the soil in critical state theory then uncertainty in the uniqueness of this reference jeopardizes the integrity of the whole framework. Therefore, it is necessary to address the observed discrepancy. In fact the idea

of a unique relationship between stress and void ratio which will be ultimately reached is the building block of the Critical State Soil Mechanics (CSSM).

Been et al. (1991) carried out a series of laboratory tests on Erksak sand which included variation in stress path, drainage condition, preparation method, initial state and loading technique. The results of these experiments supported the idea of utilization of steady state line (or critical state line) as the reference state for sands. However, it is strongly emphasized that to determine a unique steady state line it is required that the critical state is clearly distinguished from the quasi-critical state (or phase transformation as introduced by Ishihara et al. (1975)). Figure 3-2 helps to understand the concept of quasi-steady state and phase transformation.

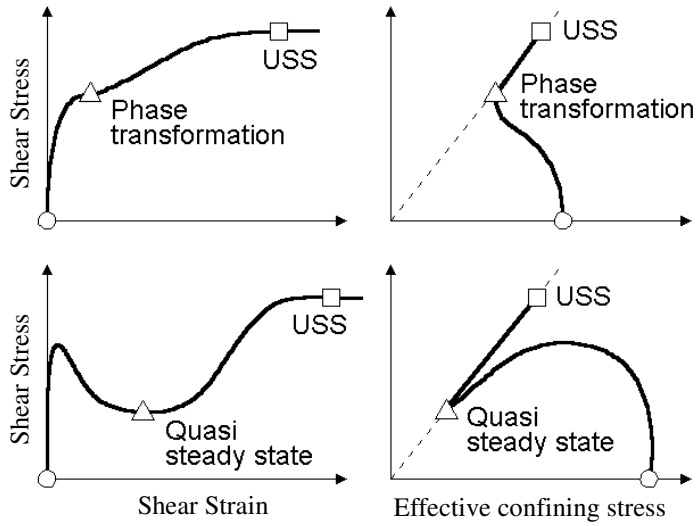

Figure 3-2 Phase transformation and quasi steady state(afterYoshimine and Ishihara (1998))

Yoshimine and Ishihara (1998) used the result of triaxial tests performed by Verdugo (1992) to clarify the distinction of phase transformation and steady state. In Figure 3-3 the phase transformation states of a number of triaxial tests are located. Those phase transformation states which belong to the same initial confining pressures are connected

together to form a curve called phase transformation line, PTL. In this figure, also the ultimate steady states of samples are depicted. These final states all occur around a certain locus indicating the existence of a unique critical state line for Toyoura sand. Figure 3-3 suggests that for very loose or highly confined samples the phase transformation coincides with critical state line.

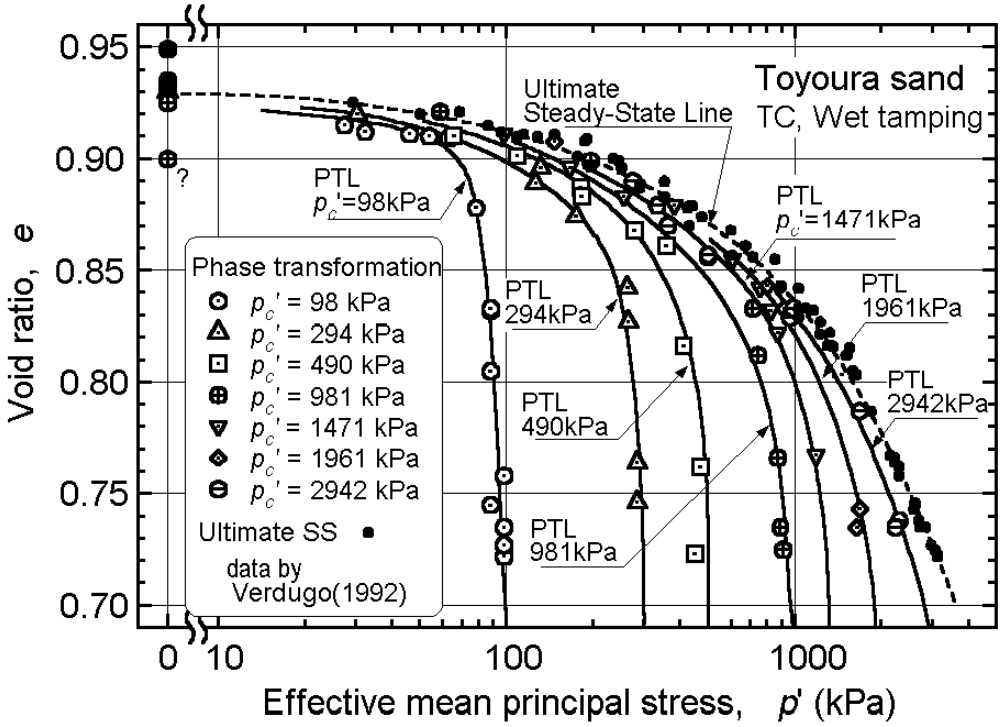

Figure 3-3 Phase transformation and the steady state line (afterYoshimine and Ishihara (1998))

It should be acknowledged that the uniqueness of the critical state line has been a controversial debate and is disputed by a number of studies through the past few decades. Some researchers have concluded that critical state line is distinctly influenced by various factors such as loading technique (Castro, 1969; Hird & Hassona, 1990), stress path (Vaid et al., 1990) or initial void ratio (Yamamuro & Lade, 1998). On the other side, arguments have been made in favour of a unique critical state line. Figure 3-4 shows stress-strain

paths of a number of triaxial tests which were carried out by Verdugo (1992). These samples all have an initial void ratio of 0.833 in common. This figure reveals that in order to reach a unique and distinct ultimate state, especially when the confining pressure is not extremely high, shear strain of about 50% must be applied to Toyoura sand. As it will be shortly seen materialization of high shear strains in triaxial apparatus is in fact the main argument Been et al. (1991) made in refutation of those conclusions against uniqueness of CSL.

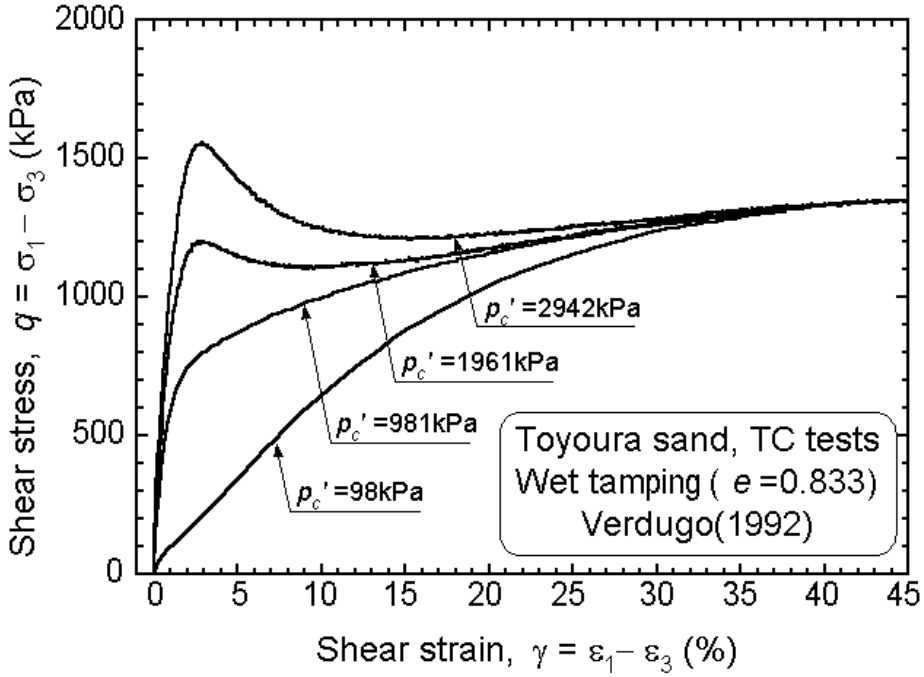

Figure 3-4 Critical state for Toyoura sand at high starins (after Yoshimine and Ishihara (1998))

Jefferies and Been (2006) used NorSand critical state constitutive model to clarify the inconsistency between steady state line derived based on drained tests and undrained tests. Figure 3-5 shows the initial and ultimate state of a few drained and undrained triaxial tests of the same soil but with different states. In this figure the tests are followed

as far as 20% of axial strains which is achievable limit of triaxial apparatus. As the figure below suggests at 20% of axial strain the critical state is not yet achieved.

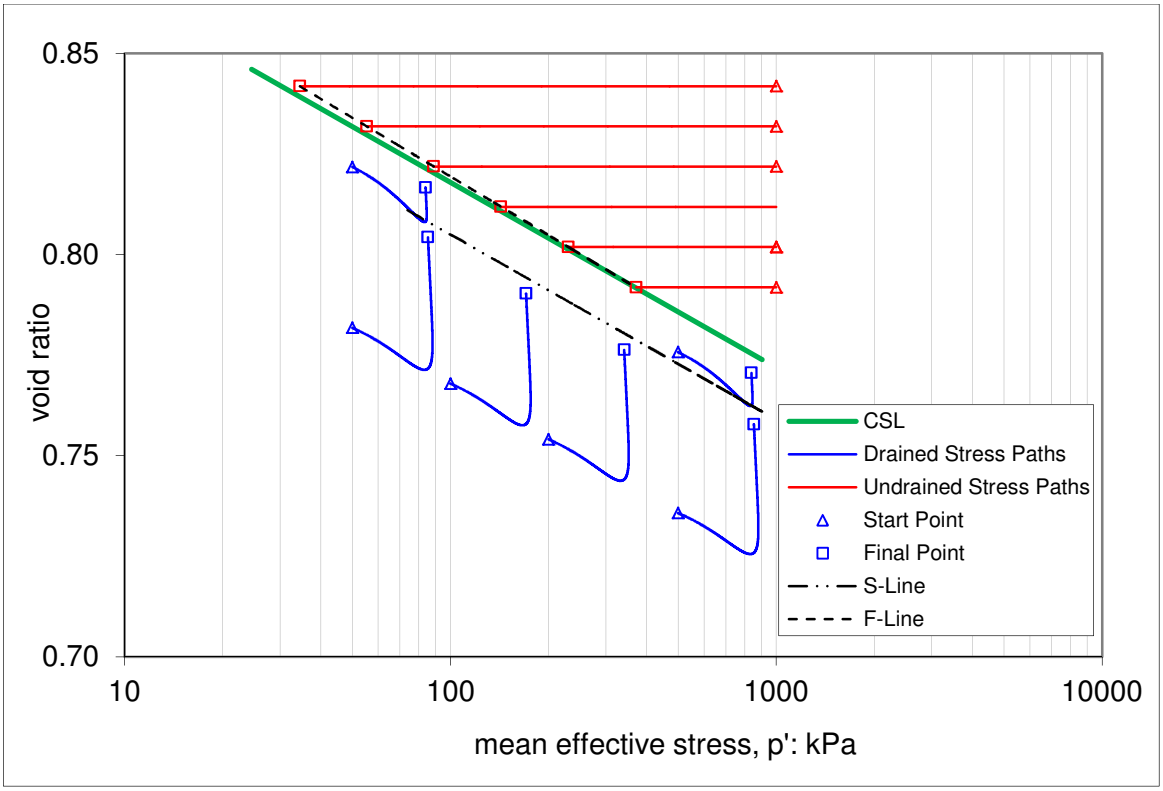

Figure 3-5 Critical State derived from drained and undrained triaxial tests

Since denser samples of sand are usually required to be sheared about 50% or more of axial strain before they reach to the steady state, it would appear essential that the triaxial test be carried out on the highly contractive loose samples which clearly reach to the critical state within the strain limitation of the triaxial apparatus. Jefferies and Been (2006) showed that using a specific CSL, it is possible to capture a wide range of responses just through changing the NorSand parameters which represent the soil fabric, i.e. H, χ_{tc} and I_r (see Table 3-1). This implies that CSL is independent from sample preparation method and a variety of soil behaviour can be simulated by a unique CSL.

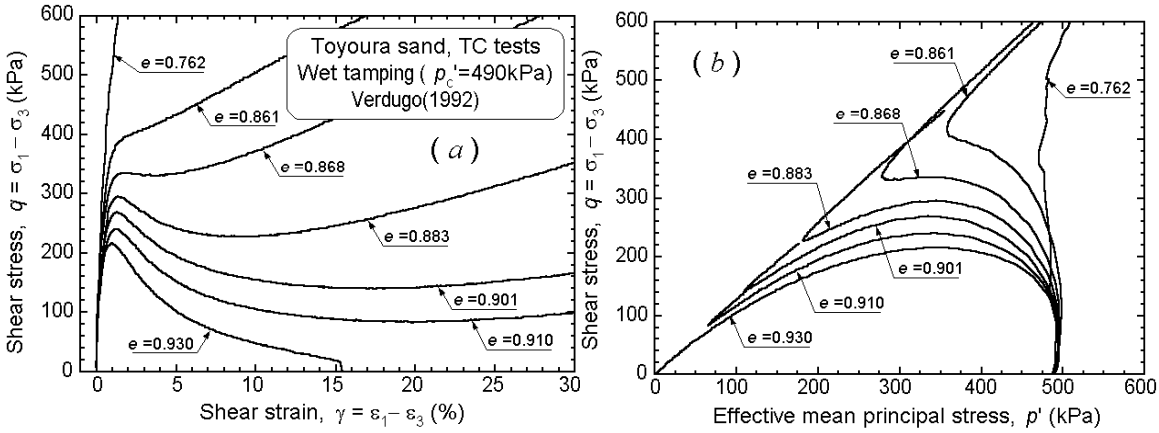

Figure 3-6 Effect of density on undrained behaviour of sands

As already mentioned a number of researches challenged the uniqueness of critical state, nevertheless, Been et al. (1991) attributed these results to not differentiating the critical state from phase transformation as the latter is heavily dependent to stress path, preparation method and etc. based on their experimental observation. The current state of the art generally considers the steady state line and the critical state line unique and identical lines for clean sands (Poulos et al. (1988); Been et al. (1991); Ishihara (1993); Chu (1995); Verdugo and Ishihara (1996); Yoshimine and Ishihara (1998)).

3.4. State Parameter

Roscoe and Poorooshasb (1963) were the first to state the importance of the coupled effect of density and normal stress on soil behaviour. In fact they introduced critical state as a measurement for the effect of initial state of soil on its behaviour. Other researchers such as Been and Jefferies (1985), Bolton (1986), Ishihara (1993) and Verdugo (1992) have intensively studied the effect of density and normal stress on sands. The common point of these researches is that each of them defines an index to describe the effect of initial state of sand on its behaviour. The defined index is a measure of the distance of

current or initial state from critical state. These indices are more informative than the conventional relative density D_r as they involve the effect of stress state.

Verdugo (1992) and Ishihara (1993) conducted a series of undrained triaxial compression tests on sandy soils and concluded that any two samples of a specific soil exhibit a similar stress strain or pore pressure response provided that they have the same relative initial state.

Various experiments on similar sands with different percentage of fine grains which are subjected to different configuration of density and confining pressure have shown that samples that are initially situated at the same proximity to the steady state will exhibit similar and comparable behaviour. Been and Jefferies (1985) defined the state parameter as the difference between void ratio and critical state void ratio at the same confining pressure.

Defining a state parameter such as ψ gives the advantage to describe the various behaviour of sand in a wide range of densities and stress level. Unlike relative density alone, the state parameter does not discard the effect of confining pressure on sand behaviour but appropriately highlights the physical importance of coupled stress and density on soil subsequent response.

It should be noted that state is not a characteristic parameter but rather is a description of the soil physical condition that merges the effect of void ratio and confining pressure together.

3.5. State Parameter and Sand Behaviour

The purpose of this section is to create conviction that the state parameter defines a basis through which various behaviours of sands could be sufficiently traced. This section introduces both dilative and contractive behaviours of sands under drained and undrained conditions. The objective is then to show that all these different behaviours could be methodically captured based on state parameter. The achievement of this goal in this section is abundantly important since this research relies on the precision of state parameter to encapsulate the agents that influence the response of sand and are related to are attributed to the condition of soil rather than intrinsic properties of material itself. As previously stated the definition of state is implicitly the essence of CSSM.

3.5.1. Undrained Behaviour of Sands

The quasi steady state is a temporary condition, with the sample moving from a contractive to a dilative behaviour as is readily seen in the test data (point *B* in Figure 3-7).

As it can be seen in Figure 3-7 (left), the behaviour of the dense sand is contractive from the initial state to the state of phase transformation. After the phase transformation state its behaviour becomes dilative and approaches the steady state or critical state line. The stress-strain curve for dense sands usually follows the pattern shown in Figure 3-7 (right). On the other hand the response of the loose sand in undrained condition under monotonic loading is fully contractive.

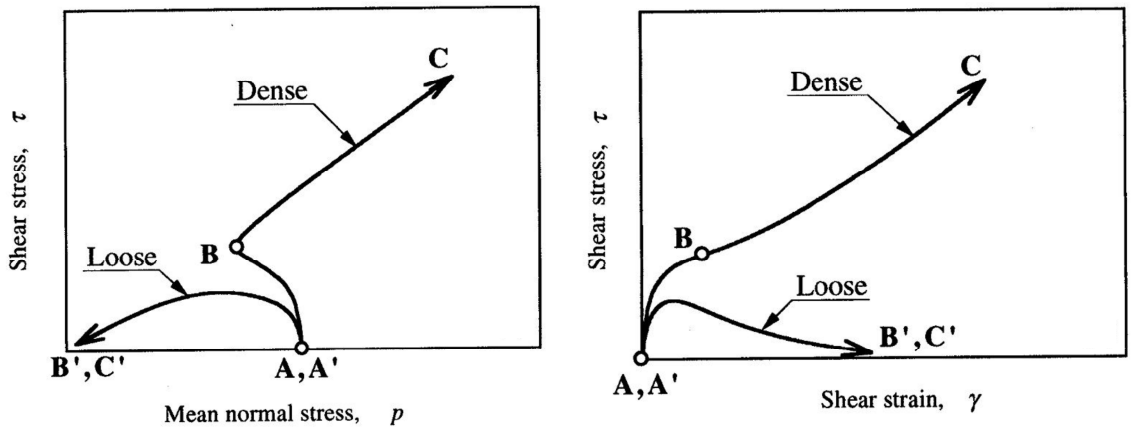

Figure 3-7 Undrained responses of dense and loose sand

Using more than 70 triaxial tests on Kogyuk sand, Been and Jefferies (1985) concluded the following results regarding state parameter by examining the stress paths of undrained tests:

- The larger and more positive initial state parameters lead to more significant shear strength drop and excessive pore pressure development.
- Samples with negative initial state pressure do not show peak strength. The reason is when the stress path reaches the proximity of the Mohr-Coulomb failure surface the dilative behaviour commences.
- Regardless of the initial state parameter, the stress paths follow a similar pattern up to the Mohr-Coulomb failure envelope. At the stress ratio of Mohr-Coulomb envelope, also known as phase transformation, the current state of samples decides the consequent contractive or dilative behaviour. Samples with negative or significant positive state parameter ψ, maintain the same sign of state parameter and exhibit contractive or dilative behaviour respectively. However, samples with small positive

initial state parameter may have negative state parameter at phase transformation and show dilative behaviour.

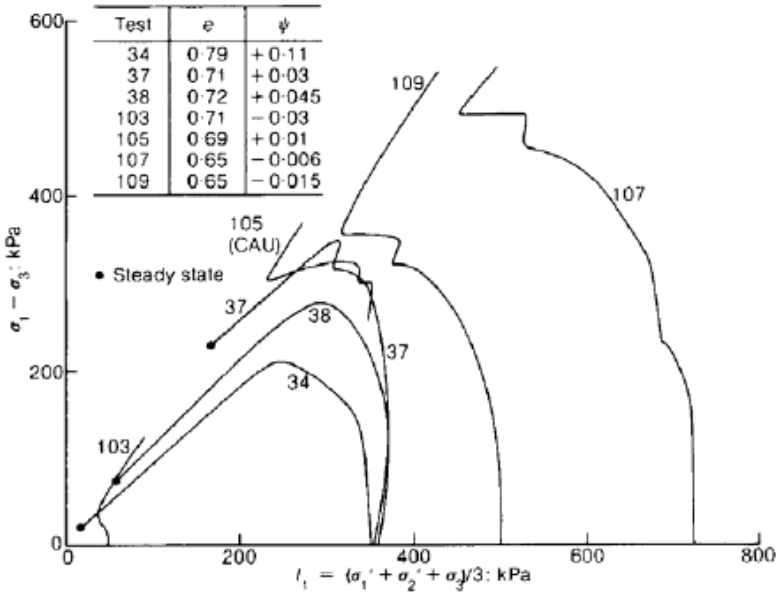

Figure 3-8 The effect of state parameter on the undrained behaviour of sand (Been & Jefferies, 1985)

Been and Jefferies (1985) showed that it is possible to describe different aspects of soil behaviour based on state parameter. They also used samples with similar relative density and examined their behaviour to demonstrate the superiority of state parameter over the relative density as the reference parameter for soil behaviour. Unlike the state parameter, the relative density does not take the effects of stress parameters into account. In fact dense sand can quite behave like loose sand if subjected to high pressure. In addition, soil strength is highly depends on dilatancy which is the ratio of volumetric strain increment, and not void ratio, over shear strain increment. It is also observed that the dilatancy is inversely proportional to the confinement pressure; therefore the presence of stress level in the parameter that defines the soil behaviour is essential.

3.5.1. Drained Behaviour of Sands

The behaviour of the sand under drained condition is depicted in Figure 3-9. This figure shows that loose samples of sand exhibit a ductile behaviour with volume contraction. On the other hand, the dense samples of sand initially show a stiff response until the soil reaches its peak strength. After this point the soil exhibits softening behaviour and moves toward critical state. This process is accompanied with volume dilation.

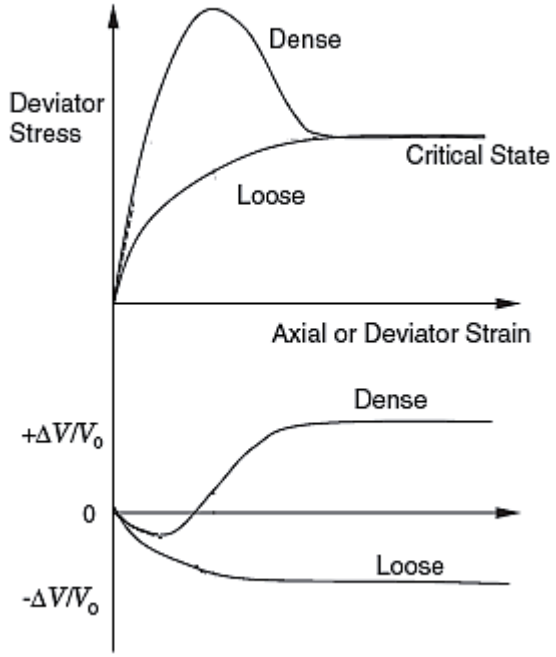

Figure 3-9 The behaviour of sand under drained condition

For numerical analysis to yield reliable results, it is essential that a soil constitutive model is employed that can capture these different behaviours of sands accurately. This study focuses on the development and implementation of a constitutive model that can simulate

the behaviour of sand, of different type and under different conditions, more precisely than those models already exist in ABAQUS Explicit software package.

3.6. Soil Modeling

The theory of effective stress of Terezaghi was the first conceptual model that successfully considered the mechanical response caused by biphase nature of saturated soils. The elastic constitutive model, despite its abundance of usage, is not suitable for geologic material because the behaviour of soil, even in small strains, is mostly inelastic. The early classic models for elastic-plastic behaviour of soils such as Tresca, Von Mises, Mohr-Coulomb and Drucker-Prager managed this problem to some extent. The complexity of sands, especially saturated sands under drained and undrained conditions and also the effect of void ratio, density and confining stress on their behaviour stress the need for more complex and modern constitutive models for simulation of behaviour of this type of soils. The constitutive model used to conduct this research is based on the classic Drucker-Prager but the current version has been significantly changed and improved to better simulate the behaviour of the soils.

3.7. Plasticity

The theory of plasticity was first used to describe the mechanism of the failure of the metals. Although the internal processes that take place in other engineering materials are different from those in metals from a microscopic point of view but experimentally it is shown that under compressive pressures these material behave similarly to the

elastoplastic response of the metals. Therefore, with a few changes the concept of theory of plasticity of metals can be generalized for other material such as soils.

The stress-strain relation in the theory of plasticity is defined in a way that when stress is applied on a body and released consequently, a permanent strain called plastic strain remains in the system. An introduction to the basics of the theory of plasticity follows.

3.7.1. Yield surface

The first step to represent the behaviour of elastic-plastic materials like soil mathematically is to determine the limit where the materials yield. The yield surface or the yield function divides the stress space in two parts. Inside this surface only the recoverable strains occur while on this surface in addition to recoverable deformations plastic or permanent deformations might happen. Generally the equation of yield surface would be defined in the form of eq. 3-3. In this equation σ_{ij} are the components of the stress tensor.

$$f(\sigma_{ij}) = 0 \qquad \textbf{3-3}$$

Note that the stress state can be inside or on the yield surface. This principle is called the consistency condition.

Different models utilize different yield criteria to form suitable yield surfaces based on the behaviour of the materials in question. In non-porous materials such as metals the change in volumetric strain under hydrostatic pressure is insignificant. But in porous materials or granular material, like soil which is a multiphase media, large volumetric strain can occur through various mechanisms such as elastic deformations of the grains,

permanent deformations by replacement of the grains and filling the void spaces between the grains or sliding of grains over each other.

In order to account this behaviour the implementation of closed yield surface along the hydrostatic axis in contrary of open yield surfaces for metals is proposed as an option. During unloading a small part of the volumetric strains would be recovered for most soils. Therefore for granular materials it is necessary to define the volumetric yielding in addition to shear strains. Increasing the hydrostatic pressure in soils leads to higher shear strength therefore the shape of yield surface resembles a cone in soil models.

Among the famous classic criteria for the non-porous media, Tresca (1864) and Von Mises (1913) can be named as examples of ideal plastic criteria. The yield surfaces of these two models are shown and compared in Figure 3-10. On the other hand, Coulomb (1773) and Drucker-Prager (1952) are two classic criteria that are used for porous media.

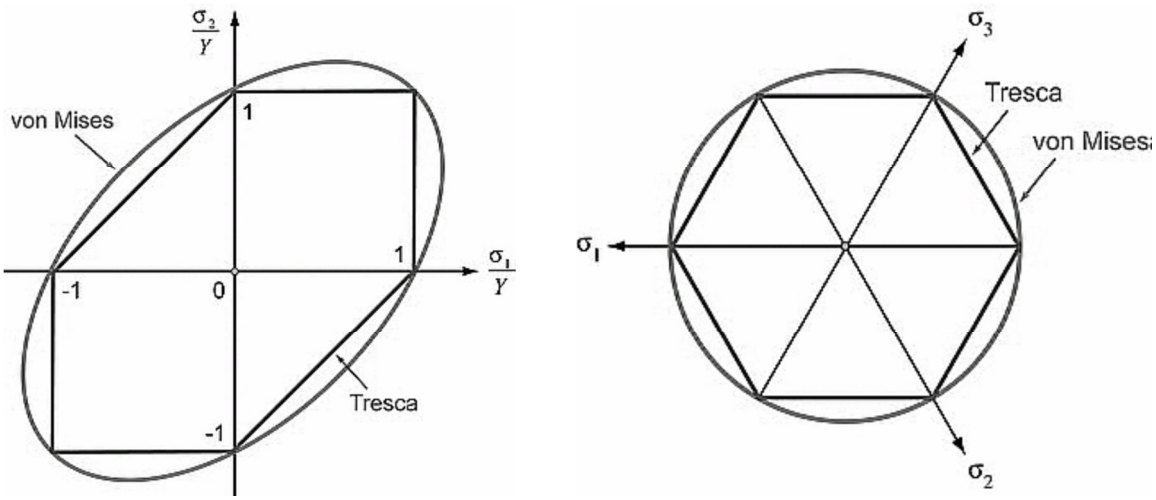

Figure 3-10 Common yield criteria for metals, Tresca and Von Mises

3.7.2. Flow rule

The flow rule is one of the fundamental rules in the theory of plasticity. Obviously in uniaxial conditions the strains are in the same direction as the applied loading is. However, in the general situation where the stresses and strains consist of 6 components the flow rule is specified to address the relation of the direction of the stress and the strain components. The flow rule defines a mathematical function called the plastic potential function.

When a load increment $d\sigma$ is applied on a body yielding plastic deformations, the state of stress would be on the yield surface. According to the flow rule $d\varepsilon_{ij}^{p}$ in the space of plastic strain would be in form of a vector outward the elastic zone and orthogonal to the plastic potential function. This principle is called normality and mathematically is shown in eq. 3-4 below:

$$d\varepsilon_{ij}^{p} = d\lambda \frac{\partial g}{\partial \sigma_{ij}} \qquad \textbf{3-4}$$

In eq. 3-4 $d\lambda$ is a non-negative scalar parameter which its value represent the magnitude of the plastic strain increment vector. g is the plastic potential function. The potential function is the locus of the points whose tangents are always perpendicular to the plastic strain vector. The plastic potential function determines the direction of the plastic strain increment vector which is usually a function of stress or more often combined effects of stress and plastic strain or a representing internal variable.

Generally, yield surface and plastic potential surface are two distinctive functions. However, if these two functions are same then the flow rule can be written as in 0:

$$d\varepsilon_{ij}^{p} = d\lambda \frac{\partial f}{\partial \sigma_{ij}} \qquad \textbf{3-5}$$

Where the plastic potential surface and the yield surface are the same the flow rule is called the associated flow rule. Otherwise, when yield surface and plastic potential surface are different the flow rule is non-associated.

Depending on the nature of yield surface the elastic-plastic models might also be categorized in the two following groups:

- The elastic-plastic models with open yield surfaces (e.g. Mohr Coulomb)
- The elastic-plastic models with closed yield surface (e.g. Cam Clay and Drucker Prager Cap model)

The main different between these two categories is that in the former only shearing can cause the plastic deformation but in the latter either shearing or applying hydrostatic pressure or both of them together could generate plastic strain. Therefore, it can be concluded that the models with closed yield surfaces simulate the behaviour of soils more realistically especially when the soil in question exhibits large volumetric deformation during applying the stresses.

3.7.3. Hardening law

The elastic zone of the hardening materials changes under the loading. In fact, the yield stress depends on the plastic loading history or the plastic deformations. Therefore, determination of the dependence of yield stresses to plastic loading history is very essential. The hardening law is defined to address this issue. In other word the hardening law shows how the yield stresses change according to the plastic strains in the hardening

materials. As the result the yield surface is not only a function of the stress but also depends on the plastic strains.

In the real soils because of the strain hardening or strain softening it is usually impossible to achieve the collapse load limit directly. For soils strain hardening models such as Drucker et al. (1957); Roscoe and Burland (1968); Schofield and Wroth (1968); DiMaggio and Sandler (1971); Zienkiewicz and Naylor (1972) have been proposed which were relatively successful in simulating the deformational behaviour of the soils.

The hardening law depending on the hardening parameter can be strain hardening or work hardening. In the strain hardening the effective plastic strain ($\varepsilon_p = \int \sqrt{d\varepsilon^p . d\varepsilon^p}$) is chosen as the hardening parameter.

In the similar way that different materials are divided in two groups of isotropic and anisotropic, the hardening behaviour can be also classified in the same categories of isotropic hardening and anisotropic hardening. The anisotropic hardening itself is divided in two groups: kinematic hardening and mixed hardening. Under isotropic hardening an initially isotropic material subjected to deformation remains isotropic. While under anisotropic hardening such material might exhibit anisotropic behaviour. When the yield surface merely contracts or enlarges and maintains the initial shape then the hardening law is called isotropic otherwise it is anisotropic hardening law. Figure 3-11 (a) shows the initial yield surface and the subsequent yield surface under isotropic hardening rule. As it is shown in this figure the yield surface maintain its shape during the hardening. On the other hand, Figure 3-11 (b) shows how the position of the yield surface may change under kinematic hardening. As it can be seen, in kinematic hardening the size of yield surface

remains unchanged. In mixed hardening both size and position of yield surface can change.

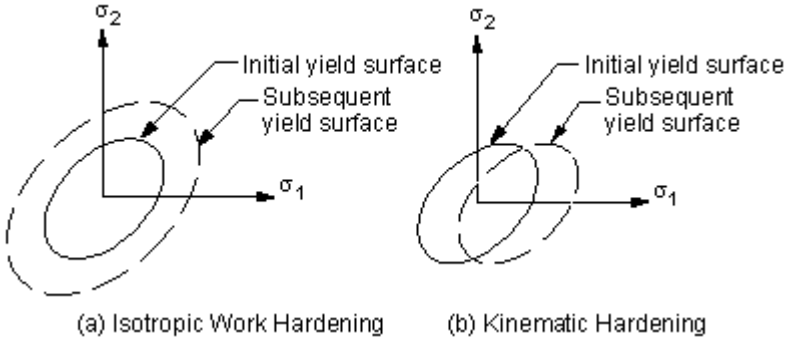

Figure 3-11 Schematic description of (a) isotropic hardening and (b) kinematic hardening

Provided that there is no hardening occurs in a body that plastically strained then the material is called ideal plastic. In such materials the yield surface is express as only a function of stress components:

$$f(\sigma_{ij}) - k = 0 \qquad \textbf{3-6}$$

σ_{ij} shows the stress state and *k* is a constant that displays the size of the yield surface.

Tresca and Von-Mises (Figure 3-10) are two examples of the models that utilise ideal plasticity.

Isotropic hardening is based on the assumption that the yield surface enlarges without any rotation or translation during the loading. The mathematical expression for the yield surface would be:

$$f(\sigma_{ij}, k) = F(\sigma_{ij}) - \kappa(k) = 0 \qquad \textbf{3-7}$$

Where $\kappa(k)$ is the hardening function which defined the size of the yield surface and *k* is the hardening parameter which its value presents the plastic loading history.

Kinematic hardening law assumes that under plastic deformation the yield surface translate in space like a rigid body without any rotation. Therefore, shape and size of the yield surface remains unchanged. The mathematical expression for such yield surface is shown in eq. 3-8:

$$f(\sigma_{ij}, \alpha_{ij}) = F(\sigma_{ij} - \alpha_{ij}) - k = 0 \quad \textbf{3-8}$$

In this relation k is a constant value and α_{ij} is called back stress which represents the plastic loading history. α_{ij} is the coordinates of the yield surface origin and changes due to the development of the plastic strains.

And finally the combination of the isotropic and anisotropic hardening law conclude a more general law called the mixed hardening law (Hodge, 1957)

$$f(\sigma_{ij}, \alpha_{ij}, k) = F(\sigma_{ij} - \alpha_{ij}) - \kappa(k) = 0 \quad \textbf{3-9}$$

In this case the yield surface can either translate or expand.

Since the isotropic hardening neglects the Bauschinger effect it is not reliable in prediction of material behaviours under cyclic or seismic loads and usually is applied in the static and monotonic loading. However, because of its simpler mathematical formulation the isotropic hardening law is preferred.

3.8. Drucker-Prager Constitutive Model

The constitutive model that is implemented and improved in ABAQUS through the VUMAT subroutine is a Drucker-Prager cap model. This model is introduced in this section. It should be noted that in the formulas of this section all stress components and invariants are based on the effective values. This model is assumed to be isotropic. The

assumption of isotropy is significantly limiting for simulating the behaviour of the soils because the stress induced anisotropy or inherent anisotropy are always present in the soil. However, this framework has advantage of simplification of the mathematical structure of the model to an acceptable level. The assumption of isotropy is common in the elastic-plastic models. Isotropy has the following consequences:

- All internal parameters of the models are the same in different directions.
- The dissipation function is dependent on the rate of the plastic strain vector through its invariants.
- Yield function or plastic potential function is dependent only to the invariants of the stress tensor.
- Flow rule implicitly indicates the coaxiality between stress and plastic strain tensors.

Figure 3-12 compares the classic Drucker-Prager model with Von Mises. As this figure shows unlike Drucker-Prager yield surface, the yield surface in Von Mises criterion is independent of the hydrostatic pressure. This gives an advantage to Drucker-Prager model over the Von Mises for general simulation of the soils behaviour.

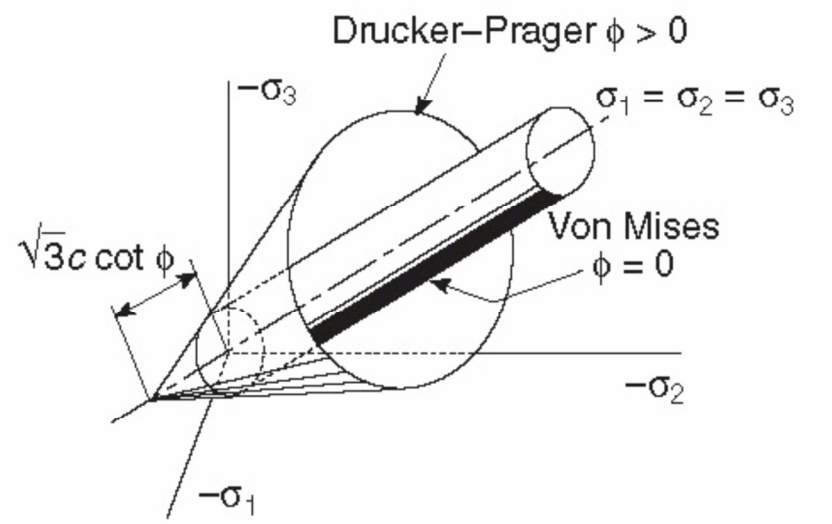

Figure 3-12 Comparison of Drucker-Prager model with Von Mises

3.8.1. Plasticity in Drucker-Prager Cap Model

Figure 3-13 shows the Drucker-Prager cap model. The model yield surface consists of three parts. The shear zone where the shearing is dominant, the cap zone where accounts for plastic compaction and features a hardening mechanism and finally the third part is a transition zone that smoothly bridges the two segments of shear and cap zone. The implementation of this region is solely for numerical stability. The yield surface could either harden or soften depending on the stress state and internal parameters and therefore vary the model parameters. The elastic properties of the model are kept constant during the loading history but this assumption could be modified to provide the possibility of varying elastic properties such as the Young's modulus.

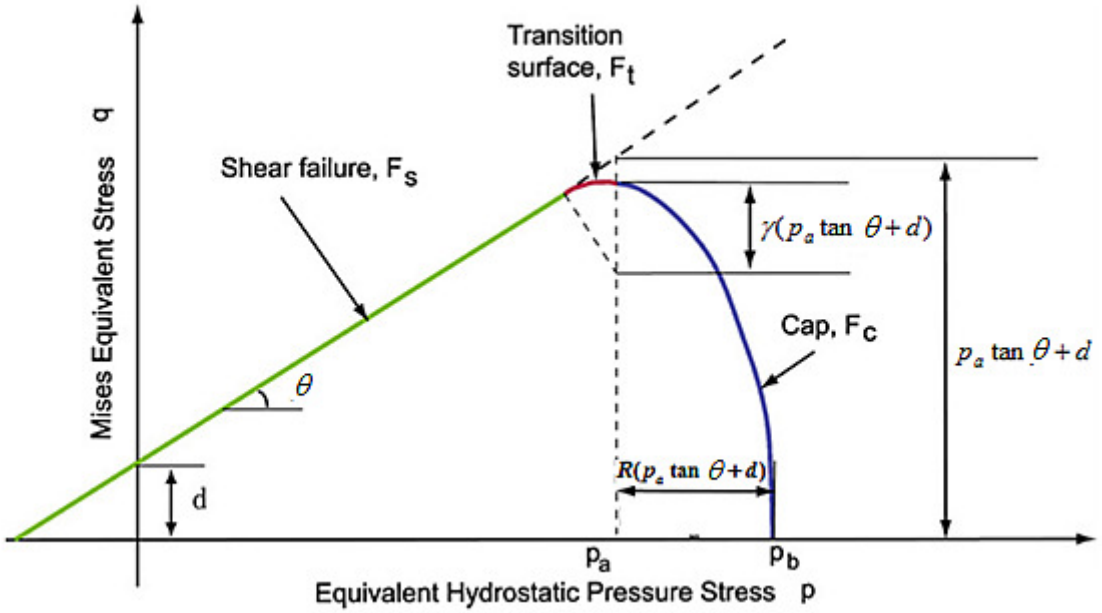

Figure 3-13 Drucker-Prager cap model with transition zone

The shear failure in the Drucker-Prager model is defined in eq. 3-10 below:

$$F_s = q - p' \tan\theta - d \qquad \textbf{3-10}$$

In this relation θ is the material friction angle, d is the cohesion of the material, p is the mean pressure and q is the Mises equivalent stress.

$$p' = -\frac{\sigma_1' + \sigma_2' + \sigma_3'}{3} \qquad \textbf{3-11}$$

$$q = \sqrt{\frac{1}{2}\left((\sigma_1' - \sigma_2')^2 + (\sigma_2' - \sigma_3')^2 + (\sigma_1' - \sigma_3')^2\right)} \qquad \textbf{3-12}$$

σ_1, σ_2 and σ_3 are the principal stresses.

θ and d in eq. 3-10 above can be derived from soil parameters obtained from triaxial tests.

$$\theta = \frac{2\sin\phi}{\sqrt{3}(3-\sin\phi)} \quad \textbf{3-13}$$

$$d = \frac{6c\cos\phi}{\sqrt{3}(3-\sin\phi)} \quad \textbf{3-14}$$

The cap bounds the yield surface along the hydrostatic pressure axis so that under hydrostatic compression the material may yield plastic deformations. This provides a basis for a hardening mechanism. The cap also serves as an operative to control the dilation in the shear zone since the location of p_a, the evolution parameter of the yield surface, determines the shape of shear plastic potential surface. During the yielding of a material on the shear zone the volume would increase which leads to softening of the yield surface and as the result the decrease of the dilation. The formulation of cap surface is shown in eq. 3-15 below:

$$F_c = \left(\frac{p' - p_a}{B}\right)^2 + \left(\frac{q}{A(1+\gamma-\gamma/\cos\theta)}\right)^2 - 1 \quad \textbf{3-15}$$

Where p_a is the evolution parameter of the yield surface and its value is controlled by the hardening/softening law.

$$A = d + p_a \tan\theta \quad \textbf{3-16}$$

$$B = p_b - p_a \quad \textbf{3-17}$$

p_b is the hydrostatic yield pressure which is usually defined as a function of the plastic volumetric strain.

$$p_b = f(\varepsilon_v^p) \quad \textbf{3-18}$$

γ in Eq. 3-15 is a small number called the transition factor that defines a smooth transition surface between shear zone and cap surface.

In the above formulation of the Drucker-Prager *B*, the horizontal radius of cap, is defined as a multiplication of the *A*, the vertical radius of the cap:

$$B = RA \tag{3-19}$$

The formulation of the transition zone is shown in eq. 3-20:

$$F_t = q - (1 - \gamma/\cos\theta)\alpha - \sqrt{(\alpha\gamma)^2 - (p - p_a)^2} \tag{3-20}$$

$$\alpha = d + p_a \tan\theta \tag{3-21}$$

To determine the flow rule of the model an associated plastic potential function G_c would be defined over the cap zone which is equal to the yield function of the cap and a non-associated component of flow rule G_s is defined over the shear zone and transition region.

The associated potential function of the cap region is shown in eq. 3-22:

$$G_c = \left(\frac{p' - p_a}{B}\right)^2 + \left(\frac{q}{A(1 + \gamma - \gamma/\cos\theta)}\right)^2 - 1 \tag{3-22}$$

The non-associated plastic potential function of defined over the shear failure and transition zone is shown in eq. 3-23:

$$G_s = \left(\frac{p' - p_a}{\beta}\right)^2 + \left(\frac{q}{\alpha(1 + \gamma - \gamma/\cos\theta)}\right)^2 - \varepsilon \tag{3-23}$$

These two elliptical portions of the plastic potential surface form a smooth and continuous potential surface.

Therefore, to define a unique Drucker-Prager yields surface 5 parameters of cohesion d, internal friction angle θ, evolution parameter p_a, the transition factor γ and the cap

eccentricity coefficient *R* are required. Usually p_b is determined and according to *R* the value of p_a would be concluded.

Elasticity in soil is in fact as complicated as plasticity. The selection of one out of many available elasticity models depends on the compromising of simplicity against accuracy. The elastic strains in sands are anisotropic. These strains depend on the void ratio and mean pressure of the soil. Despite of the extensive research no universal relation to address the elastic strains based on these factors has been achieved that remains valid in general. In this model the simple case of constant Poisson's ratio and generalized isotropic Hook's law is accepted.

3.9. Critical State Constitutive Model NorSand

3.9.1. Plasticity in NorSand

In this section the main components of the plasticity model NorSand are introduced.

Flow Rule

In NorSand the flow rule is based on the stress-dilatancy relation. There are several ways to define the stress-dilatancy relation. Conventionally Cam-Clay model uses the stress-dilatancy relation suggested by Schofield and Wroth (1968):

$$D^p = M - \eta \qquad \textbf{3-24}$$

However, this dilatancy relation could not accurately match sand behaviour and in fact this shortcoming was one of the main reasons why there was a lack of interest in using

Cam-Clay model for sands. Based on laboratory observations, Nova (1982) addressed this issue and altered the dilatancy rule to better represent sands.

$$D^p = \frac{M - \eta}{1 - N} \qquad \textbf{3-25}$$

Nova added a new material property *N*, the volumetric coupling coefficient. *N* is usually chosen between 0.2 and 0.4. The volumetric coupling coefficient, *N*, accounts for the variation of friction ratio in respect to the critical friction ratio for a specific value of dilatancy. Initially NorSand adopted the Nova rule for the stress-dilatancy relation or the flow rule of the model (Jefferies, 1993). In Nova rule *M* is a constant equal to M_{tc}. Rowe has several years before acknowledged the fact that critical friction ratio is not constant in soil. Based on idealized particle packing, Rowe (1962) proposed the following stress-dilatancy relations for triaxial condition:

$$\frac{\sigma_1'}{\sigma_2'} = K\left(1 - \frac{\dot{\varepsilon}_v}{\dot{\varepsilon}_1}\right) \qquad \textbf{3-26}$$

In this relation parameter *K* is a function of mineral to mineral friction of the soil particles, ϕ_μ.

$$K = \frac{1 + \sin\phi_\mu}{1 - \sin\phi_\mu} \qquad \textbf{3-27}$$

Through further experimental observations, Rowe concluded that in order to achieve a better consistency between theory and test data ϕ_μ should be replaced with functional friction angle ϕ_f. This parameter is also known as operational friction angle or mobilized friction angle.

$$K = \frac{1+\sin\phi_f}{1-\sin\phi_f} \qquad \textbf{3-28}$$

The reason why this substitution is necessary comes from the fact that *K* in Rowe stress-dilatancy rule must relate the strain increments to shear stress at different states and not only at peak stress or critical stress. It can be shown that if Rowe's stress-dilatancy theory is applied to a sample of soil using $\phi_f = \phi_\mu$ the predicted strain field is smaller than the real behaviour and on the other hand, if $\phi_f = \phi_{cv}$ is used, where ϕ_{cv} is the critical state friction angle, the predicted strains are too large to match the real soil. This implies that *K* in Rowe's stress-dilatancy should evolve according to the induced strains in the soil. Based on porosity and boundary condition functional friction angle varies such that it is bounded by inner-particle friction angle and critical state friction angle, $\phi_\mu \leq \phi_f \leq \phi_{cv}$ (Rowe, 1962).

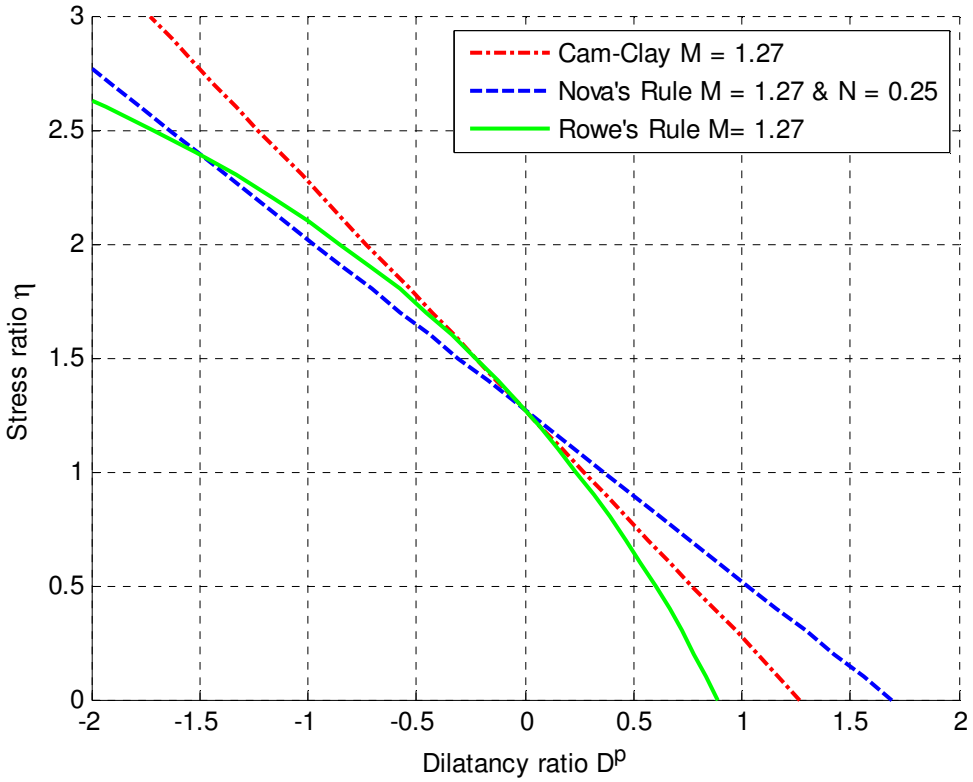

Figure 3-14 Comparison of different flow rules

During the course of last two decades NorSand has been continuously evolved. These updates to the model were mostly to improve the stress-dilatancy rule of the model. In NorSand version proposed by Jefferies and Shuttle (2002), the critical friction ratio was replaced by a variable parameter called image critical friction ratio, M_i. The word "*image*" implies that at image state only one condition out of the two critical state conditions is met. That is at image state only the dilation rate is zero. This modification results in a stress-dilatancy rule similar to the flow rule of Cam-Clay:

$$D^p = M_i - \eta \qquad \textbf{3-29}$$

M_i is a function of state parameter and stress level. The new stress-dilatancy relation can be derived using $N = 0$ in the Nova rule and replace the critical friction ratio with the

image critical friction ratio. The implementation of a variable image friction ratio, M_i, into the stress-dilatancy relation is compatible with Rowe's conclusions to employ an evolving operational friction angle, ϕ_f since M_i varies with boundary condition and soil state. The new stress-dilatancy rule eliminates the material property N and honours laboratory findings in regard of varying mobilized friction but on the other hand necessitates the definition of rule to address the evolution of M_i as the result of shearing.

Yield Surface

To derive the yield surface of NorSand the usual approach of critical state models is followed. The stress-dilatancy relation is chosen as the flow rule. Then based on the Drucker's stability postulate (Drucker, 1957) the normality would be applied to integrate the flow rule and obtain the yield surface. Based on Drucker stability postulate and normality one can conclude:

$$\frac{dq}{dp} = -\frac{d\varepsilon_v}{d\varepsilon_q} = -D^p \qquad \textbf{3-30}$$

To derive the NorSand yield surface the Nova rule (1982) is considered as the origin:

$$D^p = \frac{M - \eta}{1 - N} \qquad \textbf{3-31}$$

Based on normality;

$$\frac{dq}{dp} = -\frac{M - \eta}{1 - N} \qquad \textbf{3-32}$$

Based on the definition of stress ratio, η, a relation between stress invariants p and q can be established by differentiating $q = \eta p$:

$$\frac{dq}{dp} = \eta + \frac{p}{dp} d\eta \qquad \textbf{3-33}$$

Referring back to equation 3-32:

$$-\frac{M-\eta}{1-N} = \eta + \frac{p}{dp} d\eta \qquad \textbf{3-34}$$

Equation above can be rewritten to result the following differential equation:

$$\frac{dp}{p} = (1-N)\frac{d\eta}{N\eta - M} \qquad \textbf{3-35}$$

The yield surface can be easily derived by integrating the above differential equation. Since $p \to p_i \implies \eta \to M$ the lower bound of left and right side of the differential equation can be chosen as p_i and M, respectively.

$$\int_{p_i}^{p} \frac{dp}{p} = (1-N)\int_{M}^{\eta} \frac{d\eta}{N\eta - M} \qquad \textbf{3-36}$$

After simplification the following yield surfaces would be obtained:

For $N \neq 0$:

$$q = \frac{Mp}{N}\left[1 + (N-1)\left(\frac{p_i}{p}\right)^{\frac{N}{1-N}}\right] \qquad \textbf{3-37}$$

For $N = 0$:

$$q = Mp\left[1 + \ln\left(\frac{p_i}{p}\right)\right] \qquad \textbf{3-38}$$

Hardening Law

Been and Jefferies (1986) published the observed maximum dilatancy of a series of tests in terms of initial state parameter, ψ_0. Jefferies (1993) then presented the same data in terms of state parameter transformed to image state, ψ_i, in order to linearly idealize maximum dilatancy as a function of ψ_i. Initially the following relation was proposed to calculate the maximum dilatancy:

$$D_{\max} = 3.5\psi_i \qquad \textbf{3-39}$$

In NorSand the hardening law is defined in such a way to limit the yield surface size in accordance with the maximum dilatancy. Using the model yield surface and the proposed maximum dilatancy relation above, the limiting hardness, $(p_i/p)_{max}$, can be defined as:

For $N \neq 0$:

$$\left(\frac{p_i}{p}\right)_{\max} = \left(1 + 3.5\psi_i \, N/M\right)^{(N-1)/N} \qquad \textbf{3-40}$$

For $N = 0$:

$$\left(\frac{p_i}{p}\right)_{\max} = \exp\left(-3.5\psi_i/M\right) \qquad \textbf{3-41}$$

Limiting the size of the yield surface by a maximum dilatancy which is derived from experimental data ensures that if based on Drucker's postulate normality is employed to obtain the soil dilatancy, the result would agree with reality. Jefferies (1993) proposed a simple form of hardening law that was compatible with both limited maximum hardness concept and second axiom of critical state theory in which the critical state is defined as the ultimate state of a soil if continually sheared.

$$\frac{dp_i}{p} = H\left(\left(\frac{p_i}{p}\right)_{\max} - \frac{p_i}{p}\right)d\varepsilon_q^p \qquad \textbf{3-42}$$

In this hardening law the hardening modulus, H, is a new material property. Unlike Cam-Clay the proposed hardening law is a function of shear strain increment. The reason is if plastic volumetric strain is used then the stress would not pass over the image point since provided $p \to p_i$ then $d\varepsilon_v^p \to 0$. This means that critical state might never be reached. In Cam-Clay this is not the case as the critical state implicitly intersects the yield surface. The hardening law equation measures the difference between the current hardness of the yield surface and the current maximum allowable hardness to determine the magnitude and direction of the evolution of the yield surface as shear deformation accumulates. The implication of this hardening law is that the evolution of the yield surface ceases when the current maximum hardness is achieved (i.e. the critical state) regardless of the continuing shear deformation.

$$\varepsilon_q^p \to \infty \Rightarrow \psi_i \to 0 \Rightarrow \left(\frac{p_i}{p}\right)_{\max} \to \frac{p_i}{p} \qquad \textbf{3-43}$$

To comply with self-consistency it is required that the isotropic hardening would be independent from the Lode Angle, q, as it is indefinite in an isotropic condition. Nevertheless the hardening law must address this condition as isotropic compression is an anticipated loading condition of soils. Jefferies and Shuttle (2002) suggested that the ratio M/M_{tc} is added to hardening law:

$$\frac{dp_i}{p} = H\frac{M}{M_{tc}}\left(\left(\frac{p_i}{p}\right)_{\max} - \frac{p_i}{p}\right)d\varepsilon_q^p \qquad \textbf{3-44}$$

This modification implicitly satisfies the independence of the hardening law from Lode angle in an isotropic compression as in such situation $d\varepsilon_v^p = M\, d\varepsilon_q^p$ considering the fact that when $\eta \rightarrow 0$ then $D^p \rightarrow M$, consequently:

$$\frac{dp_i}{p} = \frac{H}{M_{tc}}\left(\left(\frac{p_i}{p}\right)_{\max} - \frac{p_i}{p}\right) d\varepsilon_v^p \qquad \textbf{3-45}$$

Or as desired:

$$\frac{dp_i}{d\varepsilon_v^p} = \frac{H}{M_{tc}}\, p\left(\left(\frac{p_i}{p}\right)_{\max} - \frac{p_i}{p}\right) \neq f(\theta) \qquad \textbf{3-46}$$

To achieve a better fit with experimental data another modifier $e^{\left(1-\frac{\eta}{M_{tc}}\right)}$ was implemented to the hardening law as part of the process of model improvement (Jefferies & Shuttle, 2002). This modification is simply to depend the hardening on the stress level.

$$\frac{dp_i}{p} = H\,\frac{M}{M_{tc}}\exp\left(1-\frac{\eta}{M_{tc}}\right)\left[\left(\frac{p_i}{p}\right)_{\max} - \frac{p_i}{p}\right] d\varepsilon_q^p \qquad \textbf{3-47}$$

In this research the updated version of NorSand presented by Jefferies and Been (2006) is adopted. The main improvement in hardening law is to incorporate M_i into the model formulation in order to comply with real soil behaviour as discussed earlier in derivation of NorSand flow rule.

$$\frac{dp_i}{p_i} = H\,\frac{M_i}{M_{i,tc}}\left(\frac{p}{p_i}\right)^2\left[\left(\frac{p_i}{p}\right)_{\max} - \frac{p_i}{p}\right] d\varepsilon_q^p \qquad \textbf{3-48}$$

Jefferies and Shuttle (2002) introduced a new model parameter χ to define the maximum dilatancy based on image state parameter. While the linearity of the maximum dilatancy and image state parameter shown in eq. 3-39 maintained, the universal 3.5 multiplier was

replaced with the parameter χ and the multiplier $M_i/M_{i,tc}$ was added for consistency with other modifications:

$$D_{\max} = \chi\psi_i \frac{M_i}{M_{i,tc}} \quad \textbf{3-49}$$

Therefore the maximum hardness of the yield surface based on the maximum allowable dilatancy in the hardening law, eq. 3-48, could be derived from eq. 3-50 below:

$$\left(\frac{p_i}{p}\right)_{\max} = \exp\left(-\chi\psi_i / M_{i,tc}\right) \quad \textbf{3-50}$$

3.9.2. Obtaining Model Parameters

It is quite possible to formulate complicated constitutive models that incorporate numerous factors and utilize a large number of input parameters. However, in a practical point of view what outstands a constitutive model is the compromise between accuracy and simplicity. To employ a numerical model in real problems it is essential that a reasonable number an input parameters are required to define the material and they are derived through relatively simple procedures as well.

The NorSand model implemented in this study requires 9 parameters. Seven of which are material properties and the other two parameters specify the initial state of the soil.

Table 3-1 Typical Range of NorSand Parameters

Parameter	Typical Range	Description
Critical State		
Γ	0.8 - 1.4	CSL altitude at 1kPa
λ	0.01 - 0.07	CSL slope in semi log pressure - void ratio space
M_{tc}	1.2 - 1.5	Stress ratio at critical state under triaxial condition (reference state)
Plasticity		
H	50 - 500	Hardening modulus

χ	2.5 - 4.5	Multiplier to relate critical state to maximum dilatancy
Elasticity		
I_r	100 - 800	Rigidity modulus
ν	0.1 - 0.3	Poisson ratio
Initial State		
ψ_0	-0.3 - 0.15	Initial state parameter
R		Overconsolidation ratio

Jefferies and Shuttle (2005) introduced the procedures to calibrate the NorSand model. To measure the elasticity properties of the model, I_r and ν, bender element test can be performed (Atkinson, 2000). The elasticity properties, i.e. elastic shear modulus, can be obtained from unloading/reloading triaxial tests. However, it should be noted that such approach includes uncertainties related to inducing small strains in addition to yielding plastic strains in unloading cycles. The bender element test is performed for very small strain; for the large strain analyses of ice gouging the latter method, i.e. unloading/reloading triaxial tests, is more preferred.

In order to find CSL at least four tests should be carried out, two of which in drained condition and the other two in undrained condition. The undrained samples should be preferably very loose to show contractive behaviour and therefore result in a certain determination of critical state mean pressure of those samples. If dense samples are used very large effective mean pressures are need to make sure that critical state is reached. These large pressures cannot be conveniently applied in triaxial apparatus. The drained samples should be loose as well to ascertain the contractive behaviour and achievement of critical state within the triaxial apparatus limits. The best line that fits the processed data *in e- p* space is the CSL. It should be noted that experimental results suggests that the CSL is a curved line. However, for practical purposes the approximation of CSL with a

straight line is acceptable enough. Figure 3-15 demonstrates how CSL can be determined from triaxial tests.

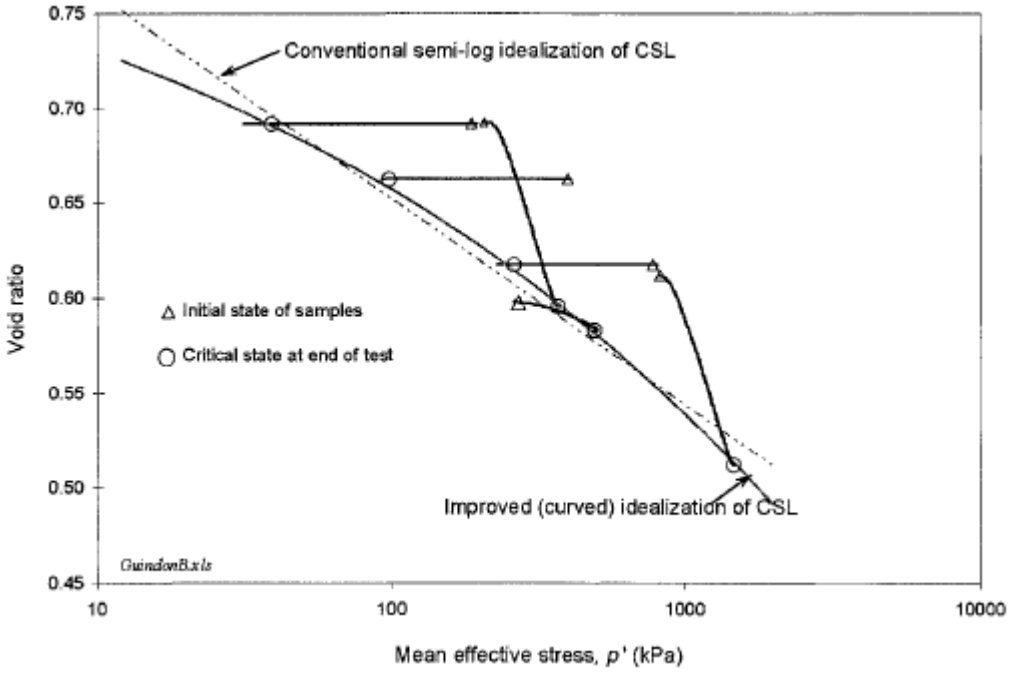

Figure 3-15 Derivation of CSL from triaxial tests (Jefferies & Shuttle, 2005)

The end condition of these triaxial test results can be used to determine the critical stress ratio at triaxial compression condition, M_{tc}. To determine M_{tc} it is preferred to consider the results of drained samples due to the uncertainties arise from development of low effective mean pressures at the end of the undrained tests.

The procedure to determine χ is to perform a drained test as dense as possible and then calculate the maximum dilatancy. The maximum dilatancy can be found using the stress - dilatancy plots (η - D). At maximum strength the elastic strain increments are zero therefore the associated dilatancy is the maximum plastic dilatancy. Having already established the CSL, the state parameter and therefore χ can be easily determined.

The proposed procedure to estimate H is to compare the computed stress-strain behaviour to the measured behaviour of drained samples in the lab. Based on experience H is a function of initial state parameter in a linear form:

$$H = a + b\psi \quad \textbf{3-51}$$

Therefore, it is necessary to try to find the best values of H that fit both dense and loose samples. The two loose samples used for determining CSL and the one dense sample used to obtain χ are helpful in establishing a relation for H. As previously mentioned the hardening law, H, must be independent from the Lode angle thus the determining the hardening modulus based on triaxial condition should be adequate.

As discussed earlier H, χ_{tc} and I_r are the parameters that capture the fabric of the soil therefore for real problems it would be preferable to derive these parameters in situ instead of performing laboratory tests. Jefferies and Been (2006) introduces methods to determine model parameters in situ.

3.9.3. Critical Stress Ratio *M*

The relation between stress invariants at critical void ratio is widely accepted to be as shown in equation below:

$$q = Mp \quad \textbf{3-52}$$

Many studies have examined this relation through a wide range of stress levels (e.g. Vaid and Sasitharan (1992)) and currently the accuracy of this relation is not seriously disputed.

Both Mohr-Coulomb and Matsuoka-Nakai (Matsuoka & Nakai, 1974) criteria are suitable for derivation of critical stress ratio, *M*. These two criteria define *M* as a function of Lode angle, θ. The Mohr-Coulomb yield surface can be rewritten as:

$$F = \frac{1}{3} J_1 \sin\phi + J_{2D}^{1/2}\left(\cos\theta - \frac{\sin\theta \sin\phi}{\sqrt{3}} \right) = 0 \qquad \textbf{3-53}$$

The stress invariants J_1 and $J_{2D}^{1/2}$ can be replaced by *p* and *q* respectively in relation above to form:

$$q = \frac{3\sin\phi}{\sqrt{3}\cos\theta - \sin\theta\sin\phi} p \qquad \textbf{3-54}$$

Which suggests:

$$M(\theta) = \frac{3\sin\phi}{\sqrt{3}\cos\theta - \sin\theta\sin\phi} \qquad \textbf{3-55}$$

Assuming the triaxial compression situation, $\theta = \pi/6$:

$$M_{tc} = \frac{6\sin\phi}{3 - \sin\phi} \qquad \textbf{3-56}$$

M(θ) can be alternatively expressed as follow based on Mohr-Coulomb criterion:

$$M(\theta) = \frac{3\sqrt{3}}{\cos\theta\left(1 + \frac{6}{M_{tc}}\right) - \sqrt{3}\sin\theta} \qquad \textbf{3-57}$$

On the other hand the Matsuoka-Nakai criterion can be written as follow:

$$\frac{27 - 3M^2}{3 - M^2 + \frac{8}{9}M^3 \sin\theta\left[\frac{3}{4} - \sin^2(\theta)\right]} = \frac{27 - 3M_{tc}^2}{3 - M_{tc}^2 + \frac{2}{9}M_{tc}^3} \qquad \textbf{3-58}$$

There is no close solution for $M(\theta)$ based on Matsuoka-Nakai criterion and it should be solved using numerical methods such as Newton or bisection. The numerical range for $M(\theta)$ is between M_{te} and M_{tc}.

In Figure 3-16 the two criteria are compared with each other. In NorSand the average of the two is selected to define critical stress ratio. The average of the two criteria is also shown in Figure 3-16 by red dotted line.

$$M(\theta) = \frac{M_{MC} + M_{MN}}{2} \qquad \textbf{3-59}$$

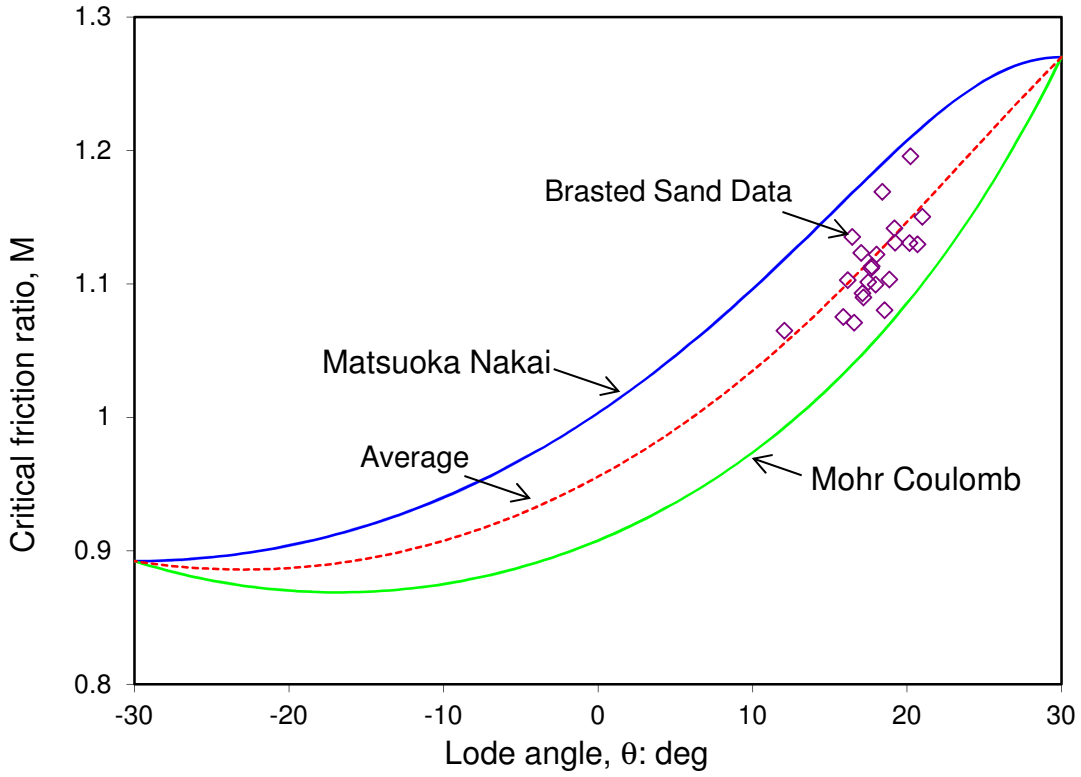

Figure 3-16 Comparison of *M(θ)* functions and laboratory tests values (Jefferies & Shuttle, 2002)

The third stress invariant is extremely important in three dimensional numerical analyses of geotechnical problems. It also significantly determines the accuracy of capturing the

soil behaviour. Therefore, in this thesis especial attention is devoted to the consideration of the third stress invariant. A significant goal of this research is to integrate the effect of third stress invariant in the numerical modeling of the soil behaviour.

The importance of the third stress invariant is acknowledged in this section by defining the critical stress ratio as a function of the Lode angle in the NorSand model. Therefore, in the NorSand model the critical stress ratio evolves during the analysis as the third stress invariant changes.

Throughout the future sections of this thesis the importance of the third stress invariant in the development of the formulation of the implemented constitutive models will be highlighted.

3.10. Summary

In this chapter the Critical State Soil Mechanics is introduced. It is shown that the critical state of the soil could be chosen as a unique reference framework that represents the state of the soil. Different state parameters have been proposed through which the effects of density and stress level on the soil behaviour are combined together. It is shown that two sample of soils with the same initial state parameter show similar behaviour under laboratory loading while samples with the same density or same stress level could exhibit different responses. In this chapter particular emphasize was placed on the behaviour of the sand since the main interest of this research is the ice gouging of the sandy seabed. It is shown through massive set of experiments that at the failure, sands behave in a dilative manner if ψ is negative and contractively if ψ is positive (Been & Jefferies, 1985).

This chapter introduces the elastic-plastic modeling of the soil behaviour. To conduct the current research two constitutive models are being used, the Drucker-Prager Cap model and the critical state soil model NorSand. These two models are described in details in this chapter.

The modification and implementation of the constitutive models will be discussed in the next chapter.

4. Implementation of Constitutive Models

4.1. Introduction

In this chapter the implementation of new constitutive material models in finite element software ABAQUS is discussed. These material models are called user material in ABAQUS and are implemented using special subroutines. Although the concept of adding a user material to the finite element package ABAQUS is basically the same throughout different units of this program but the implementation algorithm varies depending on which solver is employed in the analyses, i.e. explicit or standard. ABAQUS Standard uses subroutine UMAT to define the user materials while in ABAQUS Explicit the VUMAT subroutine is used. This chapter briefly discusses the two implicit and explicit approaches which are used in ABAQUS. The rest of the chapter is devoted to the implementation of user subroutine VUMAT in ABAQUS Explicit which is selected to analyze the problems of this study. More discussion about the implicit and explicit methods will come in chapter 1. This chapter also studies the ability of the

implemented constitutive material models to adequately capture the different behaviours of the soil. The models are validated based on the results of common soil laboratory tests.

One of the advantages of implicit method is that it is unconditionally stable. However, when a complicated three-dimensional model is considered various difficulties might occur. For instance when the time increment is reduced during the analysis the cost of the numerical computations to obtain successive tangent stiffness matrices would be significantly increased. Additionally local instabilities make the force equilibrium more difficult to be achieved.

These shortcomings led to establishment and use of explicit techniques. In explicit technique the computational cost is approximately proportional to the size of finite element meshing unlike implicit method where small changes in the meshing size dramatically affect the computing costs associated with implicit integration of nonlinear equations. Therefore, ABAQUS/Explicit is attractive for very large problems.

On the other hand the explicit method is not unconditionally stable. The criterion of stability in explicit method is defined so that the maximum time increment must be less than a critical value of the smallest transition times for a dilatational wave, i.e. the compressional wave or pressure wave which concerns the oscillation of particles in direction of the wave propagation, to pass any element in the finite element meshing. The explicit method works well for short transient problems. In the quasi-static problems the inertia effects must be small enough to be neglected. In order to disregard the effect of inertia one way is to limit the kinematic energy to be always less than 5 percents of the strain energy.

The explicit integration method is more efficient than the implicit integration method for solving highly discontinuous problems. It is feasible to solve complex and general 3D contact problems with deformable bodies using the explicit integration scheme of ABAQUS/Explicit. Problems involving stress wave propagation can be far more efficient computationally in ABAQUS/Explicit than in ABAQUS/Standard.

One disadvantage of explicit method in ABAQUS is that right now only first order displacement method elements (4-node quadrilaterals, 8-node bricks, etc.) and modified second-order elements are available for explicit analysis. In addition each degree of freedom in the element must have an assigned mass or rotary inertia.

In an implicit dynamic analysis the integration operator matrix must be inverted and a set of nonlinear equilibrium equations must be solved at each time increment. This significantly adds to the computation cost. ABAQUS/Explicit uses the central-difference operator. In ABAQUS the explicit procedure is based on an explicit integration scheme using the diagonal element mass matrices.

Implementing an explicit central difference integration formulation, the equation of the motion of a particle can be expressed as Eqs. 4-1 to 4-3.

$$u^{(i+1)} = u^{(i)} + \Delta t^{(i+1)} \dot{u}^{(i+1)} \qquad \textbf{4-1}$$

$$\dot{u}^{(i+1/2)} = \dot{u}^{(i-1/2)} + \frac{1}{2}\left(\Delta t^{(i+1)} + \Delta t^{(i)}\right)\ddot{u}^{(i)} \qquad \textbf{4-2}$$

Where $\dot{u}$ is the velocity and $\ddot{u}$ is the acceleration. In these equation i is the increment number and $i \pm 1/2$ is the mid increment number.

Considering the force equilibrium and using the diagonal element mass matrices the acceleration could be obtained as in Eq. 4-3:

$$\ddot{u}^{(i)} = \mathbf{M}^{-1}\left(F^{(i)} - I^{(i)}\right) \quad \textbf{4-3}$$

M is the mass lumped matrix, **F** is the applied external load vector and **I** is the internal force vector.

To assure the stability of the explicit analysis the time step should satisfy the following relation.

$$\Delta t \le \frac{2}{\omega_{\max}} \quad \textbf{4-4}$$

$\omega_{\max}$ is the maximum eigenvalue of the elements of the meshing.

ABAQUS uses a conservative estimate of the $\omega_{\max}$ to find the stable time increment value based on

$$\Delta t = \min \frac{L_e}{c_d} \quad \textbf{4-5}$$

Where c_d is the current effective dilatational wave speed of the material and L_e is the characteristic length of element which is a measure of the element size.

For the models that deal with fast contact problem the cost of computation would be less in explicit technique rather than implicit method. In the slow contact case the solutions are usually more unstable due to the high frequency and therefore numerical noises become more significant. In such condition the implicit method remove noises and concludes more valid results. This outcome is associated with numerical damping amplitude decay which is usually presents in the implicit technique. In addition as the time increment is larger in the conditionally stable explicit method in the case of slow contact the implicit method is more superior.

In Figure 4-1 the different steps of an explicit analysis are illustrated. ABAQUS Explicit allows the user to control the solver phase of the analysis by, among others, defining and implementing a constitutive model. It is also possible to develop Python scripts and perform the required post-processing tasks after the completion of the analysis in order to obtain the requested results. These features have been used in this study.

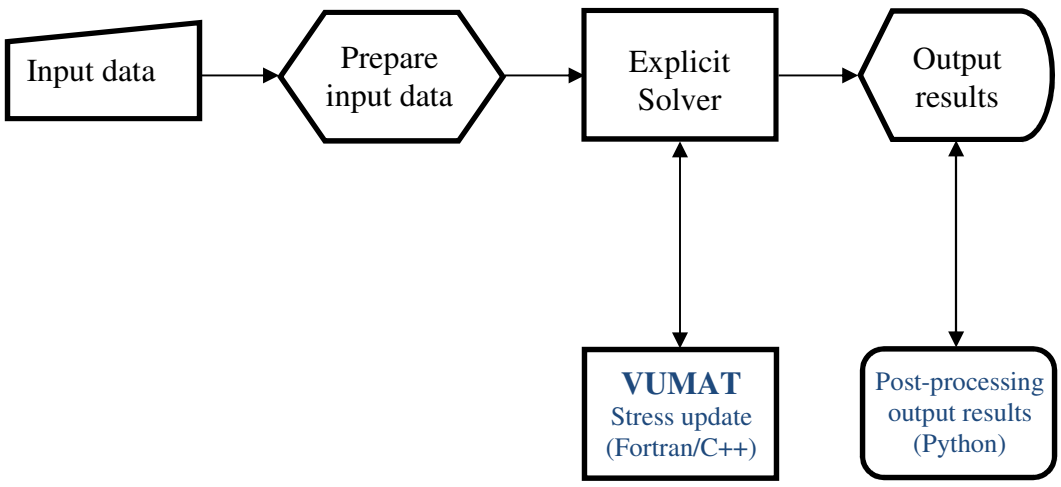

Figure 4-1 Steps of a finite element analysis using ABAQUS Explicit

4.2. User Defined Material Subroutine

Existing soil constitutive models in ABAQUS FE software are relatively simple but may not be always suitable for use in finite element analyses of ice gouging problems. In order to avoid some of the limitations, J. Barrette and Phillips (2011) enhanced the built-in Drucker-Prager model of ABAQUS by defining the angle of internal friction and dilation angle as function of plastic strain as a solution dependent variable in accordance with the real behaviour and compared their results to gouge test data.

ABAQUS Explicit also allows the users to develop their own material models and enhance the explicit analyses by implementation of user defined material subroutine VUMAT. This feature in ABAQUS is helpful in problems like ice gouging where the available built-in models have a number of limitations. In this study, advanced soil constitutive models are implemented in ABAQUS. Figure 4-2 shows how the user subroutine VUMAT is incorporated in the ABAQUS Explicit analysis. An explicit analysis is divided into many small time increments. At the beginning of each time increment, based on the dynamic laws and equations of equilibrium the new configuration of the system is derived. The system deformation then accordingly is translated to strain increments. The current stress and user defined state variables as well as the strain increment are sent to the VUMAT subroutine. Subsequently based on the constitutive equations of any desired material model, the user material subroutine updates the stress components and state variables. The updated stress components and user defined state variables are eventually sent back to the ABAQUS Explicit solver and are utilized as VUMAT inputs in the next time step.

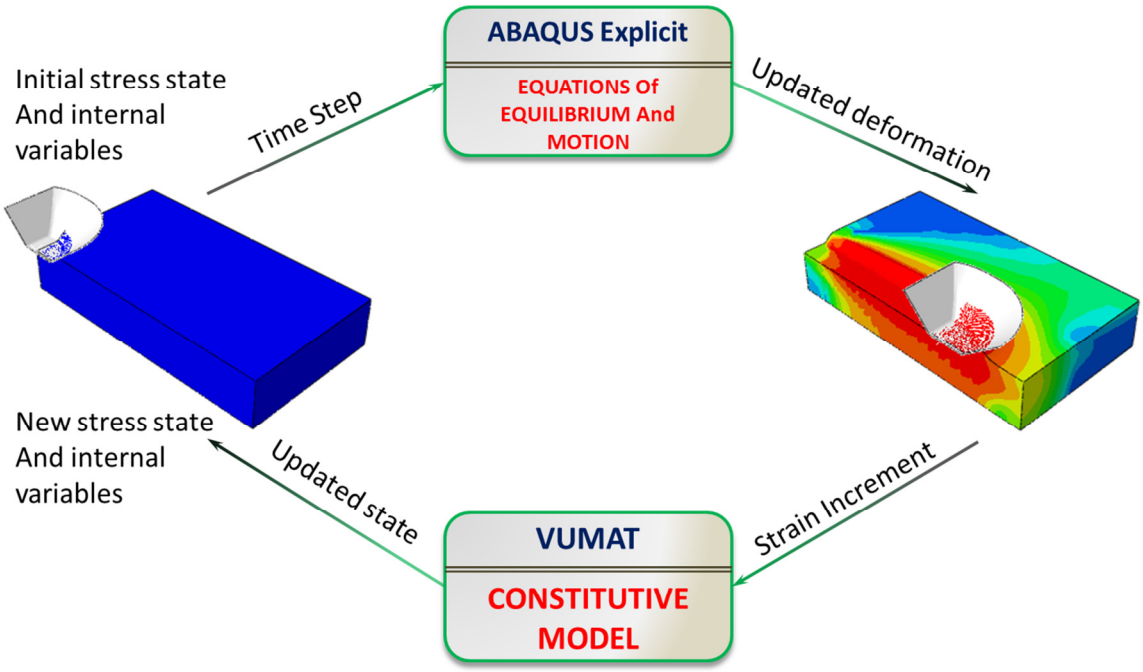

Figure 4-2 VUMAT in ABAQUS Explicit

4.2.1. Structure of User Defined Material Subroutine VUMAT

In this study the concept of an elastic predictor-plastic corrector algorithm is adopted in the VUMAT subroutine to update the stress and state variables at each time increment. As described in section 4.1 the explicit solver derives the displacements based on the equations of motion. The displacements are transformed in strain field and are sent to the VUMAT subroutine. The purpose of the user material subroutine VUMAT in ABAQUS Explicit is to update the stress based on the input strains at a time increment. The stress update approach that is implemented in the user subroutines VUMAT of this study is described in the following sections.

The theory of plasticity requires that the stress state of a material point always exists within the corresponding yield surface or on the boundaries of the yield surface. In the

elastic predictor phase the material is assumed to behave purely elastically. As the result of this assumption a trial stress σ^* could be obtained as shown in eq.4-6:

$$\sigma^*(t+\Delta t) = \sigma(t) + C\Delta\varepsilon \quad \textbf{4-6}$$

In this equation **C** is the elastic matrix which is defined in eq. 4-7:

$$C = 2GI + (K - 2G/3)\delta \otimes \delta \quad \textbf{4-7}$$

Where G is the shear modulus, K is the bulk modulus, I.is the identity matrix and δ is the Kronecker delta. The trial stress could be converted into the stress invariants which are usually applied to represent the constitutive models. In case of the soil, the yield surfaces of the material models are regularly expressed in the $p' - q$ space.

$$\sigma^*(t+\Delta t) \Rightarrow p'^* \,\&\, q^* \quad \textbf{4-8}$$

The trial stress could be either within the yield surface as shown in Figure 4-3 (left) or violate the yield surface and be located outside of its boundary as is the case in Figure 4-3 (right).

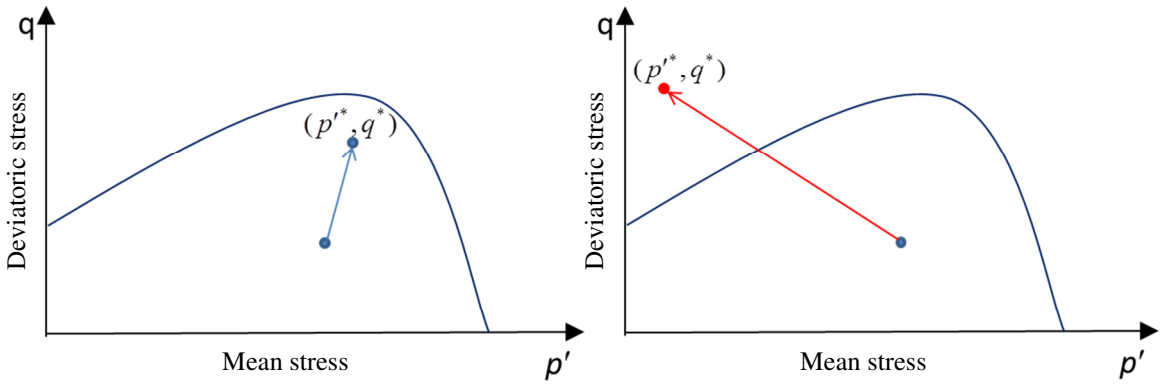

Figure 4-3 Trial stress based on pure elasticity

When the trial stress is inside the yield surface it is implied that the material exhibits elastic response. In this case no correction is needed and the stress of the material at the end of the time increment is updated with the trial values.

$$\sigma(t+\Delta t) = \sigma^{*}(t+\Delta t) \qquad \textbf{4-9}$$

On the other hand, if the trial stress violates the yield condition the corrector phase should be applied to return the stress state onto the yield surface as shown in Figure 4-4.

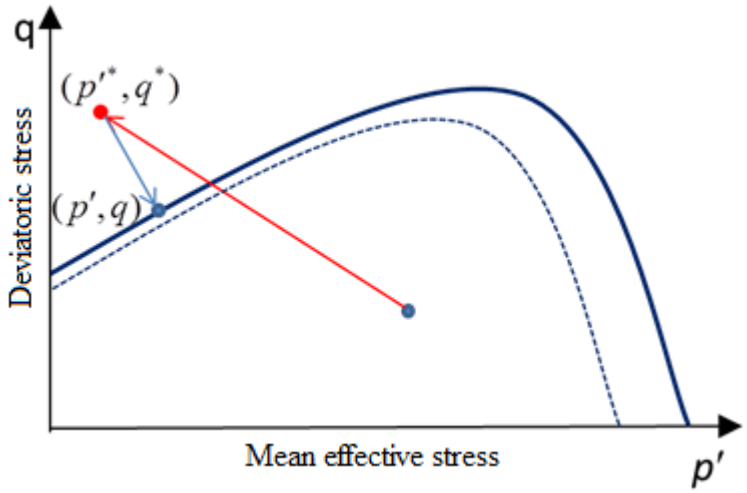

Figure 4-4 Plastic corrector phase

The plastic corrector phase is based on the normality to the plastic potential surface and the consistency condition. The consistency condition, as noted earlier, enforces the stress state to be on the yield surface as shown in eq. 4-10:

$$dF = \frac{\partial F}{\partial \sigma} d\sigma + \frac{\partial F}{\partial \kappa} d\kappa = 0 \qquad \textbf{4-10}$$

In Eq. 4-10, κ is an internal variable which controls the size of the yield surface. The plastic strain increment can be calculated as:

$$d\varepsilon_{ij}^{p} = \lambda \frac{\partial g}{\partial \sigma_{ij}} \quad \textbf{4-11}$$

Based on the flow rule in eq. 4-11, the plastic volumetric strain increment and the plastic shear strain increment could be expressed in term of the plastic multiplier, λ. Since in the theory of elasto-plasticity the strain is decomposed into two parts of recoverable (elastic) and non-recoverable part (plastic), deriving the plastic strain increments though the flow rule leads to determination of the elastic components as well in a time increment.

$$d\varepsilon = d\varepsilon^{e} + d\varepsilon^{p} \quad \textbf{4-12}$$

Therefore based on Eqs. 4-6, 4-11 and 4-12, the new stress state in $p' - q$ could be easily related to elastic moduli K and G and the plastic multiplier λ as shown in eqs. 4-13 and 4-14. Below:

$$p' = p'^{*} - K\lambda \frac{\partial g}{\partial p'} \quad \textbf{4-13}$$

$$q = q^{*} - 3G\lambda \frac{\partial g}{\partial q} \quad \textbf{4-14}$$

Both eqs.4-13 and 4-14 are expressed as functions of plastic multiplier λ. Note that in plasticity theory λ ultimately represents a comprehendible physical property. For example in Drucker-Prager model λ could be related to the equivalent plastic strain increment. Therefore the internal variable κ is also related to the plastic multiplier through the hardening law of the constitutive model in question.

$$d\kappa = f(\lambda) \quad \textbf{4-15}$$

Equations 4-13, 4-14 and 4-15 are then inserted in the consistency equation, eq. 4-10, to establish a non-linear relationship with only one unknown variable, the plastic multiplier

λ. If this non-linear equation is solved the result would be a new yield surface in accordance with desired hardening law and the stress state which is projected onto the new yield surface as shown in Figure 4-4.

In this study a simple radial return algorithm is adopted in the plastic corrector phase in order to satisfy the consistency condition and return the predicted stress state back to the updated yield surface as shown in Figure 4-5. In this figure σ_1, σ_2 and σ_3 are respectively major, intermediate and minor principal stresses.

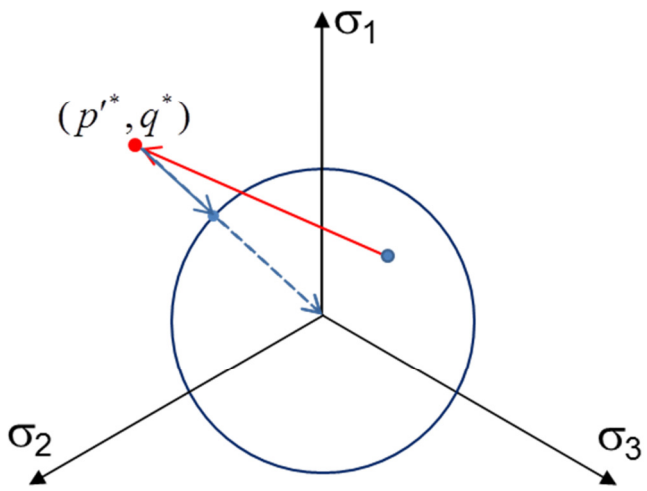

Figure 4-5 Radial return algorithm

The advantage of using the radial return algorithm is simplifying the analysis process by avoiding the complexities associated with the third stress invariant.

4.2.2. Consistency Condition for Proposed Drucker-Prager Cap Model

The consistency condition, presented in eq. 4-10, could be expressed in form of stress invariants as shown in eq. 4-16:

$$dF = \frac{\partial F}{\partial p'} dp' + \frac{\partial F}{\partial q} dq + \frac{\partial F}{\partial \kappa} d\kappa = 0 \qquad \textbf{4-16}$$

As it will be introduced in section 4.3, hardening/softening law of the proposed Drucker-Prager Cap model is governed by varying the evolution parameter, p_a, and internal friction angle, θ, through the development of plastic shear strain. Therefore:

$$\kappa = f(p_a, \theta) \qquad \textbf{4-17}$$

The different parts of the partial differential equation 4-16, the consistency condition, could be then simply obtained for the Drucker-Prager Cap model based on the yield surface and the plastic potential surface.

Since the Drucker-Prager Cap model consists of three parts of shear zone, transition zone and the cap, as thoroughly explained in chapter 3.8.1 and shown in Figure 4-6, three sets of partial differential terms are derived for each surface:

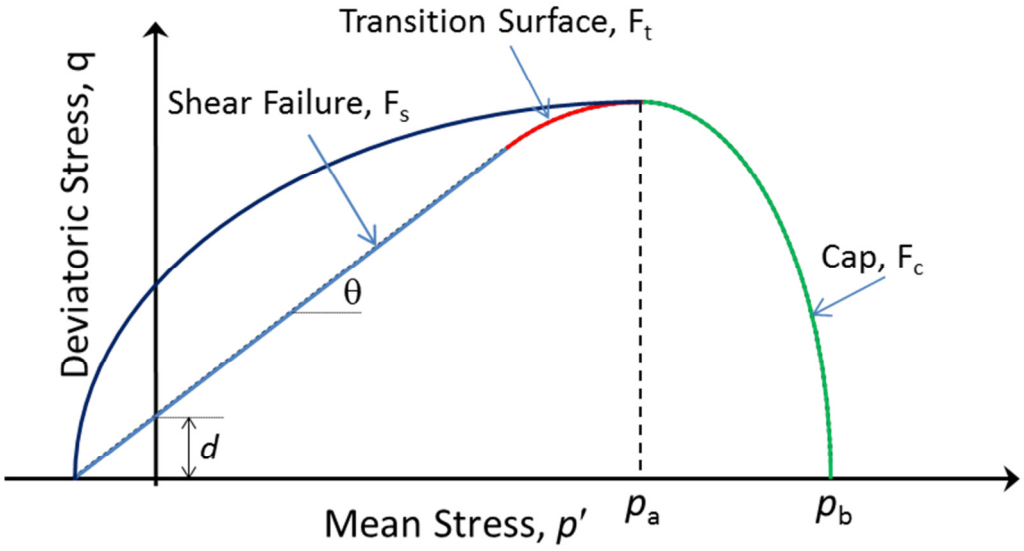

Figure 4-6 Yield Surface in the Drucker Prager Cap Model

- The shear zone:

$$\frac{\partial F_S}{\partial p'} = -\tan\theta \tag{4-18}$$

$$\frac{\partial F_S}{\partial q} = 1 \tag{4-19}$$

$$\frac{\partial F_S}{\partial p_a} = 0 \tag{4-20}$$

$$\frac{\partial F_S}{\partial \theta} = -p'(1+\tan^2\theta) \tag{4-21}$$

- The transition zone:

$$\frac{\partial F_t}{\partial p'} = \frac{p - p_a}{\sqrt{(\alpha\gamma)^2 - (p - p_a)^2}} \tag{4-22}$$

$$\frac{\partial F_t}{\partial q} = 1 \tag{4-23}$$

$$\frac{\partial F_t}{\partial p_a} = -\frac{p - p_a}{\sqrt{(\alpha\gamma)^2 - (p - p_a)^2}} - \left((1 - \gamma/\cos\theta) + \frac{\alpha\gamma^2}{\sqrt{(\alpha\gamma)^2 - (p - p_a)^2}} \right) \tan\theta \tag{4-24}$$

$$\frac{\partial F_t}{\partial \theta} = \frac{\tan\theta}{\cos\theta}\gamma\alpha - \left((1 - \gamma/\cos\theta) + \frac{\alpha\gamma^2}{\sqrt{(\alpha\gamma)^2 - (p - p_a)^2}} \right) p_a \left(1 + \tan^2\theta\right) \tag{4-25}$$

- The cap zone:

$$\frac{\partial F_C}{\partial p'} = 2\frac{p' - p_a}{B^2} \tag{4-26}$$

$$\frac{\partial F_C}{\partial q} = \frac{2q}{\left(A\left(1 + \gamma - \gamma/\cos\theta\right)\right)^2} \tag{4-27}$$

$$\frac{\partial F_C}{\partial p_a} = -2\frac{p' - p_a}{B^2} - \frac{2}{A}\left(\left(\frac{p' - p_a}{B}\right)^2 + \left(\frac{q}{A\left(1+\gamma-\gamma/\cos\theta\right)}\right)^2\right)\tan\theta \quad \textbf{4-28}$$

$$\frac{\partial F_C}{\partial \theta} = \frac{\gamma\tan\theta q}{\left(1+\gamma-\gamma/\cos\theta\right)\cos\theta}\frac{2q}{\left(A\left(1+\gamma-\gamma/\cos\theta\right)\right)^2} - \frac{2}{A}\left(\left(\frac{p' - p_a}{B}\right)^2 + \left(\frac{q}{A\left(1+\gamma-\gamma/\cos\theta\right)}\right)^2\right)p_a\left(1+\tan^2\theta\right) \quad \textbf{4-29}$$

Substituting Eqs.4-18 to 4-29 into the consistency condition, Eq. 4-16, results in a nonlinear relation that could be solved for plastic multiplier, λ.

4.2.3. Consistency Condition for NorSand Model

The same argument that discussed in previous section, 4.2.2, could be made for NorSand model. By establishing the required partial differential terms of the consistency condition it is then possible to complete the plastic predictor phase of the elastic-plastic algorithm for NorSand model in this implementation. The yield surface of the critical state model NorSand described in section 3.9.13.9 could be expressed as in eq. 4-30:

$$F = q - M_i p' + M_i p' \ln\left(\frac{p'}{p_i}\right) = 0 \quad \textbf{4-30}$$

Therefore the consistency condition could be written as:

$$dF = \frac{\partial F}{\partial p'}dp' + \frac{\partial F}{\partial q}dq + \frac{\partial F}{\partial \theta}d\theta + \frac{\partial F}{\partial p_i}dp_i \quad \textbf{4-31}$$

In this equation θ_L is the Lode angle.

$$dF = \frac{\partial F}{\partial p'}dp' + \frac{\partial F}{\partial q}dq + \frac{\partial F}{\partial \theta_L}d\theta_L + \frac{\partial F}{\partial p_i}dp_i \quad \textbf{4-32}$$

The partial differential terms of the consistency equation could be obtained according to eqs. 4-33 to 4-42.

With respect to mean pressure:

$$\frac{\partial F}{\partial p'} = M_i \ln\left(\frac{p'}{p_i}\right) \quad \textbf{4-33}$$

With respect to deviatoric stress:

$$\frac{\partial F}{\partial q} = 1 \quad \textbf{4-34}$$

With respect to Lode angle:

$$\frac{\partial F}{\partial \theta_L} = \frac{\partial F}{\partial M_i}\frac{\partial M_i}{\partial \theta_L} \quad \textbf{4-35}$$

$$\frac{\partial F}{\partial M_i} = -p' + p' \ln\left(\frac{p'}{p_i}\right) \quad \textbf{4-36}$$

As explained in section 3.9.3 the critical stress ratio in NorSand is an average of the Mohr-Coloumb criterion and Matsuoka-Nakai criterion, therefore:

$$\frac{\partial M_i}{\partial \theta_L} = \frac{\partial M}{\partial \theta_L} = \frac{1}{2}\left(\frac{\partial M_{MC}}{\partial \theta_L} + \frac{\partial M_{MN}}{\partial \theta_L}\right) \quad \textbf{4-37}$$

$$\frac{\partial M_{MC}}{\partial \theta_L} = \frac{\sqrt{3}\cos\theta_L + \left(1 + \frac{6}{M_{tc}}\right)\sin\theta_L}{3\sqrt{3}} M_{MC}^2 \quad \textbf{4-38}$$

Based on Eq 3-58 the partial differential of the Masuoka-Nakai criterion in respect to the Lode angle could be indirectly derived as in Eq. 4-39:

$$\frac{\partial M_{MN}}{\partial \theta_L} = -\frac{2/3 M_{MN}^2 \cos\theta_L \left(1 - 4\sin^2\theta_L\right)}{8/3 \sin\theta_L \left(3/4 - \sin^2\theta_L\right) M_{MN} + 2\left(3/A - 1\right)} \quad \textbf{4-39}$$

The partial differential of the consistency relation in respect to the image pressure, p_i, is obtained through the chain rule. It should be noted that the :

$$\frac{\partial F(M_i(p_i), p_i)}{\partial p_i} = \frac{\partial F(M_i(p_i))}{\partial M_i(p_i)} \frac{\partial M_i(p_i)}{\partial p_i} + \frac{\partial F(p_i)}{\partial p_i} \quad \textbf{4-40}$$

The differential terms involved in Eq. 4-40 are derived as following:

$$\frac{\partial M_i}{\partial p_i} = -\frac{e - \Gamma + \lambda \ln(p_i)}{|e - \Gamma + \lambda \ln(p_i)|} \frac{\lambda}{p_i} \quad \textbf{4-41}$$

$$\frac{\partial F}{\partial p_i} = -\frac{M_i p'}{p_i} \quad \textbf{4-42}$$

Having all terms required in the consistency condition, it is now possible to establish a nonlinear equation based on the plastic multiplier as defined in the flow rule. Using the Newton method, the nonlinear equation could be efficiently solved and determine the new the new stress state.

4.3. Modification of Drucker-Prager Cap Model

The Drucker-Prager Cap constitutive model was introduced in chapter 3. As mentioned, in the current version of Drucker-PragerCap, the elasticity law is chosen as the simple constant of elastic Young's modulus, *E*, and the Poisson's ratio, ν. Therefore two more parameters should be added to the parameter list of the model. It would make more sense to relate the elasticity to the density and the straining history of the material in future studies.

The variants of Drucker-Prager model are widely used for geotechnical numerical analyses both in research and practice. The simplicity of the model, in term of obtaining the input parameters and the way the model itself is formulated, is the main appeal of the

model especially among the practical engineers. The original Drucker-Prager model does not employ a cap which means the soil can be isotropically loaded without yielding. Drucker-Prager Cap model is an attempt to more realistically capture the behaviour of soil. Figure 4-7 reviews a schematic representation of the Drucker-Prager Cap model as already described in chapter 3.

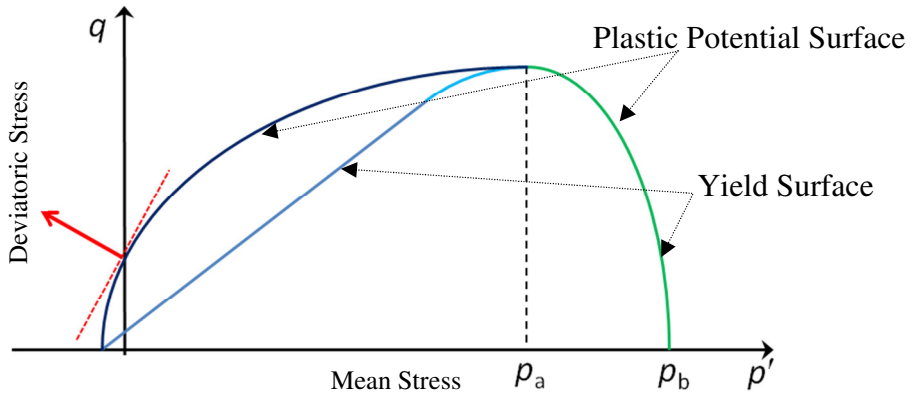

Figure 4-7 DP Cap yield surface and plastic potential function

The cap in the DP Cap model also functions to control the dilation rate and the hardening law. As it can be seen in Figure 4-7 the potential function of the Drucker-Prager Cap model could result in high dilatancy rates at low pressures. This is one of the shortcomings of the model which may lead to numerical instability in the geotechnical numerical analyses, especially the analyses which involve large deformation. This study aims to modify the potential function the of the Drucker-Prager Cap model to avoid excessive and unrealistic dilation rates. The hardening law of the model will be improved as well in accordance with steady state concept. The consequence of these modifications should be a constitutive model implemented in ABAQUS Explicit which is more stable

and robust than the built-in Cap model and is able to capture the hardening/softening behaviour of sand more reasonably.

The hardening law of the model is defined in a simple manner to comply with the critical state mechanics concepts. This framework required the yield surface to approach and intersect the critical state as the plastic shear strains increase. The critical state is a combination of the void ratio and stress level at which soil can deform continuously without any change in stress level or the mass volume. The simple set of relations shown below in Eqs. 4-43 and 4-44 satisfy this assumption of the approach of yield surface to the critical state:

$$\frac{dp_a}{p'} = H\left(\frac{p_{a,\max}}{p_{\max}} - \frac{p_a}{p'}\right)d\varepsilon_q^p \qquad \textbf{4-43}$$

$$d\theta = H(\theta_{\max} - \theta)d\varepsilon_q^p \qquad \textbf{4-44}$$

In the other word the relations above change the yield surface through parameters θ and p_a so that the zero dilatancy or constant volume situation would be achieved.

In order to use the hardening law, the Eqs.4-43 and 4-44, an estimation of the peak values $p_a$and θ are required to substitute the values of $p_{a,max}$ and θ_{max}. In fact these values represent the maximum achievable value of each of them at any time. The hardening rule tries to compensate the divergence from the estimated values by approaching them.

To relate the peak values of θ and p_a the experimental relation of Bolton (1986) which describes the dilatancy of sands is applied. As shown in Figure 4-8, Bolton assumes that the maximum dilatancy corresponds to the peak strength of the soil. This assumption is

not exact but is fairly valid. In Figure 4-8 ε_1, ε_v, σ'_1 and σ'_3 are respectively the axial strain, volumetric strain major principal effective stress and minor principal effective stress.

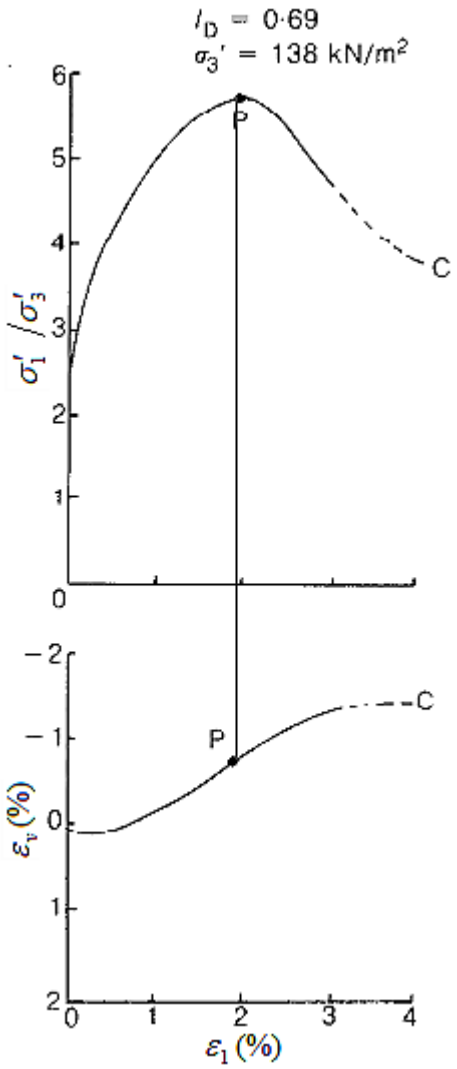

Figure 4-8 The maximum dilatancy occurs at peak strength (Bolton, 1986)

The Bolton relation defines a dilatancy index as shown in Eq. 4-45:

$$I_R = I_D(10 - \ln p') - 1 \qquad \textbf{4-45}$$

Here I_D is the relative density:

$$I_D = \frac{e_{\max} - e}{e_{\max} - e_{\min}} \quad \textbf{4-46}$$

Bolton proposed an empirical formula which suggests the value of angle of internal friction at peak.

$$\phi_{\max} = \phi_{cr} + 3I_R \quad \textbf{4-47}$$

This value can be converted into internal friction suitable for Drucker-Prager model through the Eq. 4-48:

$$\theta = \tan^{-1}\left(\frac{6\sin\phi}{3-\sin\phi}\right) \quad \textbf{4-48}$$

Bolton also defines the dilatancy as the ratio of plastic volumetric strain over first plastic principal strain and estimates its value at the peak (Bolton, 1986). Note that in order to be consistent with ABAQUS, unlike the accepted convention in soil mechanics, the sign for compression is assumed to be negative as it is the same in solid mechanics.

$$D_B^p = -\frac{d\varepsilon_v}{d\varepsilon_1} \quad \textbf{4-49}$$

Which is related to the dilatancy index:

$$D_B^p = 0.3I_R \quad \textbf{4-50}$$

The dilatancy can be deduced from the Drucker-Prager yield surface and establish a relation between the maximum dilatancy estimated by Bolton relation and the stress state at the peak.

$$D^p = \frac{d\varepsilon_v^p}{d\varepsilon_q^p} = -\frac{\dfrac{\partial \phi}{\partial p}}{\dfrac{\partial \phi}{\partial q}} = -\frac{p' - p_a}{q}\left(\frac{\alpha}{\beta}\right)^2 \quad \textbf{4-51}$$

Therefore, according to Eq. 3-23 maximum dilatancy can be derived as shown in Eq. 4-52:

$$D^p_{\max} = -\frac{p'_{\max} - p_{a\max}}{q_{\max}} \tan^2 \theta_{\max} \quad \textbf{4-52}$$

$$q_{\max} = p'_{\max} \tan \theta_{\max} + d \quad \textbf{4-53}$$

Assuming d is negligible comparing to $p_{\max}$,which is the case of non-cohesive sands, Eq. 4-54 would be obtained.

$$\frac{p_{a\max}}{p'_{\max}} = 1 + \frac{D^p_{\max}}{\tan \theta_{\max}} \quad \textbf{4-54}$$

As it can be seen in Eqs.4-49 and 4-51 above, the definition of dilatancy in Bolton formula and the dilatancy deduced from Drucker-Prager plastic potential surface are different. Therefore to use the dilatancy obtained through Bolton formula as a criterion that specifies the peak stress state it should be first transformed to the *p-q* space where the plastic potential surface is defined. This transformation is explained in the following:

Referring to 3-11 and 3-12 for *p* and *q*:

$$\frac{\partial p}{\partial \sigma'_1} = -\frac{1}{3}\frac{\partial I_1}{\partial \sigma_1} = -\frac{1}{3} \quad \textbf{4-55}$$

And:

$$\frac{\partial q}{\partial \sigma'_1} = \sqrt{3}\frac{\partial J_2^{1/2}}{\partial \sigma_1} = \frac{3}{2}\frac{s'_1}{q} \quad \textbf{4-56}$$

Where the first principal deviatoric stress, s'_1, could be defined as:

$$s_1' = \sigma_1 - \frac{1}{3}J_1 = \sigma_1 + p = \frac{2\sigma_1' - \sigma_2' - \sigma_3'}{3} \quad \textbf{4-57}$$

In order to have a pair of work conjugate strain and stress invariable they should relate to principal stress and strain as shown in Eq. 4-58 below:

$$qd\varepsilon_q^p - p'd\varepsilon_v^p = \sigma_1'd\varepsilon_1^p + \sigma_2'd\varepsilon_2^p + \sigma_3'd\varepsilon_3^p \quad \textbf{4-58}$$

Where:

$$d\varepsilon_v^p = d\varepsilon_1^p + d\varepsilon_2^p + d\varepsilon_3^p \quad \textbf{4-59}$$

Therefore:

$$qd\varepsilon_q^p = (\sigma_1' + p')d\varepsilon_1^p + (\sigma_2' + p')d\varepsilon_2^p + (\sigma_3' + p')d\varepsilon_3^p \quad \textbf{4-60}$$

$$d\varepsilon_q^p = \frac{s_1'd\varepsilon_1^p + s_2'd\varepsilon_2^p + s_3'd\varepsilon_3^p}{q} \quad \textbf{4-61}$$

The definition for dilatancy in Bolton formula is shown in Eq. 4-62:

$$D_B^p = -\frac{d\varepsilon_v}{d\varepsilon_1} \quad \textbf{4-62}$$

Based on the normality:

$$D^p = \frac{d\varepsilon_v^p}{d\varepsilon_q^p} = \frac{-\frac{\partial\phi}{\partial p}}{\frac{\partial\phi}{\partial q}} = -\frac{p' - p_a}{q}\left(\frac{\alpha}{\beta}\right)^2 \quad \textbf{4-63}$$

Therefore:

$$D^p = -rD_B^p \quad \textbf{4-64}$$

r is a coefficient that transform Bolton dilation rate to the dilatancy derived according normality to the plastic potential surface.

$$r = \frac{d\varepsilon_1^p}{d\varepsilon_q^p} \tag{4-65}$$

Therefore:

$$r = \frac{d\varepsilon_1^p}{d\varepsilon_q^p} = \frac{q d\varepsilon_1^p}{s_1' d\varepsilon_1^p + s_2' d\varepsilon_2^p + s_3' d\varepsilon_3^p} \tag{4-66}$$

According to the flow rule and using the chain rule:

$$d\varepsilon_1^p = d\lambda \frac{\partial \phi}{\partial \sigma_1'} = d\lambda \left(\frac{\partial \phi}{\partial p'} \frac{\partial p'}{\partial \sigma_1'} + \frac{\partial \phi}{\partial q} \frac{\partial q}{\partial \sigma_1'} \right) = d\lambda \left(-\frac{1}{3} \frac{\partial \phi}{\partial p'} + \frac{3}{2} \frac{s_1'}{q} \frac{\partial \phi}{\partial q} \right) \tag{4-67}$$

Two similar relations can be derived for second and third principal plastic strain rates. Substituting these three relations into Eq. 4-66 results the Eq. 4-68:

$$r = \frac{q \left(\frac{3}{2} \frac{s_1'}{q} \frac{\partial \phi}{\partial q} - \frac{1}{3} \frac{\partial \phi}{\partial p'} \right)}{s_1' \left(\frac{3}{2} \frac{s_1'}{q} \frac{\partial \phi}{\partial q} - \frac{1}{3} \frac{\partial \phi}{\partial p'} \right) + s_2' \left(\frac{3}{2} \frac{s_2'}{q} \frac{\partial \phi}{\partial q} - \frac{1}{3} \frac{\partial \phi}{\partial p'} \right) + s_3 \left(\frac{3}{2} \frac{s_3'}{q} \frac{\partial \phi}{\partial q} - \frac{1}{3} \frac{\partial \phi}{\partial p'} \right)} \tag{4-68}$$

Or:

$$r = \frac{q \left(\frac{3}{2} \frac{s_1'}{q} \frac{\partial \phi}{\partial q} - \frac{1}{3} \frac{\partial \phi}{\partial p'} \right)}{\frac{1}{q} \left(\frac{3}{2} \left(s_1'^2 + s_2'^2 + s_3'^2 \right) \right) \frac{\partial \phi}{\partial q} - \frac{1}{3} \left(s_1' + s_2' + s_3' \right) \frac{\partial \phi}{\partial p'}} \tag{4-69}$$

Since:

$$s_1' + s_2' + s_3' = 0 \tag{4-70}$$

And:

$$q^2 = 3J_{2D} = \frac{3}{2} \left(s_1'^2 + s_2'^2 + s_3'^2 \right) \tag{4-71}$$

Therefore:

$$r = \frac{q\left(\frac{3}{2}\frac{s_1'}{q}\frac{\partial\phi}{\partial q} - \frac{1}{3}\frac{\partial\phi}{\partial p'}\right)}{\frac{1}{q}\left(q^2\right)\frac{\partial\phi}{\partial q}} \quad \textbf{4-72}$$

Finally, it could be easily concluded that:

$$r = \frac{q\left(\frac{3}{2}\frac{s_1'}{q} - \frac{1}{3}\frac{\frac{\partial\phi}{\partial p}}{\frac{\partial\phi}{\partial q}}\right)}{q} = \frac{3}{2}\frac{s_1'}{q} + \frac{1}{3}D^p \quad \textbf{4-73}$$

According to Eq. 4-64 :

$$D^p = -\left(\frac{3}{2}\frac{s_1'}{q} + \frac{1}{3}D^p\right)D_B^p \quad \textbf{4-74}$$

Or:

$$D^p = -\frac{9}{2}\frac{s_1'}{q}\frac{D_B^p}{3+D_B^p} \quad \textbf{4-75}$$

The principal effective stress can be defined in term of Lode angle, θ_L, and deviatoric stress as shown in Eq. 4-76:

$$\begin{Bmatrix} s_1' \\ s_2' \\ s_3' \end{Bmatrix} = \frac{2}{3}q\begin{Bmatrix} \sin\left(\theta_L + 2\pi/3\right) \\ \sin\theta_L \\ \sin\left(\theta_L + 4\pi/3\right) \end{Bmatrix} \quad \textbf{4-76}$$

Therefore:

$$D^p = 3\sin(2\pi/3 - \theta_L)\frac{D_B^p}{3+D_B^p} \quad \textbf{4-77}$$

The hardening law now can either harden or soften the yield surface according to the current state of stress and density. As described above the hardening law requires 4 more

parameter which are maximum void ratio $e_{\max}$, minimum void ratio $e_{\min}$, initial void ratio e_0 and a calibrating parameter *H*.

As previously noted, in this version of Drucker-Prager Cap model steps are taken to restrict the dilation rate while the soil yields on the shear zone. Ice gouging simulations using conventional Drucker-Prager model or Drucker-Prager Cap occasionally result in excessive volume increase of the soil which is unjustifiable. To cope with this problem the plastic potential surface in the shear zone is altered to limit the dilatancy to a specified value. To do so, as shown in Figure 4-9the plastic potential function representing the part of the yield surface prior to the pressure corresponding to the specified limiting dilatancy,$p_{D^p_{max}}$ in Figure 4-9, is replaced with a straight line. However, the plastic potential function after this point and up to the evolution parameter p_a would remain unchanged. The replaced straight line is defined in a way to represent this specified dilation when the normality principal is applied. The specific value of dilatancy is chosen to be the maximum dilation given by Bolton formula in Eq. 4-60and therefore varies according to the current state of stress and density. Assuming the Bolton maximum dilation as the limiting dilatancy concludes the formula in Eq. 4-78for the hydrostatic pressure corresponding to the point at which the plastic potential surface changes to a straight line:

$$p_{D^p_{\max}} = \frac{p_a \tan^2\theta - D^p_{\max} d}{D^p_{\max} \tan\theta + \tan^2\theta} \qquad \textbf{4-78}$$

As the result the potential surface would be the same standard ellipse followed by a straight line whose slope represents the maximum dilatancy suggested by Bolton

formulas shown in Figure 4-9. In this figure the original plastic potential surface is drawn as the ellipse.

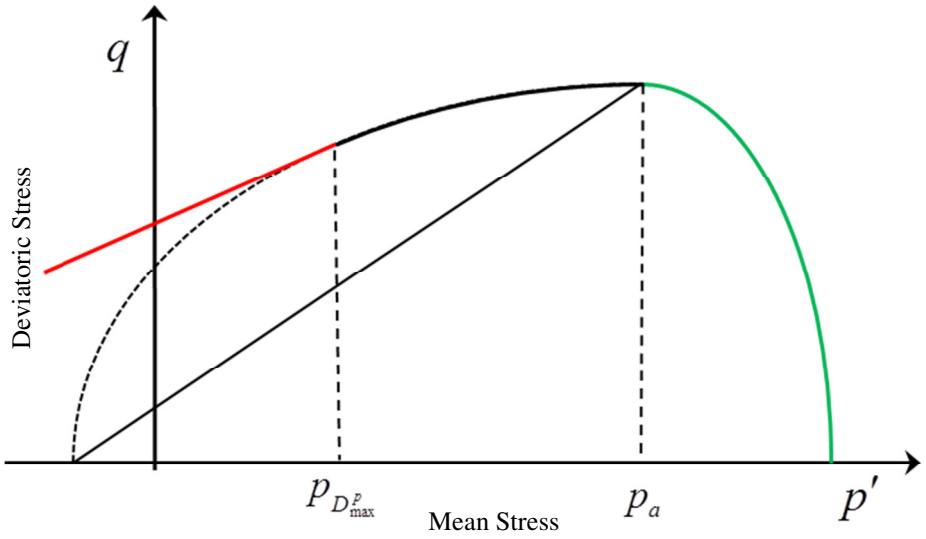

Figure 4-9 Two segment plastic potential function in shear zone

During shearing the value of $p_{D_{max}^p}$ is changing because I_R is a function of current state of stress and density. Therefore, the shape of the plastic potential function should be updated with progress of the shearing. Figure 4-10 shows that the plastic potential surface of the model dynamically changes as a function of the soil state. In other word, the current hydrostatic pressure corresponding to the maximum dilatancy determines the shape of the plastic potential surface.

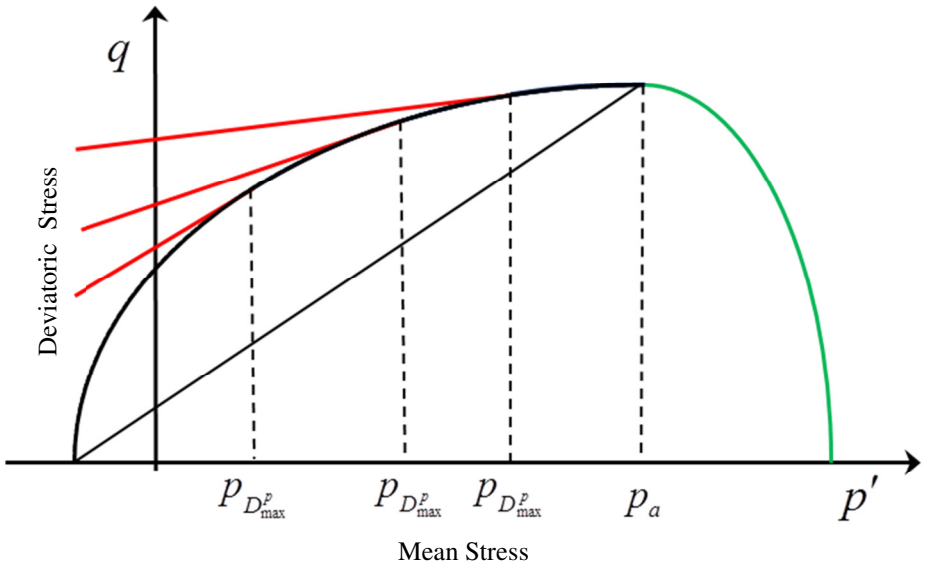

Figure 4-10Variations of plastic potential surface as function of the soil state

As $p_{D_{max}^p}$ evolves it could become equal to p_a as shown in Figure 4-11.

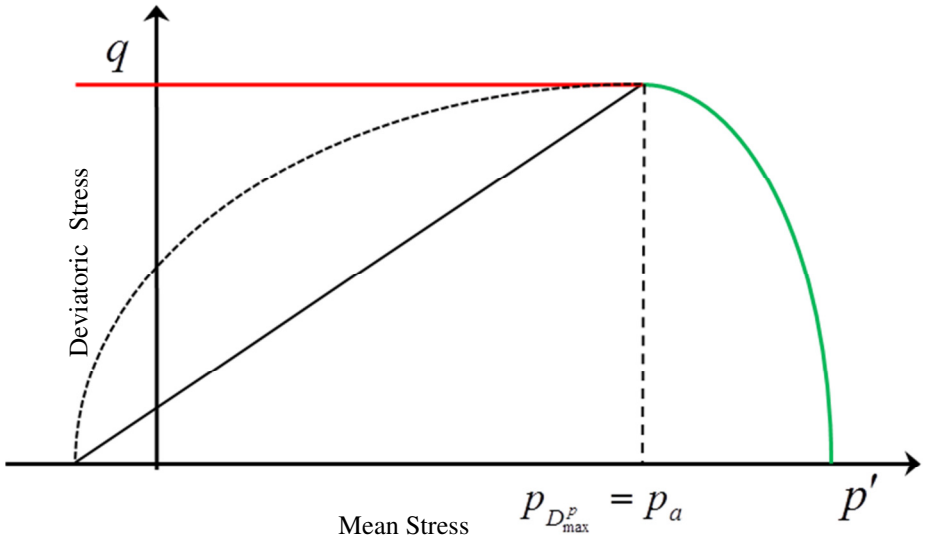

Figure 4-11 Zero dilation condition

At such situation, according to Eq. 4-78, the maximum dilation rate becomes zero which represents zero dilatancy state. A flat plastic potential function is generated then which characterizes the constant volume condition (Figure 4-11).

Jefferies and Been (2006) compiled a large number of triaxial test data on various sands available in the literature. In this study a total of 203 tests results are considered as the required information are available.

Figure 4-12 shows a comparison between measured and predicted dilatancy rate using Eq. 4-79. Equation 4-79 is an extension of Eq. 4-77 derived earlier for triaxial compression where $\theta_L = 30$. Note that, the value of D^p obtained from Eq. 4-79 is positive. However, in order to be consistent with Jefferies and Been (2006), where the dilation rate at the peak has been reported as minimum value, D^p has been shown with a negative sign in Figure 4-13. The identical solid line is drawn to compare measured and predicted dilatancy rates. As shown, Eq. 4-79 predicts the dilation rate reasonably well considering the fact that there is a wide variation in these tests such as specimen preparation, loading, saturation and others.

$$D^p = -\frac{d\varepsilon_v^p}{d\varepsilon_q^p} = \frac{3D_B^p}{3+D_B^p} \qquad \textbf{4-79}$$

Bolton (1986) also proposed a relationship between the angles of internal friction at peak stress (ϕ'_{max}) and at critical stress (ϕ'_{cr}), and dilatancy index (I_R) as:

$$\phi'_{\max} = \phi'_{cr} + 3I_R \qquad \textbf{4-80}$$

Figure 4-13 shows the comparison between the measured values (Jefferies & Been, 2006) and predictions using Eq. 4-80. A total of 165 triaxial test results are plotted in this figure. A reasonably good comparison was also found for angle of internal friction.

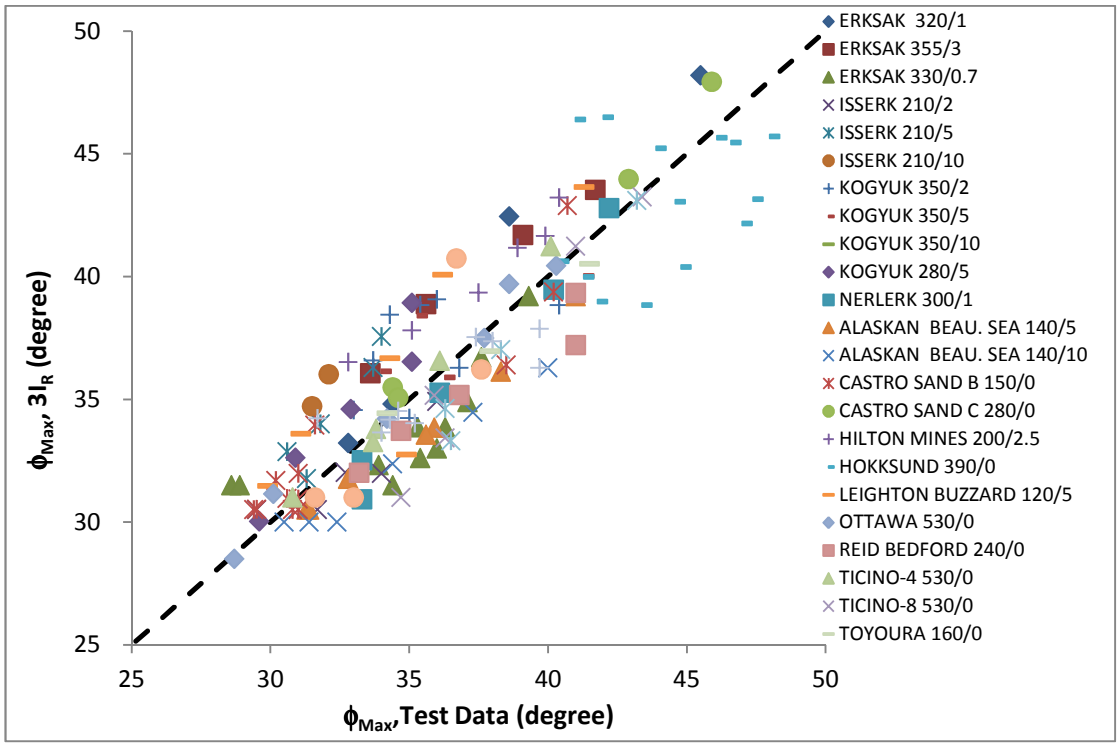

Figure 4-12 Dilatancy rate at peak stress

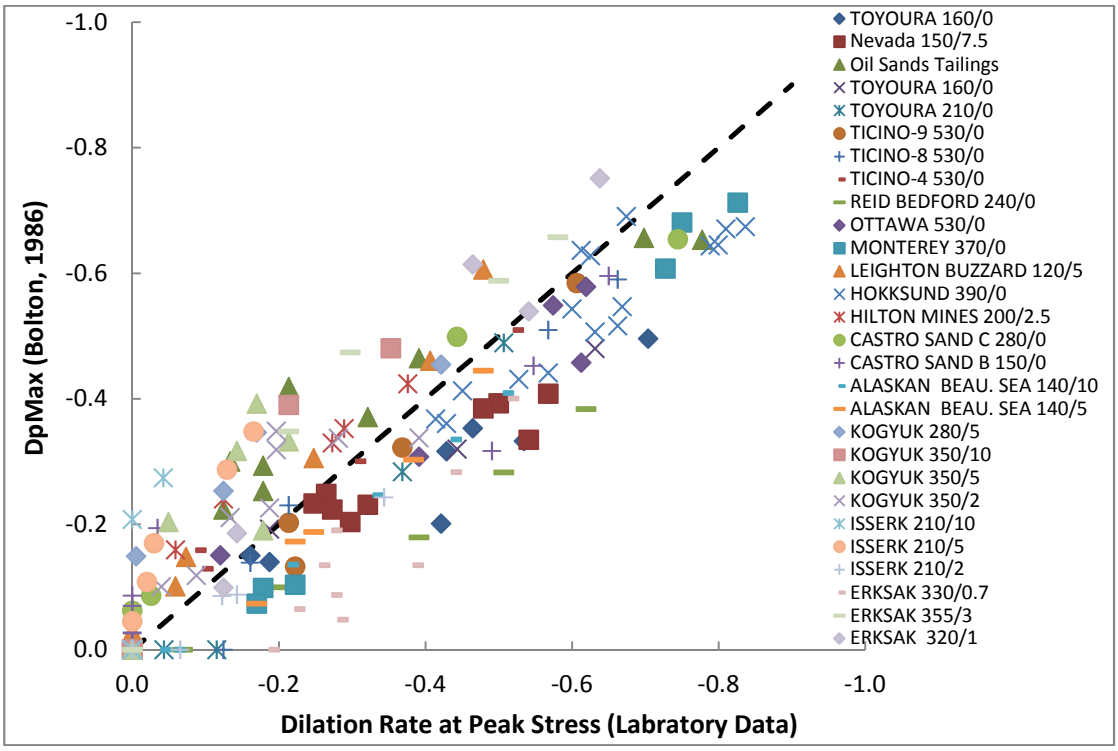

Figure 4-13 Predicted ϕ'_{max} using Bolton's dilatancy index against measured test data

4.4. Validation of the Modified Drucker-Prager Cap Model

The proposed model is used to simulate some triaxial test results of sand samples under different loading and initial conditions (Jefferies & Been, 2006). A total of 10 input parameters are required for this model, which are the module of elasticity E, Poisson's ratio ν, cohesion intercept d, the slope of the failure line θ_{cr}, evolution parameter p_a, minimum void ratio e_{min}, maximum void ratio e_{max}, void ratio e, hardening modulus H and eccentricity parameter R. The parameters used in these analyses are listed inTable 4-1. The value of θ_{cr} is obtained from the plot of respective test data in p' - q space. Since the analysis has been performed only for sand, d = 0 is used. The elastic modulus E,

hardening modulus H and cap eccentricity R have been estimated based on density and confining stress of the specimen. The value of Poisson's ratio $\nu = 0.2$ is adopted.

Figure 4-14 to Figure 4-17 show the simulation of dense Erksak sand and in Figure 4-18 to Figure 4-23 the response of loose Erksak sand is predicted using the constitutive model. Figure 4-24 and Figure 4-25 show the simulation results of triaxial test of dense Ticinio sand. As shown, the proposed model reasonably predicts the test results. In Table 4-1 the input parameters of these analyses are summarizes.

Table 4-1 Model input parameters

	Erksak 330/7 (Figure 4-14 & Figure 4-15)	Erksak 330/7 (Figure 4-16& Figure 4-17)	Erksak 330/7 (Figure 4-18& Figure 4-19)	Erksak 330/7 (Figure 4-20& Figure 4-21)	Erksak 330/7 (Figure 4-22& Figure 4-23)	Ticinio 530/0 (Figure 4-24& Figure 4-25)
E (kPa)	2.07×10^5	2.0×10^5	1.07×10^5	5.75×10^4	5.75×10^4	8.0×10^5
ν	0.2	0.2	0.2	0.2	0.2	0.33
θ_{cr} (deg)	52	53	49	49	50	54
e_{max}	0.747	0.747	0.747	0.747	0.747	0.89
e_{min}	0.521	0.521	0.521	0.521	0.521	0.6
e	0.59	0.667	.775	0.82	0.776	0.66
H	300	200	55	75	75	150
R	2.5	2.5	1.2	1.2	1.2	3
p_0 (kPa)	130	60	1000	200	200	100

The value of p_a is derived according to p_0, R and θ

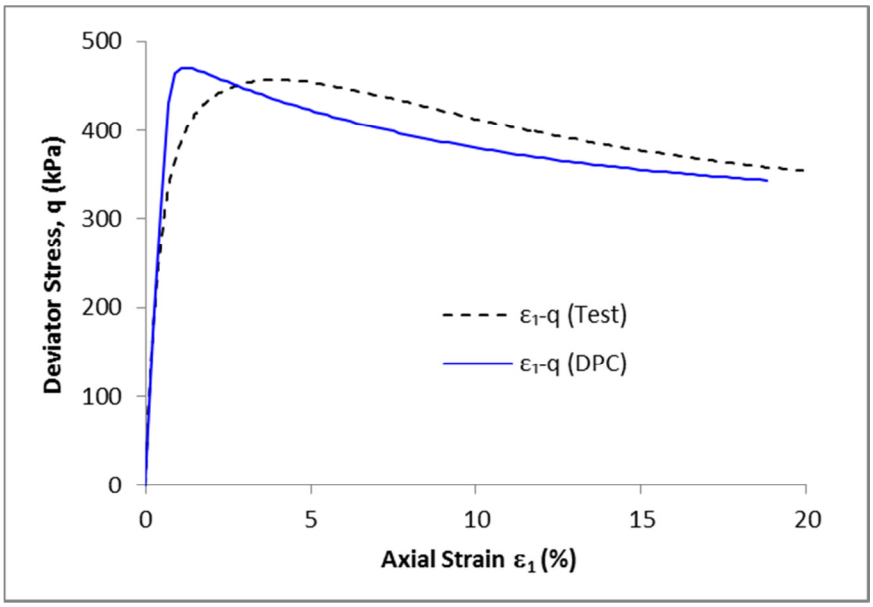

Figure 4-14 Drained dense sand sample, deviatoric stress – axial strain (Erksak 330/7)

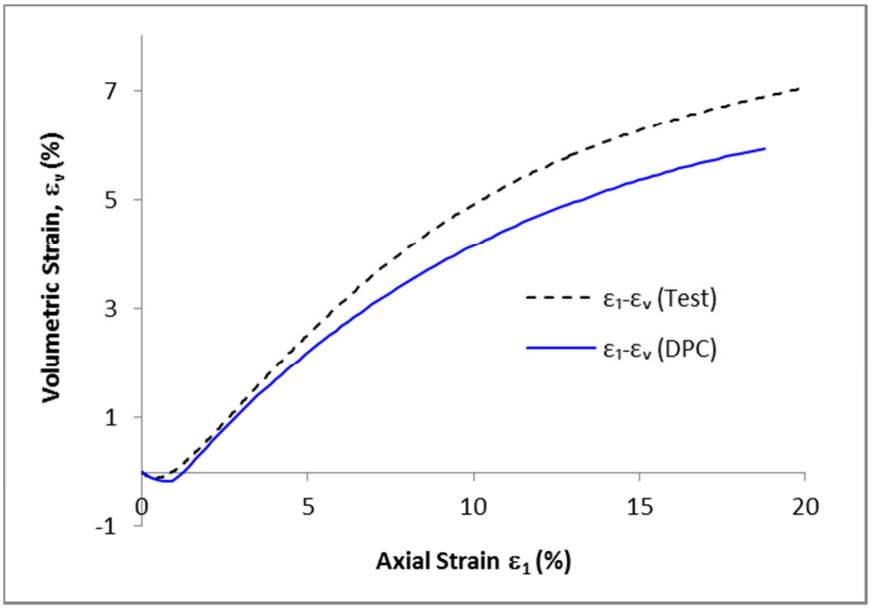

Figure 4-15 Drained dense sand sample, volumetric strain – axial strain (Erksak 330/7)

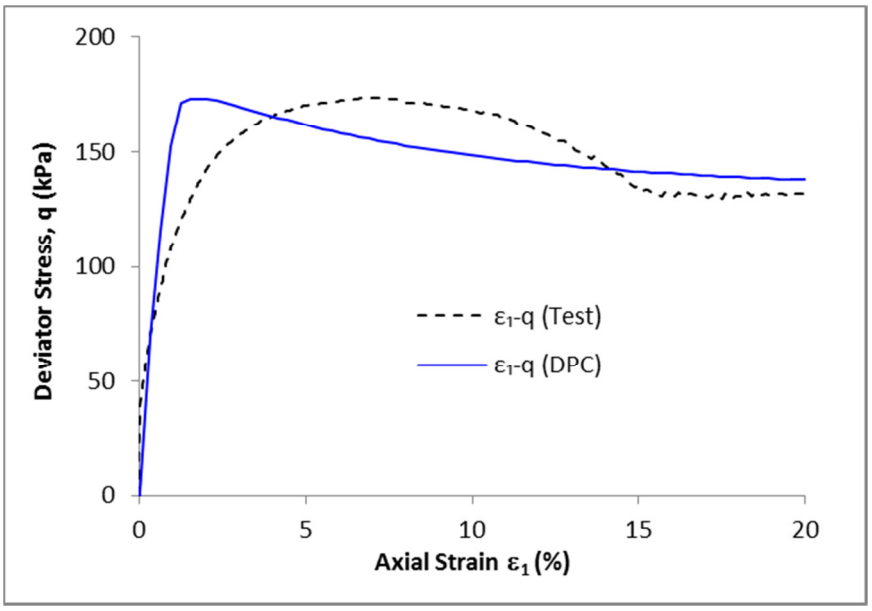

Figure 4-16 Drained dense sand sample, deviatoric stress – axial strain (Erksak 330/7)

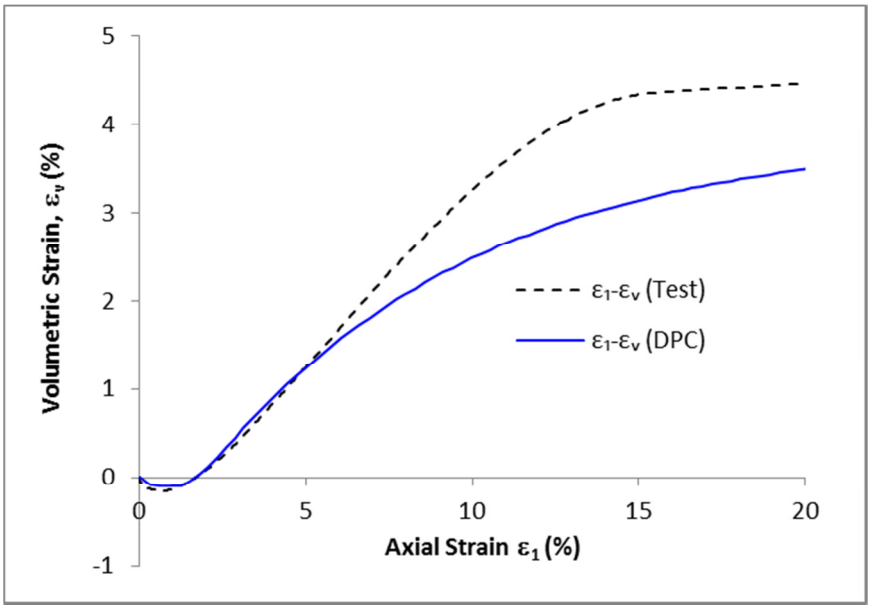

Figure 4-17 Drained dense sand sample, volumetric strain – axial strain (Erksak 330/7)

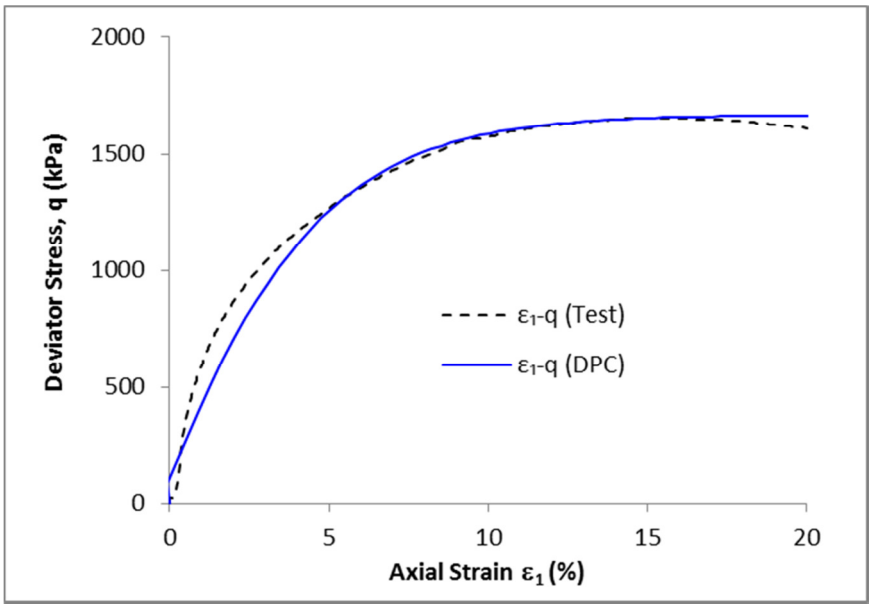

Figure 4-18 Drained loose sand sample, deviatoric stress – axial strain (Erksak 330/7)

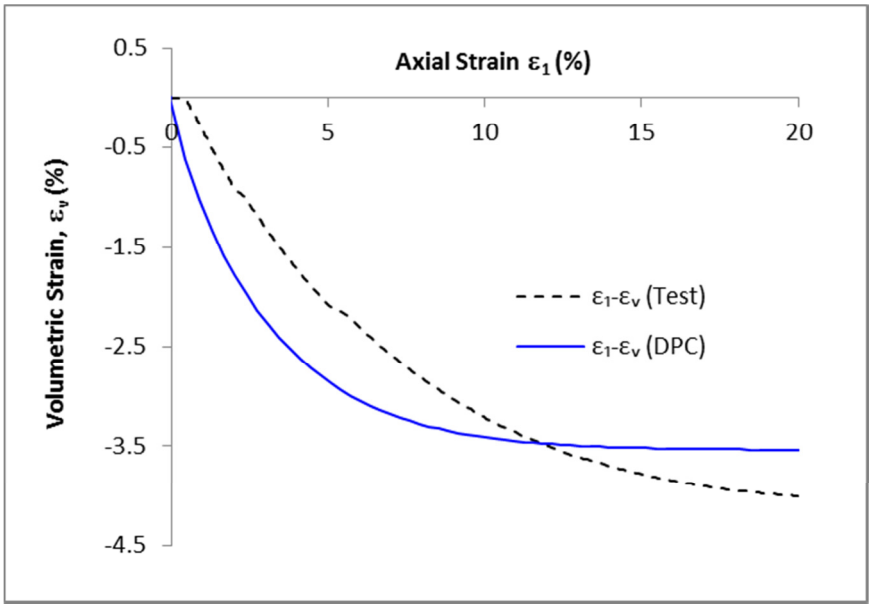

Figure 4-19 Drained loose sand sample, volumetric strain – axial strain (Erksak 330/7)

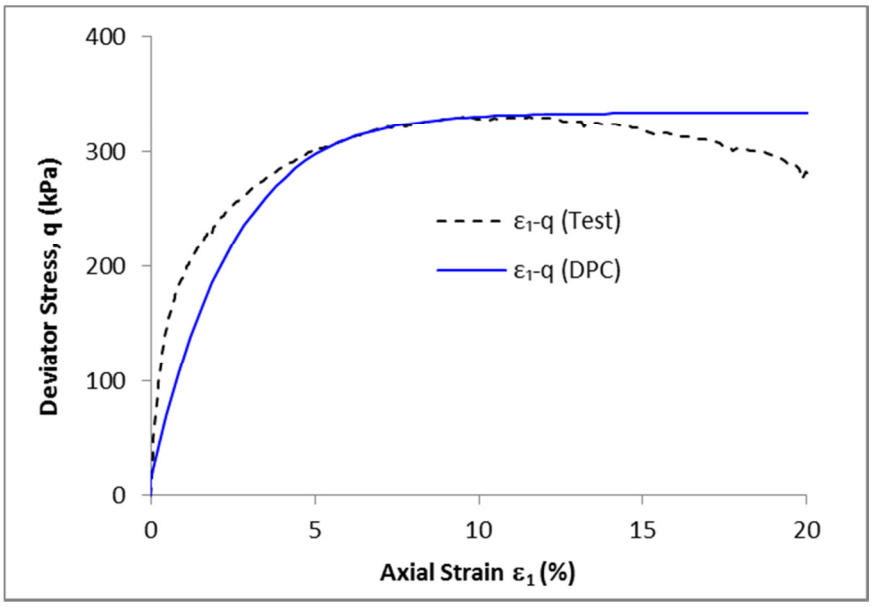

Figure 4-20 Drained loose sand sample, deviatoric stress – axial strain (Erksak 330/7)

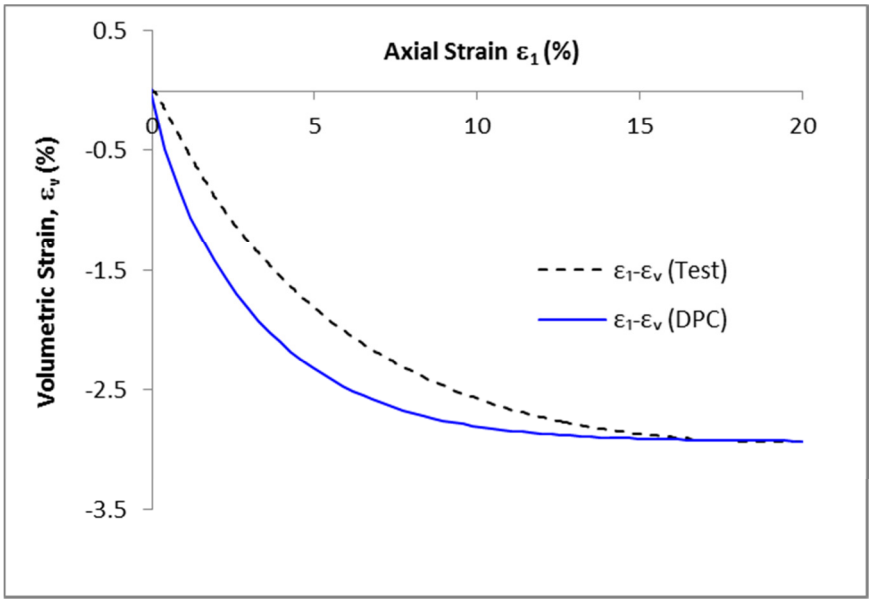

Figure 4-21 Drained loose sand sample, volumetric strain – axial strain (Erksak 330/7)

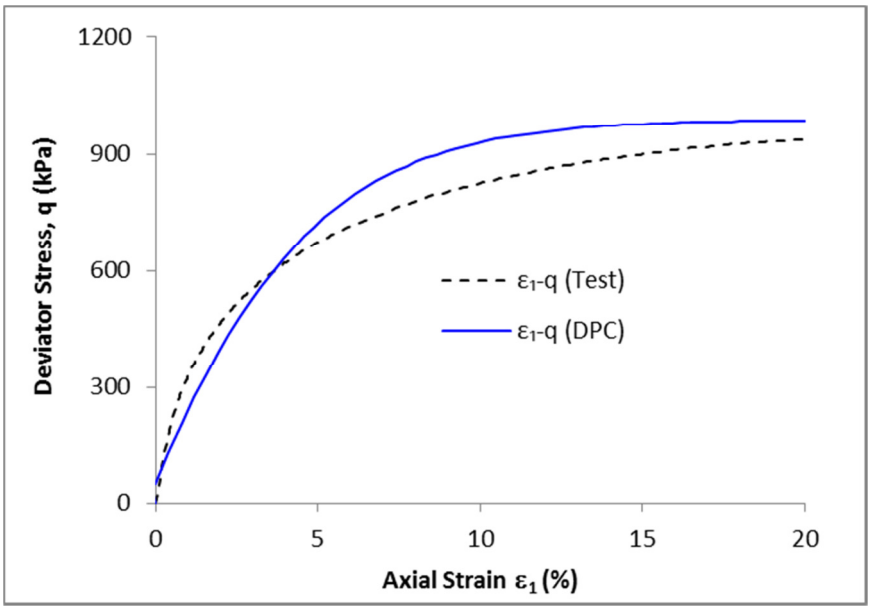

Figure 4-22 Drained loose sand sample, deviatoric stress – axial strain (Erksak 330/7)

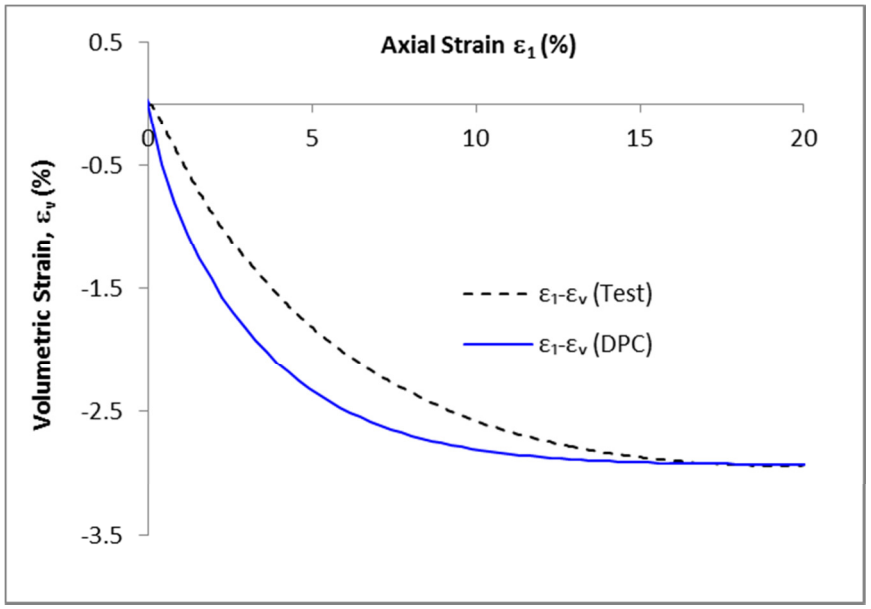

Figure 4-23 Drained loose sand sample, volumetric strain – axial strain (Erksak 330/7)

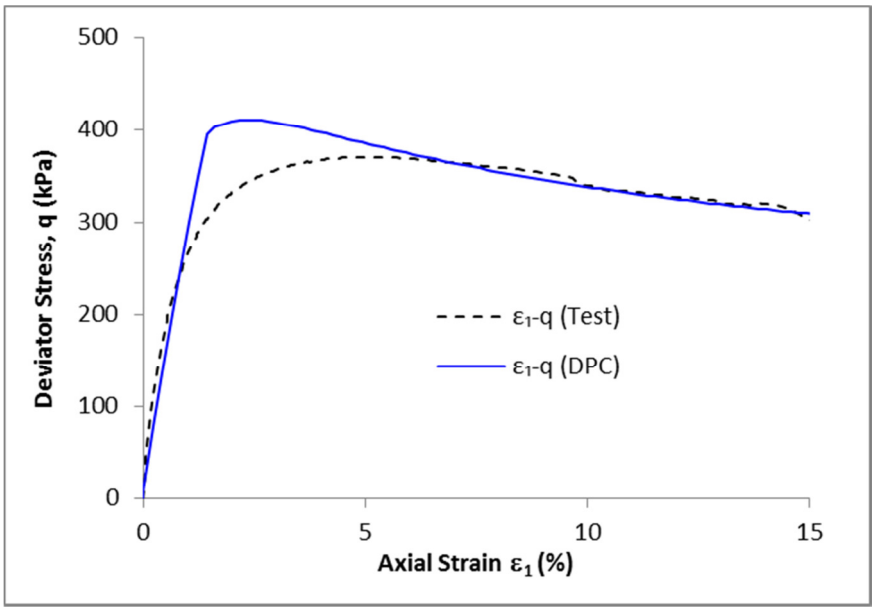

Figure 4-24 Drained dense sand sample, deviatoric stress – axial strain (Ticinio 530/0)

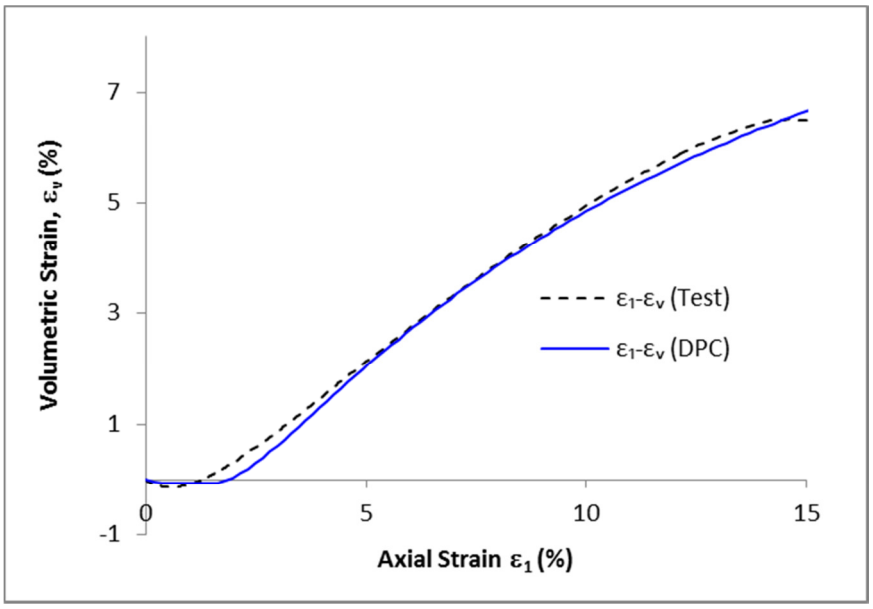

Figure 4-25 Drained dense sand sample, volumetric strain – axial strain (Ticinio 530/0)

The built-in Drucker-Prager model in ABAQUS is in fact just a particular parameter set of the developed model in this study. To validate the implemented Drucker-Prager Cap model in three-dimensional condition, it was compared with a built-in Drucker Prager model to simulate an ice gouging event. The parameters for the VUMAT model are chosen to exactly represent the built-in model of ABAQUS. In this analysis the attack angle is 30 degrees, the gouging depth is 1 meter and the keel width is 10 meters. The internal friction angle, θ, in Drucker Prager model is 50 degrees and the elastic modulus is 30 MPa. Figure 4-26 compares the horizontal and vertical keel reactions for the two analyses. This figure shows the reaction forces are quite compatible for the two models.

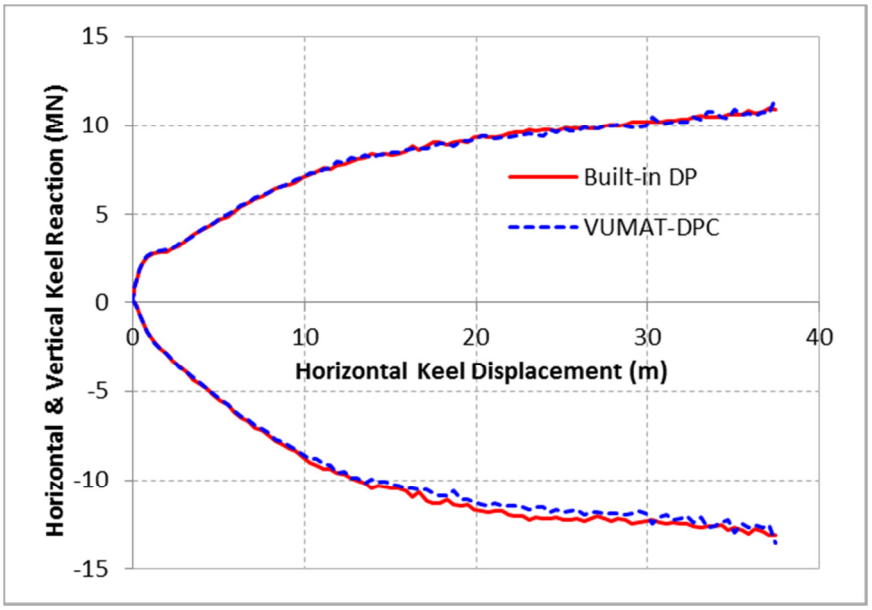

Figure 4-26 Keel reaction forces using VUMAT and built-in Drucker-Prager model

Figure 4-27 compares the sub-gouge deformation of the soil beneath the keel at the end of analyses. This figure also shows that the VUMAT model can very well duplicate the results of the built-in Drucker-Prager model. Based on these two figures it could be

concluded that the implemented VUMAT model may be used in three-dimensional ice gouging problems.

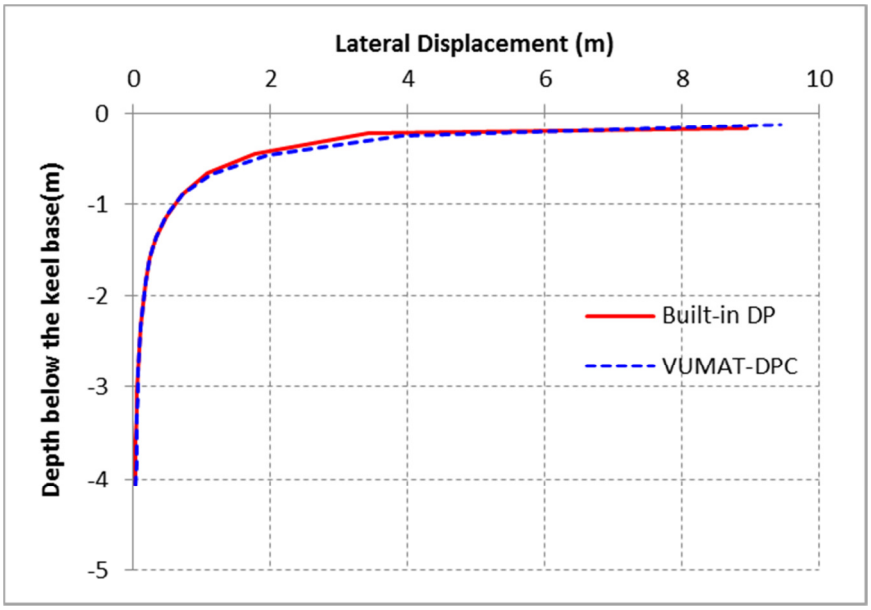

Figure 4-27 Subgouge deformation under the keel using VUMAT and built-in Drucker-Prager model

4.5. Parametric Study of the Developed Drucker-Prager Cap Model

In this section the model sensitivity to the variation of input parameters is investigated. The parameters used in baseline analysis are shown in Table 4-2. The parametric study is performed for four critical parameters (E, θ, D_r and H) which have significant influence on model performance. The parametric study has been carried out by varying one parameter at a time while keeping all other parameters at the same value as that of the baseline analysis (Table 4-2). Figure 4-28 to Figure 4-31 show the predicted results for various conditions. One line in these figures show the baseline analysis while the other two lines show the effects of corresponding input parameters.

Table 4-2 Model parameters for sensitivity analysis

E	v	d	θ_{cr}	D_R	H	R	e_0

$2.07x10^5$kPa	0.2	0	52°	60%	150	2.5	0.58

From ε_q vs. ε_v plots it is realized that the predicted dilatancy rate (i.e. slope of the curve) using the proposed model is almost zero at high strain level (e.g. $\varepsilon_q^p > 40\%$). This feature is important in large deformation problems such as ice gouging where shear strains could be even more than 100%.

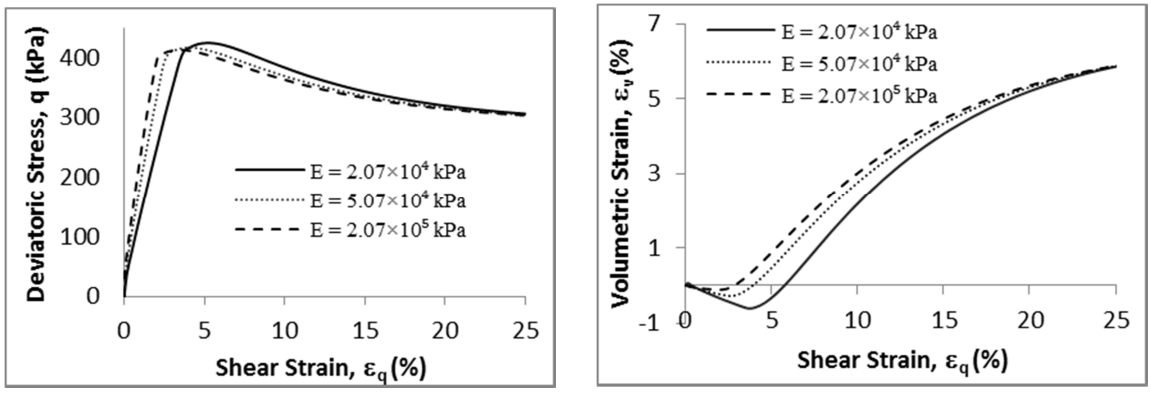

Figure 4-28 Schematic view of the model response with variation of Elastic Modulus

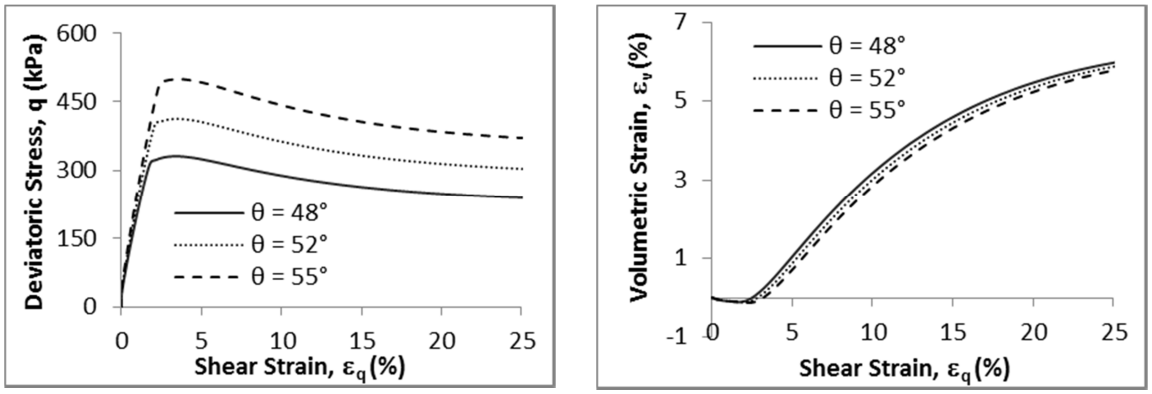

Figure 4-29 Schematic view of the model response with variation of angle of internal friction in *p'-q* space

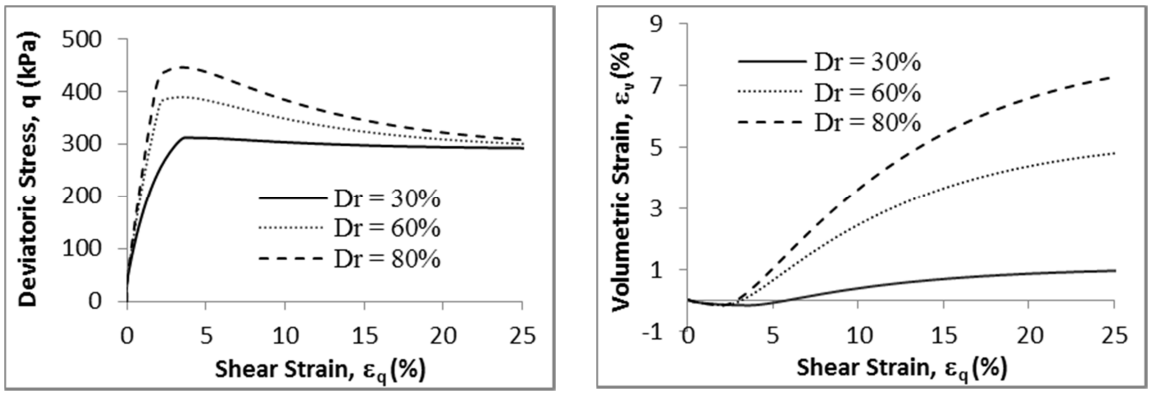

Figure 4-30 Schematic view of the model response with variation of relative density

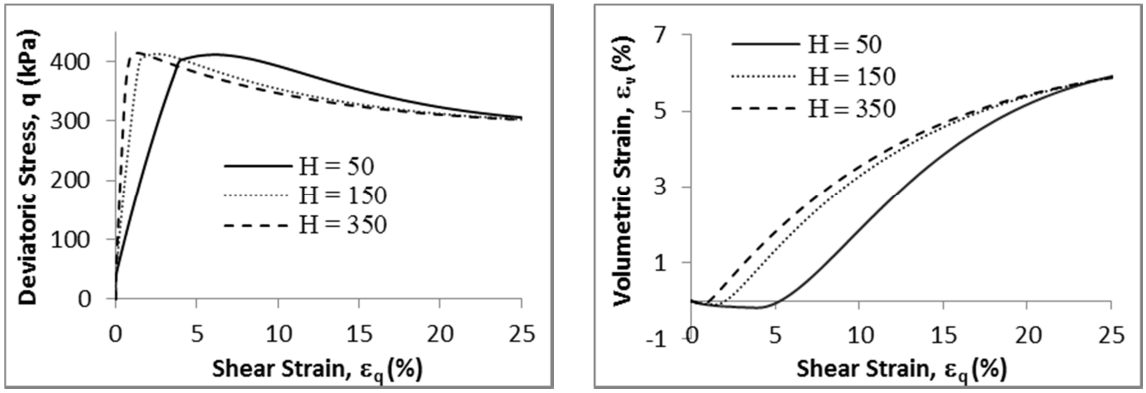

Figure 4-31 Schematic view of the model response with variation of hardening modulus

4.6. Validation of developed models through Single Element Analysis

In this section the performance and accuracy of the developed VUMAT model is validated by comparing the results of triaxial finite element models with the results of the triaxial single element analyses. The single element analyses consider only one material point and integrate the developed stresses and strains along a specific stress path. Due to the simplicity of this approach and the fact that only one material point is evaluated during the analyses, it is possible to directly employ the formulation of the constitutive material model. Theoretically, the results from single element analysis and finite element analysis of a triaxial test should exactly match each other. This provides a good basis to evaluate the implementation of the constitutive model as an initial step.

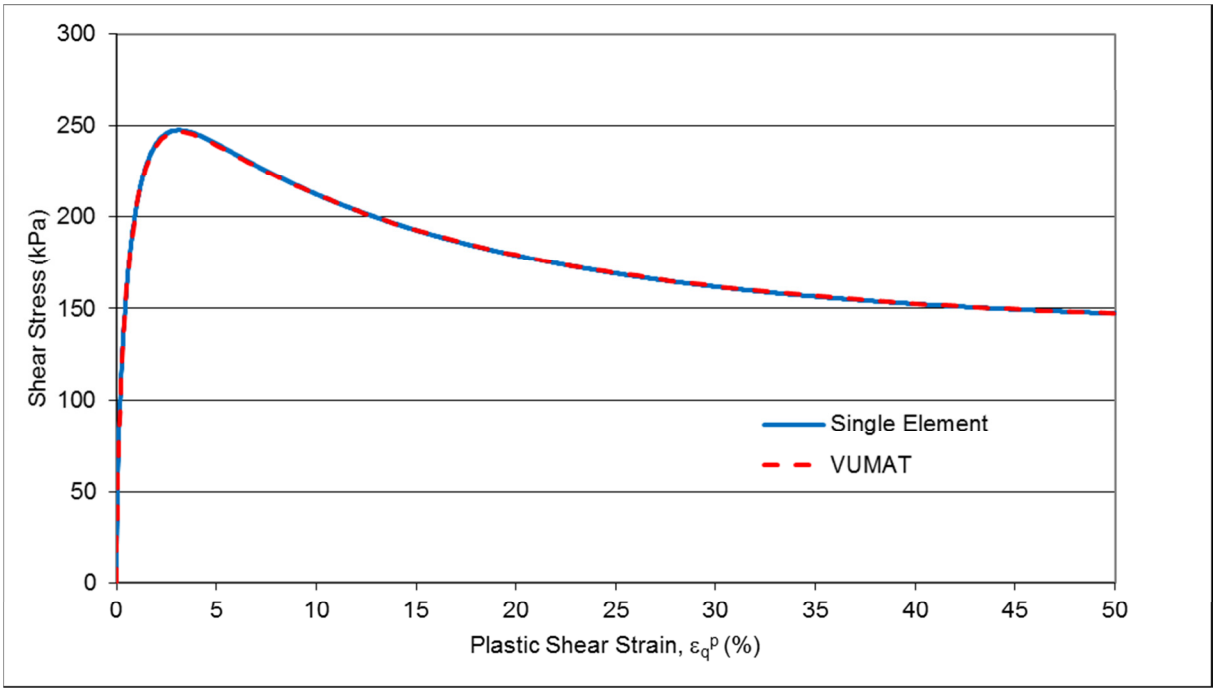

Figure 4-32 Shear stress- axial strain, single element validation of NorSand for dense sands

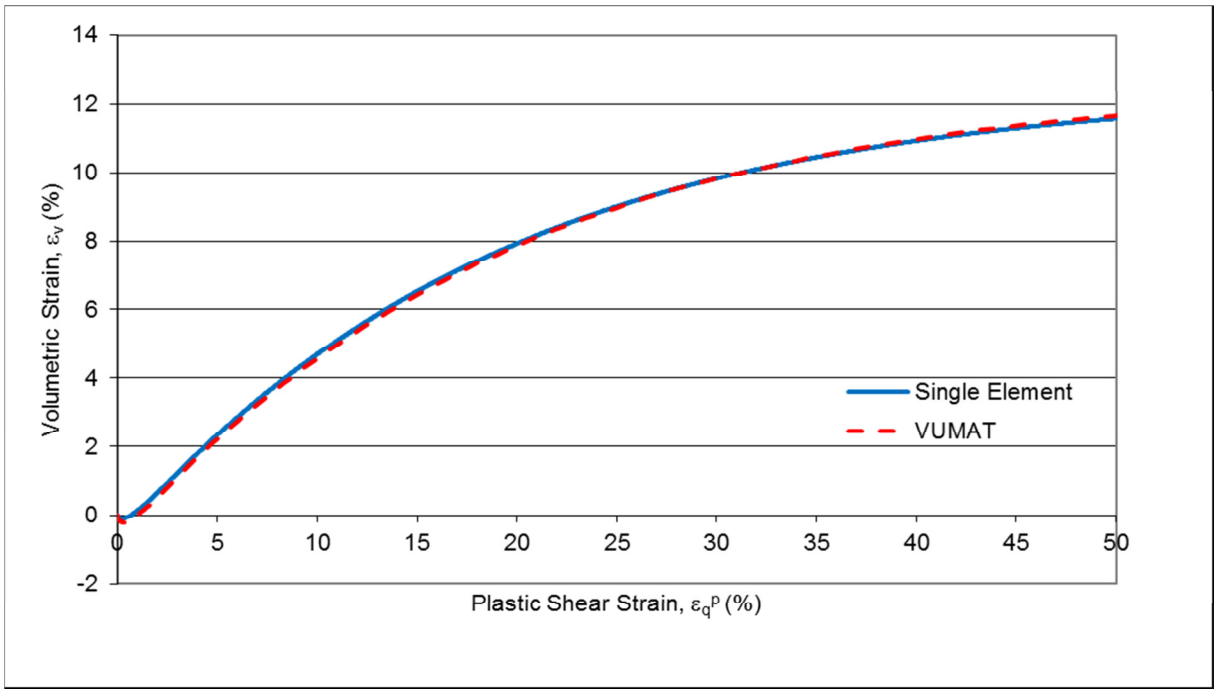

Figure 4-33 Volumetric strain- axial strain, single element validation of NorSand for dense sands

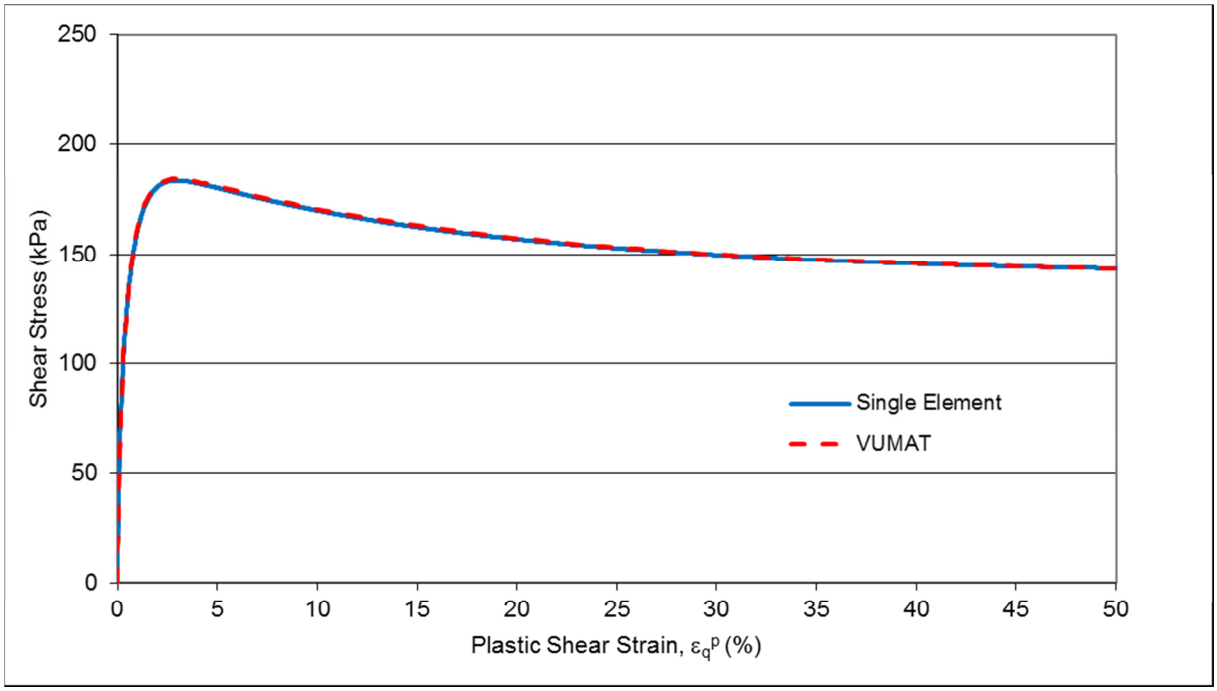

Figure 4-34 Shear stress- axial strain, single element validation of NorSand for dense sands

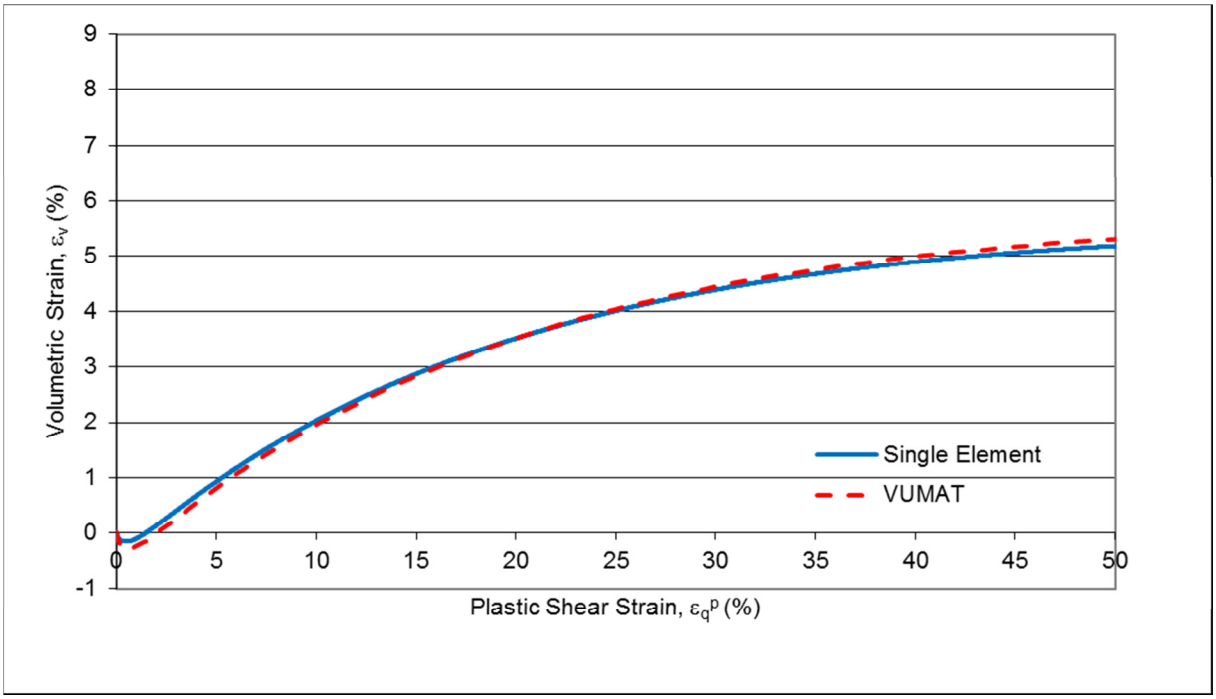

Figure 4-35 Volumetric strain- axial strain, single element validation of NorSand for dense sands

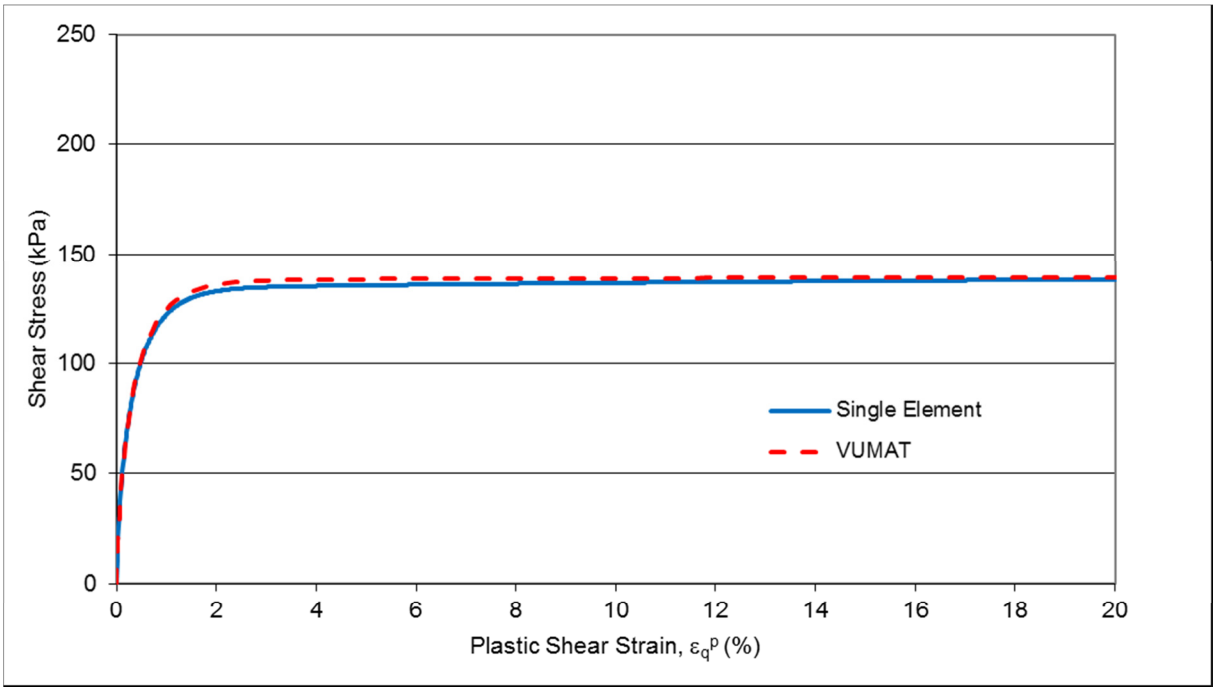

Figure 4-36 Shear stress- axial strain, single element validation of NorSand for loose sands

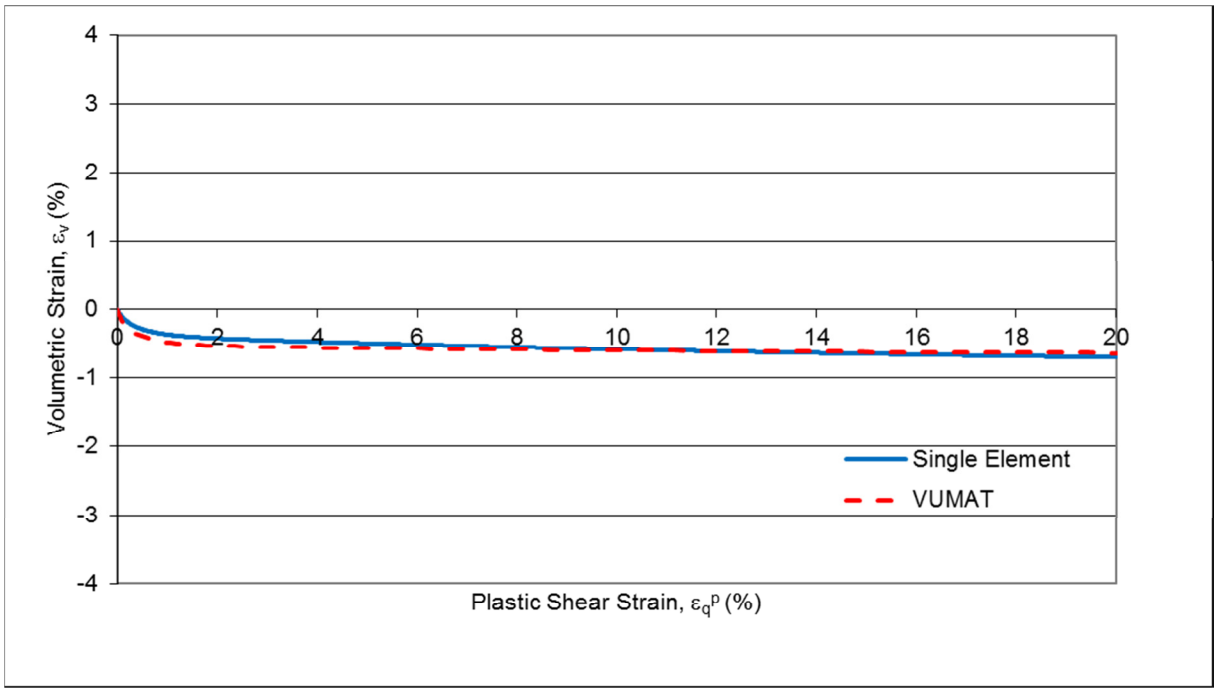

Figure 4-37 Volumetric strain- axial strain, single element validation of NorSand for loose sands

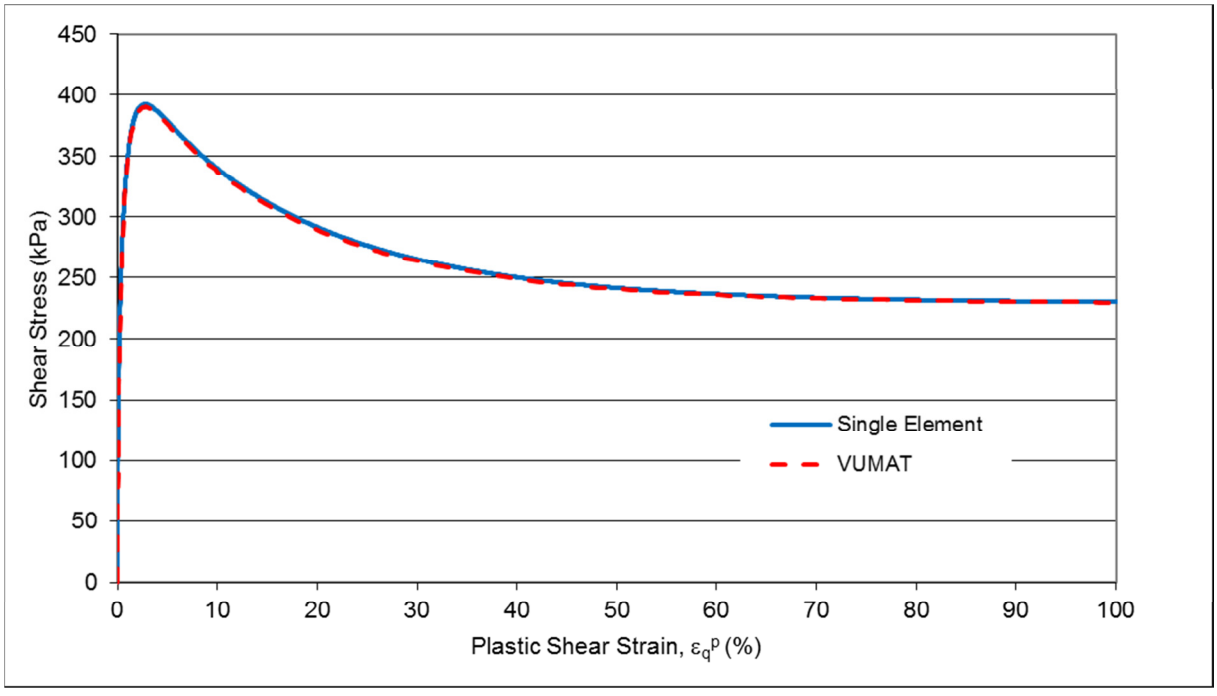

Figure 4-38 Shear stress- axial strain, single element validation of DPC for dense sands

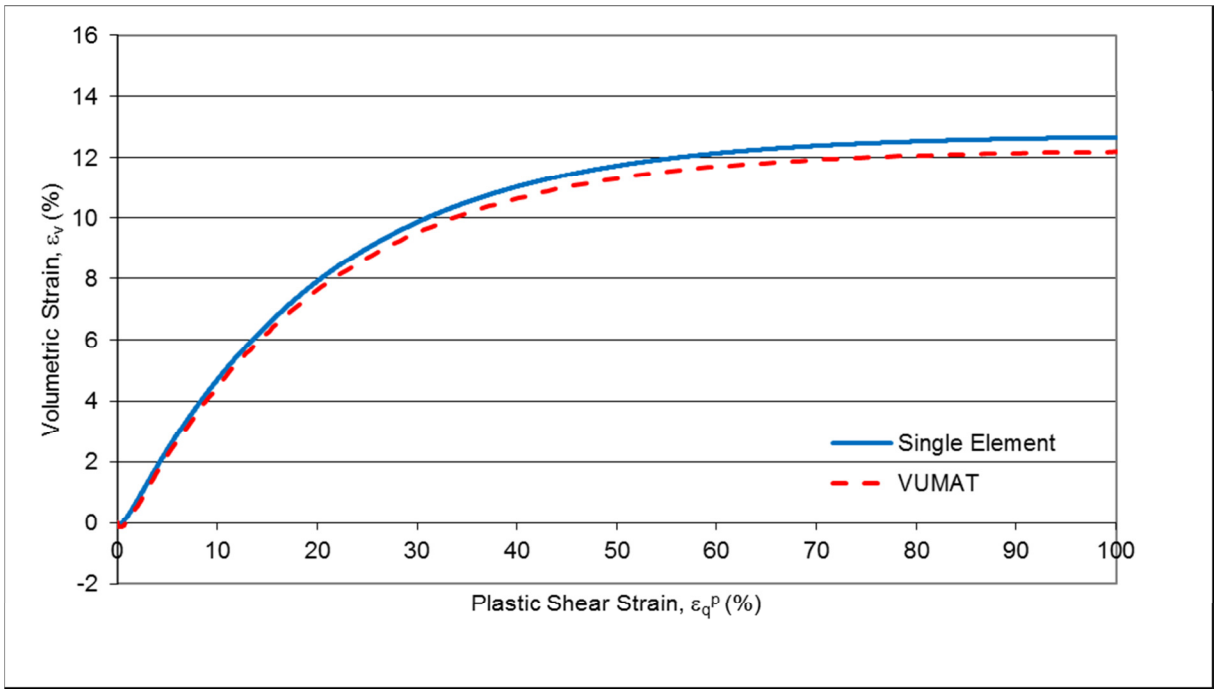

Figure 4-39 Volumetric strain- axial strain, single element validation of DPC for dense sands

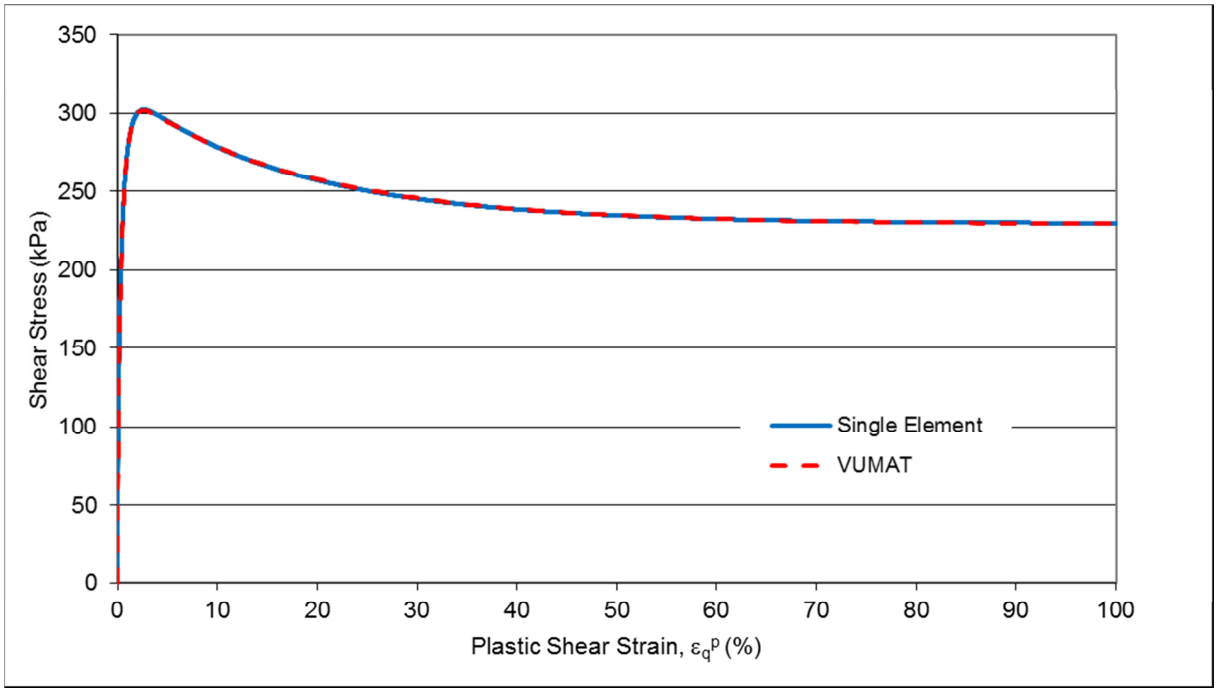

Figure 4-40 Shear stress- axial strain, single element validation of DPC for dense sands

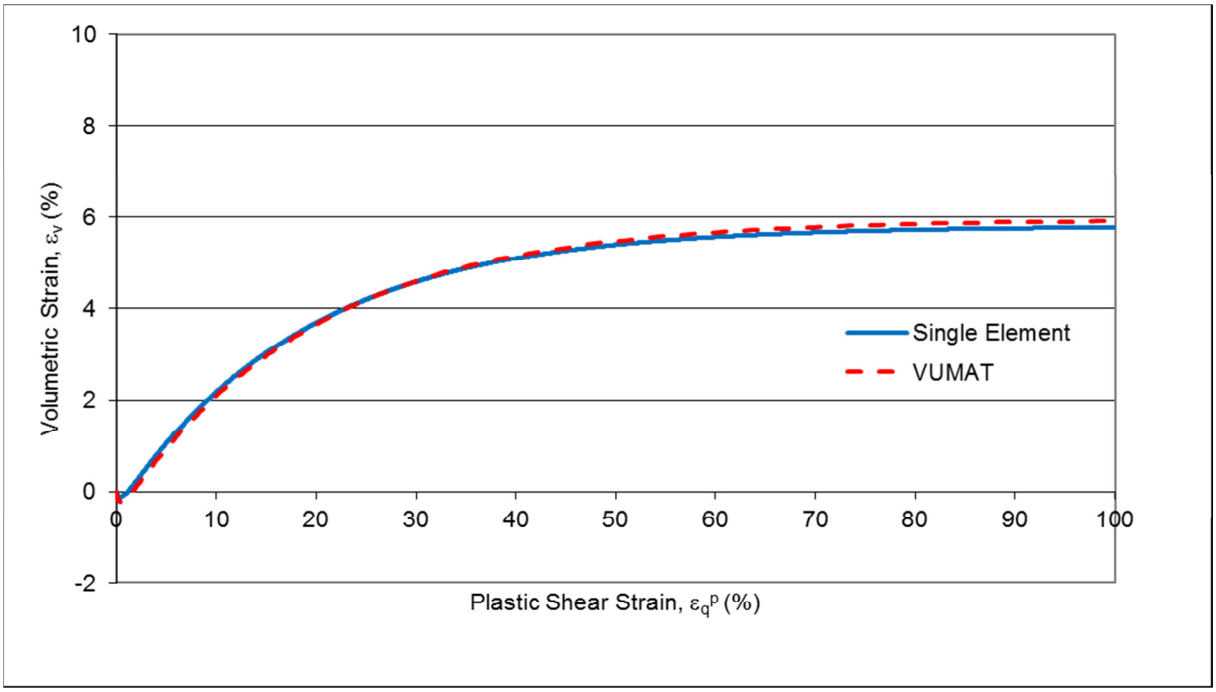

Figure 4-41 Volumetric- axial strain, single element validation of DPC for dense sands

4.7. Validation of 3D Implementation of NorSand Model

In this section the VUMAT implemention of the NorSand model in general three-dimensional space is validated. This is achieved by comparing the stress state of an integration point at the end of a strain increment with the results that are directly obtained by application of the constitutive formulas of the NorSand model under the same increment.

Initially an arbitrary stress condition as shown in Table 4-3 is assigned to the integration point.

Table 4-3 Initial stress state

σ_1	σ_2	σ_3
-40000	-25000	-35000

Random model properties are also chosen for this analysis as shown in Table 4-4.

Table 4-4 NorSand Model Properties

I_R	ν	Γ	λ	M_{tc}	H	χ	ψ	M_{te}	pi
150	0.25	0.6	0.016	1.4	200	3.5	-0.1	0.95	19126

The material in the current stress and state condition then undergoes a general total strain increment. The components of strain increment are shown in Table 4-5.

Table 4-5 Total strain increment

$\Delta\varepsilon_1$	$\Delta\varepsilon_2$	$\Delta\varepsilon_3$	$\Delta\varepsilon_4$	$\Delta\varepsilon_5$	$\Delta\varepsilon_6$
0.0004	-0.0005	-0.0016	0.0025	0.0013	0.0017

The initial stress and state condition and material properties are fed into the VUMAT subroutine which is a Fortran code. The script calculates the updated stress state as the output. The new values of stress components are presented in Table 4-6.

Table 4-6 Updated stress state at the end of the strain increment

σ_1	σ_2	σ_3	σ_4	σ_5	σ_6
-52895.1	-50430.4	-59056.7	10269.4	5340.1	6983.2

In order to validate the accuracy of the VUMAT the constitutive formulas of the NorSand model were applied to manually calculate the updated stress state of the material point shown in Table 4-3 under the same strain increment as stated in Table 4-5.

The evolution of the yield surface and the stress state of the material point at the beginning and the end of the strain increment are shown in Figure 4-42. This figure is based on the results that are obtained through the direct application of the NorSand formulas.

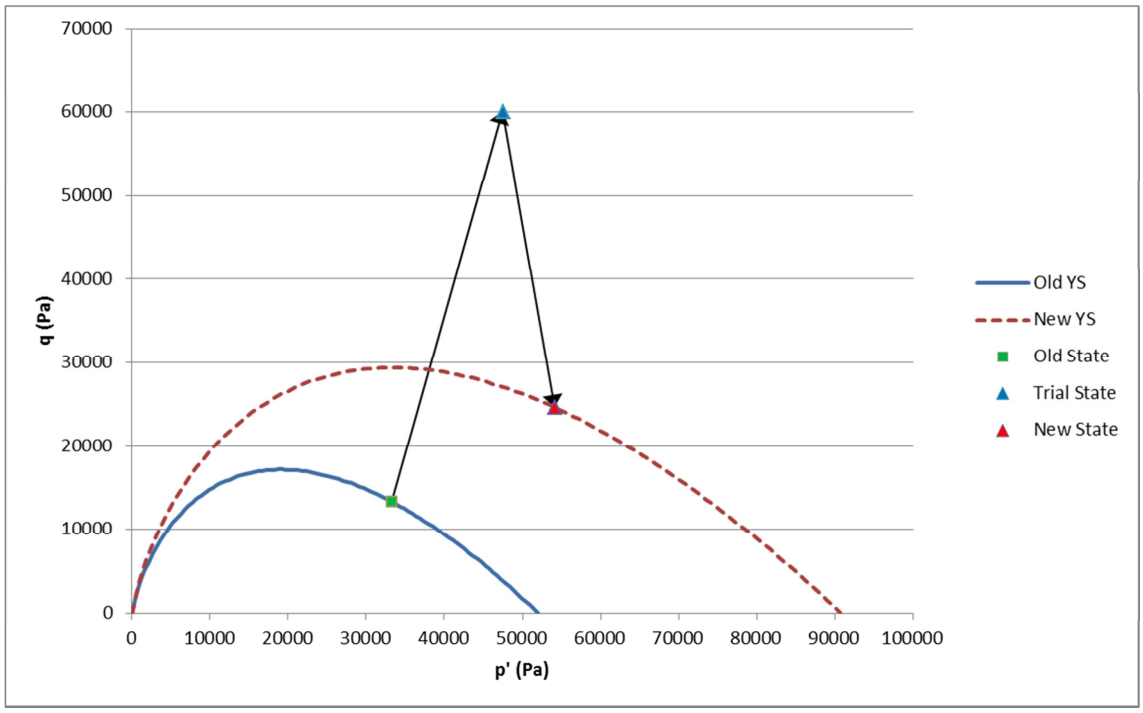

Figure 4-42 The stress and yield surface at the beginning and end of the increment

The updated stress state based on the direct application of the NorSand formulas and the results of the VUMAT subroutine are compared in Table 4-7. As this table shown, the two approaches produce almost identical results with relative difference of less than 0.1%. This is an indication that the NorSand formulas are implemented correctly in the VUMAT subroutine.

Table 4-7 Comparison of the VUMAT results and direct application of NorSand formulas

	σ_1	σ_2	σ_3	σ_4	σ_5	σ_6
NorSand Formulas	-52892.93	-50430.66	-59048.61	10259.45	5334.92	6976.43
VUMAT Subroutine	-52895.08	-50430.43	-59056.70	10269.37	5340.07	6983.17
% difference	0.0041	-0.0005	0.0137	0.0966	0.0966	0.0966

4.8. Validation of NorSand by Laboratory Triaxial Tests

In order to validate the implementation of the critical state model NorSand in ABAQUS Explicit user subroutine a number of analyses are compared with triaxial laboratory tests as published by Jefferies and Been (2006). These analyses include three dense samples (D-1, D-2 and D-3) and three loose samples (L-1, L-2 and L-3) under drained condition. For the model parameters the same values that are suggested by Jefferies and Been (2006) are adopted. These parameters are summarized in Table 4-8.

Table 4-8 Input parameters of the sample analyses as suggested by Jefferies and Been (2006)

	D-1	D-2	D-3	L-1	L-2	L-3
I_R	600	400	1000	150	250	400
ν	0.33	0.33	0.33	0.33	0.33	0.33
λ	0.031	0.031	0.031	0.031	0.031	0.031
Γ	0.816	0.816	0.816	0.816	0.816	0.816
M_{tc}	1.26	1.26	1.26	1.18	1.18	1.18
χ_{tc}	3.7	4	4.5	4	3.7	3.7
H	150	160	170	50	45	70
ψ	-0.08	-0.08	-0.08	0.070	0.045	0.040
p_0 (kPa)	140	300	60	1000	50	200

Figure 4-43 to Figure 4-48 show the results of the analyses of dense samples under drained triaxial condition. On the other hand, in Figure 4-49 to Figure 4-54 the responses of loose samples of Erksak sand (Jefferies & Been, 2006) are predicted using NorSand constitutive model.

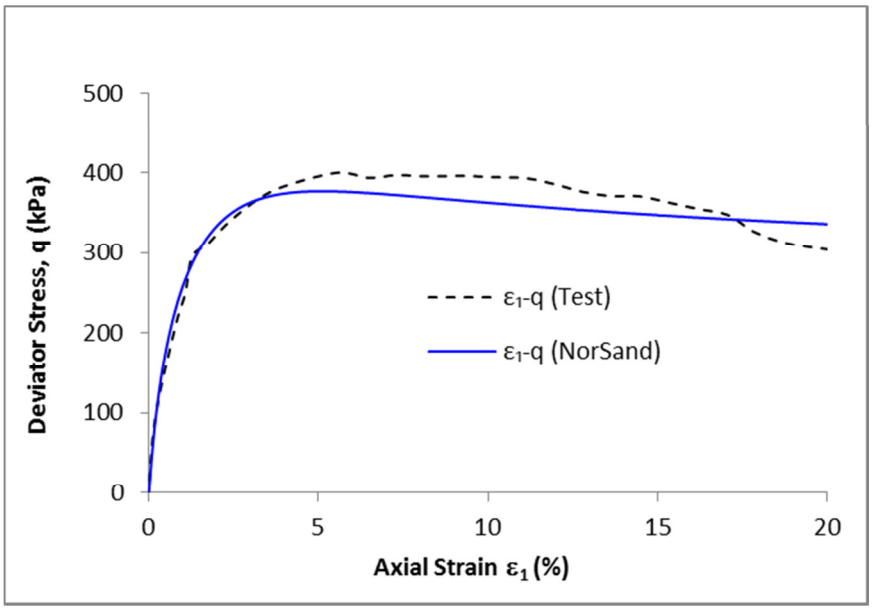

Figure 4-43 Test D-1, drained dense sand sample, deviatoric stress – axial strain

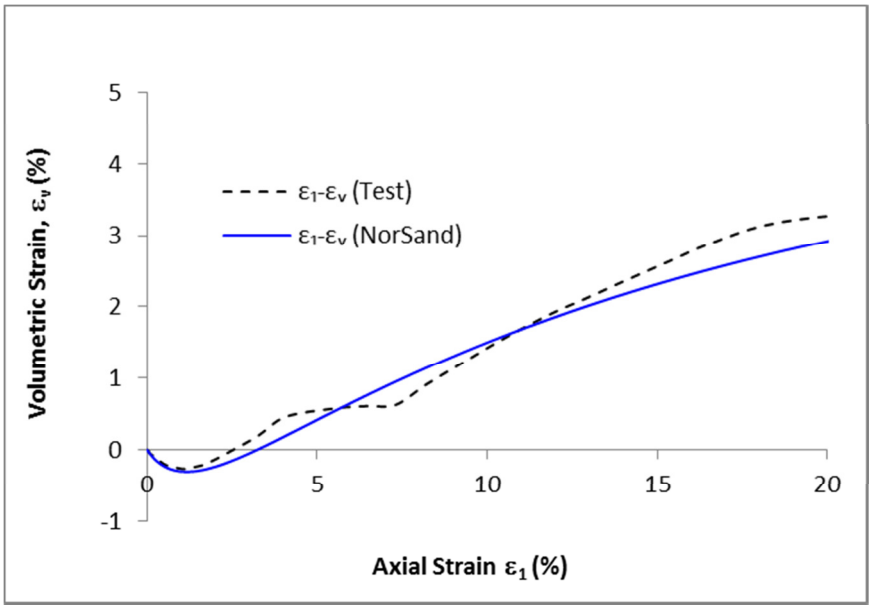

Figure 4-44 Test D-1, drained dense sand sample, volumetric strain – axial strain

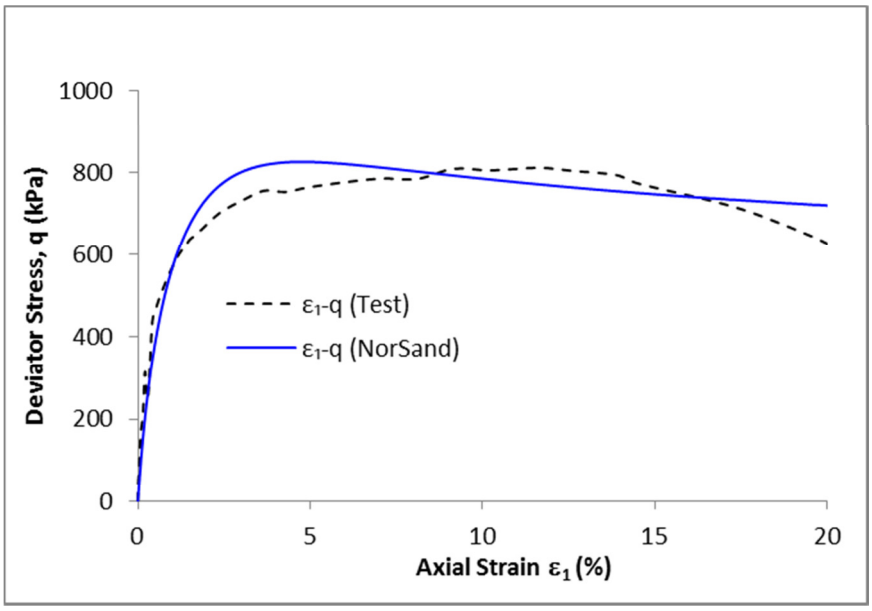

Figure 4-45 Test D-2, drained dense sand sample, deviatoric stress – axial strain

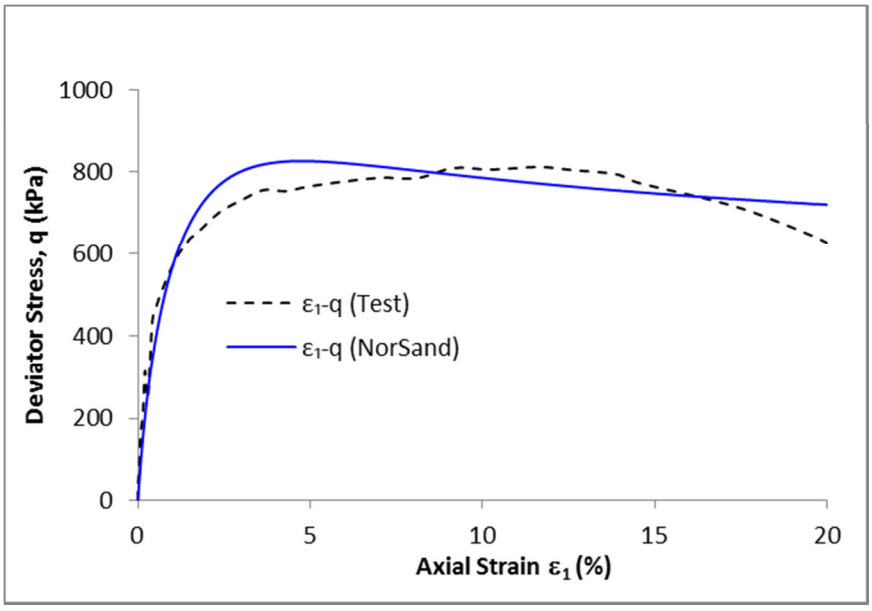

Figure 4-46 Test D-2, drained dense sand sample, volumetric strain – axial strain

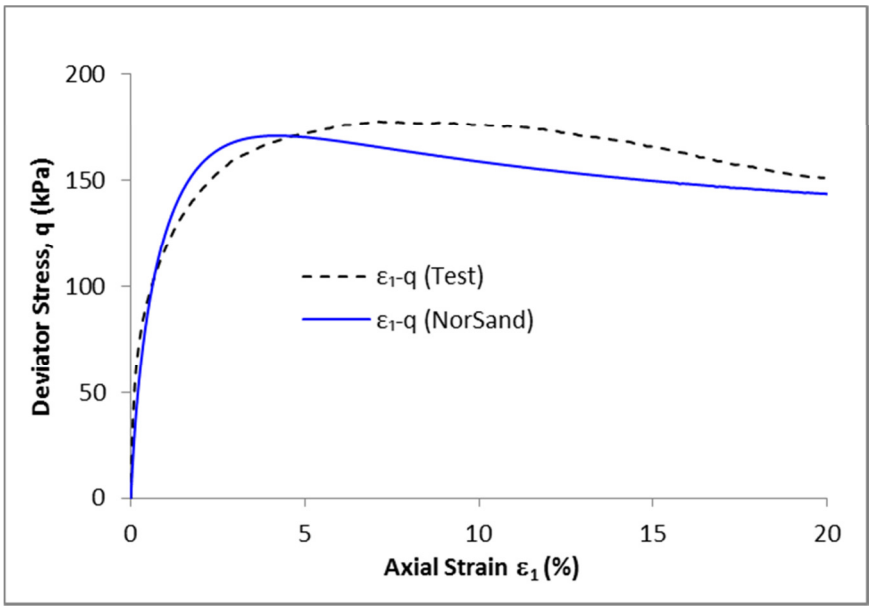

Figure 4-47 Test D-3, drained dense sand sample, deviatoric stress – axial strain

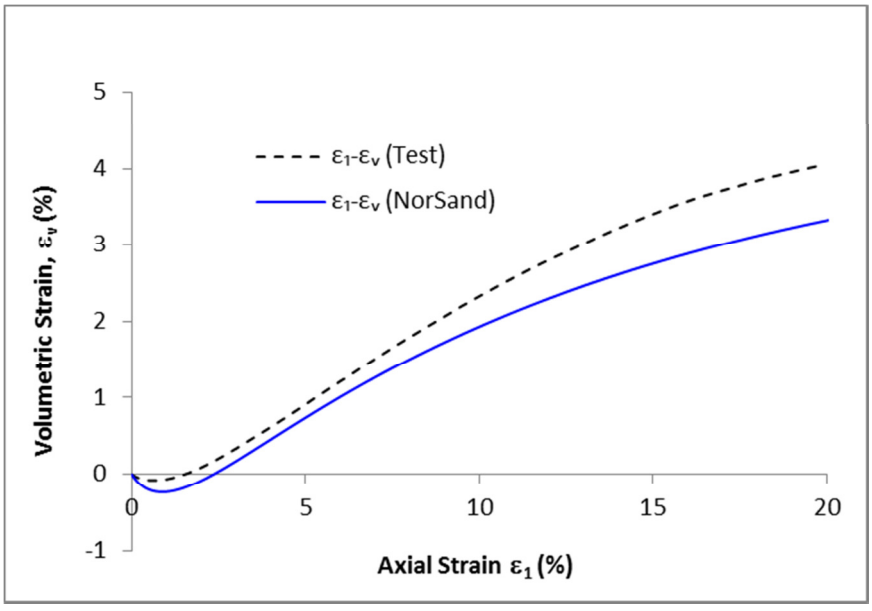

Figure 4-48 Test D-3, drained dense sand sample, volumetric strain – axial strain

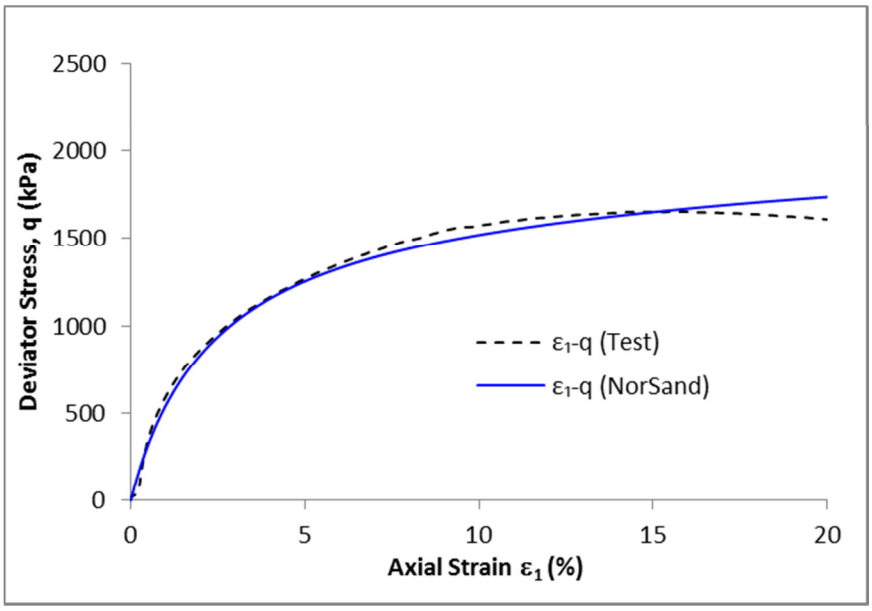

Figure 4-49 Test L-1, drained loose sand sample, deviatoric stress – axial strain

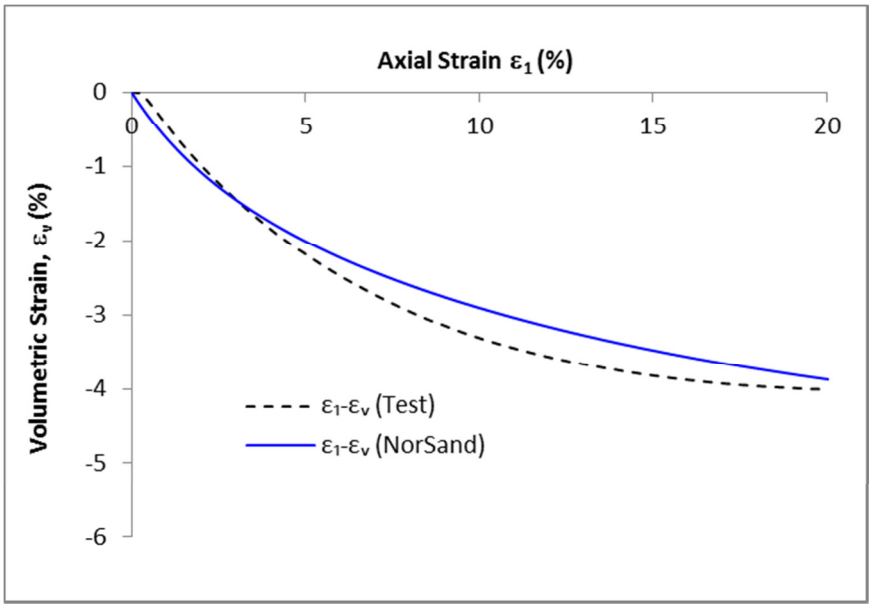

Figure 4-50 Test L-1, drained loose sand sample, volumetric strain – axial strain

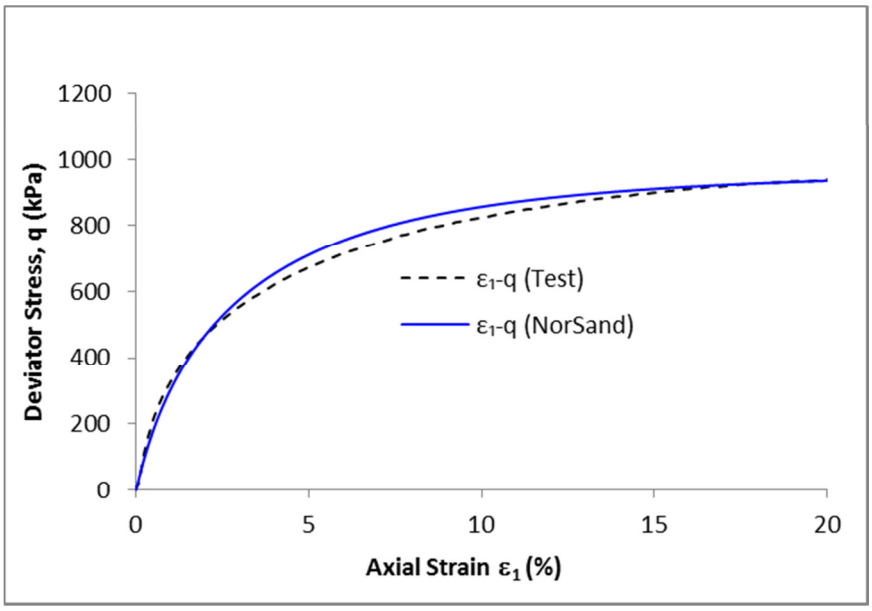

Figure 4-51 Test L-2, drained loose sand sample, deviatoric stress – axial strain

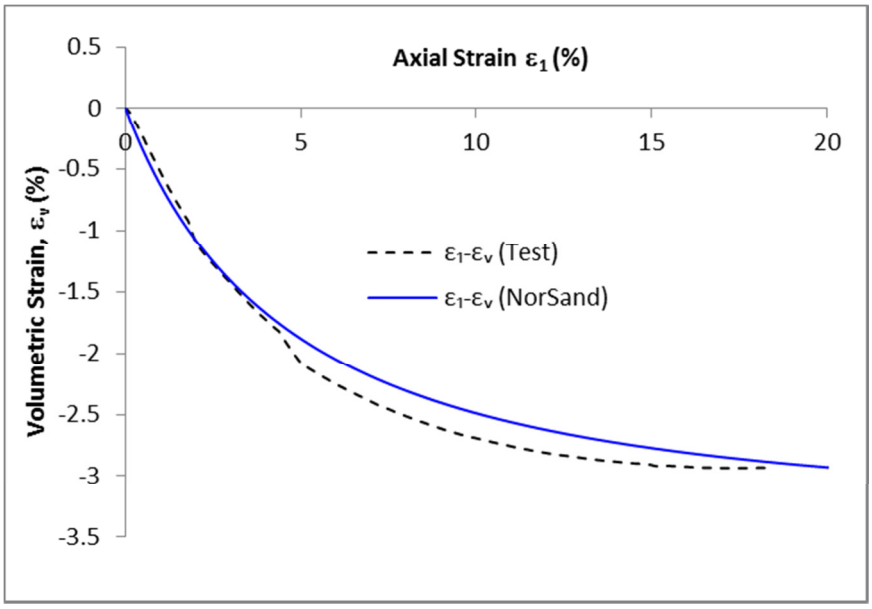

Figure 4-52 Test L-2, drained loose sand sample, volumetric strain – axial strain

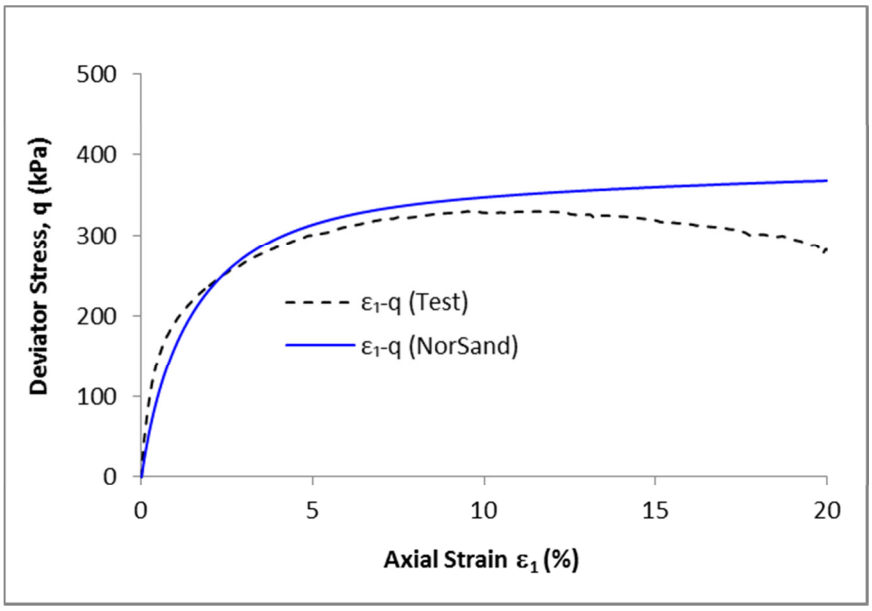

Figure 4-53 Test L-3, drained loose sand sample, deviatoric stress – axial strain

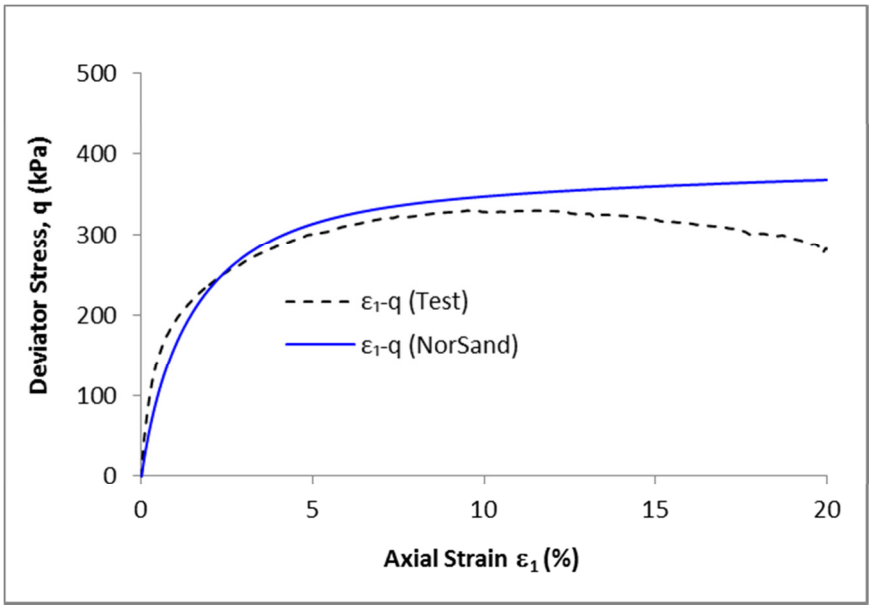

Figure 4-54 Test L-3, drained loose sand sample, volumetric strain – axial strain

All these comparisons show the predicted soil behaviour using NorSand implemented in ABAQUS Explicit is close to the published laboratory results.

To perform these comparisons a 2D axisymmetric finite element model is created to simulate the triaxial condition. However, since the main objective of this implementation is to use NorSand for ice gouging simulation, which is a three-dimensional problem, a three-dimensional triaxial model is also created to examine the performance and validity of the user subroutine VUMAT in three-dimensional space. The same set of input parameters were then used to compare the results of the 3D model with 2D axisymmetric model.

The three-dimensional finite element model for triaxial test is shown in Figure 4-55 illustrating uniform von Mises stress with less than 0.1% variation from 315 kPa.

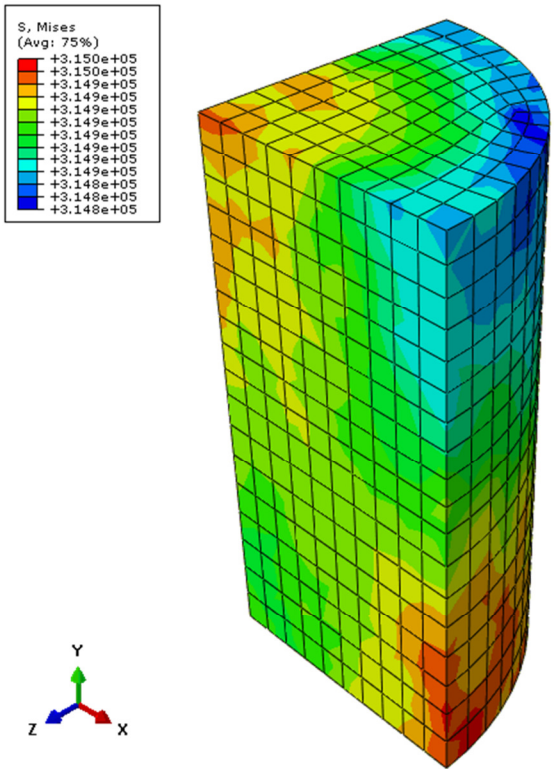

Figure 4-55 Three-dimensional Triaxial Model

Figure 4-56 shows that the results of the 3D model are identical to those of the 2D axisymmetric model. The stress and strain curves follow the same path in both 2D and 3D analyses. This indicates that the user subroutine works well in 3D condition as well and could be used in a general 3D problem like ice gouging. The input parameters used in the analyses shown in Figure 4-56, are listed in Table 4-9. It should be noted that this 3D analysis is performed in triaxial condition. In reality the critical state ratio varies with Lode angle that influences the stress-strain behaviour (Bishop, 1966). This phenomenon is captured in NorSand by defining the critical state ratio as a function of Lode angle. Therefore, in term of model formulation the only difference between general 3D analyses presented in chapter 1 and a triaxial 3D analysis shown in Figure 4-56 is that in the latter the critical state ratio, *M*, does not change through the analysis.

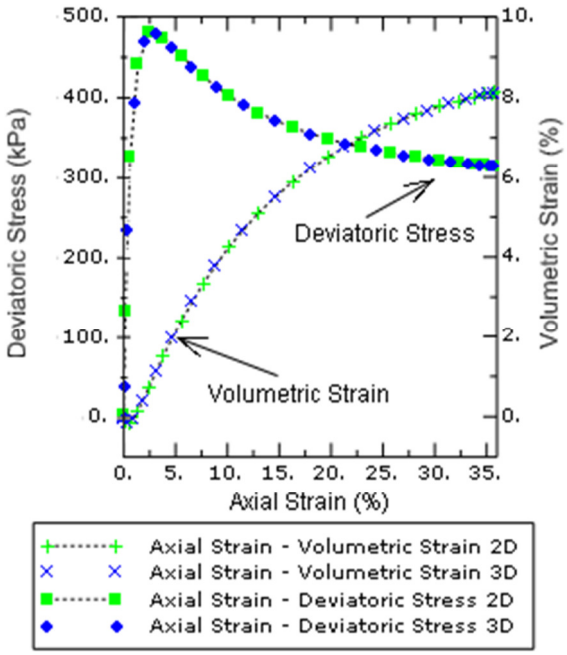

Figure 4-56Three-dimensionalTriaxialvstwo-dimensional axisymmetric triaxial results

Although it is not shown in Figure 4-56 the analyses results show that such a highly dense and dilative sample reaches to the critical state at about an axial strain of 50%.

Table 4-9 Input parameters for comparison of 3D and 2D model response

I_R	ν	λ	Γ	M_{tc}	χ_{tc}	H	ψ	p_0(kPa)
600	0.33	0.031	0.816	1.3	3.8	300	-0.171	130

It should be noted that in the developed constitutive models, there is no distinction between the implementations of the VUMATs in 2D and 3D. The developed VUMATs in this research are implemented in generalized stress space the same way that the formulas in the thesis are described in generalized space. These models treat the 2D as a special case of the 3D. It means that in the implementation of the VUMATs the stress invariants and other state parameters are calculated in three-dimensional regardless whether the analysis is 2D or 3D. As a result, the same VUMAT can be used for both 2D and 3D problems.

4.9. Calculation of Pore Fluid Pressure

The main purpose of the thesis is to analyze the slow gouging of the sand which is assumed to be drained. The undrained feature was also added to the VUMAT to extend the range of ice gouging analyses.

A rigorous implementation of undrained condition requires that the increment in elastic volumetric strains be the negative of the increment in plastic volumetric strain, i.e. $\dot{\boldsymbol{\varepsilon}}_{\boldsymbol{v}}^{\boldsymbol{p}} = -\dot{\boldsymbol{\varepsilon}}_{\boldsymbol{v}}^{\boldsymbol{e}}$. This equality results in no change in the total volumetric strain of the soil.

Due to specific structure of the VUMAT subroutine, it is not possible to implement the undrained condition of zero volumetric strain in a direct and explicit way. The Abaqus solver inputs the components of total strain into the VUMAT subroutine. Based on these components, the total volumetric strain can be calculated. Therefore, in a VUMAT subroutine there is no straightforward method to enforce that the sum of volumetric elastic strain and volumetric plastic strain equates zero. Instead, a mere but close approximation, such as $\dot{\boldsymbol{\varepsilon}}_{\boldsymbol{v}}^{\boldsymbol{p}} + \dot{\boldsymbol{\varepsilon}}_{\boldsymbol{v}}^{\boldsymbol{e}} = \dot{\boldsymbol{\varepsilon}}_{\boldsymbol{v}}^{\boldsymbol{T}} \approx 0$, should be applied. Note that at each increment of the analysis, a finite total volumetric strain is sent to the VUMAT subroutine which is based on the equation of motion. As the results the right term in equation above is not necessarily zero.

In order to satisfy the undrained condition (or as previously described: $\dot{\boldsymbol{\varepsilon}}_{\boldsymbol{v}}^{\boldsymbol{p}} = -\dot{\boldsymbol{\varepsilon}}_{\boldsymbol{v}}^{\boldsymbol{e}}$) some modifications are applied into the stiffness matrix of the soil in a way that the sum of elastic volumetric strain and plastic volumetric strain becomes very close to zero. This approach is explained in this section.

In this study using the volume constraint method, the implemented critical state model of NorSand and the proposed Drucker-Prager Cap model were also extended to simulate the undrained behaviour of soils. In this method bulk modulus of water is chosen considerably larger than the bulk modulus of soil. This ensures the total soil volume change is insignificant as expected in undrained analyses. In other hand soil exhibits an equivalent Poisson's ratio almost equal to 0.5.(Britto & Gunn, 1987).

To switch between drained analysis and undrained analysis a parameter representing the ratio of the bulk modulus of the pore fluid to the soil skeleton is defined in VUMAT

subroutine. This parameter could be set to zero or some non-zero value like 100 to respectively perform drained or undrained analysis. The procedure is described in the following.

4.9.1. Formulation of the Volume Constraint Method

When loading is applied to an element of soil, it would produce a total change of stress $\{\Delta\sigma\}$. However according to the theory of effective stress this total stress change is divided into two parts. One part is carried by the soil skeleton and the other by pore fluid. The theory of effective stress requires:

$$\{\Delta\sigma\} = \{\Delta\sigma'\} + \{\Delta\sigma_f\} \quad \textbf{4-81}$$

Where:

$\{\Delta\sigma'\}$ is the effective stress carried by soil skeleton

$\{\Delta\sigma_f\}$ is the pore fluid stress carried by the pore fluid which is usually considered as water.

As for every fluid it is assumed that this stress change $\{\Delta\sigma_f\}$ does not include shear components therefore:

$$\{\Delta\sigma_f\} = \{\Delta u \quad \Delta u \quad \Delta u \quad 0 \quad 0 \quad 0\}^T \quad \textbf{4-82}$$

$\{\Delta u\}$is the developed pore fluid pressure as the result of applied $\{\Delta\sigma\}$.

The constitutive model states that:

$$\{\Delta\sigma\} = [D]\{\Delta\varepsilon\} \quad \textbf{4-83}$$

However, assuming that the phases of system, solid and fluid, deform together the following two equations can also be concluded:

$$\{\Delta\sigma'\} = [D']\{\Delta\varepsilon\} \quad \textbf{4-84}$$

$$\{\Delta\sigma_f\} = [D_f]\{\Delta\varepsilon\} \quad \textbf{4-85}$$

Substituting theses equation into the theory of effective stress concludes:

$$[D] = [D'] + [D_f] \quad \textbf{4-86}$$

$[D_f]$is related to the bulk modulus of pore fluid and since the fluids do not carry shear stress then the shear components of this matrix are zero.

$$[D_f] = K_w \begin{bmatrix} 1_3 & 0_3 \\ 0_3 & 0_3 \end{bmatrix} \quad \textbf{4-87}$$

K_w is the equivalent bulk modulus of pore fluid where for the saturated soil $K_w = K_f$ (Naylor, 1974). Therefore it just suffices to calculate the effective stress-strain matrix from the constitutive law and then the equivalent bulk modulus of pore fluid K_w and then easily construct total stress-strain matrix $[D]$ using the formulas introduced here.

To calculate the excess pore pressure, suppose an element of soil consisting of two phase water and solid as shown in Figure 4-57 below:

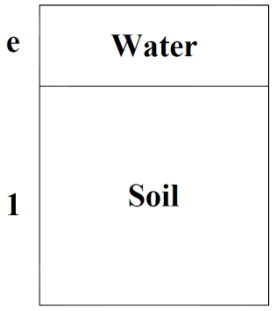

Figure 4-57 A saturated soil element

As mentioned earlier the soil skeleton and the pore fluid deform together and bear the same deformation. The water volume could be obtained based on the soil void ratio.

$$V_w = \frac{e}{1+e}V \qquad \textbf{4-88}$$

Therefore the fluid volumetric strain can be derived as follow:

$$\Delta\varepsilon_v^w = \frac{\Delta V}{V_w} = \frac{\Delta V}{\frac{e}{1+e}V} = \frac{1+e}{e}\frac{\Delta V}{V} = \frac{1+e}{e}\Delta\varepsilon_v \qquad \textbf{4-89}$$

e is the void ratio, V is the soil volume, V_w is the fluid or water volume, ΔV is the soil volume change and $\Delta\varepsilon_v^w$ is the water volumetric strain.

Having the water volumetric strain the pore pressure can be easily obtained as shown in Eq. 4-90:

$$\Delta u = \frac{1+e}{e}K_w\Delta\varepsilon_v \qquad \textbf{4-90}$$

This equation requires that the value of K_w be known in order to perform an undrained analysis. Griffiths (1985) have suggested that K_w is chosen as a multiplication of the bulk modulus of the soil skeleton.

$$K_w = \beta_w K_{skel} \qquad \textbf{4-91}$$

According to Griffiths for relatively large values of K_w the result of the undrained analysis is not sensitive to the exact value of K_w therefore for the values of β_w greater than 20 the result would barely change and they are almost the same.

Potts and Zdravkovic (1999) have studied the sensitivity of the equivalent undrained Poisson's ratio and the results are shown in Table 4-10.

Table 4-10 Achievement of equivalent undrained Poisson's ratio

β_w	ν_u

	$\nu = 0.3$	$\nu = 0.1$
10	0.4793	0.4520
100	.04977	0.4946
1000	0.4998	0.4994

It is obvious that increasing β_w produces an undrained equivalent Poisson's ratio closer to 0.5 as it is expected. Figure 4-58confirms that for void ratios in range of 0.5 to 1.5 when β_w exceeds 100 the equivalent Poisson's ratio would be almost equal to 0.5.

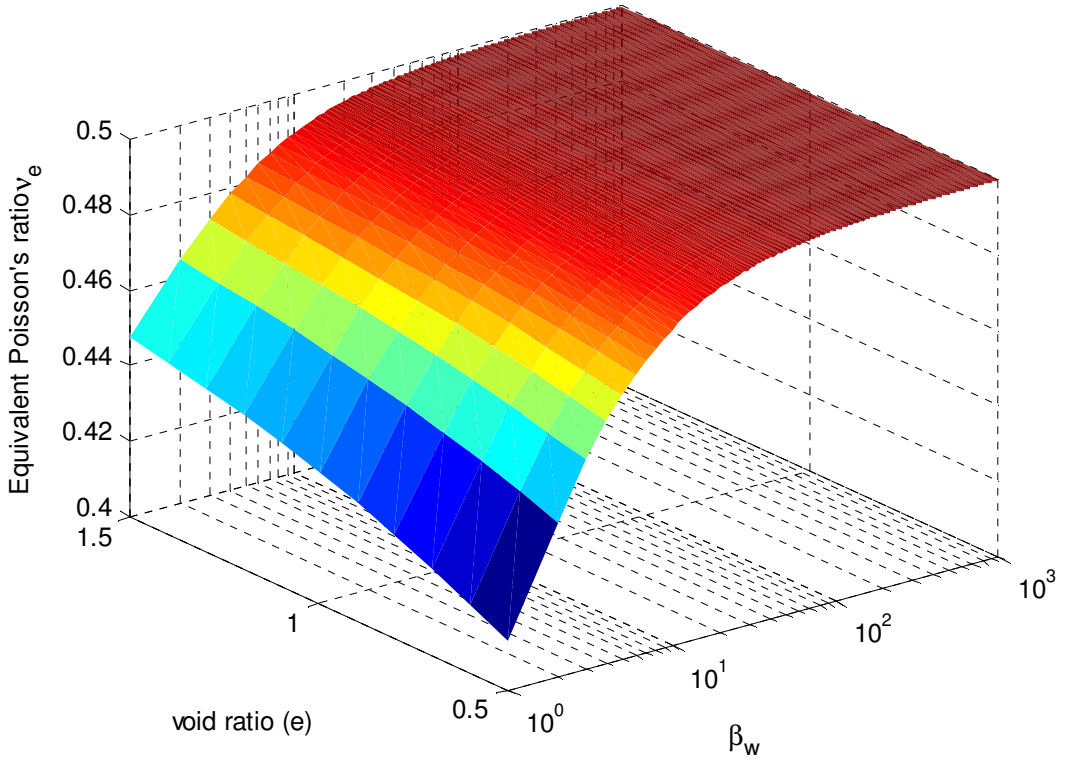

Figure 4-58 Variation of the equivalent Poisson's ratio as function of e and β_w, $\nu' = 0.25$

The advantage of this method over using a Poisson's ratio of 0.5 in the analysis is to prevent possible numerical instabilities.

4.9.2. Implementation in ABAQUS Explicit

In ABAQUS at the beginning of each step $\{\Delta\varepsilon\}$ is known and is sent to the VUMAT subroutine. Therefore $\Delta\varepsilon_v$ can be easily calculated. Having the value of volumetric strain concludes the excess pore pressure as mentioned earlier:

$$\Delta u = \frac{1+e}{e} K_w \Delta\varepsilon_v \qquad \textbf{4-1}$$

Or

$$\Delta u = \frac{1+e}{e} \beta_w K_{skel} \Delta\varepsilon_v \qquad \textbf{4-2}$$

If the value of Δu is added to the non-shear terms of the stress increment then the total stress change of the step is obtained.

Figure 4-59 shows the generation of pore water pressure in an elastic-plastic analysis. In this analysis a hypothetical sample of soil is subjected to a triaxial compression test. For more clarity the hardening modulus is assumed to be zero so the yield surface remains unchanged during the analysis. As expected the effective pressure (the vertical) remains constant and the applied pressure would be carried by the water while the material is in elastic zone. However, while yielding the effective stress path follows the yield surface and the total stress path maintains equilibrium. The analysis in Figure 4-59 is performed using the proposed Drucker-Prager Cap model.

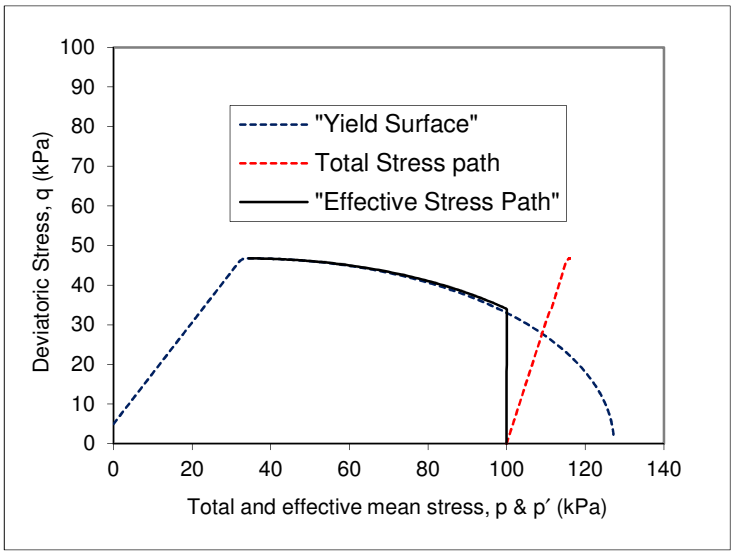

Figure 4-59 Development of pore water pressure in elastic-plastic analysis using Drucker-Prager Model

The similar undrained analysis is performed using the implemented NorSand model as shown in Figure 4-60. In this figure an arbitrary sample is yielding on the wet side.

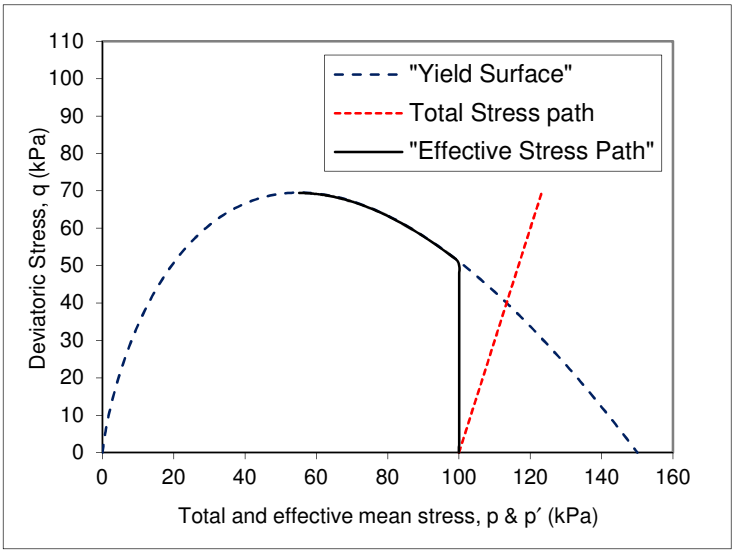

Figure 4-60 Development of pore water pressure in elastic-plastic analysis using NorSand Model

The same kind of hypothetical sample of soil is analysed under undrainedtriaxial compression test condition whose stress paths and yield surface are shown inFigure 4-61.

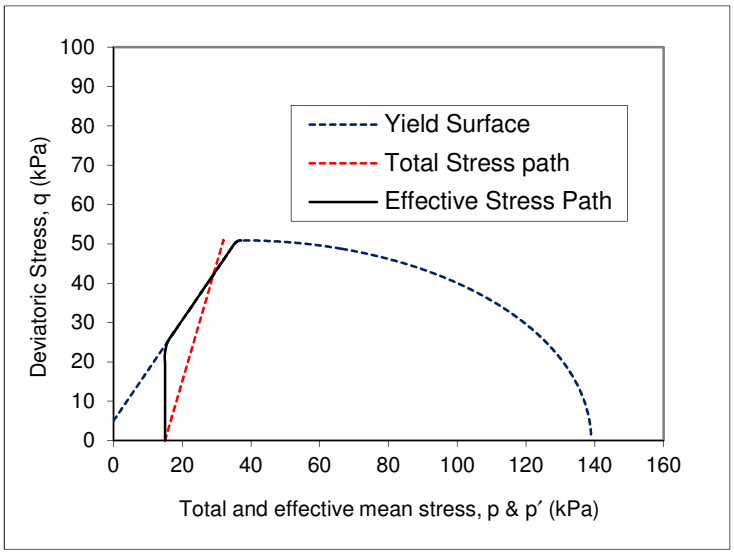

Figure 4-61 Positive excess pore pressure when the soil yields on the shear side of yield surface, using Drucker-Prager Cap

In this analysis the soil is yielding on the shear zone and it is modeled using the proposed Drucker-Prager Cap model. As can be seen in this figure the excess pore pressure might be positive.

Similarly, Figure 4-62 shows the development of the pore pressure when the sample yields on the dry side using the implemented NorSand model.

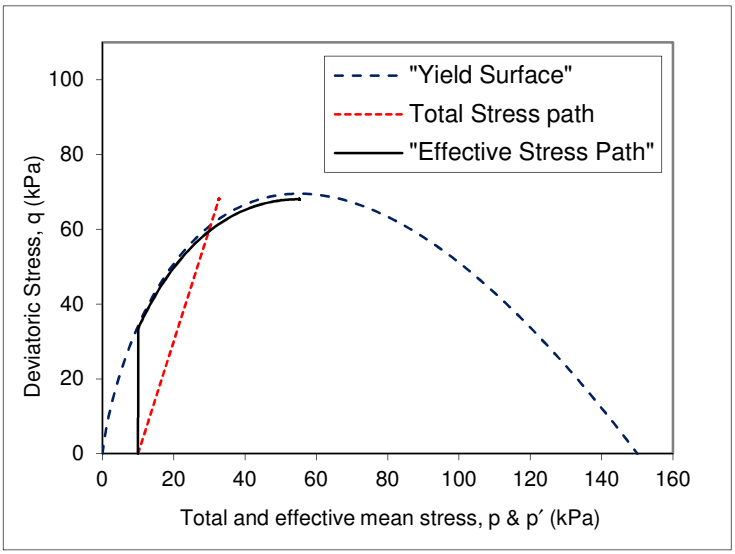

Figure 4-62 Positive excess pore pressure when the soil yields on the shear side of yield surface, using NorSand

4.9.3. Undrained Triaxial Analyses Using Drucker-Prager Cap

InFigure 4-63 to Figure 4-65the response of and undrained dense sample is predicted using the developed Drucker-Prager Cap model and the volume constraint method described in section 4.9.1. These responses include stress path, pore water pressure and deviatoric stress. Table 4-11 summarizes the input parameters of the Drucker-Prager Cap model that are used in undrained analyses.

Table 4-11 Input parameter for undrained analysis

E	ν	d	θ_{cr}	H	R	e_0	$e_{\min}$	$e_{\max}$
2.13x10^{5}kPa	0.33	1000	52°	80	2	0.617	0.521	0.747

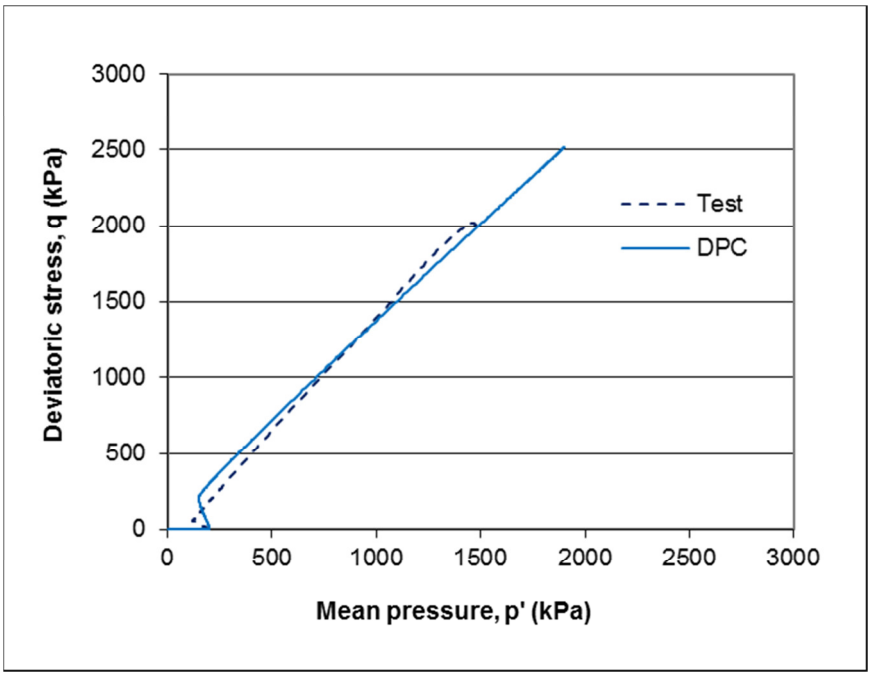

Figure 4-63 Undrained dense sand sample, shear stress – mean stress (DPC)

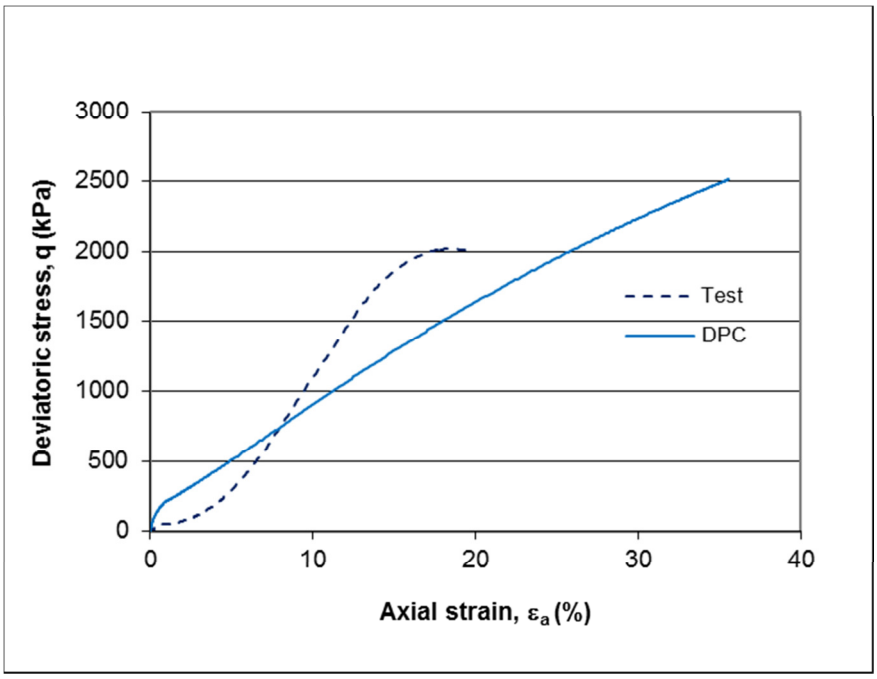

Figure 4-64 Undrained dense sand sample, shear stress – axial stress (DPC)

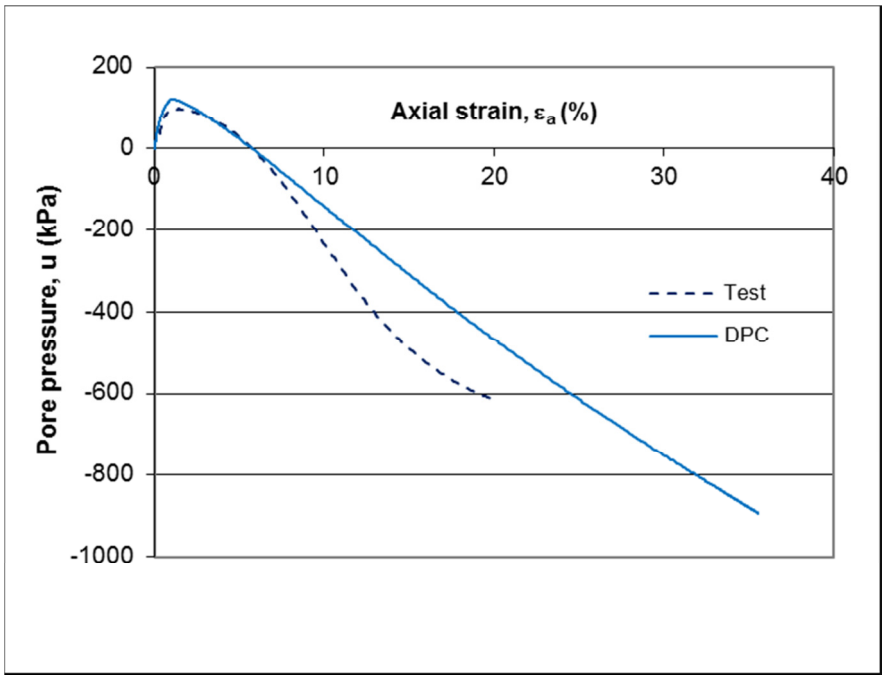

Figure 4-65 Undrained dense sand sample, excess pore pressure – axial strain (DPC)

Theses analyses show that the model is capable of predicting the behaviour of sands and can address issues that built-in ABAQUS Drucker-Prager cap model lacks such as realistic dilation and yield surface softening. The developed pore water pressure does also follow known pattern of undrained analysis.

4.9.4. Undrained Triaxial Analyses Using NorSand

In Figure 4-66 to Figure 4-74 the results of analysis of triaxial compression test under undrained condition are presented. These analyses include two undrained tests on loose sand and one undrained test on dense sand. The input parameters for these tests are derived from Jefferies and Been (2006).

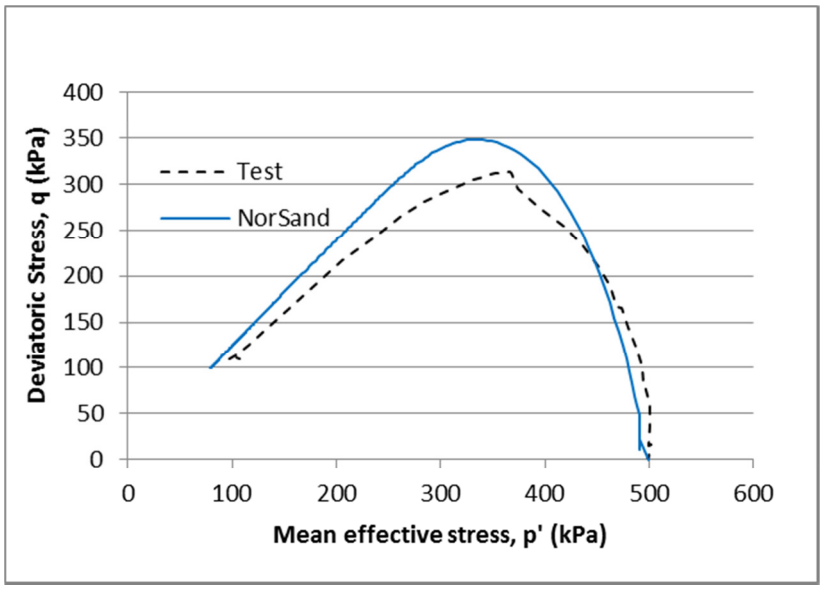

Figure 4-66 Undrained loose sand sample, shear stress – mean stress

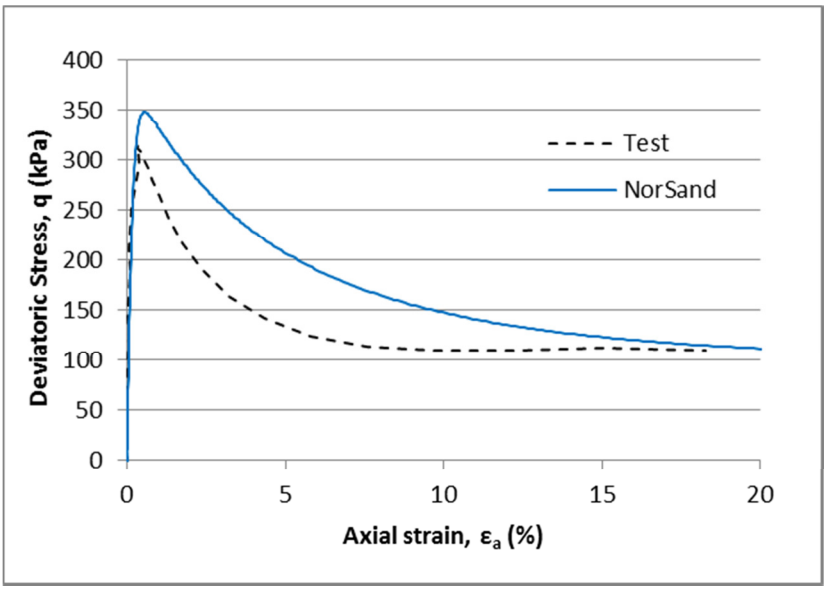

Figure 4-67 Undrained loose sand sample, shear stress – axial strain

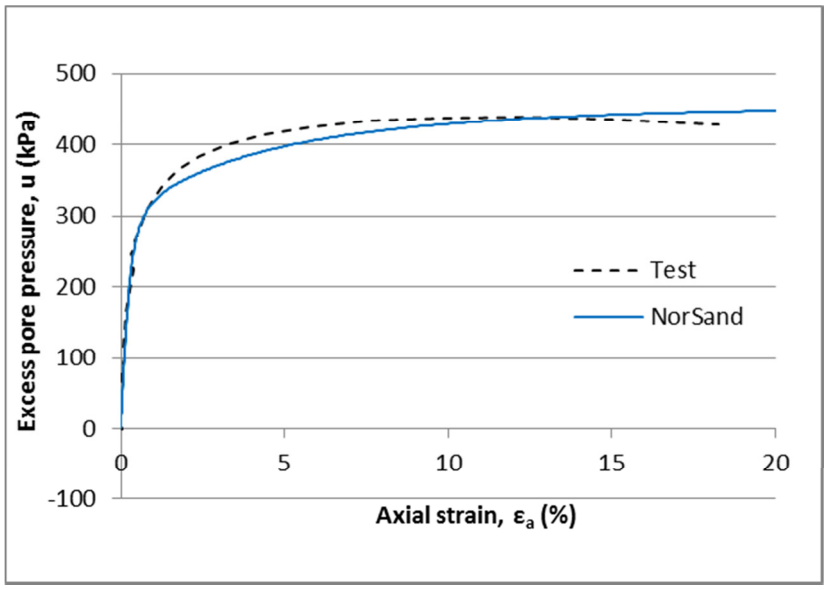

Figure 4-68 Undrained loose sand sample, excess pore pressure – axial strain

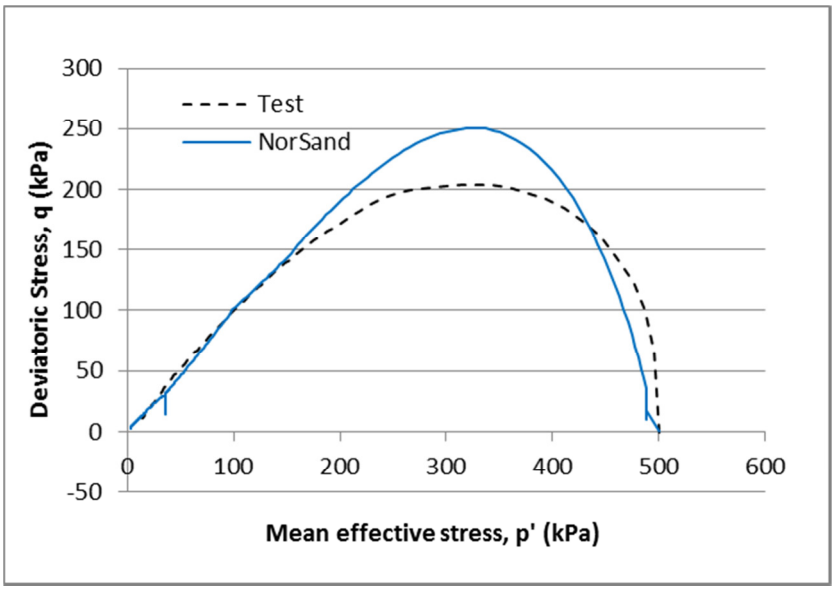

Figure 4-69 Undrained loose sand sample, shear stress – mean stress

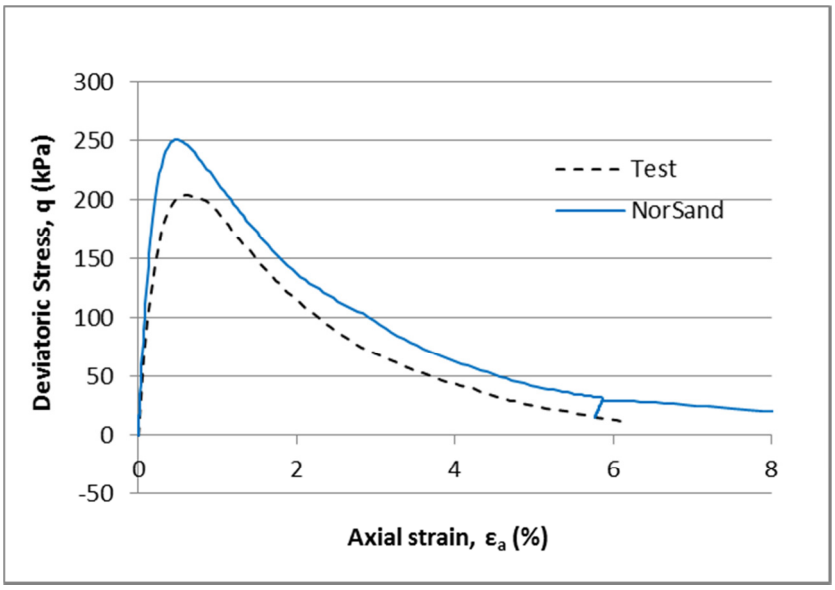

Figure 4-70 Undrained loose sand sample, shear stress – axial strain

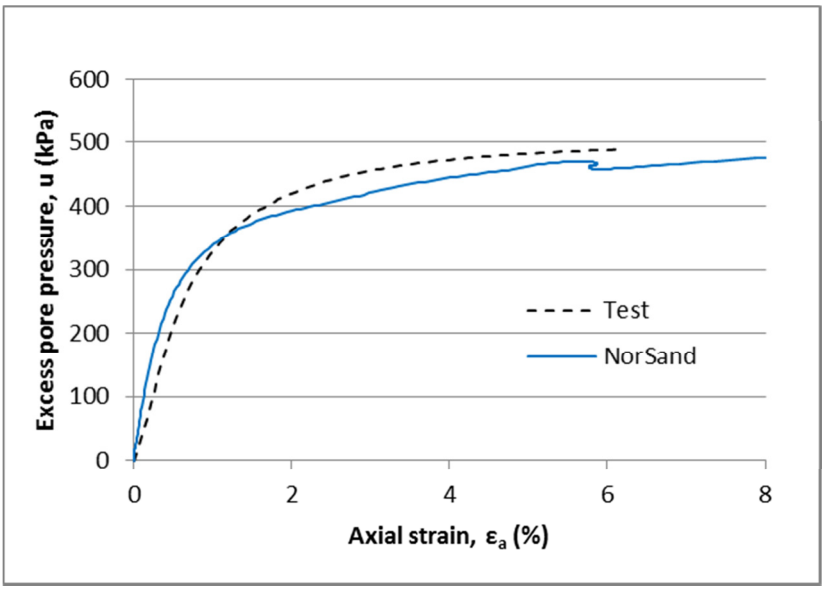

Figure 4-71 Undrained loose sand sample, excess pore pressure – axial strain

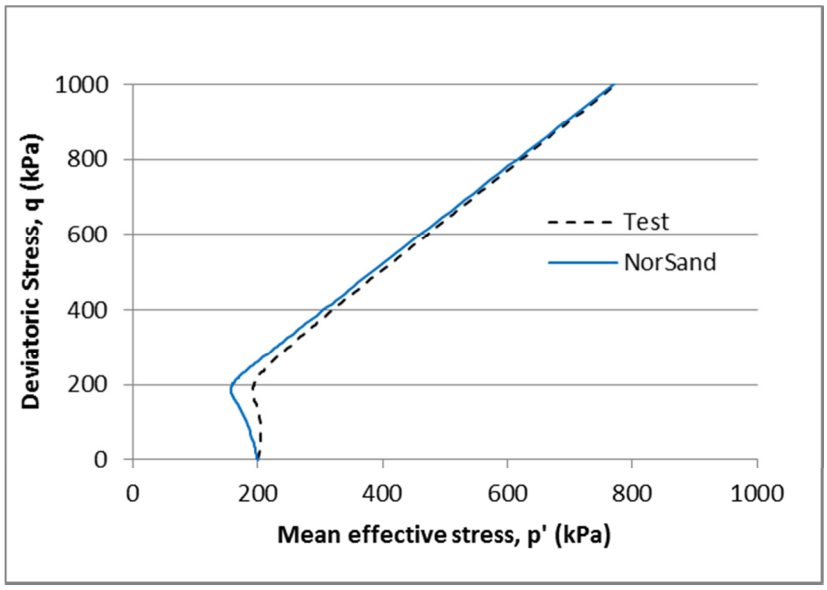

Figure 4-72 Undrained dense sand sample, shear stress – mean stress

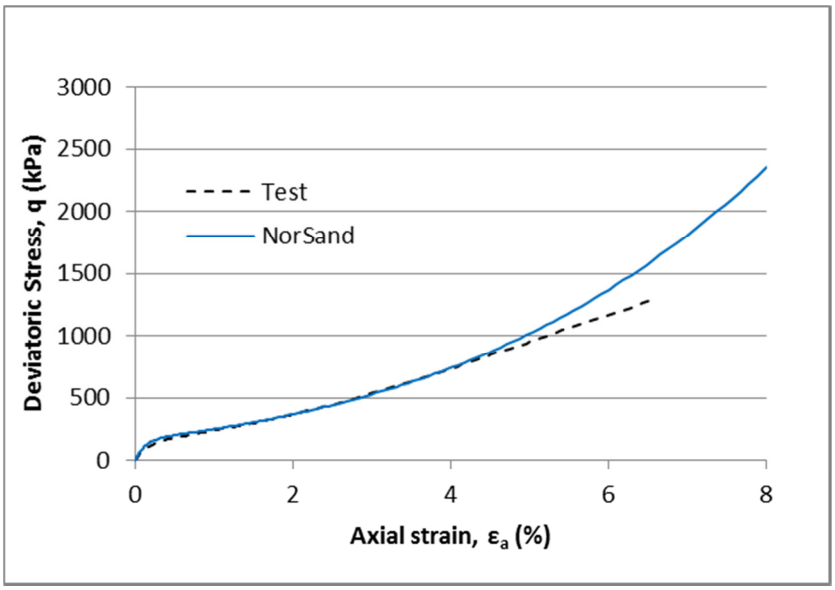

Figure 4-73 Undrained dense sand sample, shear stress – axial strain

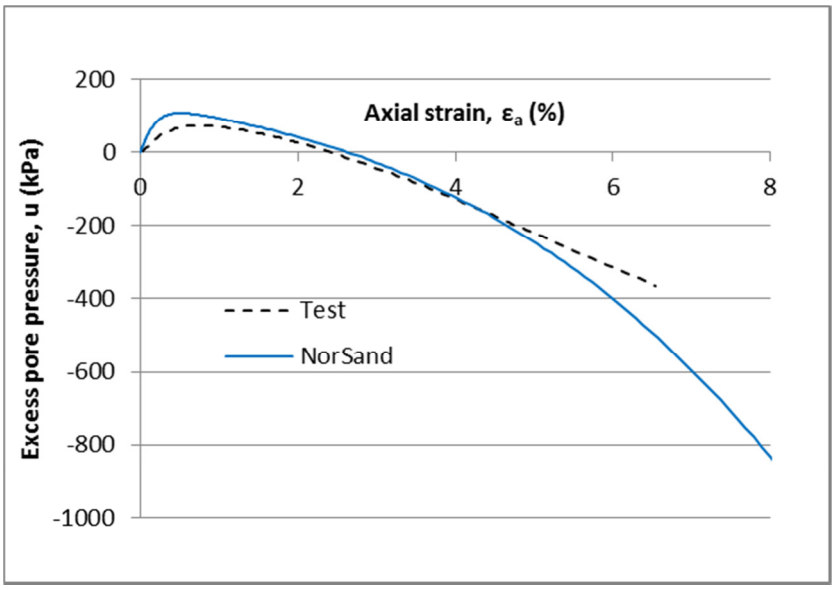

Figure 4-74 Undrained dense sand sample, excess pore pressure – axial strain

The undrained analysis using the implemented version of NorSand show relatively good agreement with the test results. The VUMAT model can also capture different undrained behaviours that are expected based on the dense or loose state of soil.

5. Three Dimensional Ice Gouging Modeling

The purpose of this research is to model the ice gouging event using developed constitutive models in ABAQUS Explicit. Different finite element models are constructed to investigate the seabed gouges under various scenarios. What these models have all in common are a moving keel and a domain of soil elements. In this chapter the technical issues that should be considered in the development of an ice gouging finite element model are first reviewed. Following the assembly of the numerical model, the key output results that are of interest from a practical point of view will be introduced. To validate the finite element model a published base case scenario is chosen to assess the performance of the developed model in duplication of the gouging results. A mesh sensitivity analysis is carried out to determine an optimum mesh density for the developed model before it is used in the ice gouging analyses. Finally, the developed model is used to study the mechanics of ice gouging event. The results of numerical analyses are presented in details at the end of this chapter.

5.1. Finite Element Ice Gouging Model

In this section the details of the developed finite element model used to perform the gouging analyses are discussed.

5.1.1. The Analysis Procedure

The finite element package ABAQUS contains two general procedures for dynamic analysis in which response of a structure under a time-varying load is considered. They are implicit and explicit approaches. Each of these procedures has advantages and

disadvantages over the other one. The implicit procedure is offered in ABAQUS Standard and the explicit method is formulated under ABAQUS Explicit product. ABAQUS Standard offers a wider library of elements which ideally include both displacement and pore pressure degrees of freedom. However, for such a large, very general, complicated and interactive dynamic problem as ice gouging is, as well as the complications regarding the large deformation, ABAQUS Explicit seems more attractive mainly due to the level of efficiency it delivers.

While in ABAQUS Explicit the computational cost rises only linearly with the model size, ABAQUS Standard demands much larger increase of resources under a similar scenario that could make the simulation of a large problem unreasonable even using the higher end mainstream technology of today. The use of Abaqus Standard (Implicit) for the analyses of this research does not seem to be an option. Although the implicit method is, in general, unconditionally stable and can use larger time increments but the fact that it needs to construct the Jacobian matrix makes it unattractive for large problems. It is very likely that the computer's physical memory required for the dynamic implicit analysis of a relatively large problem such the ice gouging problems in this thesis exceed the amount of memory installed on common computes that are available.

As it was highlighted earlier, the ice gouging event is an extremely complex numerical problem having the ice and the soil interact with each other. Depending on the specification of the problem and structure such as pipe could be also involved in this interaction. The complex environment in question is another reason why the explicit approach is the more favourable way in numerical analyses of ice gouging event. It is

more obvious why the explicit method is more practical for large problems if the formulations of the two methods are studied a little more deeply.

In a dynamic analysis the equation of motion, EOM, as shown in eq. 5-1 should be solved (either explicitly or implicitly).

$$M\ddot{u} + C\dot{u} + Ku = f(t) \qquad \textbf{5-1}$$

In which $\ddot{u}$ is the acceleration, $\dot{u}$ is the velocity and u is the displacement. $\boldsymbol{M}$, $\boldsymbol{C}$ and $\boldsymbol{K}$ are respectively discrete mass, damping and stiffness matrices. $f(t)$ is the time dependent function of external force. It should be noted that generally the matrices of $\boldsymbol{M}$, $\boldsymbol{K}$ and $\boldsymbol{C}$ can all be a function of displacement, u, in a nonlinear dynamic analysis.

The implicit dynamic analysis in ABAQUS uses the Hubert-Hughes-Taylor (HHT) method to integrate the EOM over the course of time. In HHT method the kinematic quantities, $u, \dot{u}, \ddot{u}$, at the end of an increment are defined based on the values of both the beginning and the end of that increment (Newmark formulas).

The EOM in implicit formulation can be eventually written in form of eq. 5-2 below:

$$\Phi\left(M(u_{n+1}), C(u_{n+1}), K(u_{n+1}), \alpha, \Delta t\right) u_{n+1} = \Psi(u_n, \dot{u}_n, \ddot{u}_n) \qquad \textbf{5-2}$$

In this equation α is a damping factor to cancel out the errors in high frequency responses. $\Delta t$is the time duration of an increment. The subscript n+1 in the left hand side of eq. 5-2 refers to the values of the end of the increment n. It can be seen that the mass, damping and stiffness matrices are a function of the displacement at the end of current increment. This means that the displacement at the end of each increment should be found using many iterations in an iterative method like the Newton method. The iterative

algorithm must continue until the obtained displacement satisfies the equation within a specific convergence criterion.

On the other hand, ABAQUS Explicit uses half step central difference equation in order to define the kinematic quantities at the end of each increment. A central difference scheme enables the solver to relate the kinematic quantities at the end of an increment only to the kinematic quantities of the beginning of that increment (i.e. the results of the previous increment). Based on the described approach, adopted in ABAQUS Explicit, the EOM can be simply represented as shown in eq. 5-3 below:

$$M(u_n)u_{n+1} = \Theta(u_n, \dot{u}_{n-1/2}) \quad \textbf{5-3}$$

This equations shows that there is no need for iteration in an increment to derive the displacement at the end of the increment and its value can be readily obtained. In addition, in explicit method the mass matrix is diagonal therefore the inversion of *M* in eq. 5-3 above is very simple and efficient whereas in implicit method this inversion is very costly. However, it should be noted that the time step in an explicit analysis should be small to avoid the loss of accuracy.

The implicit dynamic analyses can fairly quickly progress for small varying external forces or motions since larger time steps can be utilized due to the unconditionally stable nature of the implicit analysis (provided $-1/3 < \alpha < 0$ in eq. 5-2). Nevertheless, Ice gouging event requires an algorithm that can handle large deformations as well as large loading rates which are caused by the velocities of the keel. The physics of the ice gouging phenomena requires the application of faster methods such as the explicit method introduced earlier.

Based on the discussion above, it can be appreciated why explicit formulation seems to be more appropriate for dynamic analyses of large problems like seabed scour. In this study the ABAQUS Explicit is used to model and analyze the ice gouging event.

5.1.2. Model Geometry and Loading

To study the ice gouging problem a three-dimensional model is created. The soil is modeled as a cubic block. The soil domain should be large enough to prevent the boundary condition effects. In this study the soil dimensions are chosen as 70 m long, 30 m wide and 25 m deep. These selected dimensions have been tested to be adequate to reach the steady state in several different ice gouging analyses. Figure 5-1 shows the general geometry of the soil part of the model. In order to reduce the computational time of the analysis the penetration phase of the ice gouging event is replaced by the keel being initially indented into the soil. The indentation depth of the keel is equal to final gouging depth. Previous numerical analyses at C-CORE showed that placing an initial berm, preferably as high as the final developed berm height, could help the analysis to reach the steady state faster and more efficiently . The soil domain consists of reduced integration eight-node linear brick elements. To avoid high mesh distortion of the soil under the large gouging strains, the Arbitrary Lagrangian Eulerian (ALE) method is applied. The ALE method permits the material to move through the elements maintaining the mesh quality by gradual transition of the nodes and continual mesh refinement. This provides the capability of handling large deformations without mesh distortion issues. Consequently, in ALE methods the nodes do not coincide with material points. This implies that to follow the material points and capture the sub-gouge deformations some tracer particles

should be implemented in the model. The displacements of these particles represent the soil deformation at these locations. As Figure 5-1 shows two sets of tracer particles are used in the developed model. The first set, tracer particles 1, is put at a distance where the steady state is occurred and the second set, tracer particles 2, is beneath the keel base at the end of the analysis.

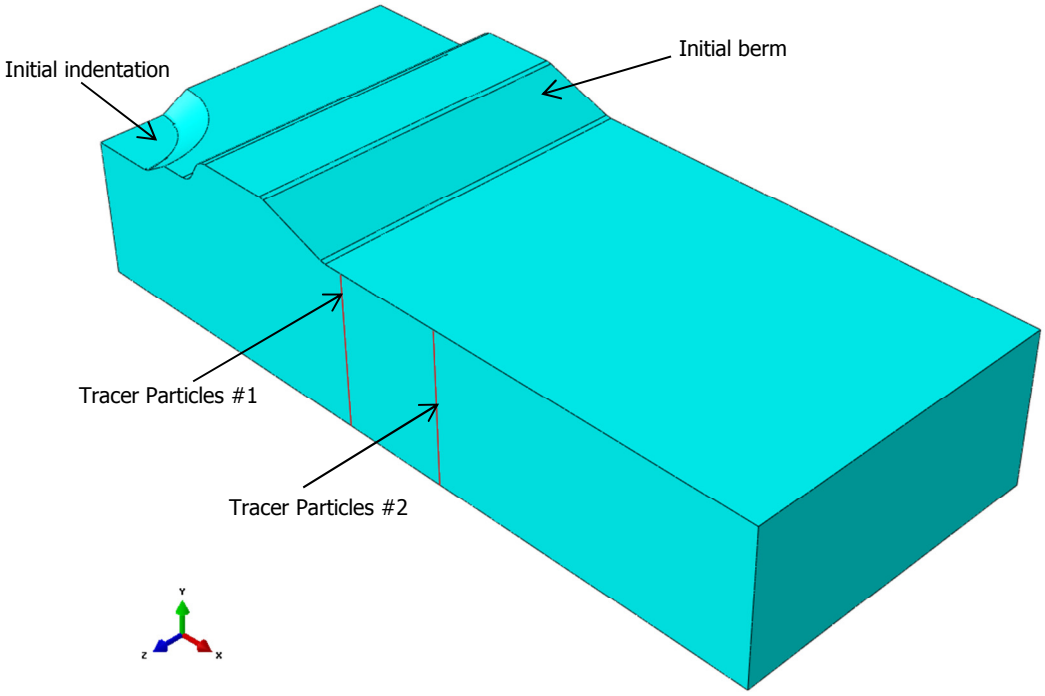

Figure 5-1 Soil geometry

The ice keel is idealized as a conical frustum with a diameter of 12.4 meters at the base. Other geometries might be used depending on different models which will be mentioned as they are presented in this study. Edges of the base are rounded to avoid numerical instabilities at the ice/soil interface. The keel attack angle varies in different analyses, so does the gouging depth of the keel. In this study the rigid keel is used to model the ice features. The keel consists of four-node three-dimensional discrete rigid elements. In addition to the conical frustum, other shapes of keel such as rectangular are used in this

study. The keel geometry will be specifically stated when the analyses results are presented. In Figure 5-2 and Figure 5-3 the general shape of the keels used in this study are presented.

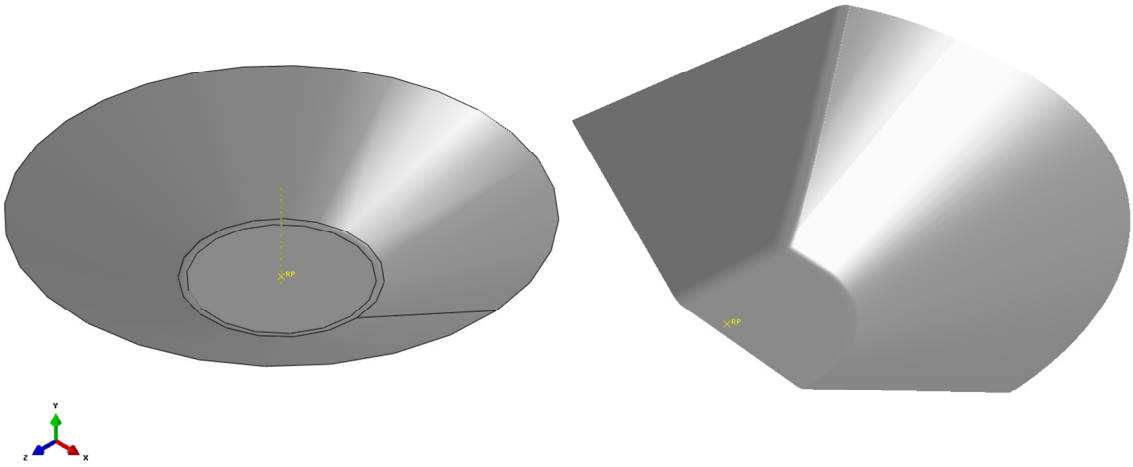

Figure 5-2 Conical frustum keels

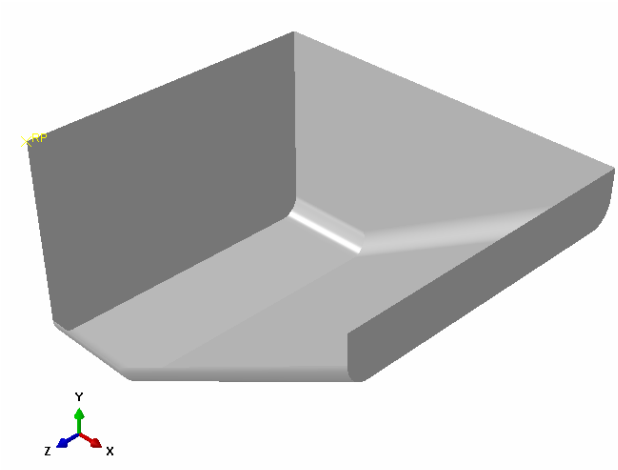

Figure 5-3 Rectangular keel

To simulate the seabed scour in numerical analyses of this study the keel advances horizontally at a model speed of 0.5 m/s gouging the soil. The applied horizontal velocity of the keel imposes the gouging loads on the soil through interaction of the soil and the keel surfaces. The low speed is selected to ensure more stability in the analyses. Since the

constitutive materials that are used in this study are time independent the horizontal velocity of the advancing keel should be inconsequential to the ice/soil response. To investigate the effect of the horizontal velocity of the gouging keel, two similar models with different velocities of 0.5 and 1 m/s were analyzed. These analyses showed similar responses indicating that effect of keel velocity is insignificant in the mentioned range.

The indented keel continues to move forward at the gouging depth to a total of about 40 meters of horizontal displacement. The goal is to continue the gouging process until the steady state is achieved. Figure 5-4 displays the horizontal velocity and displacement profile of the keel.

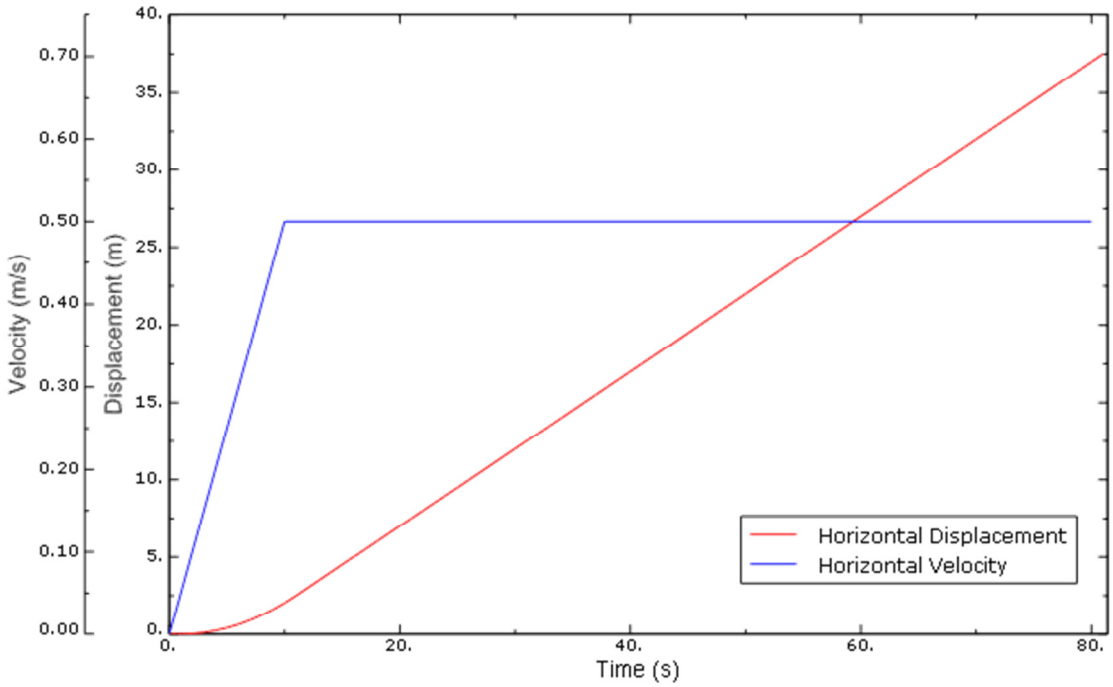

Figure 5-4 Horizontal velocity and displacement of the keel

The ice/soil interaction is preceded by an initial step in which the body forces are applied to the soil elements in order to establish the initial in-situ stress distribution in the soil.

5.1.3. Ice/Soil Contact

Similar to many other engineering problems, ice gouging events includes the interaction between a number of bodies. ABAQUS Explicit is considered as a powerful tool for simulation of interaction problems.

In the plasticity friction formulation of a contact problem at least two bodies are considered. One of them is called the "*slave*" body and the other is called the "*master*" body. Theoretically there is no difference which body is chosen as slave or master. However, from a practical point of view in contact problems the body which is stiffer or in other word the body that cannot be penetrated by the other one is usually selected as the master body. Obviously the other body into which the master body penetrates is selected as the slave body.

ABAQUS Explicit offers two different types of sliding procedures: a) small sliding and b) finite sliding. In small sliding ABAQUS initially determines which segment of the master surface and which segment of the slave surface interacts with each other. Since the sliding is assumed to be small, ABAQUS preserves the relative position of the segment of the master surface which is in contact with slave surface and the corresponding nodes of the slave surface throughout the analysis. This approach is very efficient because the solver needs to determine the interactive segments only once. On the other hand in a finite sliding procedure ABAQUS constantly updates which parts of the bodies are in contact with each other through rather complicated calculations. In an ice gouging problem ice and soil continually change contact points therefore it should be made sure that the finite sliding approach is applied for the analyses of this study.

In ABAQUS Explicit two contact algorithms are available: a) General contact and b) contact pair. The general contact algorithm can automatically distinguish the contacting surfaces and manage the interaction between bodies of a problem. This algorithm is very useful in Eulerian domains where the surfaces are not clearly defined. In this study the surface to surface interaction contact pair algorithm is used to define ice/soil interaction in ALE ice gouging simulations. Theoretically the general contact algorithm should present similar results as the surface to surface pair contact algorithm does, however it was found that the general formulation is not suitable for the Lagrangian based large deformation analyses such as the ones in this study. In order to define two surfaces that come to contact with each other the interaction properties must be specified. The interaction of two surfaces generally includes the normal and tangential behaviours. The tangential behaviour defines the frictional properties of the surfaces in contact. Since the physical model keel in centrifuge tests was built with a rough surface a "*rough*" tangential behaviour is applied to the interface of the keel in finite element model to simulate the results of centrifuge tests. The rough interaction eliminates the slipping of the surfaces in each increment. In this study the "*hard*" pressure-overclosure relationship is chosen for normal surface behaviour. The hard contact relationship minimizes the penetration of the slave body into the master body and does not permit the transfer of tensile forces at the interface of the two surfaces once they come to contact with each other.

ABAQUS Explicit utilizes two contact formulations: 1) the kinematic contact algorithm and 2) the penalty contact algorithm. In general both these methods yields similar results however, there are fundamental differences in the way each of these methods is

formulated and how they enforce the contact constraints. As the results, based on the nature of a specific problem one contact procedure might be more favourable over the other one.

The kinematic contact algorithm is a variant of the predictor-corrector methods. This algorithm is implicitly formulated. At each time increment two phases of predictor and then corrector are performed in ABAQUS Explicit. At the predictor phase ABAQUS Explicit ignores the contact conditions and advances the model parts. This will lead into possible overclosure or penetrations of the model parts into each other. The predictor phase, as mentioned earlier, will be followed by the corrector phase in which an acceleration corrector, based on the conservation of the momentum, is applied to the slave and the master nodes in order to compensate the penetration, if any, in the predictor phase. The outcome of this process is that at the end of each time step the master and the slave nodes are positioned in consistence to each other with the penetration of slave and master nodes vanished.

The penalty method does not apply a corrector phase. It uses an explicit algorithm to enforce the contact constraints. Instead of a corrector process at each time increment, the penalty method automatically inserts a set of “interface springs” into the master and the slave nodes at the following time increment in order to minimize the nodes contact penetration. The stiffness of these springs is based on the mass and the stiffness of the contacting bodies. The penalty method generally increases the overall stiffness of the contact nodes by the insertion of the interface springs. As the result, the stable time increment of the explicit analysis might be reduced when the penalty method is employed in the same way that stiffer material will decrease the calculated stable time increment.

On the other hand, the implicit kinematic algorithm has no effect on the calculation of the stable time increment of the explicit analysis.

One of the advantages of the penalty algorithm is that it provides the capability to model the contact of two rigid bodies. In addition the penalty method provides a balance master-slave approach for the interaction between rigid and deformable bodies. This is helpful in problems where sharp corners in purely master slave approach of kinematic algorithm could lead to noticeable penetration of deformable parts into the corners. The balance master-slave approach for the penalty algorithm allows the rigid body to be considered as the salve nodes, therefore, the penetration at sharp corners are reduced. The drawback of the penalty method is that the contact constraints are not exactly imposed and a residual penetration at the contact surfaces is remained. This residual penetration however is usually negligible in many problems.

In the developed model the ice/soil interaction was simulated using element based surfaces in a pure master slave interaction formulation. The rigid keel is the master surface and the deformable soil is the slave surface. In order to enforce the contact constraint the kinematic contact algorithm is selected in ABAQUS Explicit. The apparent nature of the ice gouging problem does not infer the superiority of penalty algorithm over the kinematic algorithm or vice versa in term of numerical stability. Test analyses using both methods also yield similar results. In this study the kinematic algorithm is selected due to the better efficiency that obtained during the analyses over the penalty method.

5.1.4. Constitutive Material Model

As earlier explained, to investigate the soil response under the ice gouging event user defined constitutive models are extended in ABAQUS Explicit in this study. This chapter examines the use of critical state constitutive model NorSand, introduced in chapter 3,for seabed response simulation. The capabilities of NorSand to capture the different behaviours of sands help to establish a comprehensive understanding of the mechanism of ice gouging problem under different soil conditions.

5.2. Key output results of ice gouging simulation

ABAQUS Explicit generates a large number of output results for every analysis. Among which there are a few results that are physically more comprehensible and can be better appreciated from an engineering point of view. These output results provide an invaluable source for developing design procedures. Furthermore, they deliver appropriate measures to compare the numerical results with the laboratory tests. The following list summarizes four of the most important output results to which more attention is paid in this study.

- Keel reaction forces
- Subgouge deformation
- Frontal developed mound height
- Failure mechanism, which can be studied through the plastic shear strains

It must be emphasized that among these output results the subgouge deformation has the most significance since the target of this study is the development of a categorical understanding to determine the optimum burial depth of offshore pipelines. A typical sub-gouge deformation pattern for an ice gouging event is shown in Figure 5-5.

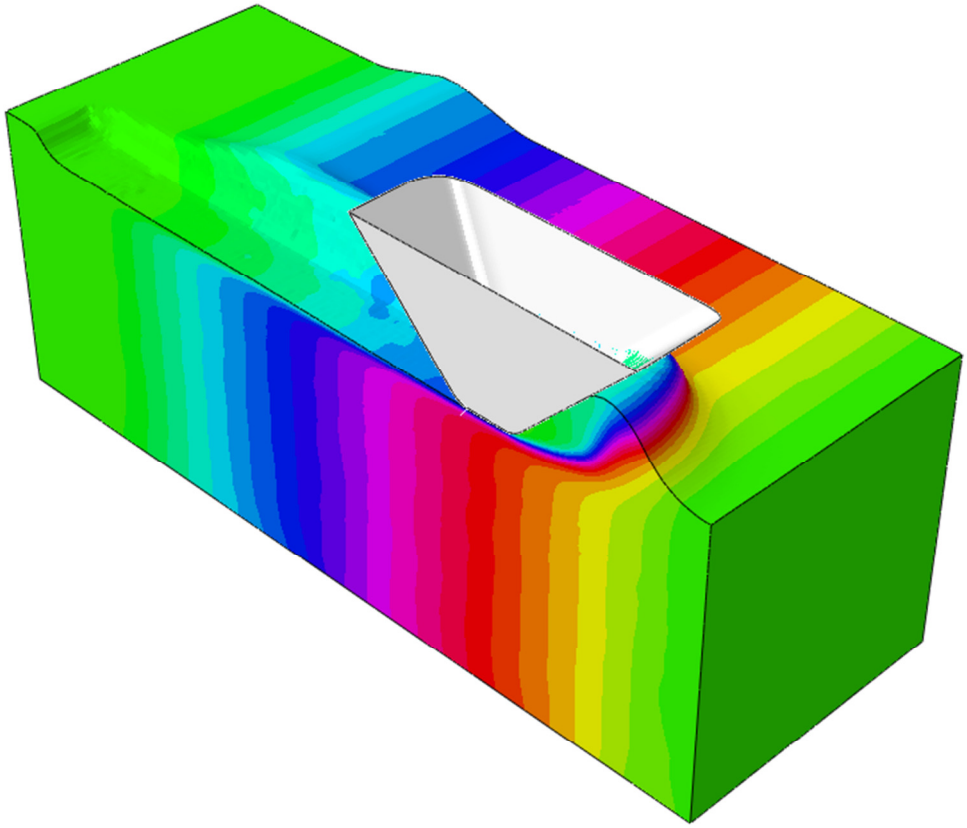

Figure 5-5 Soil 'slice' movements associated with an ice gouging event

5.3. Finite Element Model Validation

The three-dimensional model should be first validated with published data to ensure it performs consistently with previous studies. Phillips and Barrett (2011) have studied ice gouging using three-dimensional models implemented in CEL description of ABAQUS Explicit. In this section a finite element model was created and the built-in Drucker-Prager constitutive model was used to simulate the soil behavior. This model is identical to the medium size meshed model of Phillips and Barrett (2011) study with which the analysis results are compared. In both these models zero dilation is considered for the dilation angle of Drucker-Prager constitutive model. The attack angles of the keel in these models are 30 degrees and the gouging depth is 1.5 m. The yield surface is circular in the

pi-plane with an equivalent triaxial compression friction angle of 32.6°. For numerical stability a cohesion of 1.2 kPa is also selected. The submerged density of the sand was 800 kg/m3. A constant Young's elastic modulus of 3 MPa and Poisson ratio of 0.3 was used. The keel/soil interaction was modelled as rough surfaces. The gouge width is 15m (the diameter of the base of an inverted truncated conical frustum) (Phillips & Barrett, 2011).

Figure 5-6 compares the subgouge deformation based on the reference analysis and the results derived from developed model. In this figure mud line is selected as the depth origin and the vertical axis is normalized with the gouging depth which is 1.5 m in these analyses. As the result the value of "-1" on the vertical axis represents the subgouge deformation at the gouging depth.

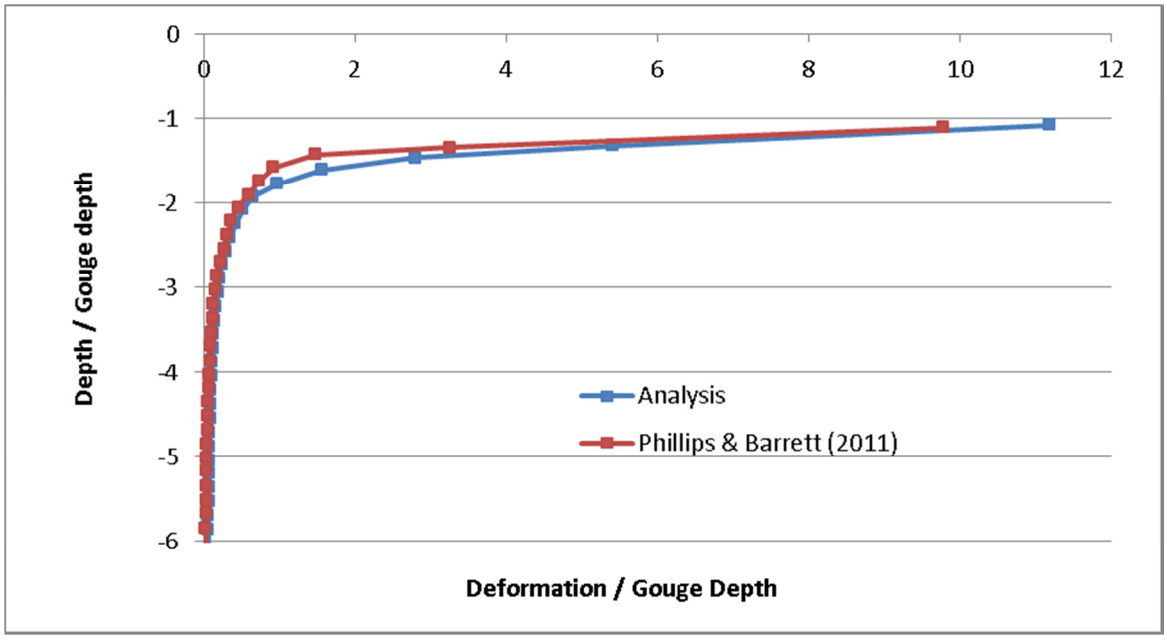

Figure 5-6 Subgouge deformation based on reference study and developed model

The results of these two analyses presented in Figure 5-6 show good agreement between the developed model and published data.

Figure 5-7 shows the keel reaction forces for the reference CEL analysis and the ALE analysis performed using developed model. This figure includes both horizontal and vertical components of the reaction force. Based on the usual consideration of upward direction as positive, the vertical component of reaction force can be identified in Figure 5-7 with negative values.

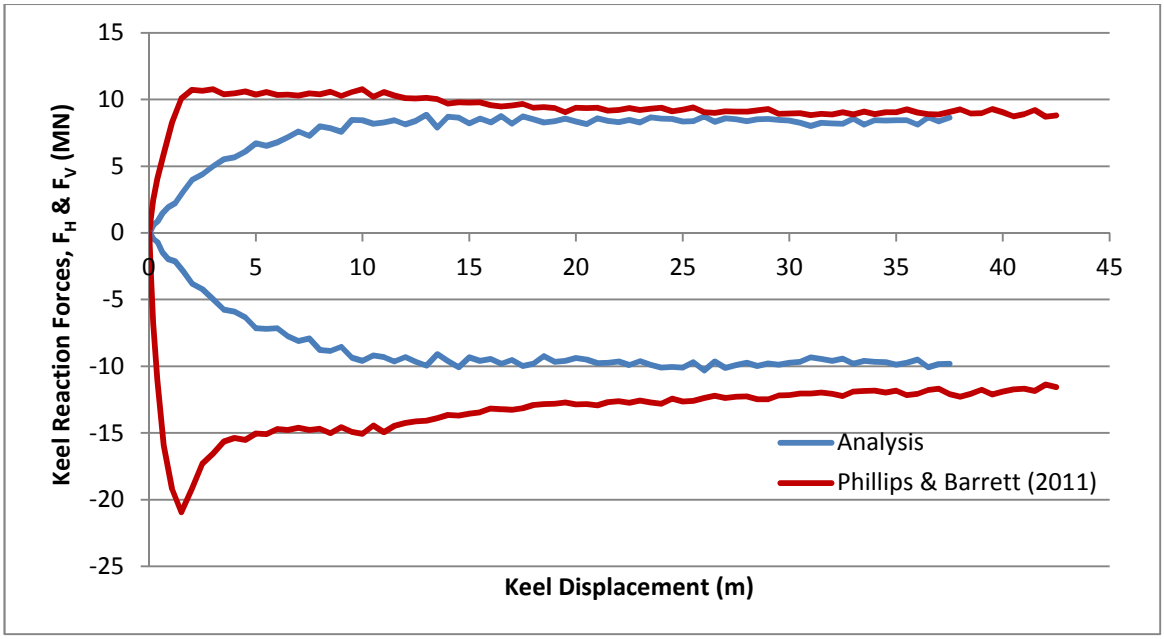

Figure 5-7 Keel reaction forces based on reference study and developed

It should be mentioned that in the CEL analysis of Phillips and Barrett (2011) the keel initially both moves downward and advances forward. The keel's penetration into the soil stops when the desired gouging depth is achieved. After this point the keel only advances horizontally. However, in the analysis performed with the developed model the vertical movement of the keel is replaced with an initial indentation of the keel to the desired

depth (in this case 1.5 m) in order to reduce the computational time in ALE analysis. The downward movement of the keel or the absence thereof is the reason why the vertical reaction force responses in Figure 5-7 are initially different in ALE and CEL analyses. It should be recognized that either vertical movement of keel, as implemented in CEL analysis of the reference, or the initial indentation of the keel, as adopted in this study, would yield same final results when the steady state is achieved. This is verified in Figure 5-8 where the reaction forces of two gouging analyses using both methods are compared applying developed three-dimensional model. In these analyses the gouging depth is 1m deep. Both pre indented and penetrating keels result in same response at steady state

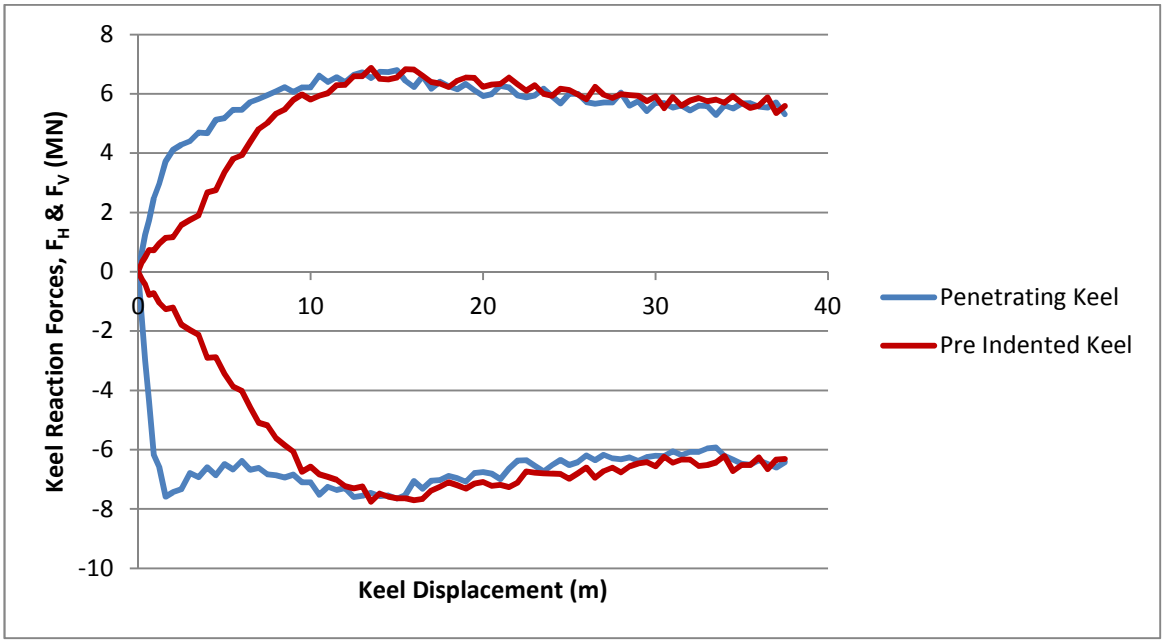

Figure 5-8 Pre indented and penetrating keel results

Figure 5-7 shows a good agreement in horizontal reaction forces. However there is a discrepancy in the CEL and ALE results for vertical reaction forces. The reaction force of

the keel is due to the ice/soil interaction. Therefore, to investigate the source of the observed inconsistency in vertical reaction forces shown in Figure 5-7 the contact pressures in the AEL analysis and the CEL analysis are presented in Figure 5-9 and Figure 5-10 respectively.

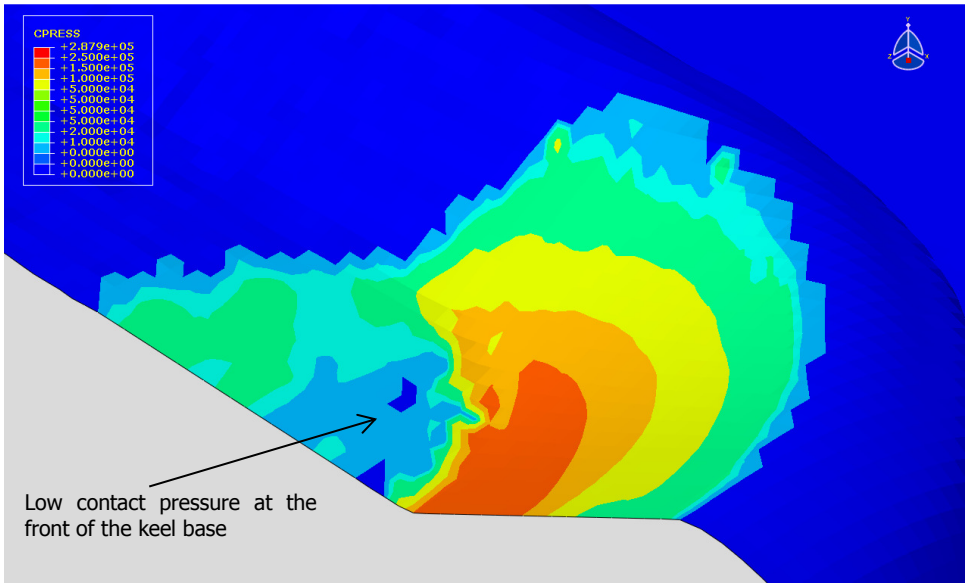

Figure 5-9 Contact pressure in the ALE analysis (unit in Pascal)

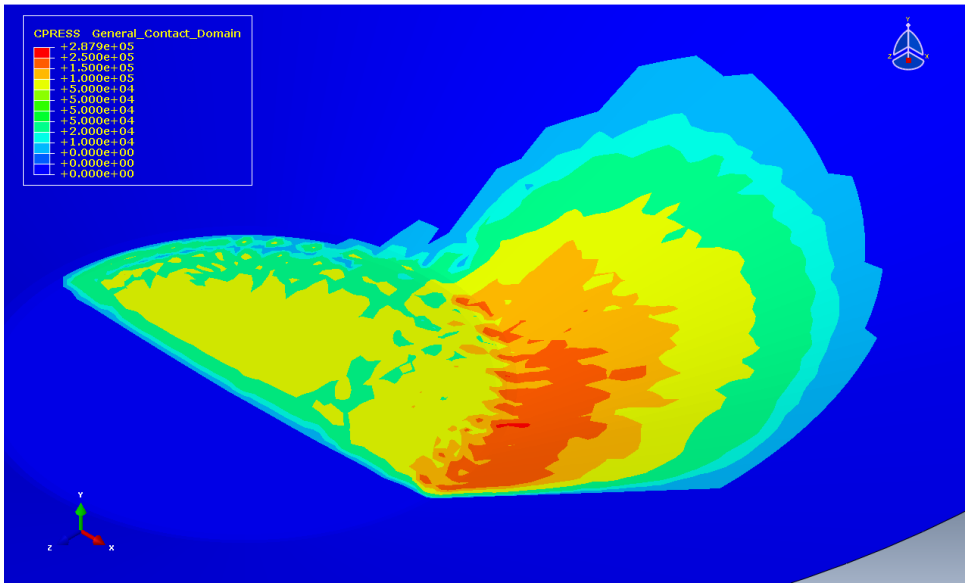

Figure 5-10 Contact pressure in the CEL analysis (unit in Pascal)

Comparing Figure 5-9 and Figure 5-10, it can be seen that the two analyses result in the same contact pressure over perimeter of the keel both at the side and in the front. However, the ALE analysis underestimates the ice/soil contact pressure at the base of the keel compared to the CEL analysis, especially at the front part of the keel base.

It appears that the contact pressure difference at the base of the keels in Figure 5-9 and Figure 5-10 is mainly due to the clearance between the keel and the soil surfaces. As explained in section 5.1.3, the developed model uses the surface to surface interaction contact pair algorithm. On the other hand an element based surface, as the soil surface is in the ALE analysis of Figure 5-9, follows the geometry of the elements. The exaggerated arrangement of soil elements in **Figure 5-11** shows that the smooth and natural configuration of elements requires the formation of a clearance, particularly beneath the toe of the keel, between the soil and keel surfaces. This justifies the low contact pressure at the front part of the keel base in Figure 5-9.

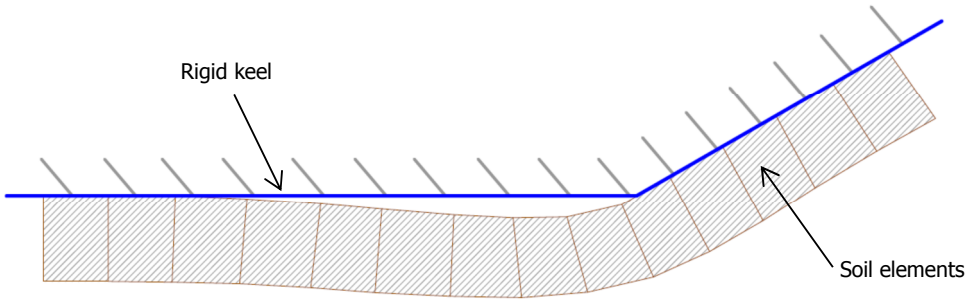

Figure 5-11 Possible development of a clearance in front of the keel base

In the ALE method the materials are bounded by the limits of the elements, thus, they should conform to the element deformation. This is not the case in the CEL analysis of Figure 5-10 where the material can partially fill a fraction of an element, as the result the soil surface is not restricted by the shape of soil elements and can virtually follow the

geometry of the rigid keel. It is postulated that the clearance between the interaction surfaces and the difference between the formulations of the general contact in CEL and pair contact in ALE are the causes for the inconsistent contact pressure at the bottom of the keel.

To further investigate the discrepancy between the vertical reaction forces of the results shown in Figure 5-7, extra analyses were performed using similar approaches to compare developed VUMAT and the built-in Drucker-Prager model in Abaqus. For these comparisons, two separate models are created in CEL and ALE formulation as shown in Figure 5-12 and Figure 5-13 respectively.

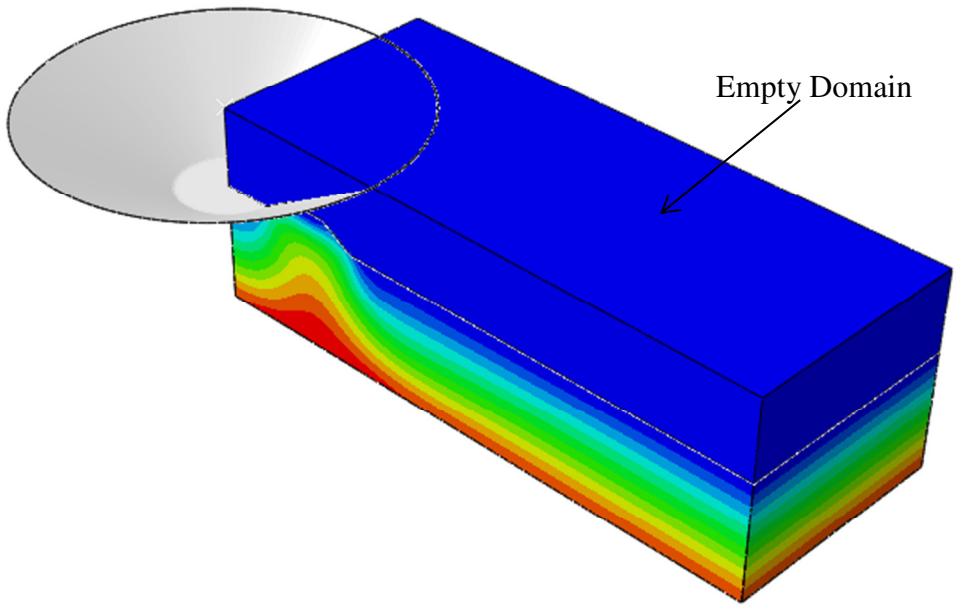

Figure 5-12 CEL model of ice gouging

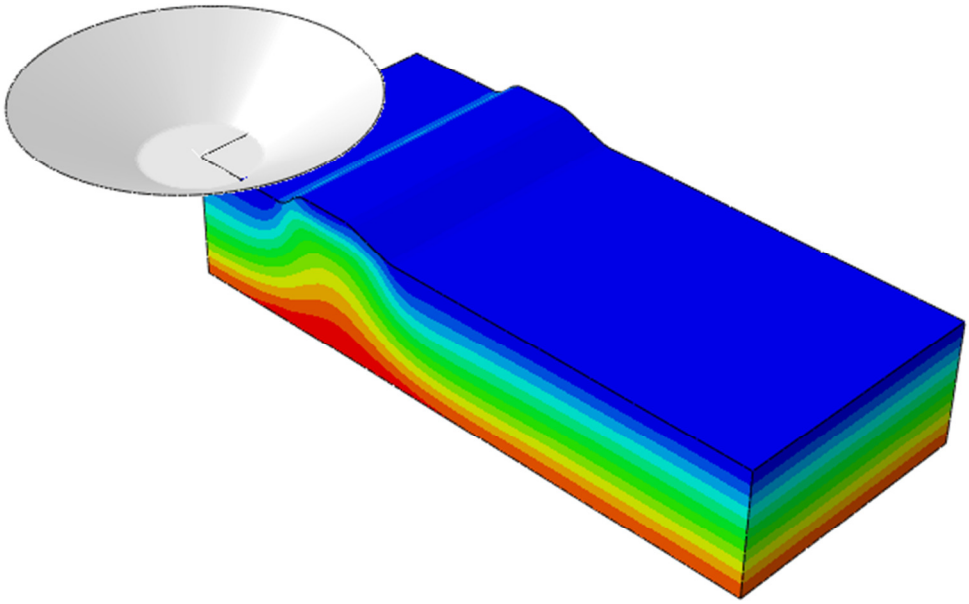

Figure 5-13 ALE model of ice gouging

The results of the reaction forces in the CEL analyses are shown in Figure 5-14. This figure shows that the implemented VUMAT model and the built-in Drucker-Prager model in the Abaqus result in similar responses. It should be noted that Appendix A.3 presents another CEL analyses in which both built-in and implemented Drucker-Prager models yield the same results.

Figure 5-15 shows the results of the reaction forces based on the analyses performed in ALE formulation. This figure also shows that the results of the built-in Drucker-Prager model and the implemented VUMAT model are consistent. These analyses can confirm that the implemented VUMAT model results the same responses as the built-in Drucker-Prager model in they are applied in similar framework.

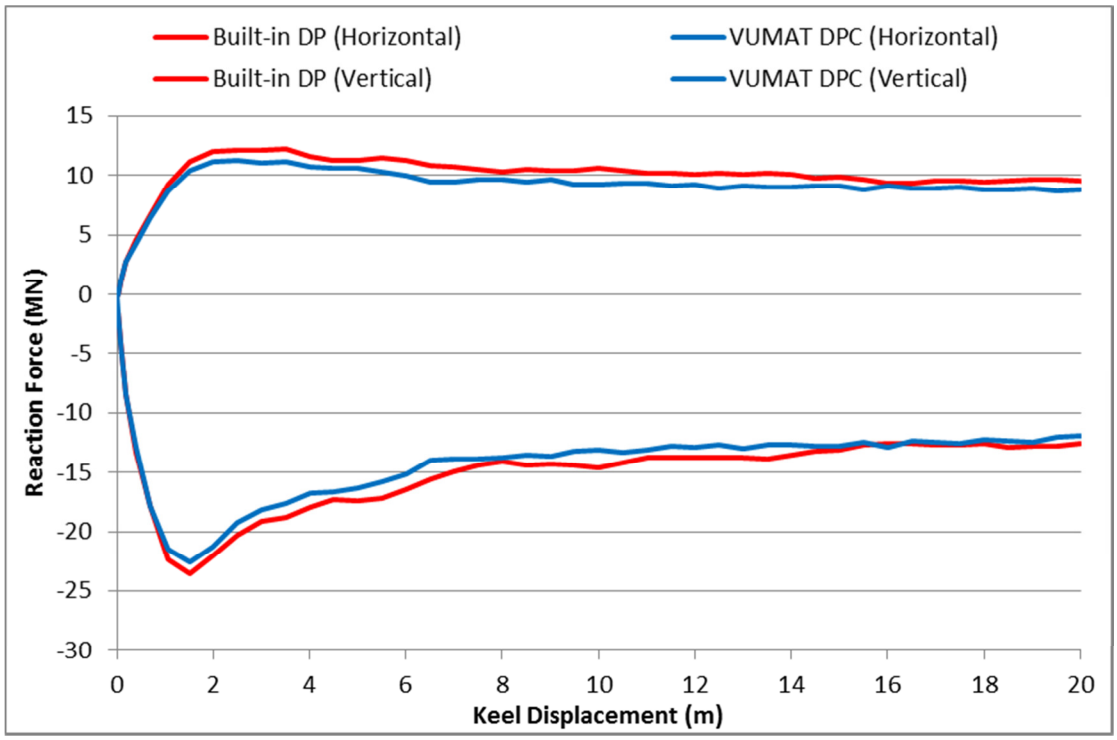

Figure 5-14 Keel reaction forces in CEL model

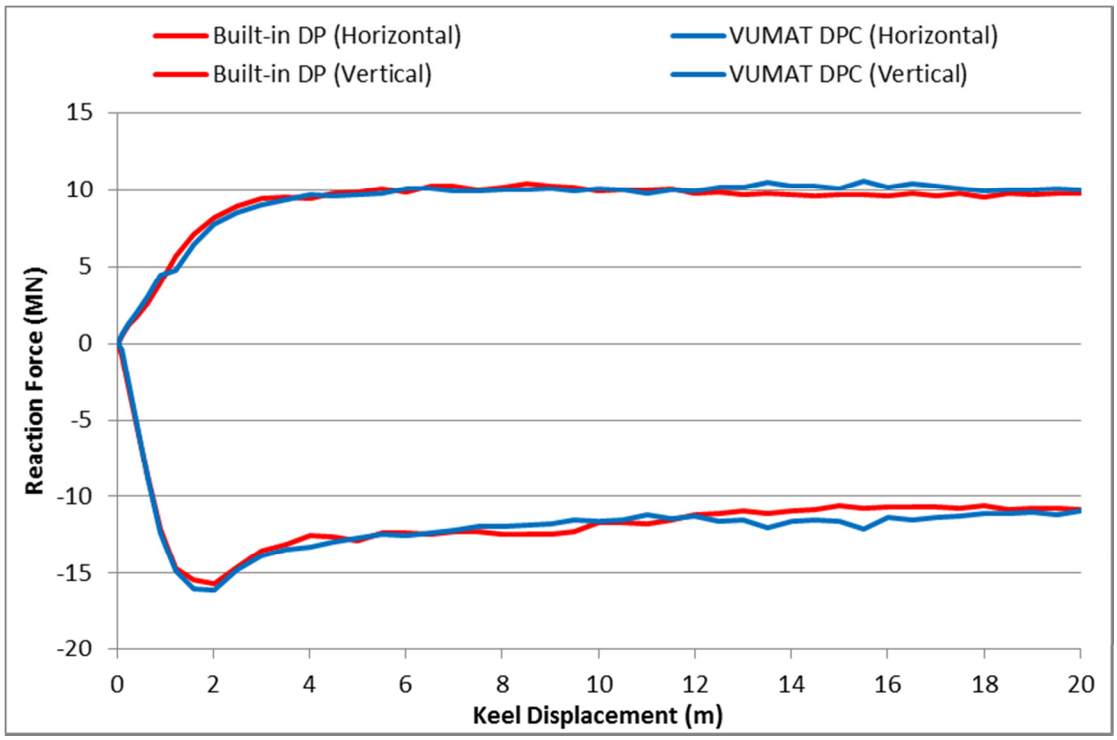

Figure 5-15 Keel reaction forces in ALE model

Nevertheless, this study is not concerned about the exact source of this disagreement because neither the difference in the keel vertical reaction forces of the two analyses nor the effect on the subgouge deformation is significant.

The developed berm heights in front of the keel in the two analyses are satisfactorily close. The CEL analysis resulted in a berm height of 3.62 m and the ALE analysis led to a height of 3.77 m.

Based on the analyses shown for the base case of 1.5 m gouging depth, the developed three-dimensional model can duplicate the previous ice gouging numerical analyses. As the result this model can be confidently applied to future analyses of ice gouging event in this study.

5.4. Mesh Sensitivity

In this section the mesh sensitivity analysis is performed on the developed model in order to derive the optimized mesh size. Finding the right size of the elements is very essential in a finite element analyses. The effect of element size is more noticeable in large problems such as ice gouging which is the subject of this study. In an explicit analysis the size of the elements of a part has a two-fold effect on the computational cost of the numerical simulation. On one hand the smaller the dimensions of the elements are the smaller the time increments will be. On the other hand a finely discretized problem means the need for more elements to constitute the finite element model. Thus, to maintain the efficiency of a finite element model and at same time to ensure that the accuracy of the results is not jeopardized it is required to perform the mesh sensitivity analyses in order to obtain the most practical mesh density in terms of both accuracy and efficiency.

Three analyses with the same input parameters and different element sizes have been carried out to study the effect of mesh density on the output results of the ice gouging simulations. In Table 5-1 below the element size of each analysis is shown.

Table 5-1 Element sizes used in mesh sensitivity analysis

Analysis	Element Dimensions (m) (length by width by depth)	CPU time ratio (compared to coarse analysis)
Coarse	1.0 x 1.0 x 1.0	1.0
Medium	0.5 x 0.5 x 0.25	20.2
Fine	0.4 x 0.25 x 0.15	95.6

The responses of these three analyses are compared in Figure 5-16 to Figure 5-20 below. These figures indicate that the "*Fine*" mesh barely offers more accuracy over the "*Medium*" mesh. However, the "*Medium*" mesh size provides more precision compared with the "*Coarse*" mesh size. Figure 5-20 shows that mesh density does not influence the berm height development noticeably. Of course it should be noted that these analyses resulted in final berms of more than 3 meters high, it is reasonable to assume that for smaller berm heights the elements depth is crucial.

Considering the satisfactory response convergence for models with "*Medium*" and "*Fine*" mesh sizes, as seen in Figure 5-16 to Figure 5-20, suggests that one could explore the possibility of the existence of a coarser than "*Medium*" mesh size which is still accurate enough for the analyses of this study. However, in order not to lose the subgouge deformation, especially at close distances to the keel where the deformation gradient is more significant, it is required that sufficient number of element are placed immediately beneath the keel base. This is due to the fact that the tracer particles that track the subgouge deformation should initially coincide with model elements. Since a coarser than

the "*Medium*" mesh might not be able to provide adequate number of elements to capture the subgouge deformation it was decided to adopt the "*Medium*" elements size for the meshing scheme of the analyses of this study.

It must be emphasized that the findings of this section is consistent with results presented in the reference publication used in section 5.3(Phillips & Barrett, 2011).

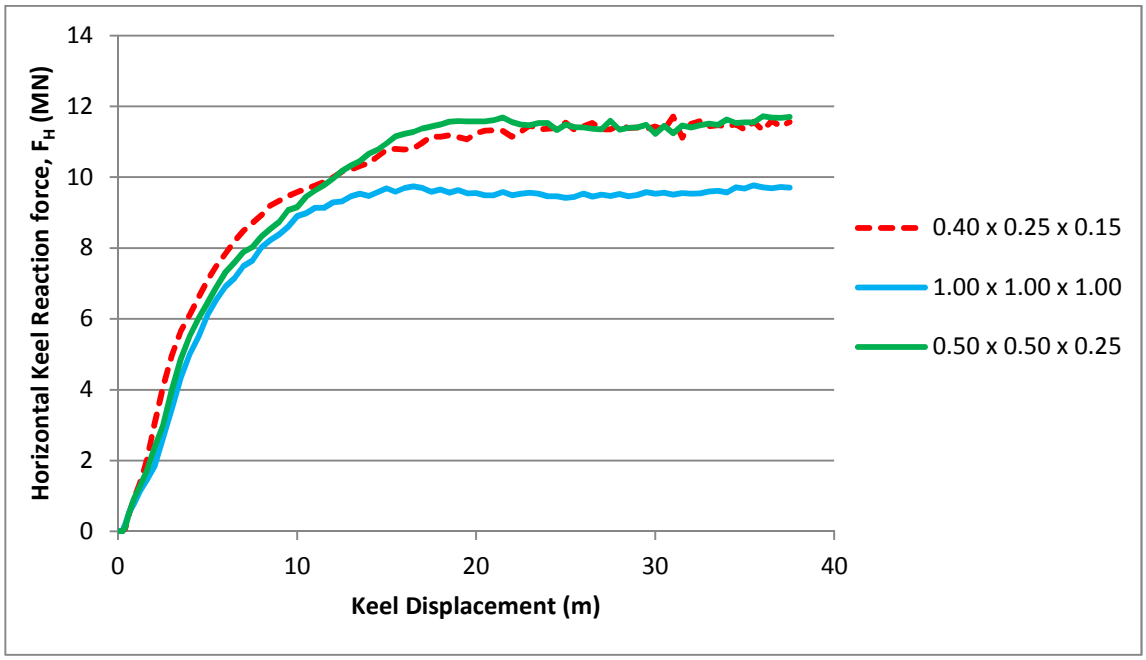

Figure 5-16 Horizontal reaction force comparison for three different mesh densities

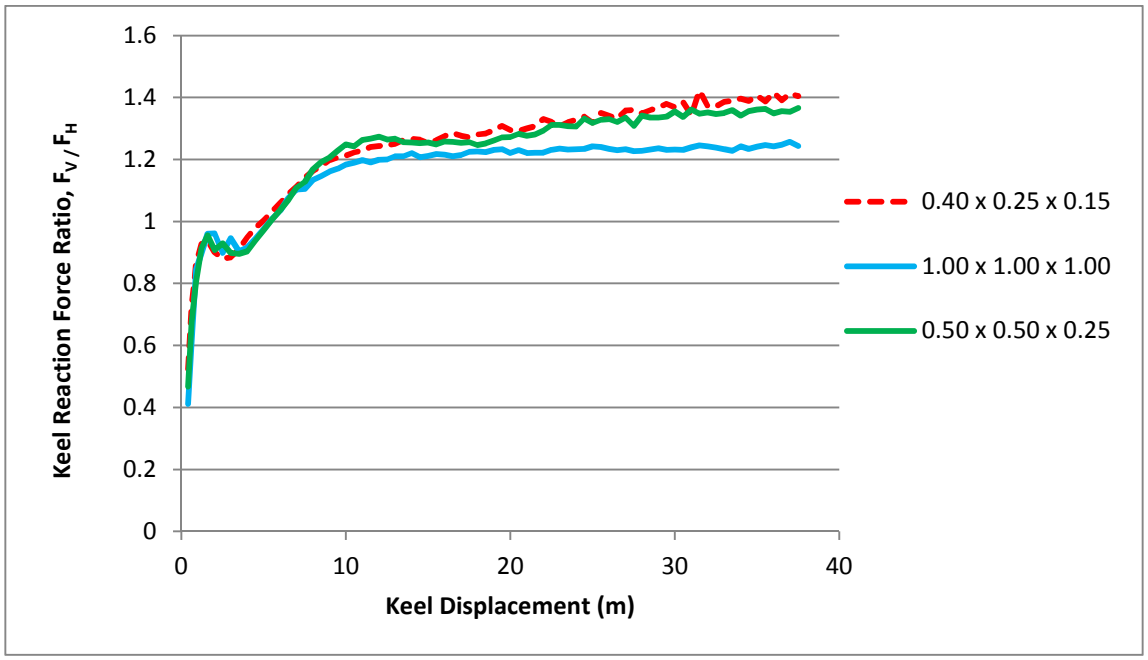

Figure 5-17 Reaction force ratio comparison for three different mesh densities

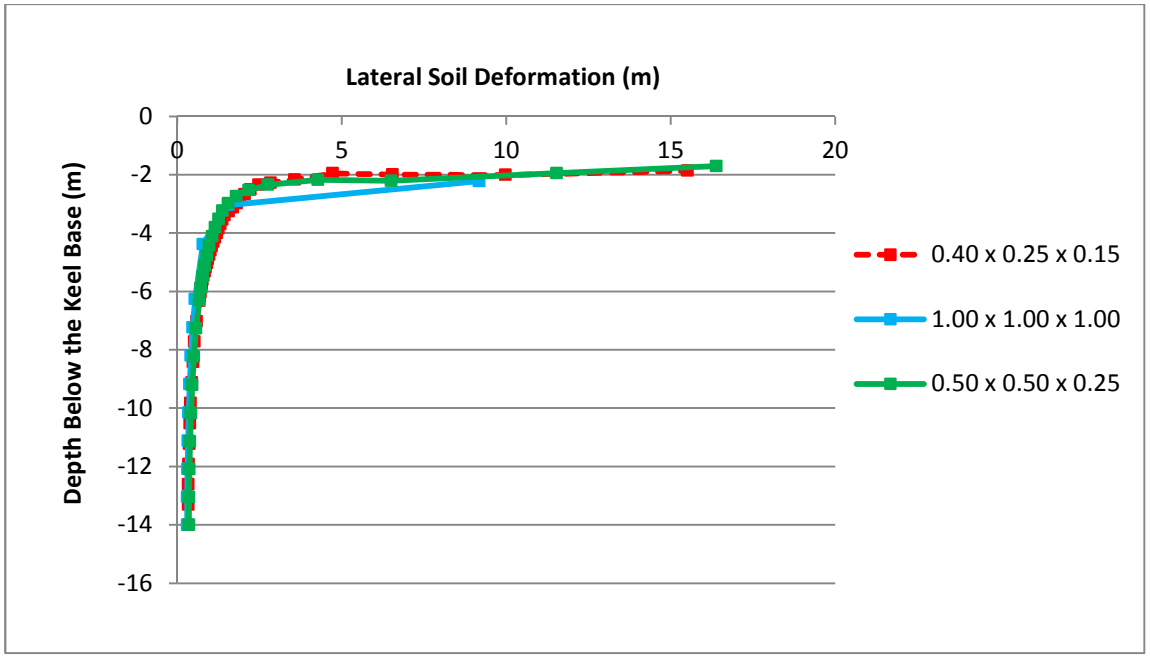

Figure 5-18 Subgouge deformation along the first set of tracer particles

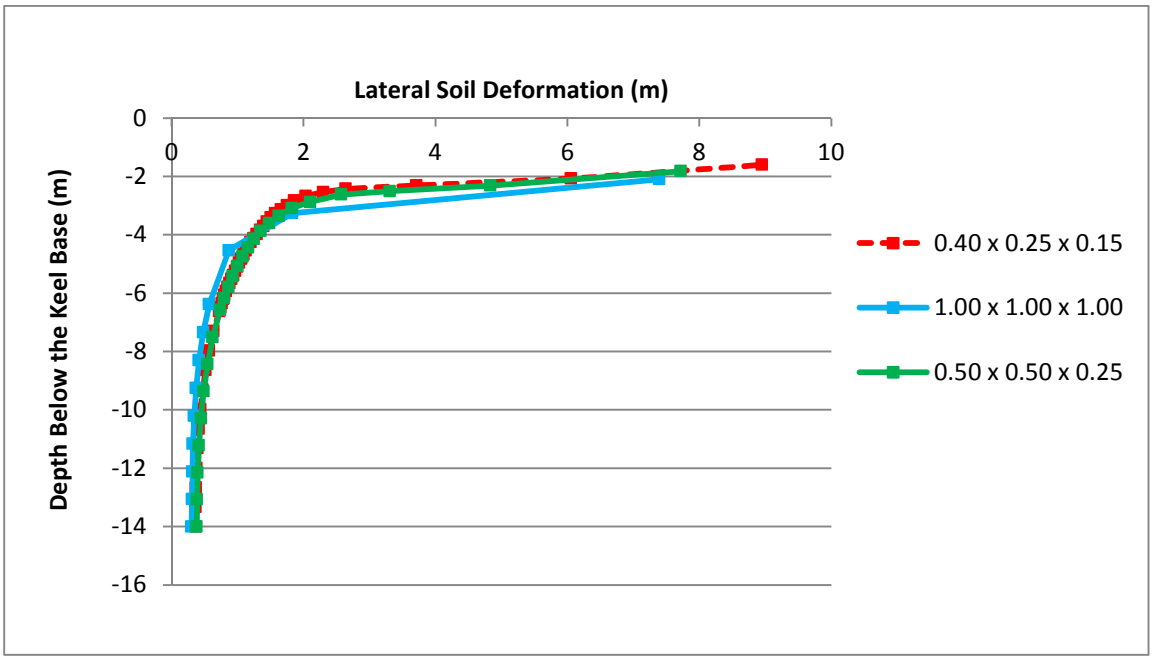

Figure 5-19 Subgouge deformation along the second set of tracer particles

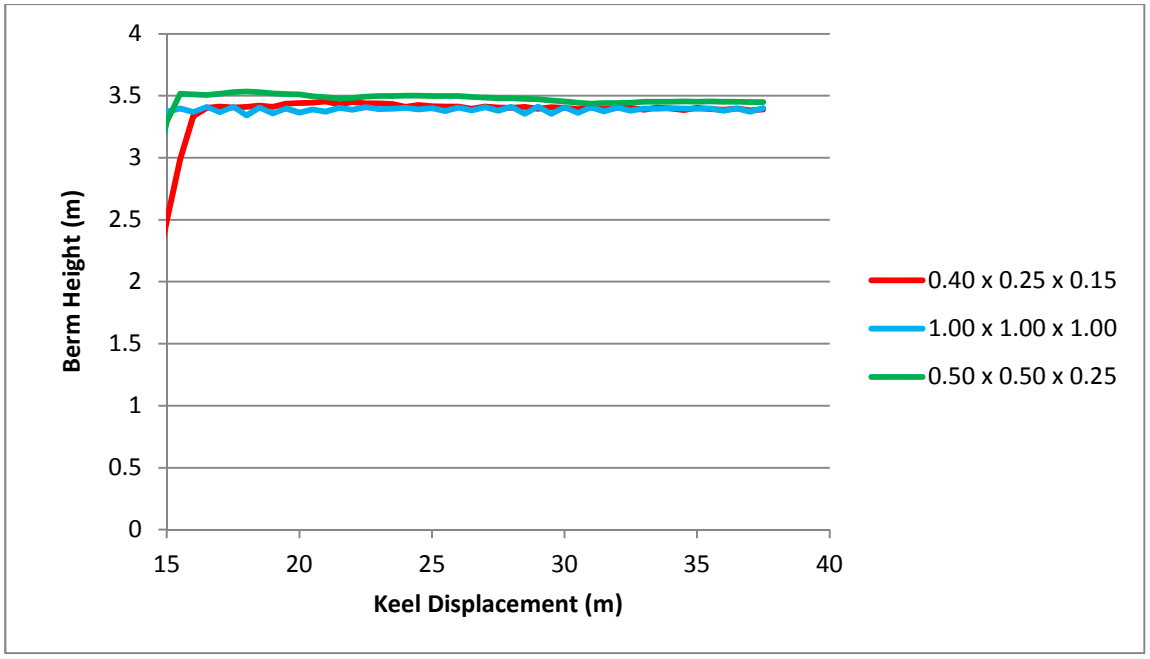

Figure 5-20 Development of berm height in front of keel

In Figure 5-20 berm heights are presented after 15 meters of horizontal gouging since soil responses at steady state are of interest.

5.5. Ice Gouging Sensitivity Analysis Using NorSand

In this section based on the critical state constitutive model NorSand the sensitivity of the ice gouging to the different factors that are involved in this process are studied. This section identifies the significance of these factors in the gouging problem. Among the soil parameters the state parameter, ψ and critical friction angle, M are chosen for sensitivity analyses. Keel attack angle and gouging depth are the other parameters whose significance will be assessed in this section.

Primarily a likely range of variation of these parameters was determined. These tentative variations are based on the expected sand properties and usual keel characteristics and common design gouge depths. Table 5-2 shows the selected range of parameters.

Table 5-2 Range of parameters in the Half-Factorial analysis

Factors	Unit	Low	High
Critical friction angle (M)	-	1.1	1.3
State parameter (ψ)	-	-0.1	0
Attack angle (A)	degree	30	45
Gouging depth (D)	meter	1	2

Other NorSand input parameters that are used in the analyses of this section are summarized in Table 5-3.

Table 5-3 NorSand input parameters

E	ν	Γ	λ	H	OCR
26 MPa	0.32	0.909	0.03	300	2

A total of 16 analyses (2^4) were carried out to study the effect of the contributing factors on the seabed gouging response. Table 5-4 shows the input parameters of these analyses. In this table the finite element results for horizontal keel reaction forces, F_H, and

developed frontal berm height, B, are also summarized. The reaction forces in Table 5-4 are presented for half model.

In following sections the effect of each of the selected factors on the seabed responses are studied in detail.

Table 5-4 Finite Element analyses results and the input parameters

ID	M	ψ (°)	θ (°)	D_s (m)	F_H (MN)	B (m)
1	1.1	-0.1	30	1	4.2	3.4
2	1.3	-0.1	30	1	5.48	3.66
3	1.1	0.0	30	1	3. 3	3
4	1.3	0.0	30	1	3.8	3.1
5	1.1	-0.1	45	1	3.72	4.05
6	1.3	-0.1	45	1	4.86	4.28
7	1.1	0.0	45	1	2.82	3.62
8	1.3	0.0	45	1	3.59	3.8
9	1.1	-0.1	30	2	9.9	4.31
10	1.3	-0.1	30	2	13.76	4.54
11	1.1	0.0	30	2	7.35	3.84
12	1.3	0.0	30	2	9.88	4.08
13	1.1	-0.1	45	2	7.69	5.01
14	1.3	-0.1	45	2	10.27	5.22
15	1.1	0.0	45	2	5.9	4.46
16	1.3	0.0	45	2	7.48	4.63

5.5.1. Critical Stress Ratio

The analyses confirm that the critical stress ratio directly correlates with the keel reaction forces. This implies that as the shear strength of the soil increases more driving forces are required in order to reach the steady state in the ice gouging event. The positive effect of the critical stress ratio on the keel reaction forces could be understood in Figure 5-21. This figure compares the responses of several analyses in which different state

parameters, attack angles and gouging depths are used. In reality it is also expected that a soil with higher shear strength shows more resistance to the gouging element.

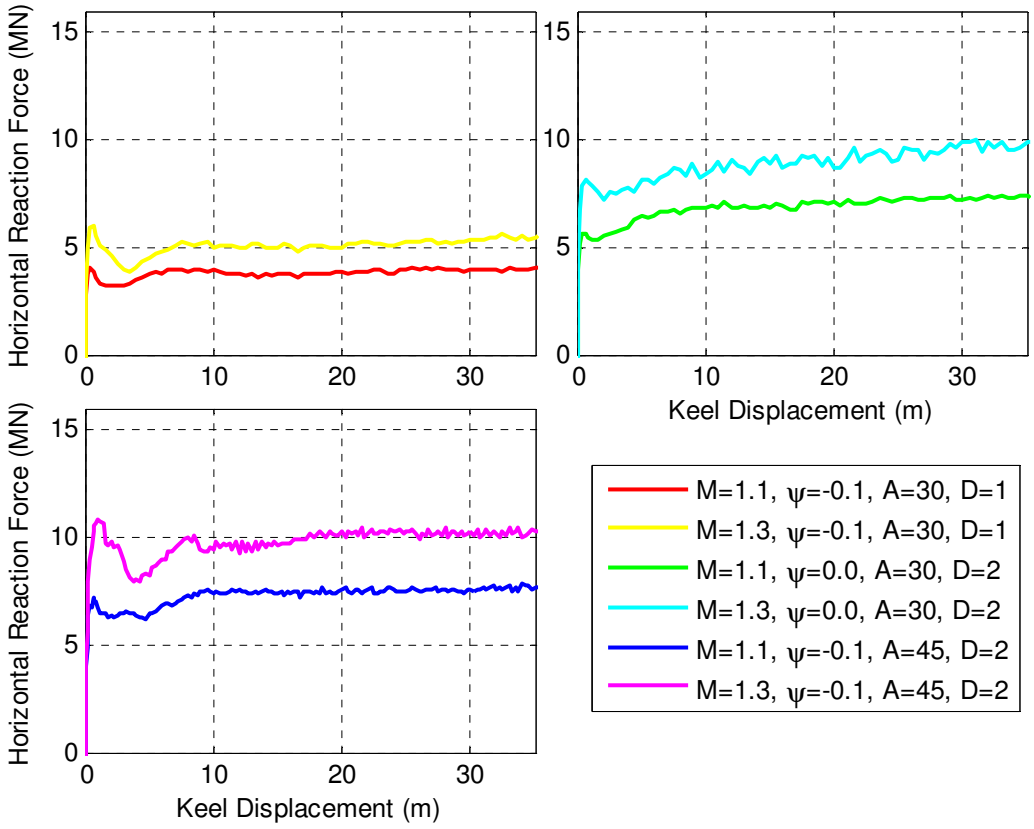

Figure 5-21 Effect of critical stress ratio on the keel reaction force

The critical stress ratio has direct effect on the developed height of the frontal berm as well. Figure 5-22 shows that regardless of other parameters, the berm height consistently enlarges with the increasing shear strength of the soil. In this figure only the final period of ice gouging in which the steady state is achieved are shown.

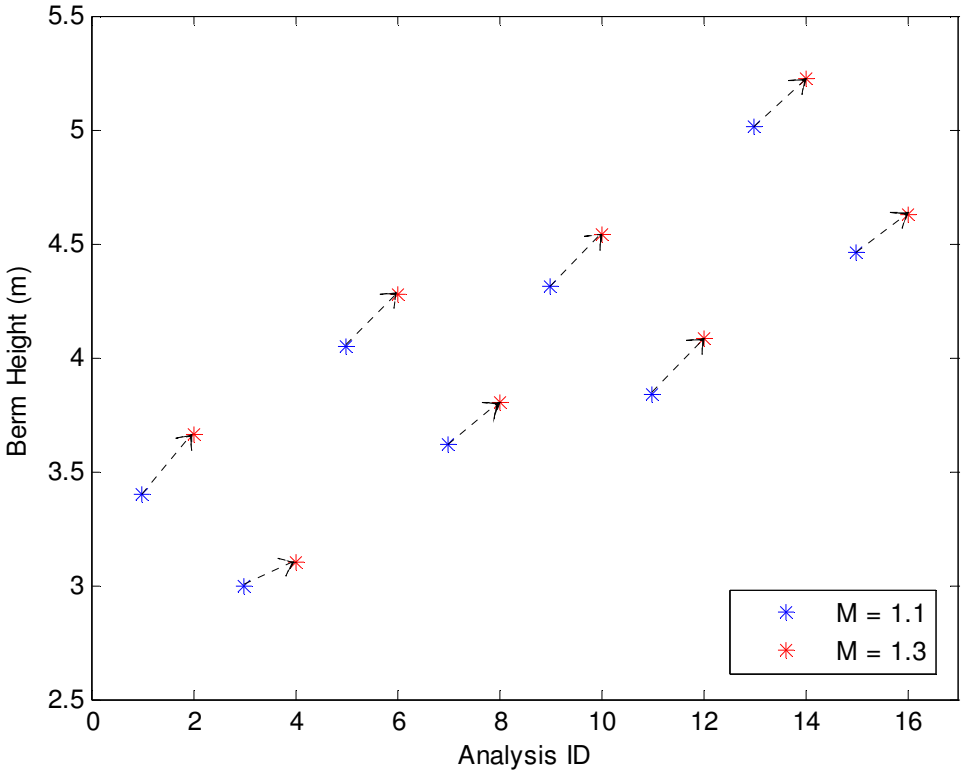

Figure 5-22 Effect of critical stress ratio on the berm height development

Another interesting aspect of the ice gouging is the sub-gouge deformation of the seabed. In Figure 5-23 and Figure 5-24 the sub-gouge deformation at the place of the tracer particles #2 are presented for several analyses. The sub-gouge profiles shown in these figure represent the steady state of the soil. These results barely reveal any certain information that links the critical stress ratio to the mechanism of the sub-gouge deformation. However, seemingly the critical stress ratio becomes more influential for deeper gouges in contrast to the shallower gouging depth in which the sub-gouge profiles are similar for the analyses with varying critical stress ratio, *M*. It could be concluded that the combination of the critical stress ratio and the state parameter has a noticeable

influence on the seabed sub-gouge deformation rather than the effect of the critical stress ratio alone.

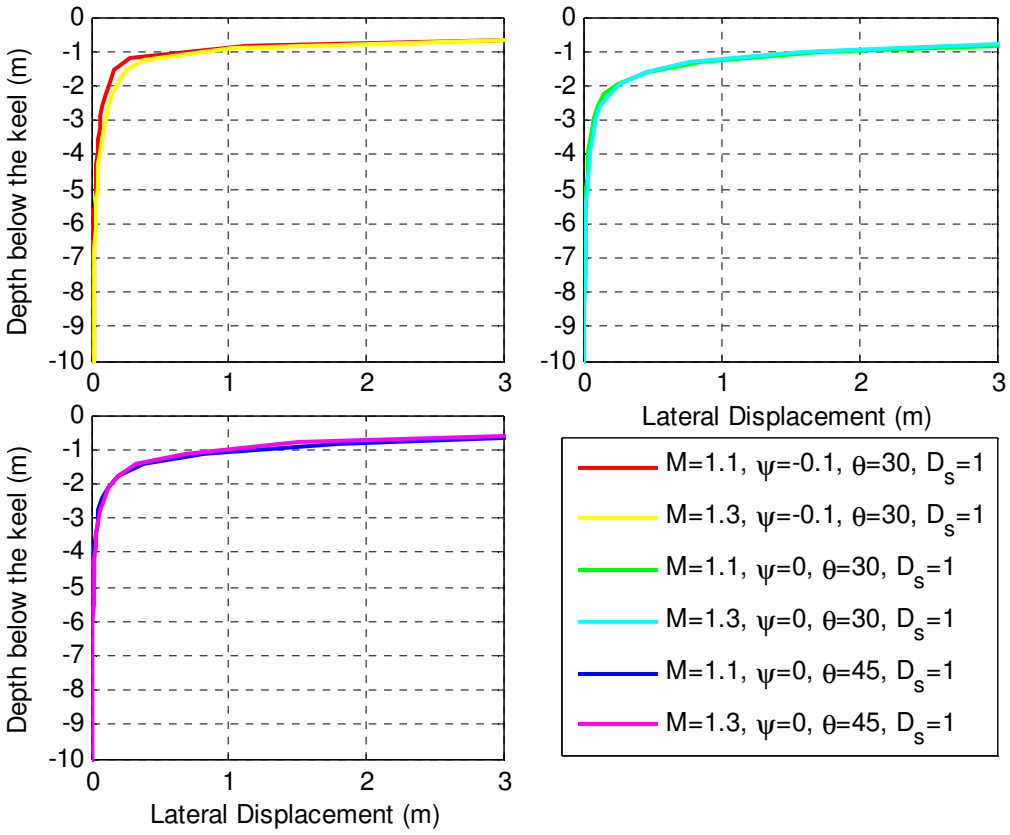

Figure 5-23 Effect of critical stress ratio on the sub-gouge deformation (gouging depth of 1 m)

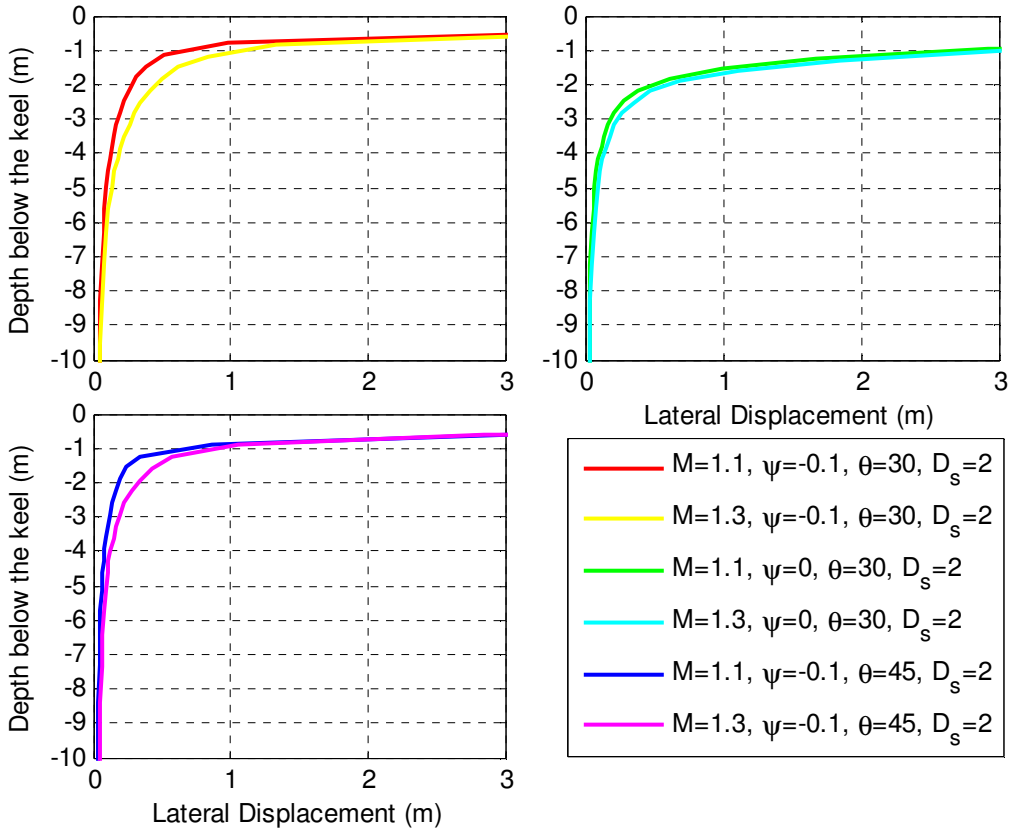

Figure 5-24 Effect of critical stress ratio on the sub-gouge deformation (gouging depth of 2 m)

5.5.2. State Parameter

In this section the effects of the state parameter on the gouging event is investigated. Based on the performed analyses of this chapter, a reverse correlation between the state parameter and keel reaction forces is evident. That is for a specific soil with higher negative state parameter greater keel reaction forces are expected to be materialized at the steady state condition. This relationship could be visually comprehended in Figure 5-25. This figure shows the consistency of the relationship between state parameter and the keel reaction force for different critical stress ratios, attack angles and the gouging depths. Given that physically the state parameter is best an implication of the relative density of

the soil, in reality it is expected that similarly more compact soils generate greater keel reaction forces before the steady state condition is reached.

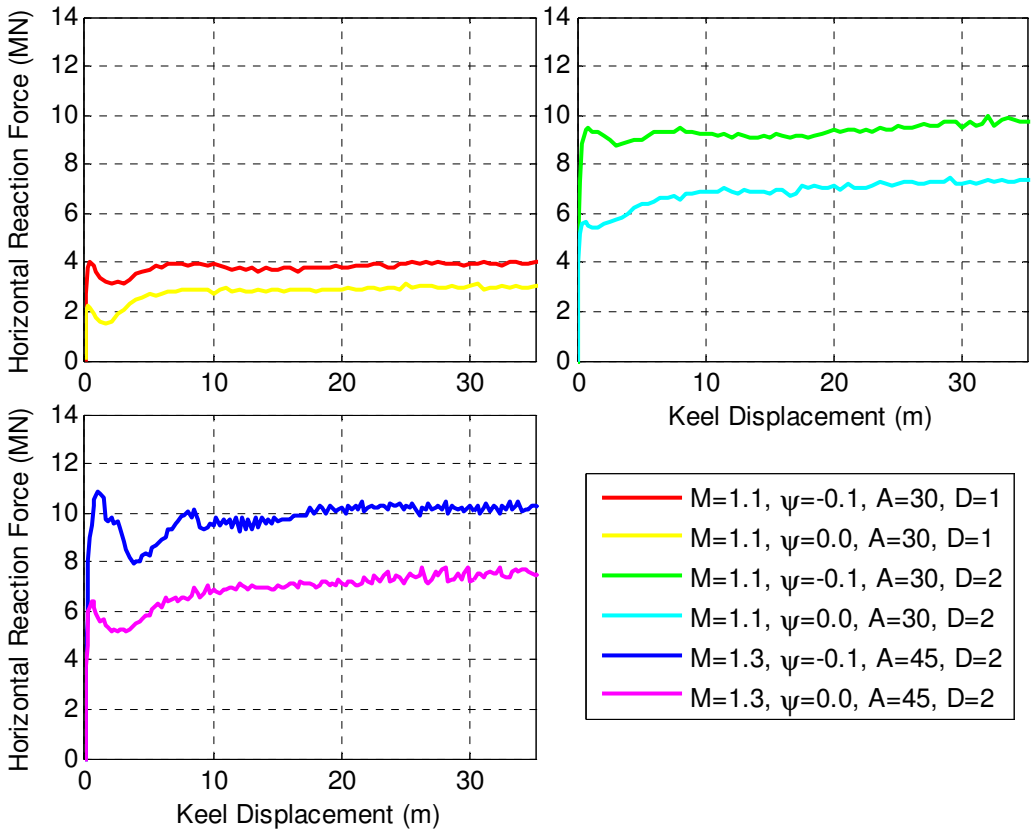

Figure 5-25 Effect of state parameter on the keel reaction force

The state parameter has also a clear direct effect on the development of the frontal berm height. Figure 5-26 shows how denser material could lead to the formation of a larger frontal berm at steady state. As this figure shows regardless of critical stress ratio, attack angle or the gouging depth the soil behaves in this way. Since the rate of dilation is specifically a function of the state parameter, i.e. the distance between the current state and the critical state, it is sensible to infer that a soil with more negative state parameter exhibits a larger berm height by triggering the dilation mechanism.

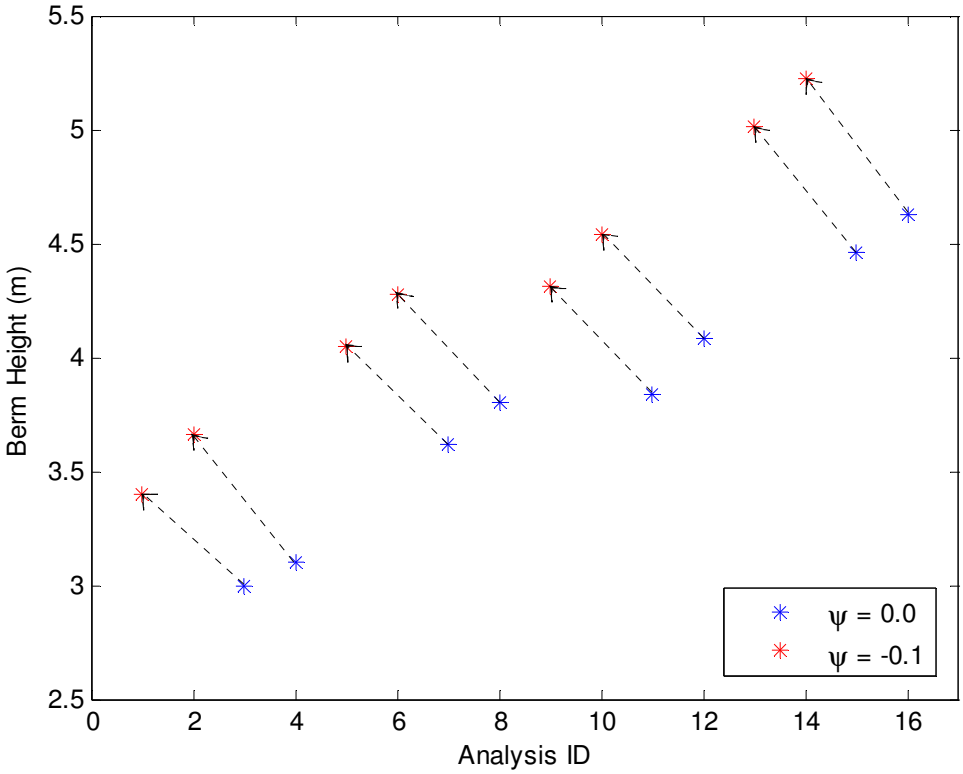

Figure 5-26 Effect of state parameter on the frontal berm development

Based on the results of the performed analyses, shown in Figure 5-27 and Figure 5-28, the extension of the sub-gouge deformations becomes shallower as the soil becomes denser, i.e. the state parameter is more negative. This observation is consistent in several analyses shown in Figure 5-27 and Figure 5-28 regardless of critical stress ratio, attack angle or gouging depth.

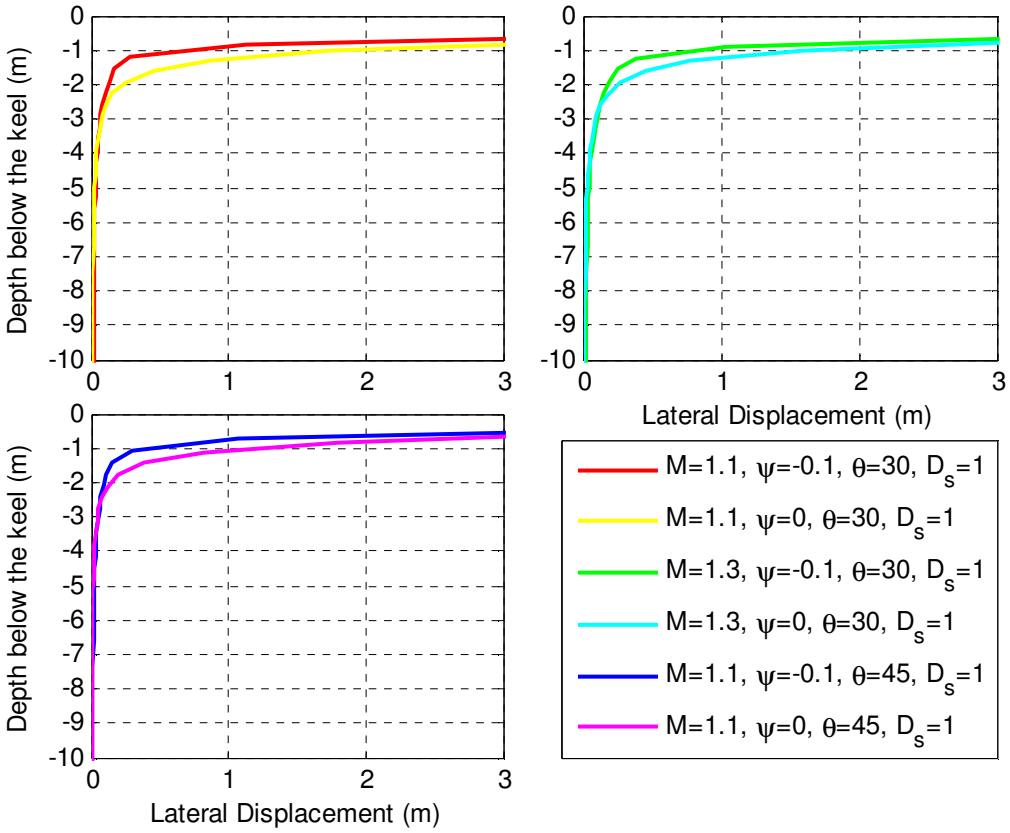

Figure 5-27 Effect of state parameter on the sub-gouge deformation (gouging depth of 1 m)

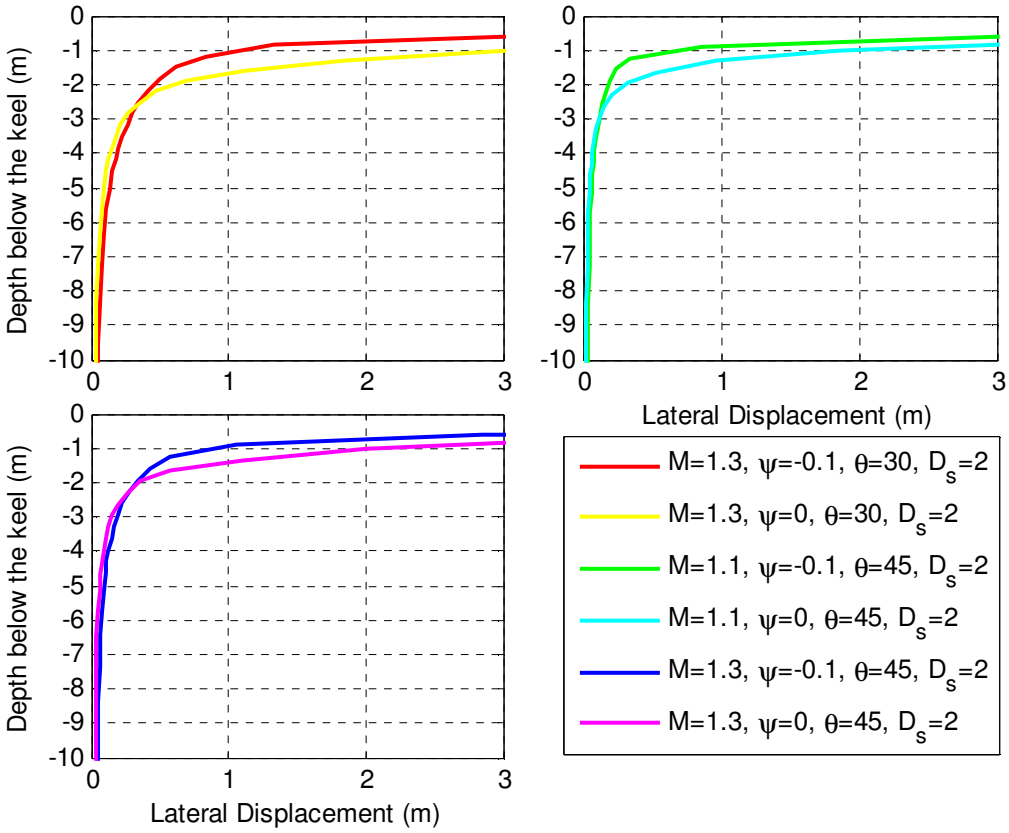

Figure 5-28 Effect of state parameter on the sub-gouge deformation (gouging depth of 2 m)

Figure 5-29 and Figure 5-30 show the development of the equivalent plastic strain for respectively a dense soil and a loose soil. As these figures show the equivalent plastic strains extend deeper in the dense soil. One of the causes of the deeper spread of the plastic strains in the dense soil is the development of larger frontal berm due to the higher dilation rates of the dense soil. In addition, the denser soil produces more shear stress under keel/soil interaction which extends deeper into the soil

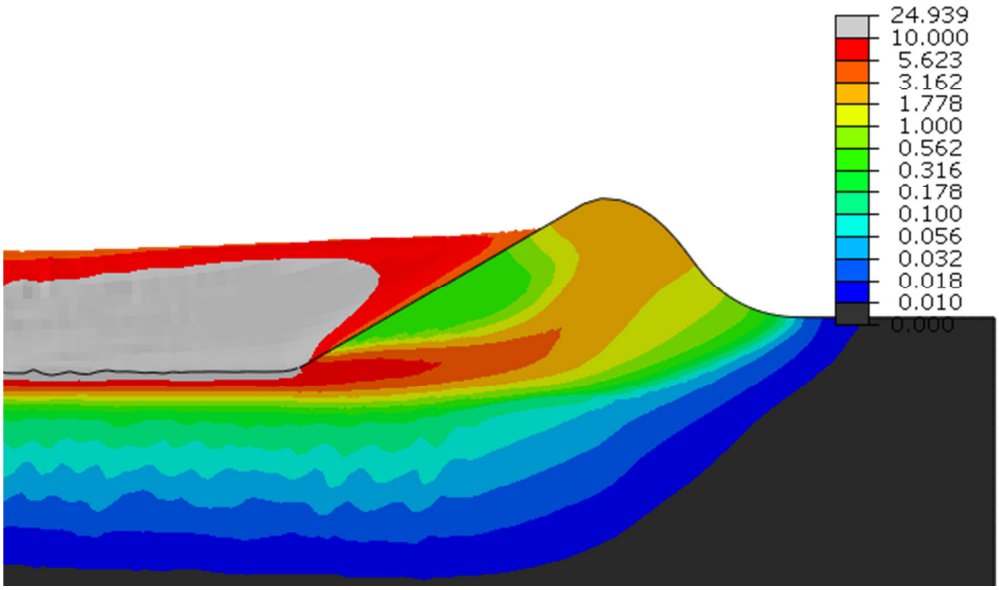

Figure 5-29 Equivalent plastic strains for a gouging analysis on dense soil

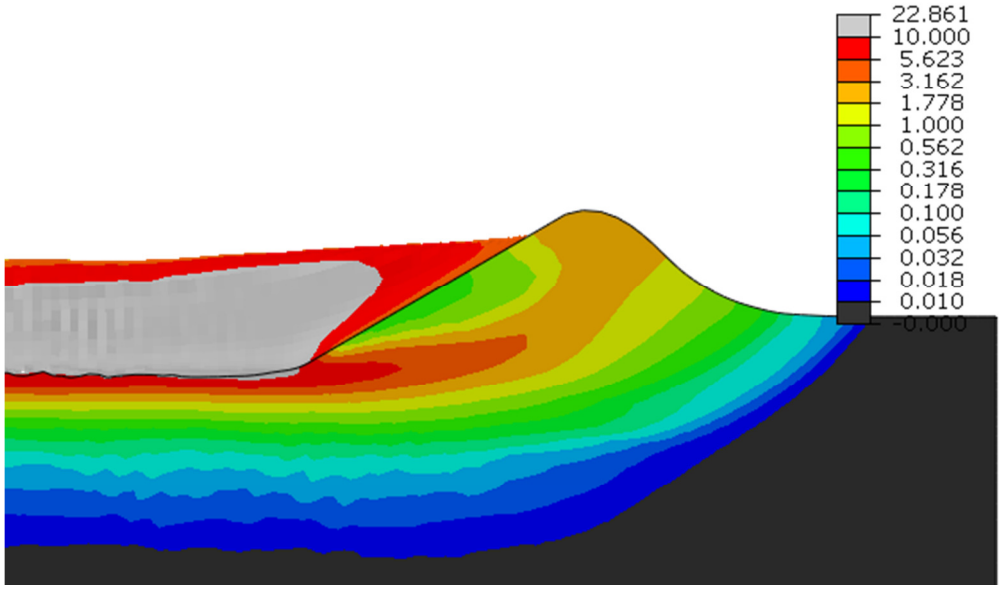

Figure 5-30 Equivalent plastic strains for a gouging analysis on loose soil

5.5.3. Attack Angle

This section considers attack angle of the ice feature as an independent variable and studies its consequences in a gouging event. Based on the Figure 5-31 an apparent

relationship between the keel reaction force and the attack angle could not be established. This figure shows that for shallower gouges the reaction forces remain practically unchanged for greater attack angles. However, in deeper gouges higher reaction forces are produced when attack angle decreases. Therefore, the combined influence of attack angle with the gouging depth should be considered too. Physically the increase of attack angle means less contact surface between the soil and the keel and therefore a smaller reaction force should be expected. Nevertheless, as it will be explained the increase of the attack angle causes a larger frontal berm height which generally translates to larger ice/soil contact forces. Depending on the balance of these two opposing factor, increase of frontal berm height and decrease of contact surface, the increase of attack angle could either increase or decrease the keel reaction force.

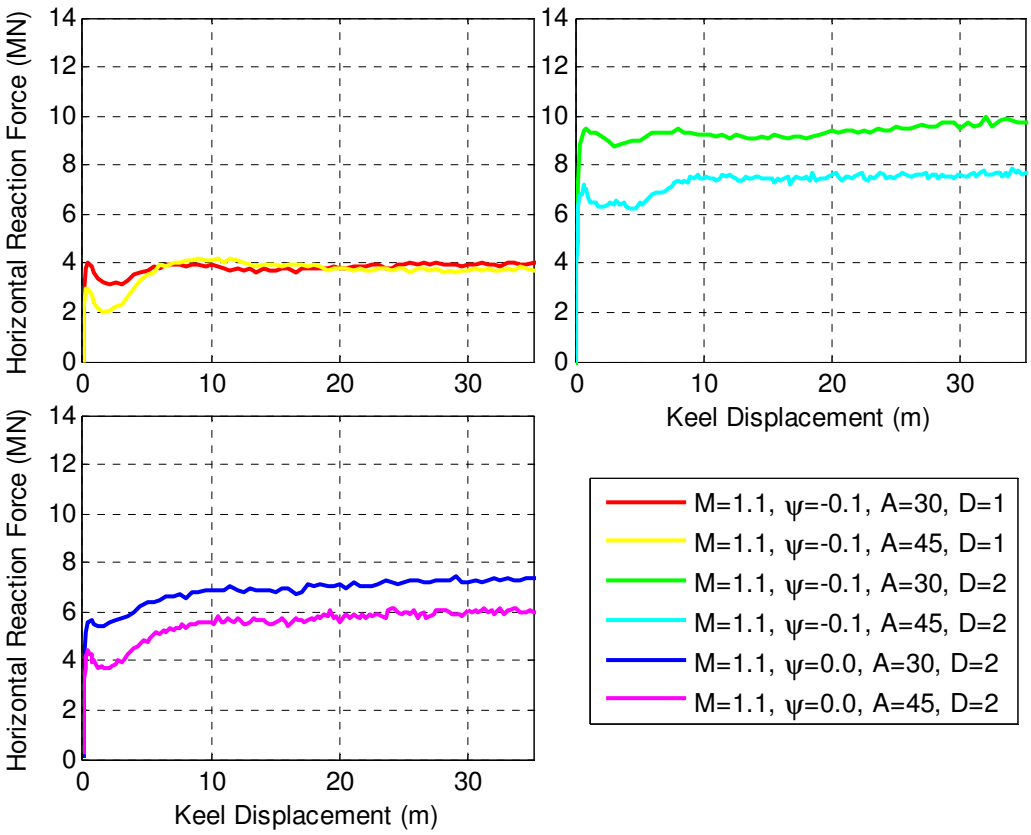

Figure 5-31 Effect of attack angle on the keel reaction force

As mentioned earlier, the increase of attack angle clearly leads to development of larger frontal berm height regardless of the level of other factors such as critical stress ratio, state parameter and gouging depth. This behaviour is depicted in Figure 5-32 for several analyses.

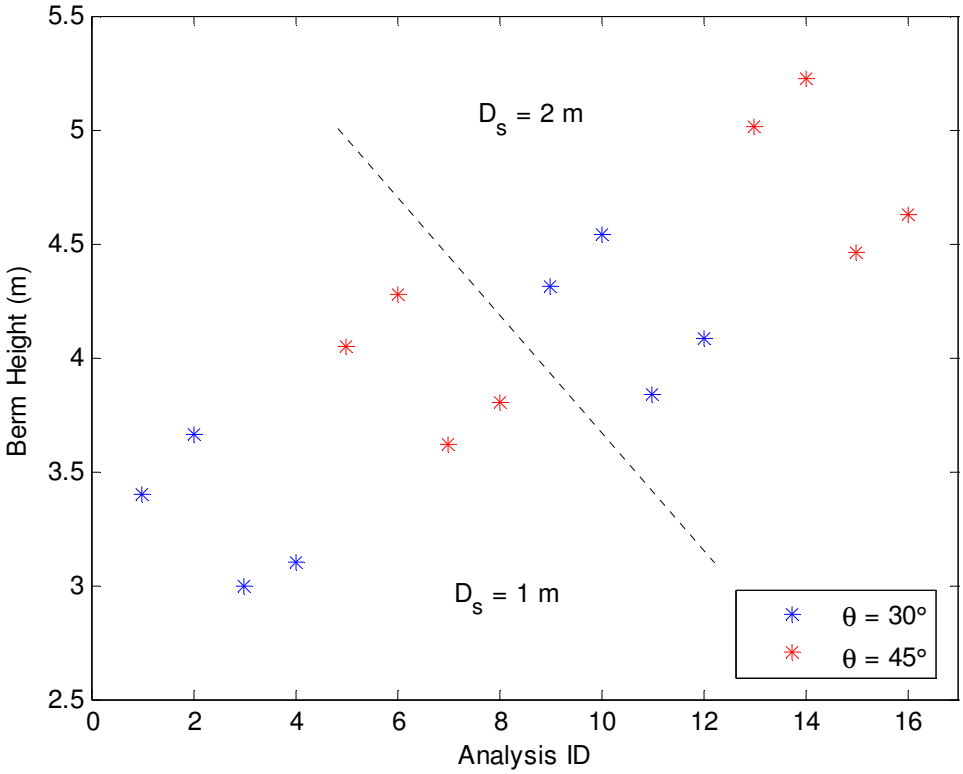

Figure 5-32 Effect of attack angle on the berm height development

Based on the Figure 5-33 and Figure 5-34 the increase of the attack angle reduces the vertical extension of the sub-gouge deformation. This behaviour is seemingly general and does not depend on the state of other parameters that are studied in this section.

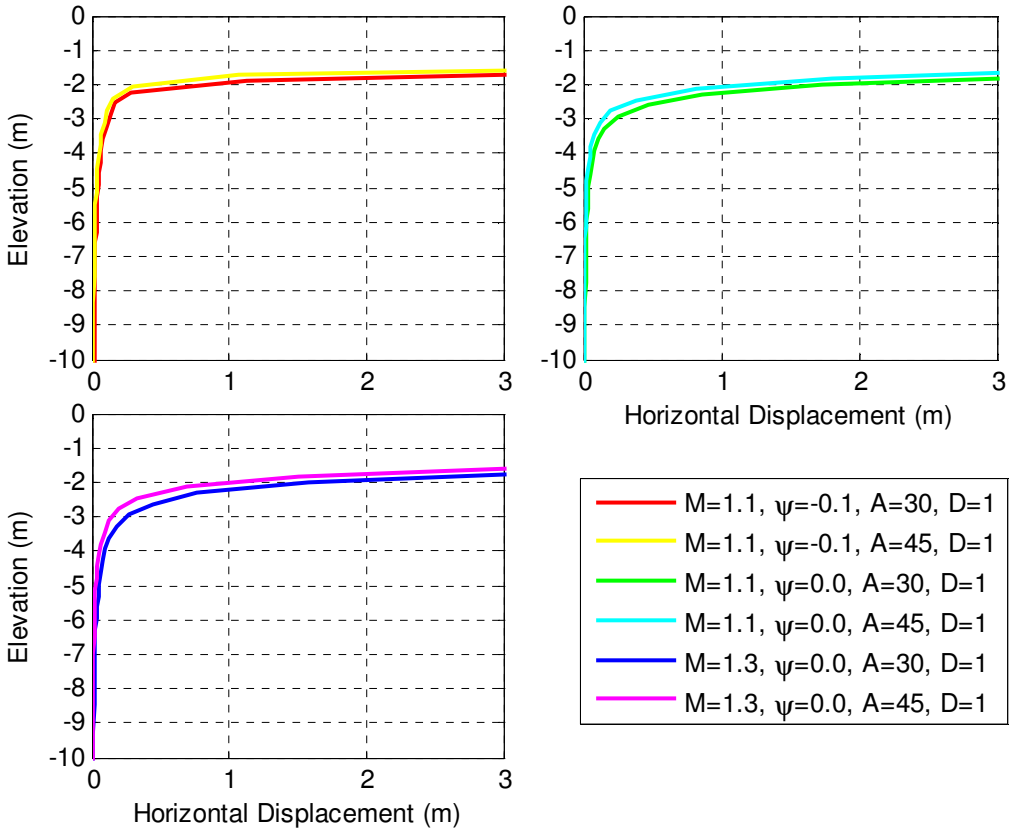

Figure 5-33 Effect of attack angle on the sub-gouge deformation (gouging depth of 1 m)

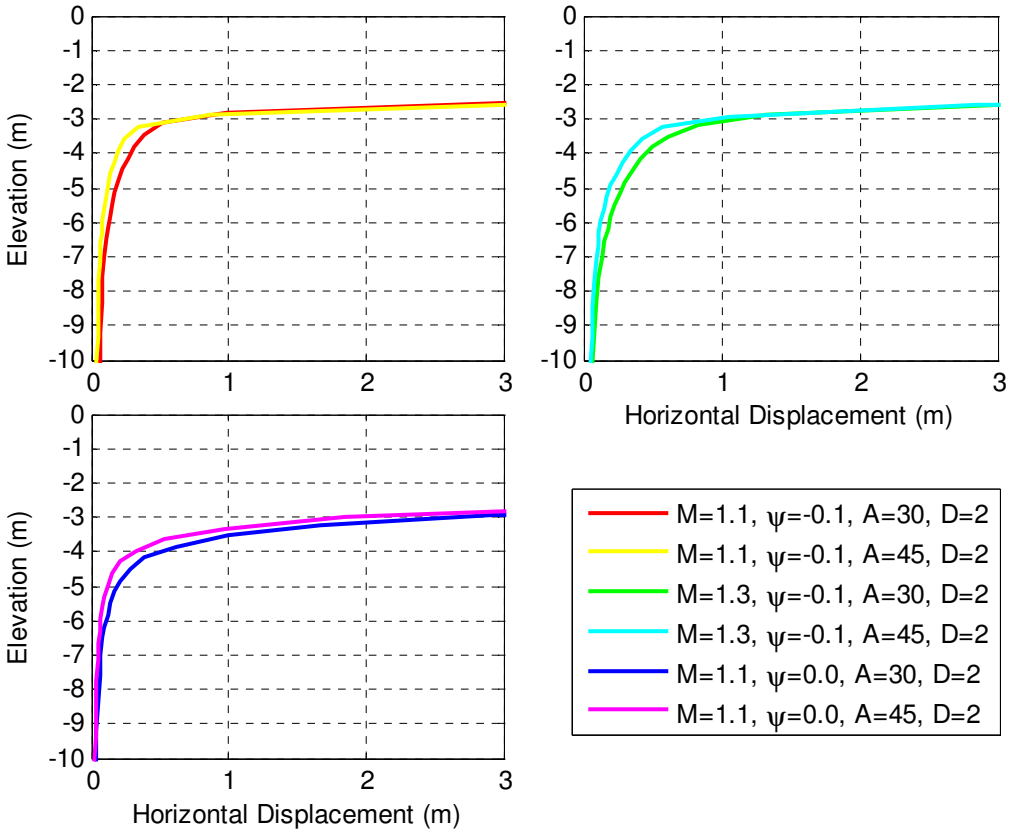

Figure 5-34 Effect of attack angle on the sub-gouge deformation (gouging depth of 2 m)

Figure 5-35 and Figure 5-36 show the development of the equivalent plastic strain for ice gouging analyses with the attack angles of respectively 30 degrees and 45 degrees. Figure 5-35 shows that for lower attack angles a high shear strain band is formed almost along the gouging path. On the other hand a dead wedge with relatively low plastic strain is developed in front of the keel which travels with the moving keel.

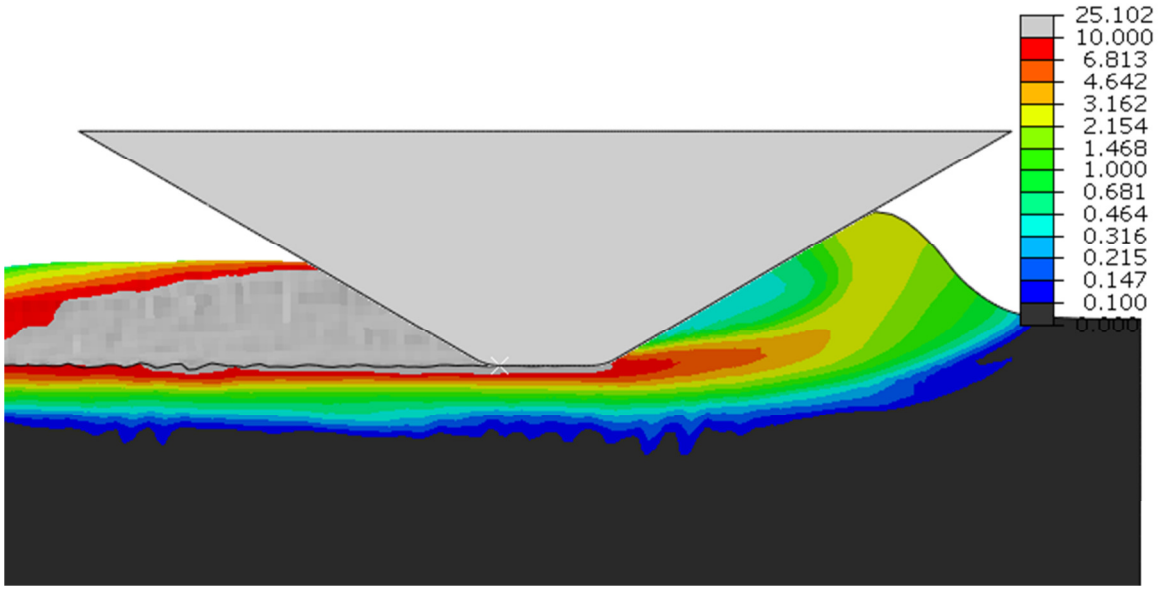

Figure 5-35 Equivalent plastic strains for a gouging analysis with keel angle of 30 degrees

The high shear strain band in gouging analyses using a keel with higher attack angle like 45 degrees tends to move upward in front of the keel as shown in Figure 5-36. This leads to higher frontal berm heights for higher keel attack angles.

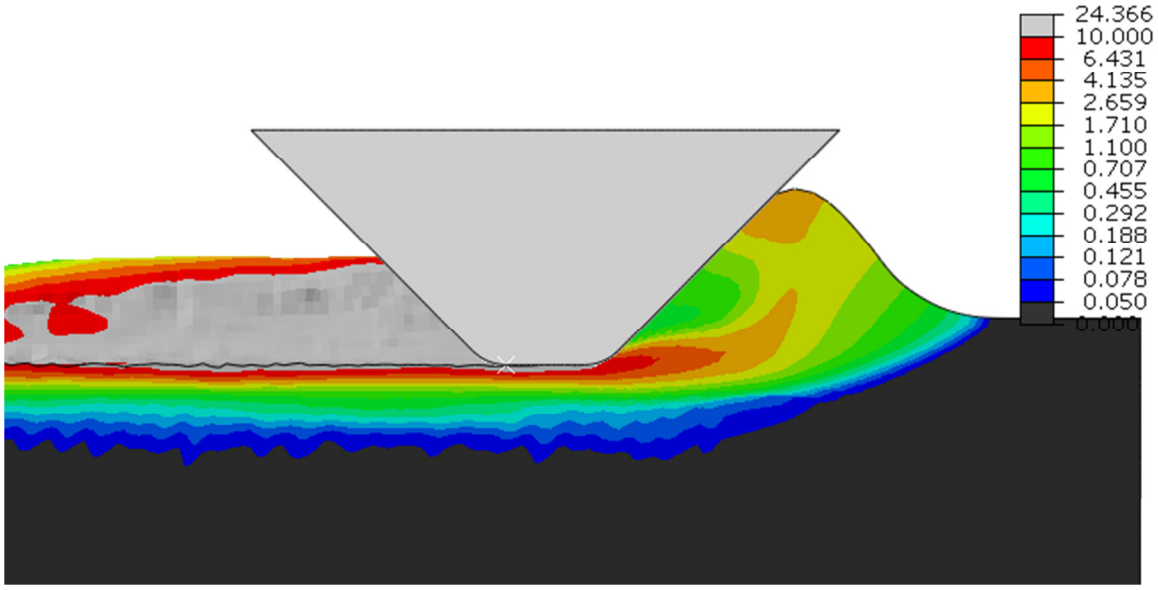

Figure 5-36 Equivalent plastic strains for a gouging analysis with keel angle of 45 degrees

The gouging mechanism shown in Figure 5-36 results in a scratching like removal of the soil from the front of the keel. On the other hand such a removal mechanism of the soil reduces the vertical extend of the sub-gouge deformations. Figure 5-37 and Figure 5-38 show the contours of sub-gouge deformations for the same type of a soil with keel angle of 30 degrees and 45 degrees respectively.

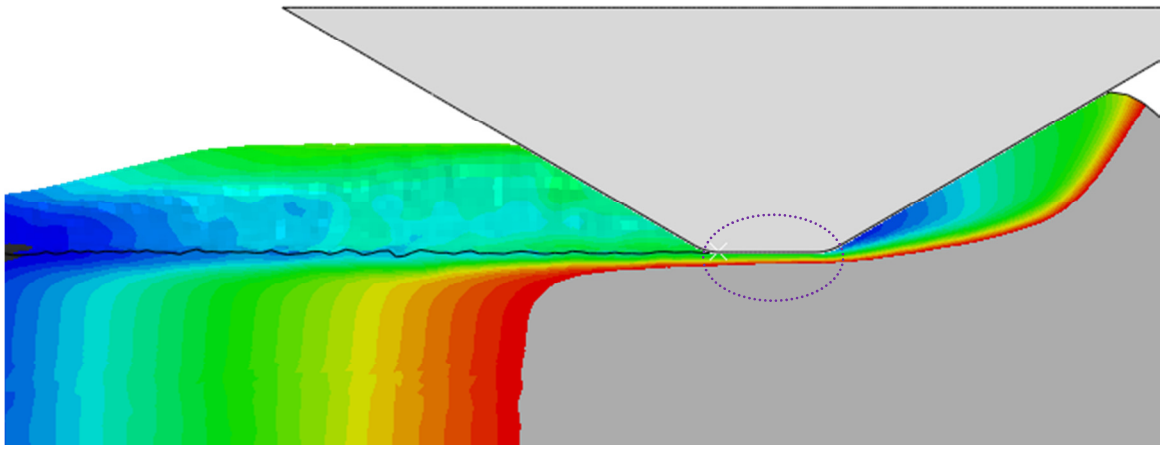

Figure 5-37 Sub-gouge deformations for a gouging analysis with keel angle of 30 degrees

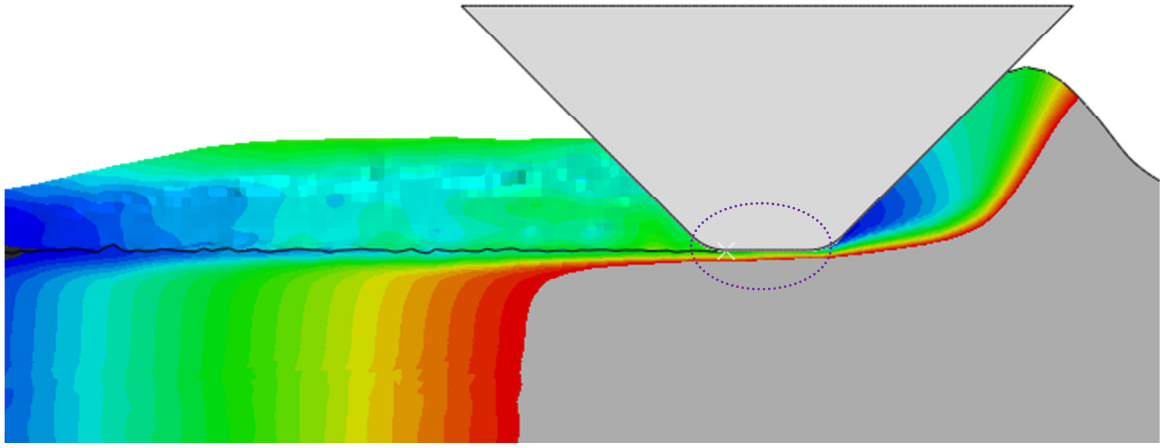

Figure 5-38 Sub-gouge deformations for a gouging analysis with keel angle of 45 degrees

The soils underneath the keels in Figure 5-37 and Figure 5-38, specified in purple oval, are zoomed in in the Figure 5-39.

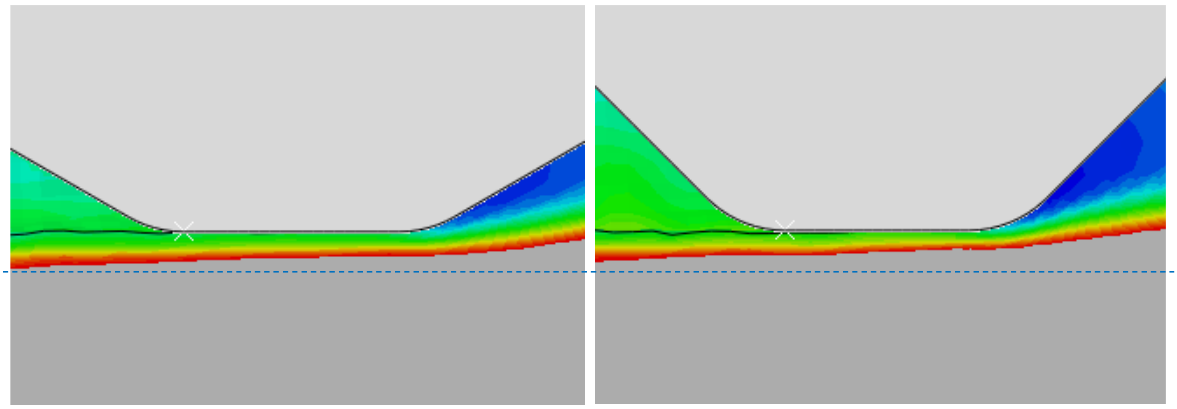

Figure 5-39 Sub-gouge deformations below the keel for attack angle of 30° and 45°

In this figure the blue horizontal line shows that the sub-gouge deformations are higher in the gouging event with keel angle of 30 degrees. The scratching mechanism that earlier explained is also evident in this figure.

As it was discussed in this section, the change in attack angle shows relatively little difference in horizontal force. As the indenter is fixed this is expected. The assumption that the keel maintains a constant gouging depth is common in current numerical analyses of the ice gouging. However, it should be noted that allowing the keel to move vertically has significant consequence on sub-gouge deformation especially if the pipeline is also modeled in the analysis. Allowing the vertical and rotational degrees of freedom results in less conservative designs.

5.5.4. Gouging Depth

As expected the most influential factor in a gouging event is the gouging depth. Figure 5-40 shows the horizontal keel reaction forces of several analyses. This figure

shows that the increase in the gouging depth has a direct effect on the keel reaction forces which consistency increases regardless of the other involved factors.

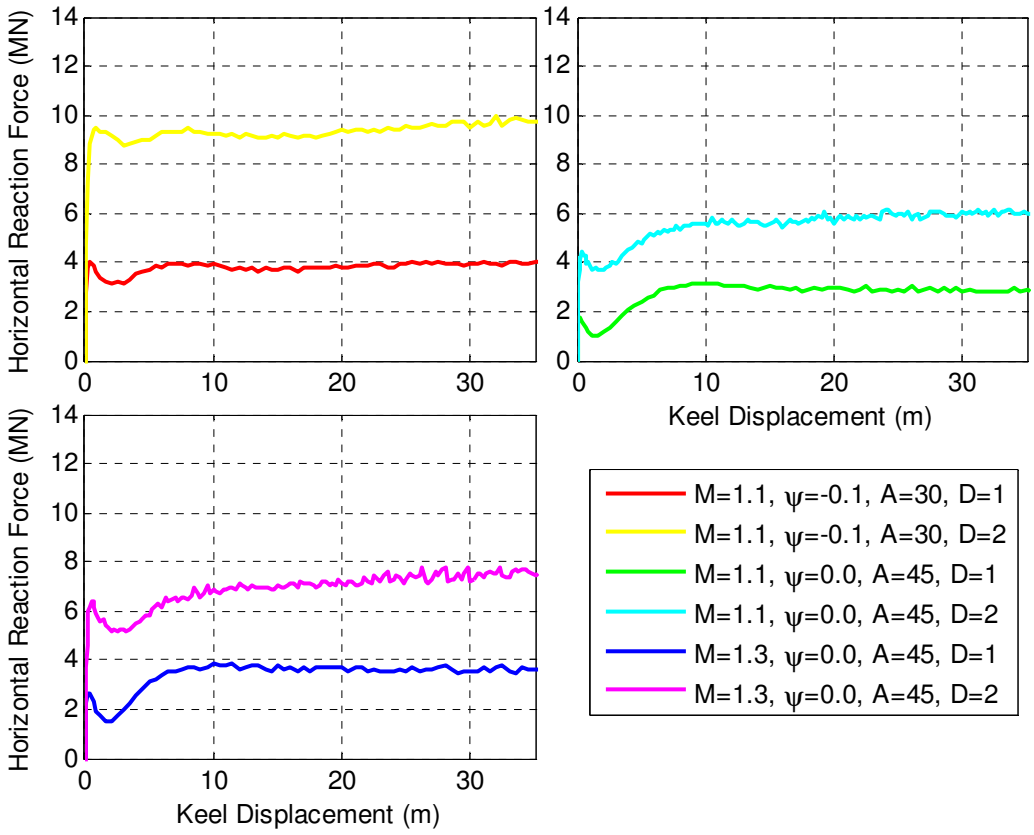

Figure 5-40 Effect of gouging depth on the keel reaction force

The gouging depth has also a clear direct effect on the development of the frontal berm height as can be seen in Figure 5-41. This figure shows that the increase in the frontal berm height due to the increase of the gouging depth is independent form other contributing factors in the gouging event.

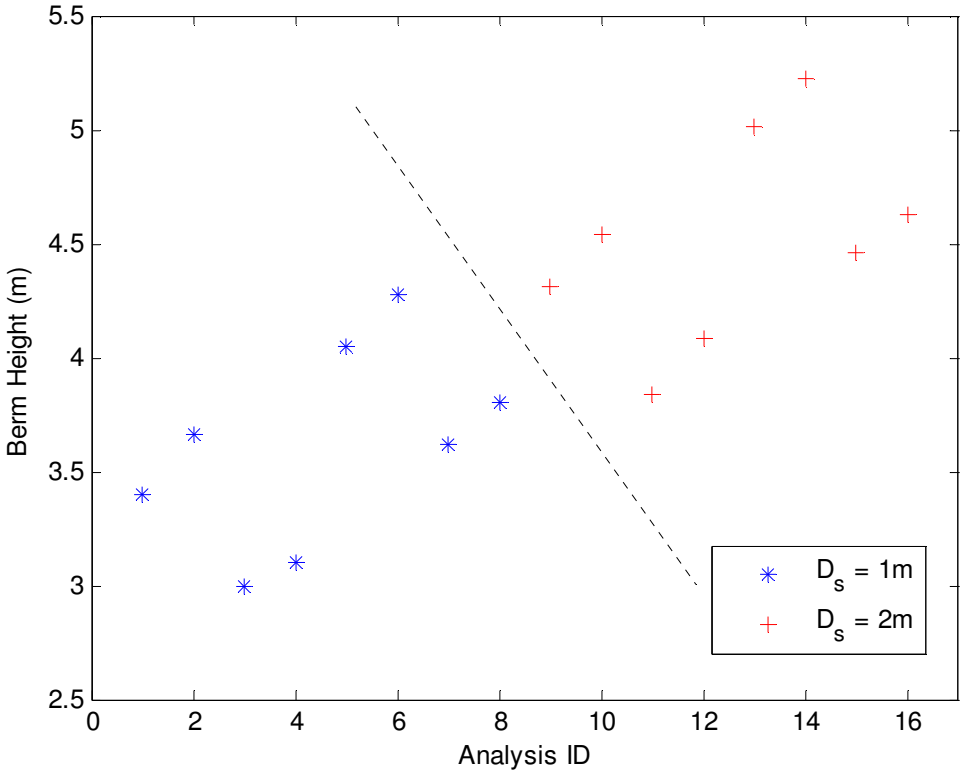

Figure 5-41 Effect of gouging depth on the berm height development

Figure 5-42 and Figure 5-43 compare the sub-gouge deformations of the several gouging analyses and illustrate the effect of the gouging depth. In these figures the sub-gouge profiles are scaled to make the comparison between one and two meters gouging depths possible. It could be concluded that deeper gouging depths result in larger sub-gouge deformations.

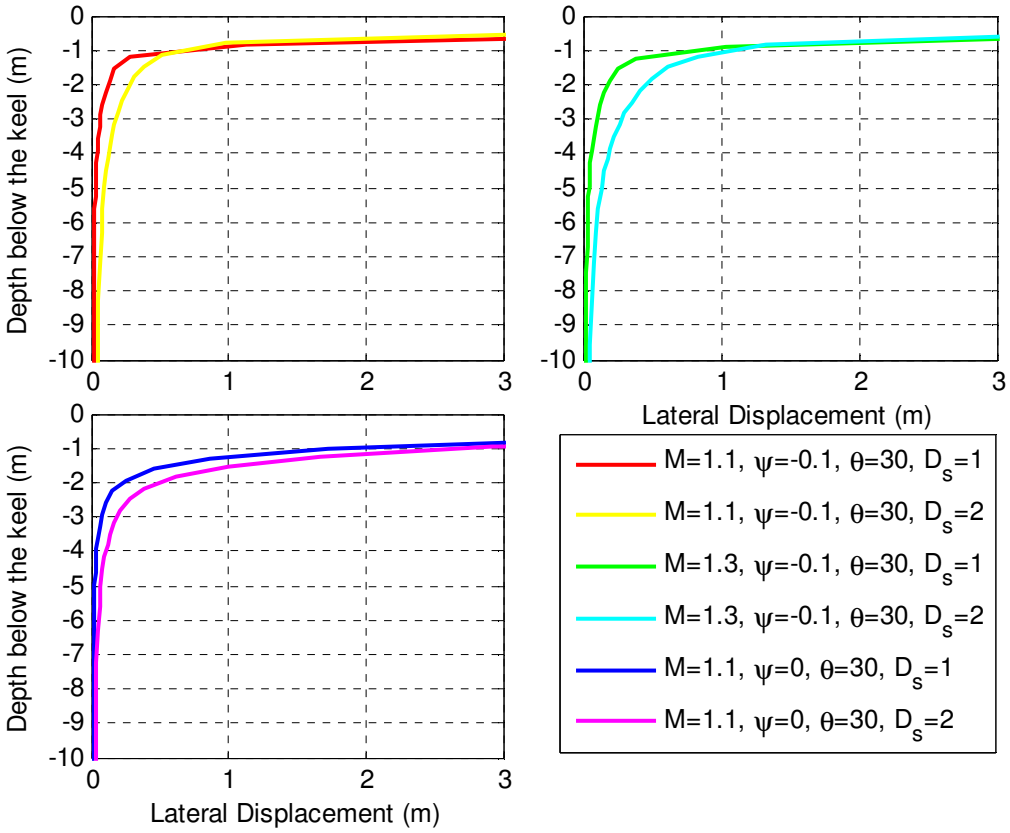

Figure 5-42 Effect of gouging depth on the sub-gouge deformation (attack angle of 30 degrees)

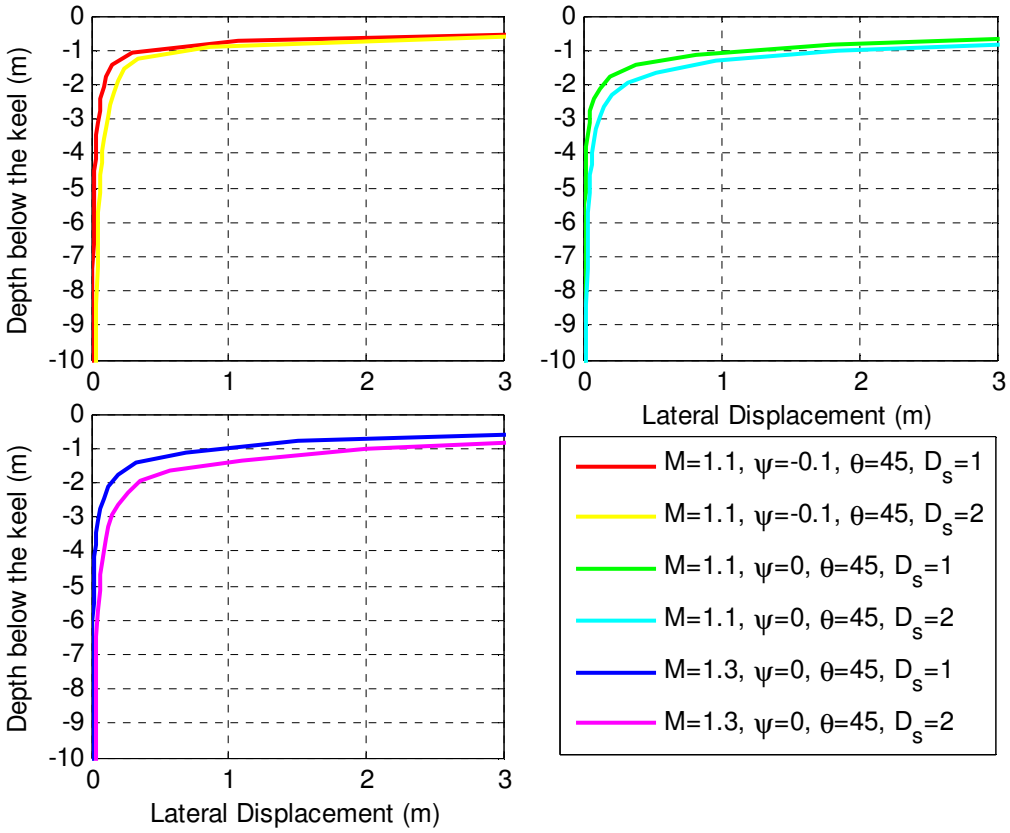

Figure 5-43 Effect of gouging depth on the sub-gouge deformation (attack angle of 45 degrees)

5.5.5. Critical State in Gouging Process

In these analyses the values of the state parameter were either 0.0 or -0.1. A state parameter of -0.1 represents an extremely dense soil which tends to dilate before it reaches to critical state. In Figure 5-44 the contours of the state parameter in a gouging analysis of such a dilative soil is depicted. In this figure the regions where the state parameter approaches to zero is coloured. As it can be seen when the keel gouges the seabed soil the high sheared regions, including the areas adjacent to the gouging path and the soil in front of the keel which resists the keel movement, reach the critical state, i.e. the state parameter becomes zero. The development of the zero state parameter is an important feature of the constitutive model NorSand which is used in these analyses.

Achievement of zero state parameter in highly sheared areas of the soil ensures that the dilative behaviour of the soil ceases at some point the way the critical state theory requires. The zero state parameter in front of the keel avoids the formation of unrealistic frontal berm heights due to the excessive dilation as is an issue with the built-in Cap model in the ABAQUS. The zero state parameter at the same time control the growth of the yield surface which is important for reaching to the steady state condition under gouging.

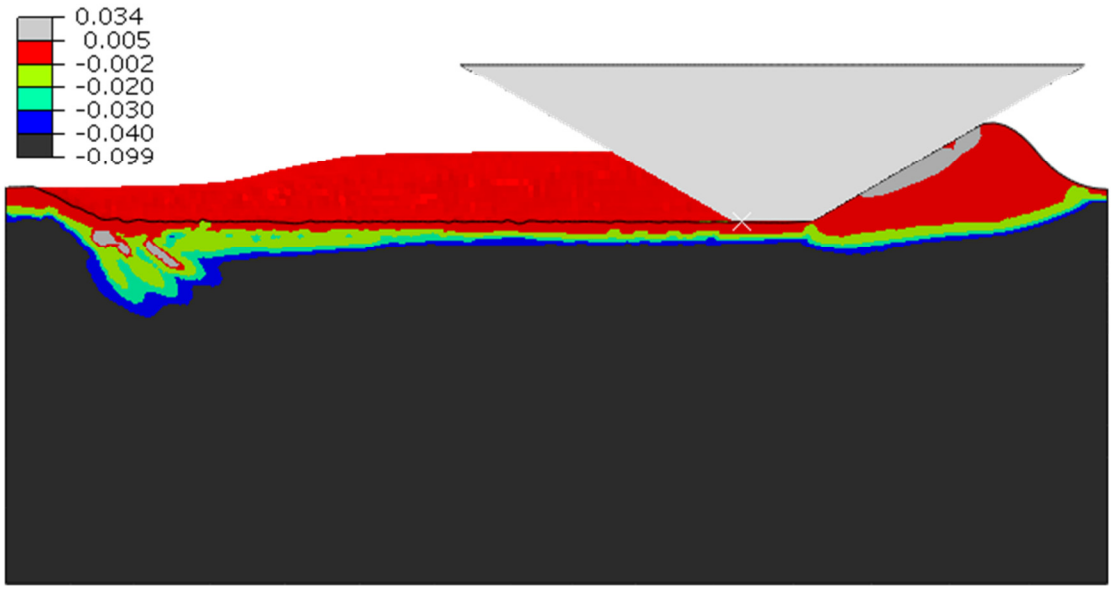

Figure 5-44 Development of the state parameter during the ice gouging

5.5.6. Dilation in Gouging Process

Dilation is an important issue in the numerical analyses of soils in general as it affects the friction angle of the soil and could considerably influence the strength properties of the soil in an analysis. In some problems, however, the dilation could be more consequential to the soil behaviour. These problems usually include some sort of kinematic constraints. In ice gouging problems of this study, the dilation could influence the sub-gouge

deformation which is essentially the most important aspect of the analyses. The dilation rate also has considerable effects on the frontal berm development as well as the keel reaction forces. This highlights how important it is to model the dilation rate reasonably in the ice gouging simulations. Figure 5-45 shows the deformation vectors for a dense soil that is undergone the ice gouging event. The deformation vectors for the same analysis on the loose soil using the same material properties are shown in Figure 5-46. If closely examined, the patterns of the deformation vectors in these figures are rather different. The deformation vectors in the analysis with the loose soil tend to be more vertical than the dense soil. On the other hand the deformation vectors of the dense soil to some extent point forward. This is due to the fact that when the dilative dense soil is yielding at front of the keel the soil volume increase leans toward the unconstrained free surface of the seabed. In other word the volume increase in the soil must conform to the boundary condition imposed by the keel front face. As the result, the frontal berm in the dense soil is larger and wider with a steeper slope.

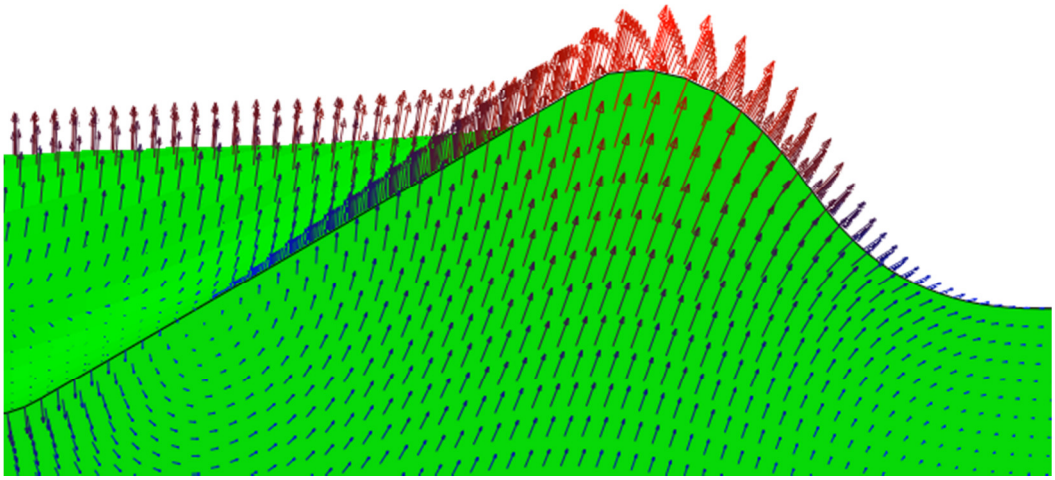

Figure 5-45 Deformation vectors of dense seabed under ice gouging

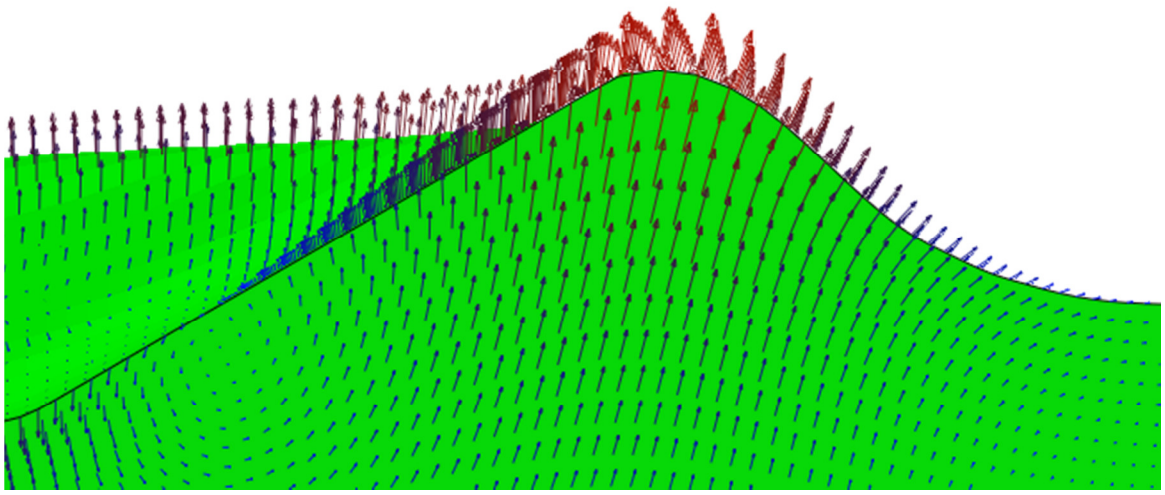

Figure 5-46 Deformation vectors of loose seabed under ice gouging

It should be noted that the loose soil supposedly starts from the critical state since the state parameter is zero. It could be expected that a more contractive soil with large positive state parameter exhibit more distinguishable response.

Figure 5-47 shows the velocity vectors in two gouging analyses with an attack angle of 30 degrees. The velocity vectors illustrate the path of soil particles movement under the gouging event. In this figure the seabed soil is dense at the left and loose at the right.

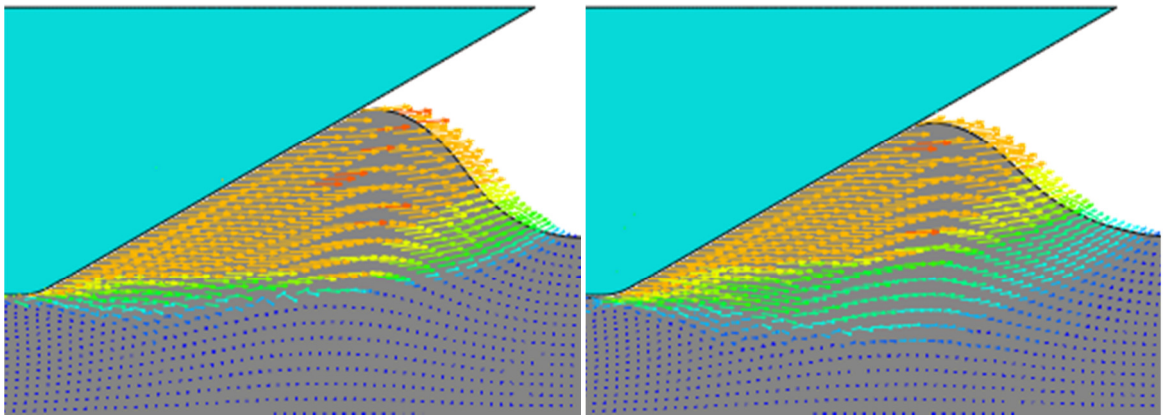

Figure 5-47 Deformation paths in gouging with keel angle of 30°, dense soil (left); loose soil (right)

The same comparison is made for a keel attack angle of 45 degrees in Figure 5-48.

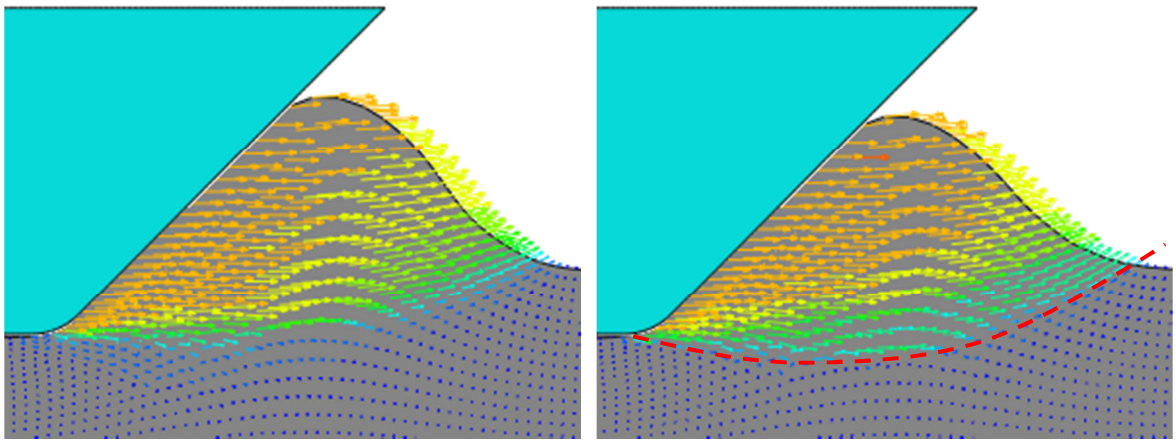

Figure 5-48 Deformation paths in gouging with keel angle of 45°, dense soil (left); loose soil (right)

Both Figure 5-47 and Figure 5-48 show consistent deformation pattern for dense soils (left figures) and loose soils (right figures). At the tip of the keel the soil is heavily confined and constrained therefore the soil behaviour is more contractive. Both dense soil and loose soil have rather similar deformation pattern at the vicinity of the keel tip. The loose soil keeps on exhibiting the contractive behaviour forming a circular slip surface on which the shear strength decreases with decreasing the effective mean stress as shown by the red dash arc in Figure 5-48 (right). On the other hand the deformation pattern is affected by the dilation mechanism in the dense soils in both Figure 5-47 and Figure 5-48. As the saw tooth dilatancy model in Figure 5-49 shows the dense soil tends to dilate due to the granular interlock when it is continuously sheared. In other word, the dilation mechanism increases the shear strength of the dilative (dense) soil. The implication of this phenomenon on the gouging event is that the sub-gouge deformation in the dense dilative seabed is shallower, due to the increase of the shear strength, and the frontal berm is larger, due to the volume increase, as it could be seen in Figure 5-47 and Figure 5-48 (the left figures).

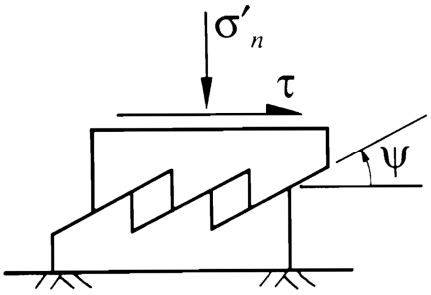

Figure 5-49 The sawtooth dilatancy model

Figure 5-50 shows the state of different zone of the seabed with respect to the dilation rate of the soil. This figure illustrates how the shear strength of a dilative soil varies at different locations.

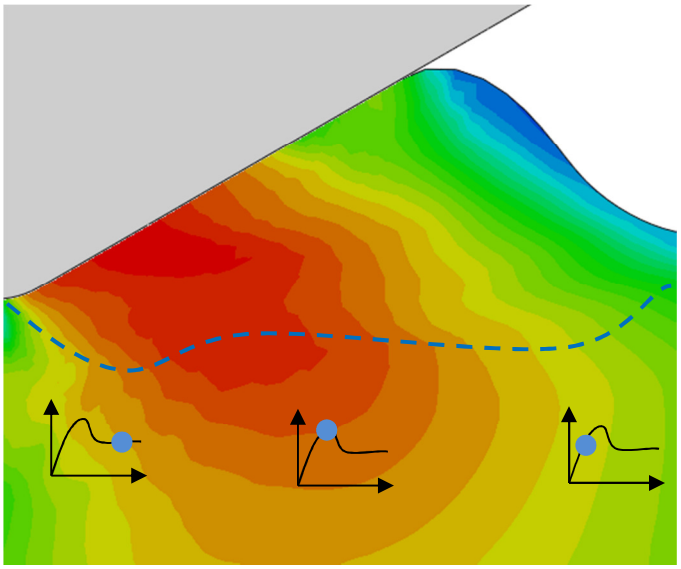

Figure 5-50 Contours of shear stress

5.6. Normalization of Horizontal Keel Reaction Forces

The PIRAM, Pipeline Ice Risk Assessment and Mitigation, JIP (Phillips et al., 2012) was devoted to enhancement of safe, cost-efficient and reliable pipeline systems in ice environments as one of the most important elements of the offshore industry. The PIRAM

keel horizontal reaction forces in sand were normalized after bearing capacity formulations by dividing them by the square of the sum of the gouging depth and the developed frontal berm as shown in eq. 55-4. The use of the deformed geometry is important due to the significant berm heights.

$$\bar{F}_H = \frac{F_H}{K(D_s + B)^2} \quad \textbf{55-4}$$

In eq. 55-4 $\bar{F}_H$is the normalized horizontal keel reaction force, $F_H$is the horizontal keel reaction force, D_s is the gouging depth, B is the developed frontal berm and K is product of submerged unit weight and gouge width. The same approach is used to normalize the reaction forces that are obtained from the finite element analyses shown in Table 5-4. In Figure 5-51 to Figure 5-54 the horizontal keel reaction force is normalized by the square of the total sum of the gouging depth and the developed frontal berm height, $(D_s + B)^2$. These figures respectively show the effects of the critical stress ratio, state parameter, attack angle and the gouging depth on the normalized horizontal keel reaction.

The analyses shown in Figure 5-51 confirm that the critical stress friction ratio directly correlates with the keel reaction forces. This implies that as the shear strength of the soil increases more driving forces are required in order to reach the steady state in the ice gouging event. In Figure 5-51 the set of data 9-16 on the right represent the analyses with deeper gouging depth of 2m. It can be inferred that the effect of the critical stress ratio is larger for deeper gouges.

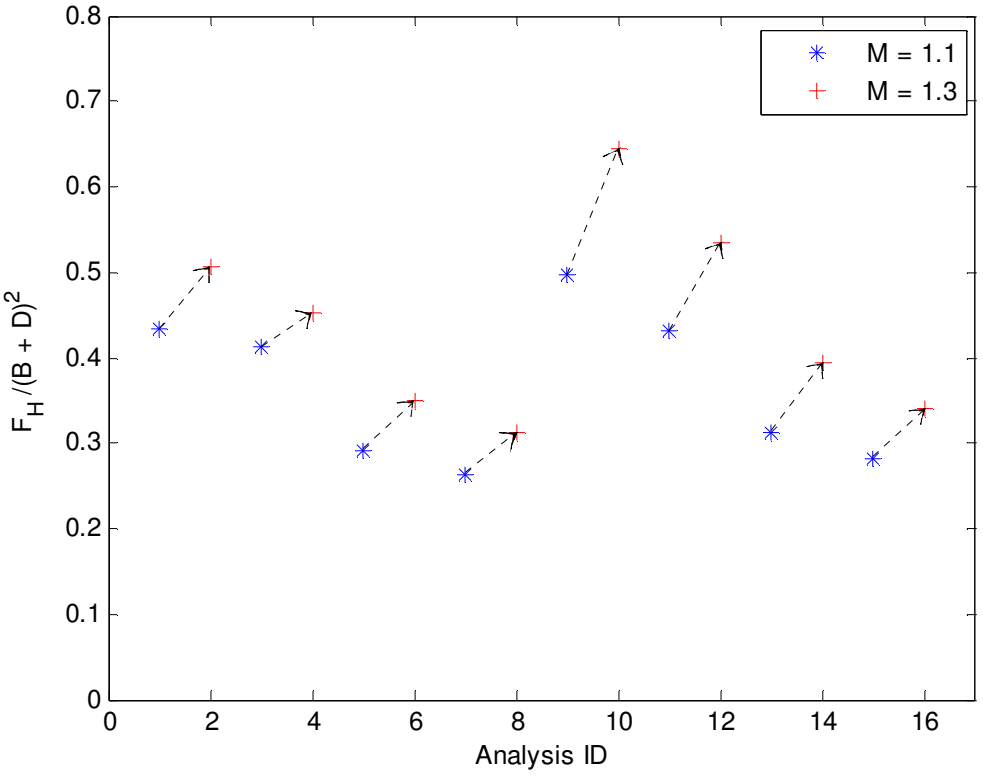

Figure 5-51 Effect of the critical stress ratio on the normalized reaction force

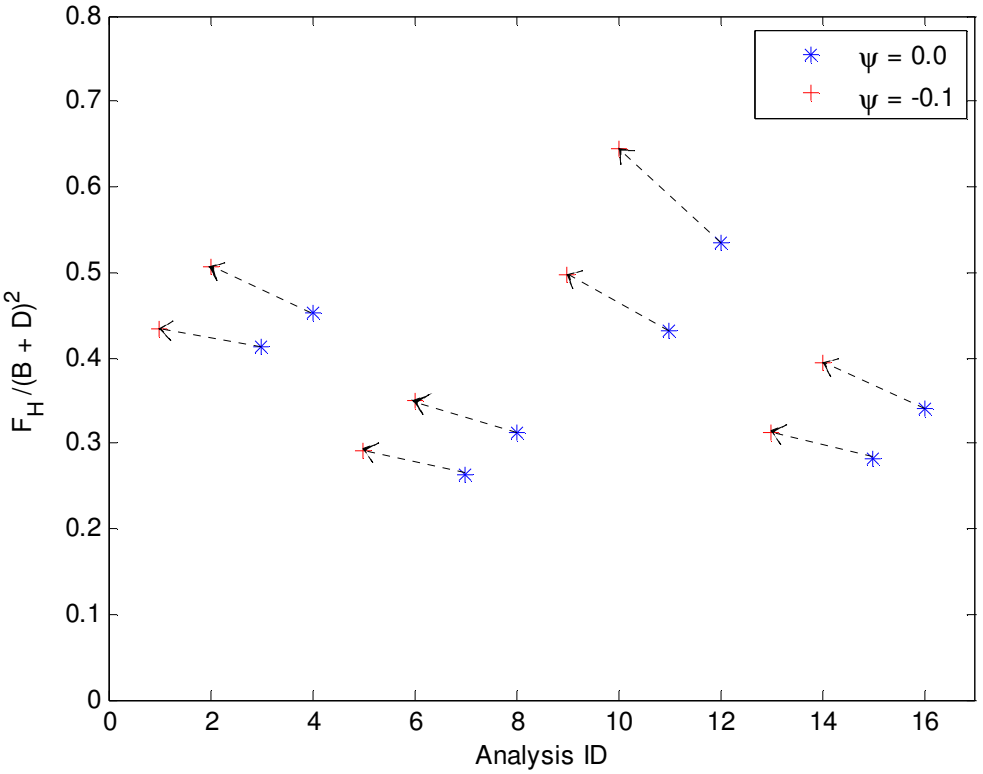

Figure 5-52 shows that for a specific soil with higher negative state parameter, (i.e. more dilative) slightly larger keel reaction forces are required at the steady state condition. Given that physically the state parameter is an implication of the relative density of the soil, in reality it is expected that similarly more compact soils generate greater keel reaction forces before the steady state condition is reached.

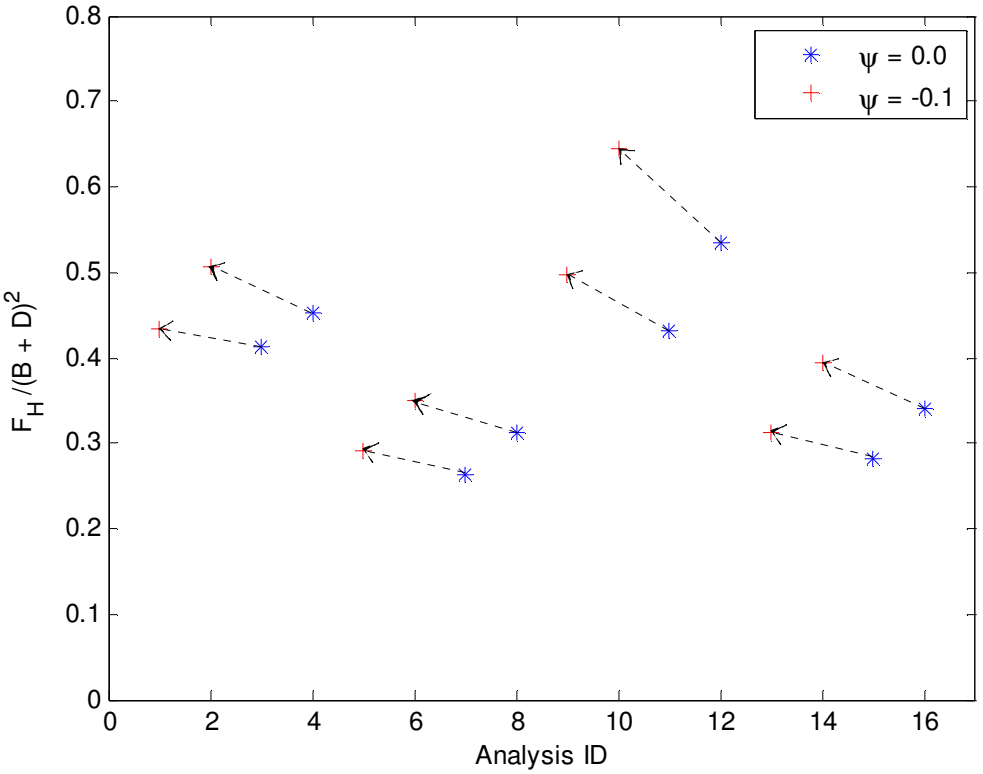

Figure 5-52 Effect of the state parameter on the normalized reaction force

The results of the analyses are summarized based on two keel attack angle in Figure 5-53. In this figure it is obvious that the keel attack angle has a negative effect on the horizontal reaction force. That is the higher attack angle yields lower keel reactions forces as the ice/soil interaction surface decreases.

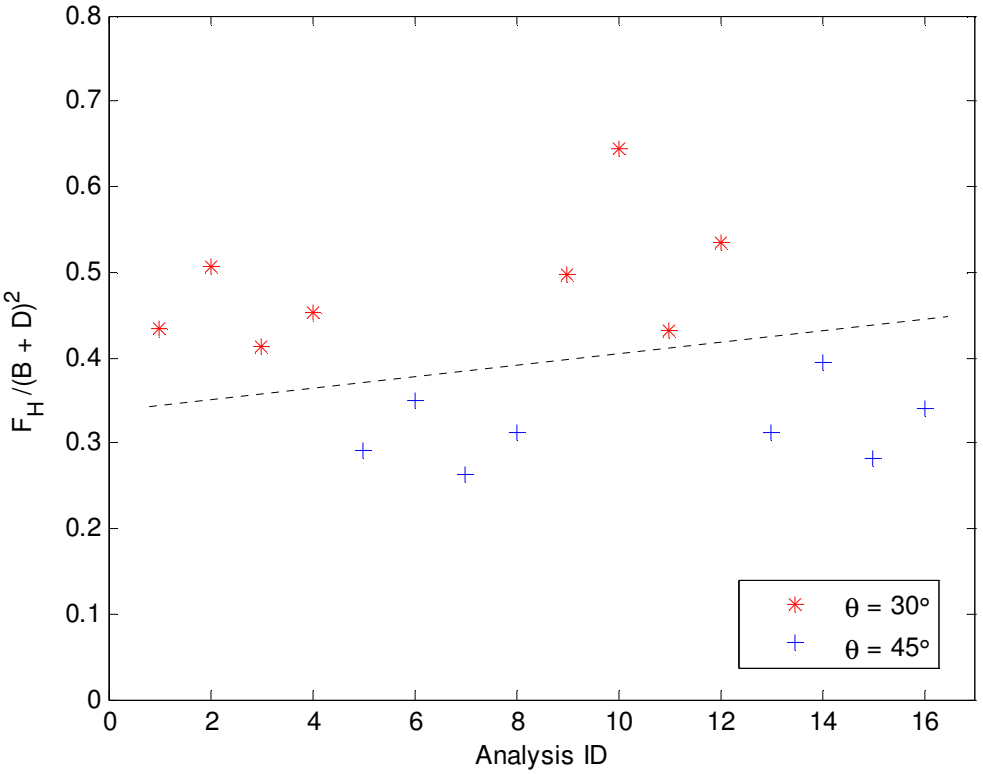

Figure 5-53 Effect of the keel attack angle on the normalized reaction force

The gouging depth has a positive effect on the keel reaction force. As it is shown in Figure 5-54 higher keel reaction forces happen in deeper gouging depths. Comparing Figure 5-54 with the other sensitivity analyses shown in Figure 5-51 to Figure 5-54 shows that the gouging depth and associated berm height have the most distinct and significant effect on the keel reaction forces.

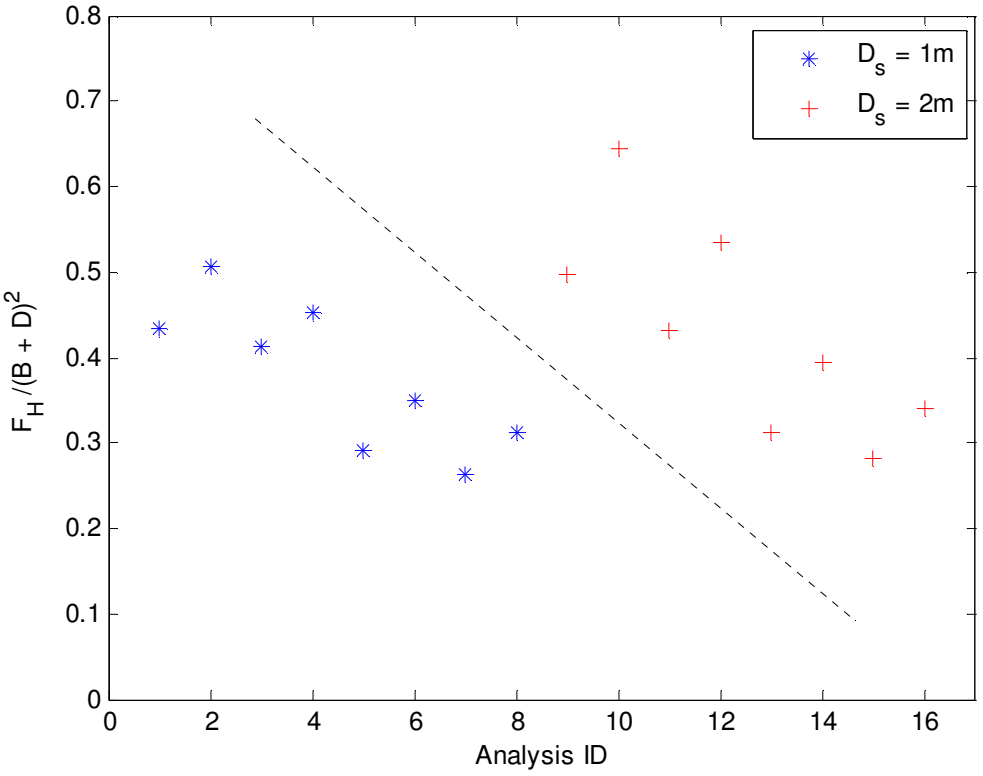

Figure 5-54 Effect of the gouging depth on the normalized reaction force

In Figure 5-55 the soil material properties, the critical stress ratio and the state parameter, are included in the normalization of the horizontal keel reaction force. In order to involve the material properties of the soil in the normalization of horizontal keel reaction force, shown in eq. 55-4, a simple relation as shown in eq. 5-5 below is applied:

$$K = \gamma W(M - 1.9\psi) \qquad \textbf{5-5}$$

To incorporate the soil properties M and ψ in the normalization of the horizontal keel reaction force, eq. 5-5, the term $M - 1.9\psi$ is introduced to represent the frictional behaviour of the soil. The frictional behaviour could be expressed by $\eta = q/p$. Based on the NorSand flow rule (Jefferies, 1993) the stress ratio could be related to the dilation rate.

$$D^p = \eta - M \quad \textbf{5-6}$$

On the other hand the maximum dilation rate is a function of the state parameter.

$$D^p_{max} = -\chi\psi \quad \textbf{5-7}$$

A common value for χ, as chosen in these analyses, is 3.8. It is assumed that resisting soil in front of the keel uniformly ranges from maximum dilation state to zero dilation. Therefore an average dilation rate of $0.5\ D^p_{max}$ is adopted. As a result eq. 5-6 could be rewritten to derive an expression for stress ratio.

$$\eta = M - 1.9\psi \quad \textbf{5-8}$$

As Figure 5-55 shows the normalized reaction forces could be categorized in two different sets that relatively exhibit similar responses for same keel attack angles. This implies that it is possible to establish relationship between soil parameters and seabed responses such as reaction forces based on the square of the sum of the gouging depth and berm height. These results are consistent with the findings of the PIRAM project.

Based on the results of the analyses for the developed frontal berm heights shown in Table 5-4 the critical stress ratio has direct effect on the developed frontal berm height. Regardless of other parameters, the berm height consistently increases with the increasing shear strength of the soil. The state parameter has also a clear direct effect on the development of the frontal berm height. The analyses show how denser material could lead to the formation of a larger frontal berm at steady state. Since the rate of dilation is specifically a function of the state parameter, i.e. the distance between the current state and the critical state, it is sensible to infer that a soil with more negative state parameter exhibits a larger berm height by dilation. The increase of attack angle leads to development of larger frontal berm height regardless of the level of other factors. As the

results of the analyses suggest the gouging depth has also a clear direct effect on the frontal berm height.

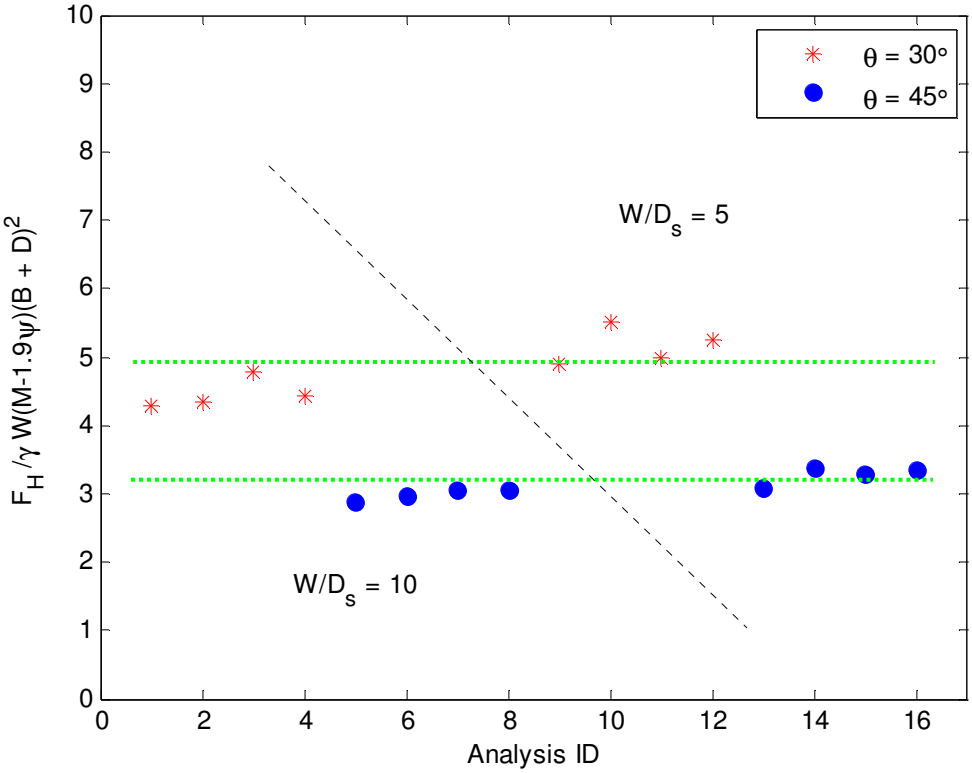

Figure 5-55 Normalization of the keel reaction forces based on the soil properties *M* and *ψ*

5.7. Summary

In this chapter a three-dimensional finite element model is created to model the ice gouging event. The different steps of the numerical modeling are explained in details. The implemented critical state model NorSand is applied to the finite element model to simulate the ice gouging. Based on the NorSand model some of the significant factors in determination of the nature of the gouging event are studied. This chapter shows how significantly these basic properties influence the seabed behaviour under the gouging

event. It is shown that how the failure mechanism could considerably change as a function of each of these parameters.

6. Ice Gouging Model Verification and Validation

The purpose of this chapter is to validate the developed finite element model against the results of previous laboratory physical model tests. The FE model is basically used to simulate some of the centrifuge test carried out by W. Yang (2010) as part of the PIRAM JIP.

6.1. Built-in Drucker-Prager constitutive model to simulate the ice gouging

Figure 6-1 shows the typical drained behaviour of loose and dense sand. Loose samples of sand exhibit a ductile behaviour with volume contraction. On the other hand, the dense samples of sand initially show a stiff response until the soil reaches its peak strength. After this point the soil exhibits softening behaviour and moves toward critical state. This process is accompanied by volume dilation.

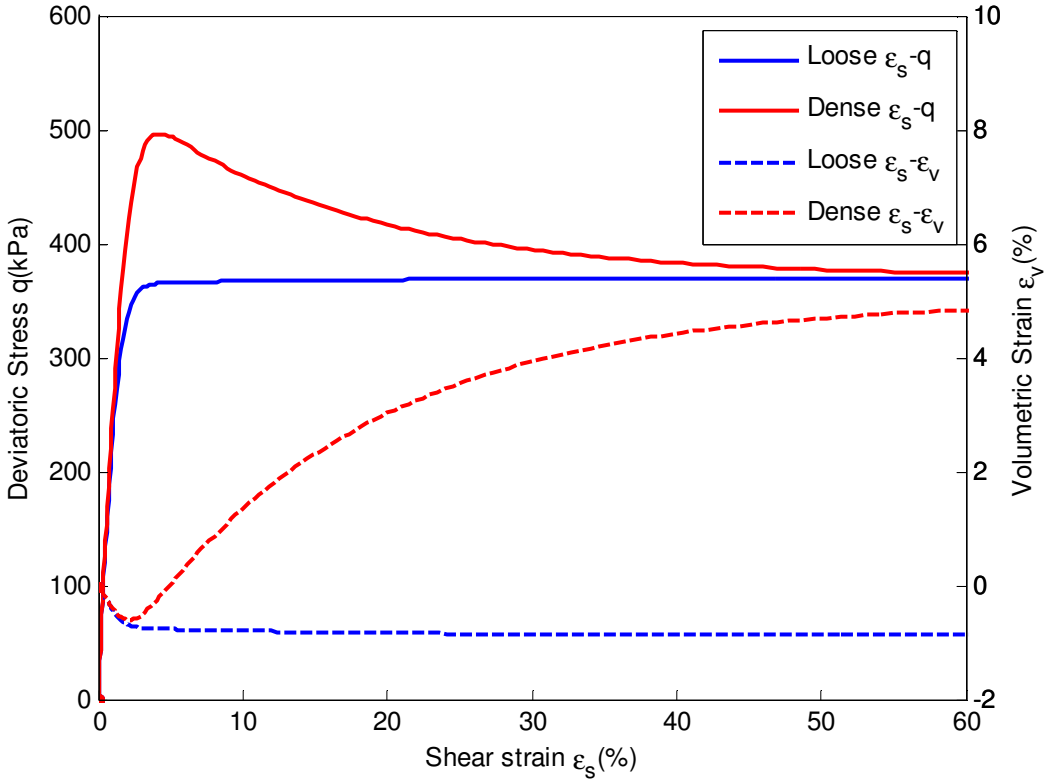

Figure 6-1 Comparison of the drained stress train behaviour of the dense and loose sand

For numerical analysis to yield reliable results, it is essential that a soil constitutive model is employed that can capture these different behaviours of sands accurately enough. Later in this chapter the development and implementation of a constitutive model that can simulate the behaviour of sand, of different type and under different conditions, more precisely than those models already exist in ABAQUS Explicit software package is presented.

To model the ice gouging problem the built in Drucker-Prager material is used in this section. The purpose of this section is to show the limitation of the built in model in ABAQUS. This section also shows the influence of the shape of the yield surface in the π plane on the outcome of the analyses.

The geometrical properties of the ice feature used in the gouging analyses of this section are summarized in Table 6-1.

Table 6-1 Gouging geometry

Attack Angle (degree)	*Gouging Depth* D_s *(m)*	*Gouging Width* W *(m)*
30	*1.5*	*14.4*

In these analyses the elasticity modulus, E, is 26 MPa, the Poisson's ratio, ν, is 0.32, the internal friction angle θ, as defined in chapter 3, depending on the case is either 39.8° or 50.2°, the cohesion, d, is 2.kPa and the dilation angle, ψ, also depending on each case could be 0 or 2°. The dilation angle in these analyses is limited to small value of two degrees or zero at all. A constant dilation angle, even relatively small, could jeopardize the numerical stability of an ice gouging problem. A gouging simulation encounters very large shear strains and if the soil is to perpetually dilate, as is in the case of the built-in Drucker-Prager with constant ψ, inevitably it exhibits excessive volume increase which eventually distorts the elements in addition to being unrealistic.

The built-in Drucker-Prager in ABAQUS inputs a material parameter which approximates the Mohr-Coulomb yield surface in π plane as shown in Figure 6-2. A conventional Drucker-Prager with circular yield surface in the π plane and a modified yield surface that approximates the Mohr-Coulomb yield surface in the π plane are used these analyses. To achieve the latter one can change the input parameter K to some value like 0.778 in ABAQUS. These values are chosen to highlight the effect of the yield surface in π plane on the soil response.

Figure 6-3 and Figure 6-4 show that the keel reaction forces and the sub-gouge deformations increase as the friction angle increases. Eq. 6-1 relates the friction angle in Drucker-Prager model to the effective shear friction angle, ϕ, in triaxial condition.

$$\tan(\theta) = \frac{6\sin\phi'}{3-\sin\phi'} \qquad \textbf{6-1}$$

These forces and deformations increase when a circular yield surface is used, i.e. K = 1.0. Both these situation represent an encompassment of a larger space in π plane and utilisation of a bigger yield surface as shown in Figure 6-2. The reason why a higher sub-gouge deformation occurs in these conditions could be investigated using Figure 6-5 and Figure 6-6. A larger yield surface results in mobilisation of a larger shear stress which spreads through the depth of the soil. With the absence of a hardening law, as is the case in these built in analyses, a higher shear stress results in higher plastic strain and consequently higher sub-gouge deformation. These figures conclude that using a built in Drucker Prager model yields high sub-gouge deformations if dense sand is modeled. The way to achieve low sub-gouge deformation, to a magnitude closer to that seen in laboratory tests, is to use low friction angle in the built in model and avoid dilation as dilation also shifts the stress path to right (more pressure) in Figure 6-5. However, this is not representative of the soil constitutive behaviour and gives unrealistically low keel reaction forces which do not represent the real soil behaviour. In Figure 6-5 and Figure 6-6 the stress paths at 1.5 meters below the keel base are shown in each analysis.

Figure 6-7 show the frontal berm height development in the analyses using the built in model. These analyses have not reached a steady frontal berm height. Specifically the

introduction of a small dilation angle could result in the development of an unrealistic berm height and quicker encounter of mess distortion.

The improvement in the hardening law and the management of the dilative behaviour is crucial.

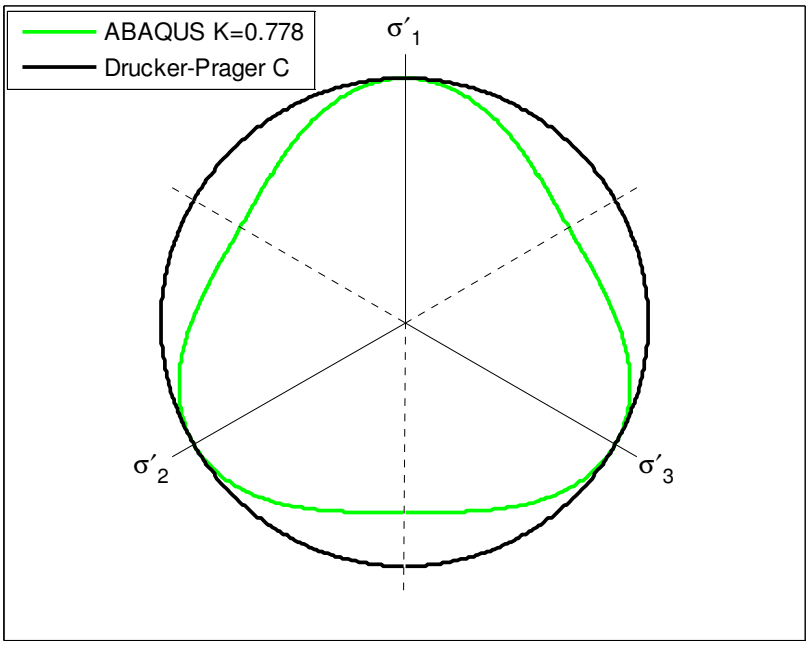

Figure 6-2 The yield surface of the ABAQUS built-in Drucker-Prager model in π plane

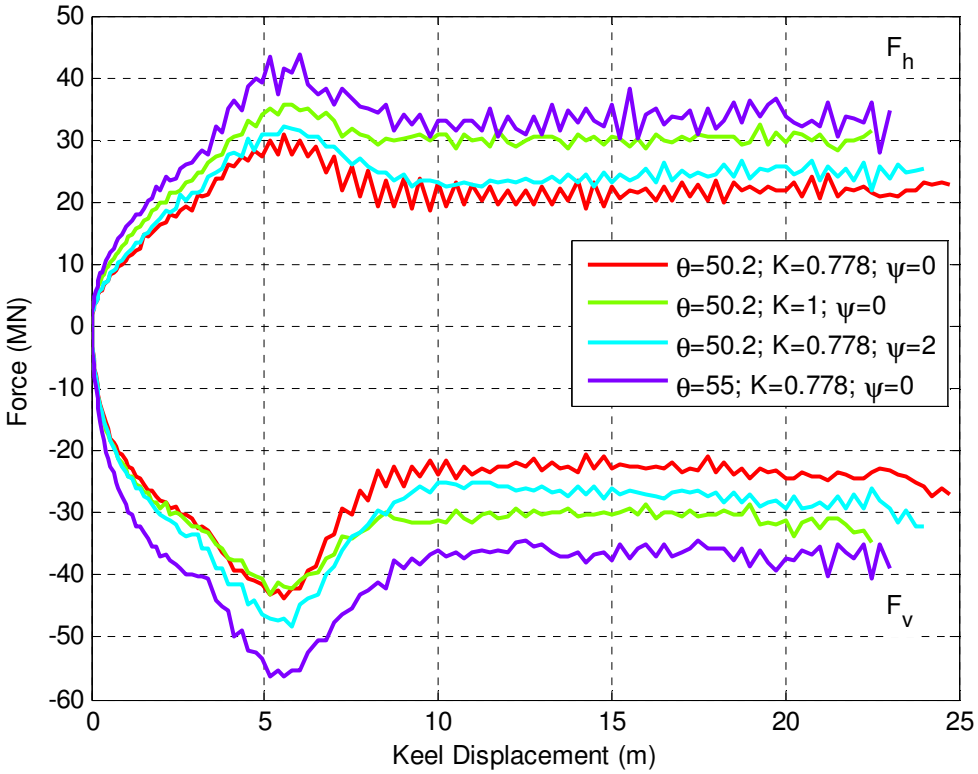

Figure 6-3 Keel reaction forces of the Drucker-Prager built in model

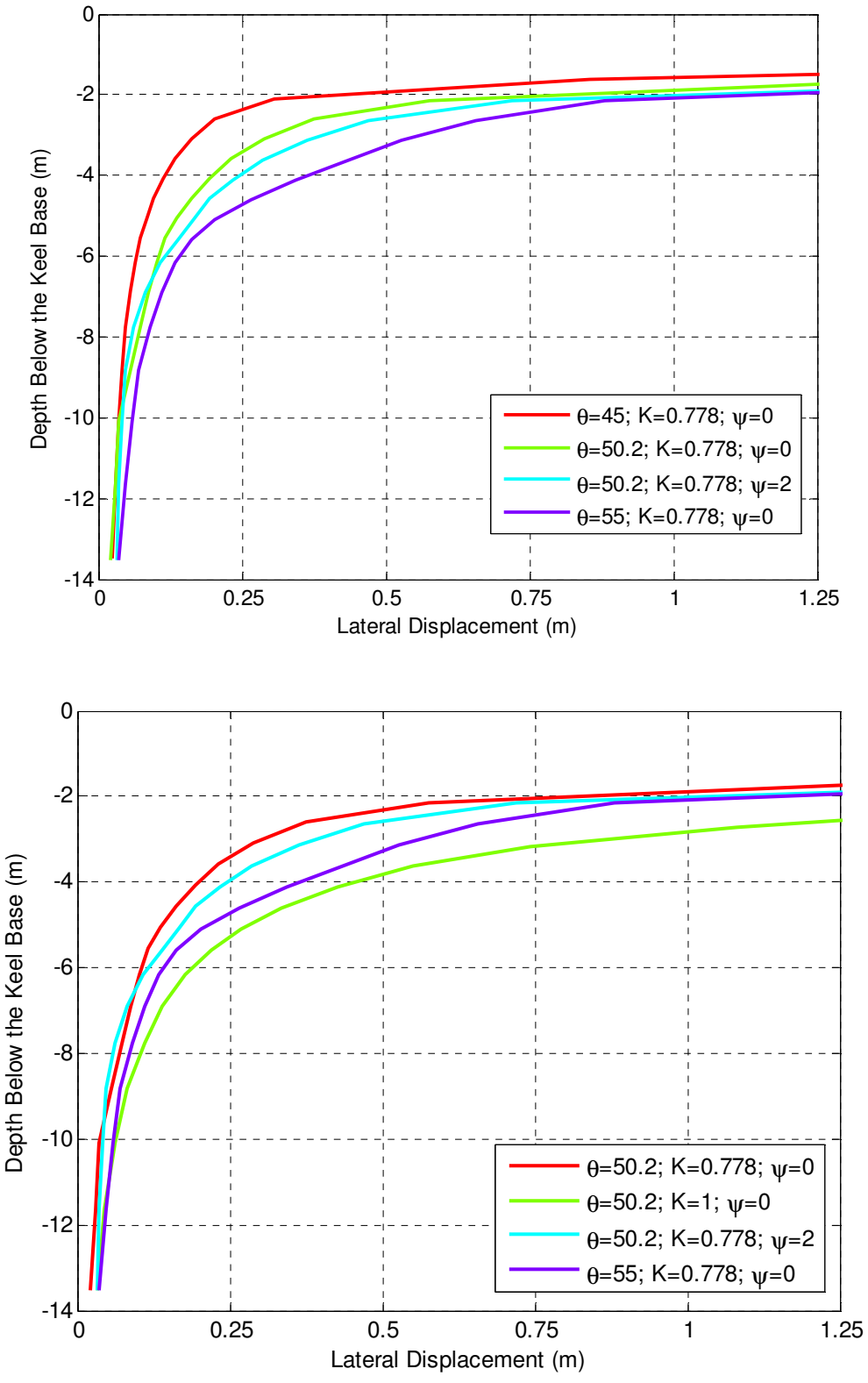

Figure 6-4 Sub-gouge deformation using the ABAQUS built in Drucker-Prager model

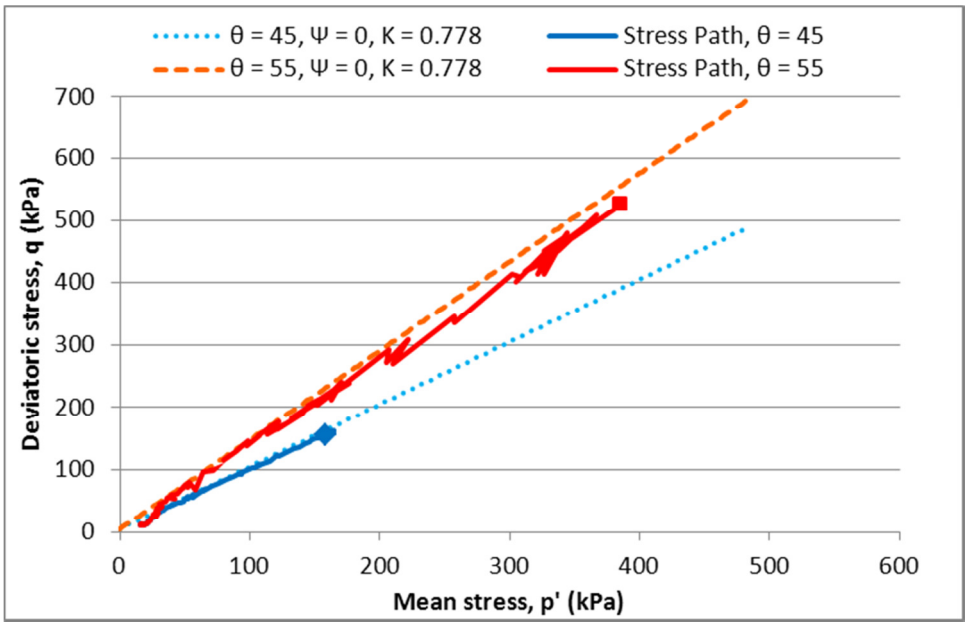

Figure 6-5 Stress paths in a specific point for two Drucker-Prager analyses

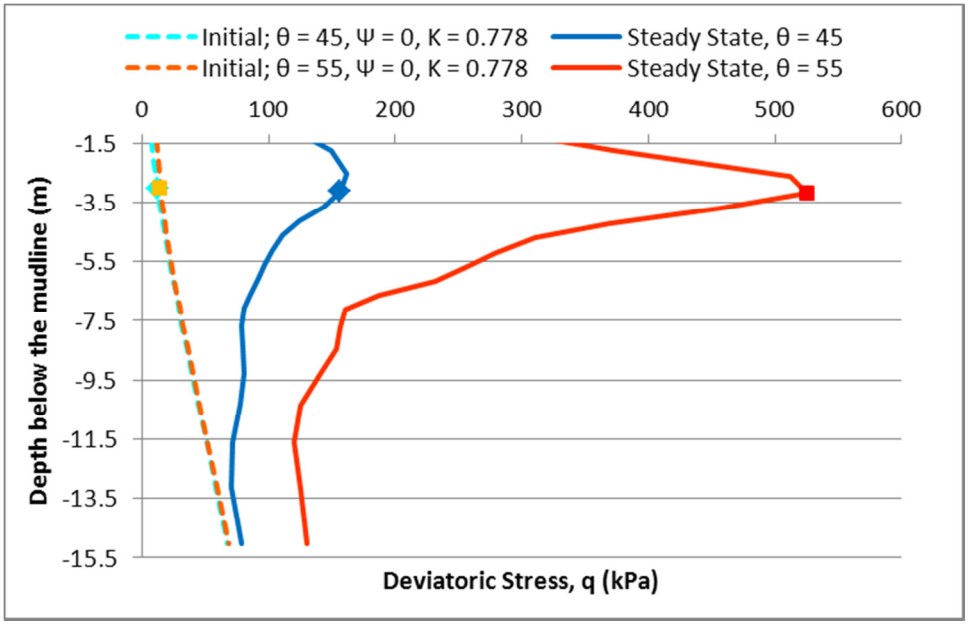

Figure 6-6 Distribution of the shear stress through the depth of the soil

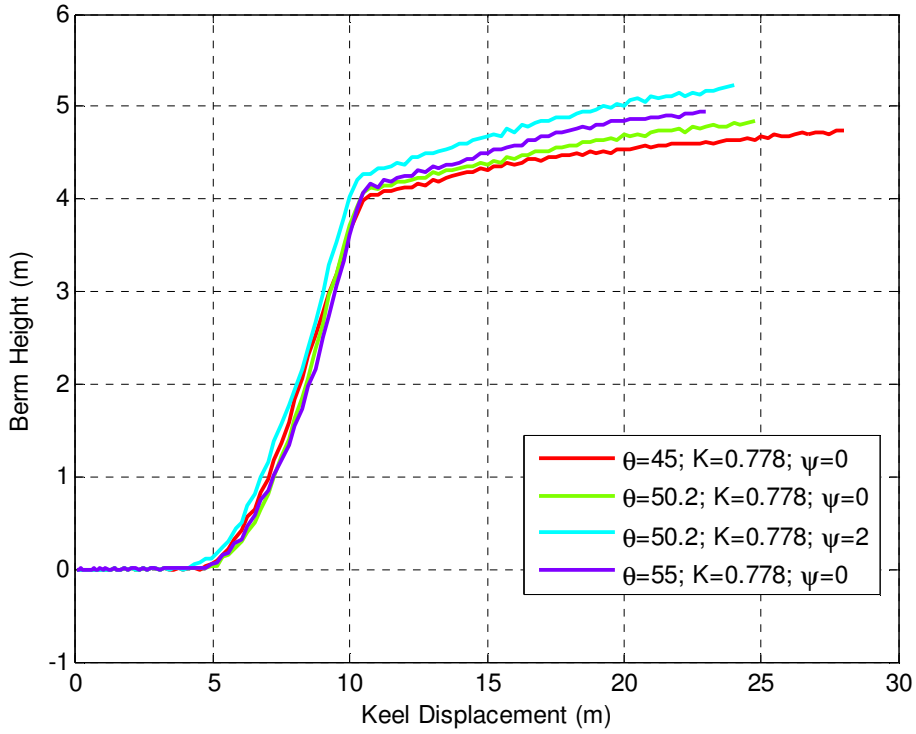

Figure 6-7 Frontal berm height development using the ABAQUS built in Drucker-Prager model

Figure 6-3 to Figure 6-7 support the fact that the built in models (with constant dilation angle) overestimate the sub-gouge deformation in the subsea if reasonable values of soil friction angle are used. In addition, unless the dilation is either prevented or highly underrated the Drucker-Prager built in model is incapable to achieve the steady state since the excessive dilation results in unrealistic volume increase which continuously increases the frontal mound as analyses advance. J. Barrette and Phillips (2011) succeeded to enhance the built-in Drucker Prager model of ABAQUS by defining a Solution Dependent Variable in a subroutine to vary the dilation angle of the soil and reduce it to zero with shear strain as shown in Figure 6-8.

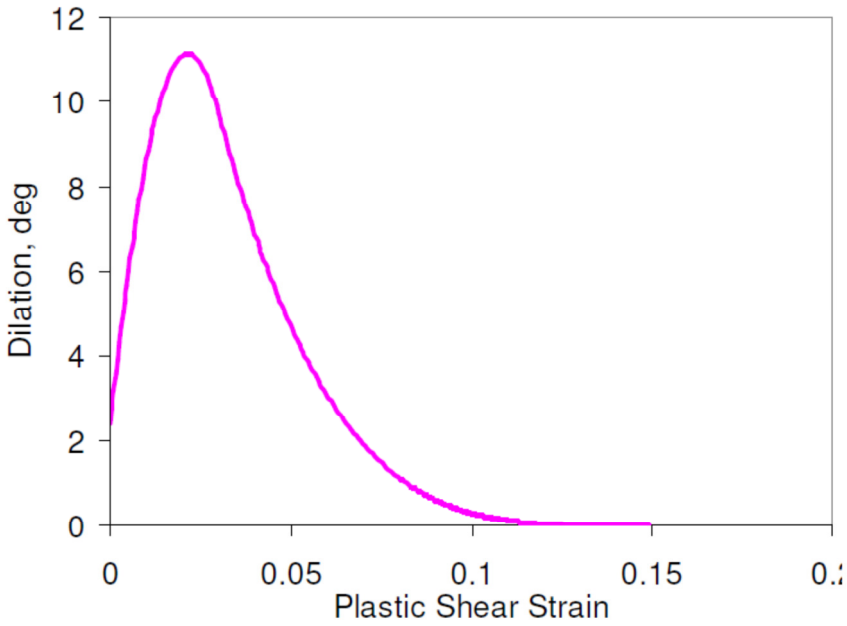

Figure 6-8 Suppression of excessive volume increase by reducing the dilation angle with shear strain (J. Barrette & Phillips, 2011)

6.2. Simulation Using Drucker-Prager Cap and the NorSand Model

In this section the Drucker-Prager Cap model and the critical state NorSand model are applied in similar gouging scenarios in order to compare their behaviour and distinguish their advantages and disadvantages of one over the other.

In order to achieve a similar representation of the same soil the input parameters of the two constitutive model responses should be related to each other as closely as possible.

To compare the developed Drucker-Prager Cap model with critical state NorSand constitutive model first the relevance of the input parameters of the two models are investigated through a triaxial compression test.

A typical effective drained friction angle, ϕ', of 30° is assumed. The frictional properties of each model could be then obtained based on the assumed internal friction angle. The

triaxial compression critical stress ratio, M_{tc}, in the NorSand model is related to the effective friction angle, ϕ', according to Eq.4-1 below:

$$M_{tc} = \frac{6\sin\phi'}{3-\sin\phi'} \quad \textbf{6-2}$$

As the result a critical stress ratio of 1.2 is chosen for the triaxial analysis of the NorSand model.

On the other hand, by comparing to the Mohr-Coulomb model, the internal friction angle θ in the Drucker-Prager model could be derived based on eq. 6-3.

$$\tan\theta = \frac{6\sin\phi'}{3-\sin\phi'} \quad \textbf{6-3}$$

Therefore an internal friction angle, θ, of $50.2°$ is adopted for the triaxial analysis using the developed Drucker-Prager Cap model.

The relative density, or consequently the soil dilative behaviour, is another issue that requires reconciliation between the two Drucker-Prager Cap and critical state NorSand model. The proper address to this issue ensures that in addition to the soil properties, a similar *"state"* is attributed to the soil samples that are analyzed under triaxial compression tests.

The maximum dilation rate of the triaxial compression tests is selected as a criterion to keep the soil initial states compatible in both constitutive models.

Based on the Bolton dilation formula, introduced in chapter 4, the maximum dilation rate could be obtained in the Drucker-Prager Cap model .This dilation rate is converted to a consistent form based on the definition of dilation as the ratio of the plastic volumetric

strain to the plastic shear strain. For the triaxial compression condition the conversion relationship is shown in eq. 6-4.

$$D^p = 3\frac{D_B^p}{3 + D_B^p} \quad \textbf{6-4}$$

In this equation D_B^p is the dilation based on the Bolton formula.

On the other hand, based on the definition of the maximum dilation rate in critical state NorSand model, introduced in chapter 3, it is possible to simply relate the dilatancy index, I_R, to the state parameter, ψ.

Typical realistic maximum and minimum void ratios of respectively 0.9 and 0.6 are chosen for soil sample used in the triaxial analysis in which the Drucker-Prager Cap model is used. Based on an initial confinement pressure of 185 kPa and a state parameter of -0.15 for a highly dense sample of sand a void ratio of 0.69 is required to produce the same dilation rate in both NorSand model and Drucker-Prager Cap model.

The input parameters for the developed models are summarized in Table 6-2 and Table 6-3 for respectively a dense soil and a medium dense soil.

Table 6-2 Properties of the dense soil

Elasticity Modulus, *E*	26 MPa	Over-consolidation Ratio, *OCR*	*2*
Poisson's Ratio, ν	0.32	Submerged Unit Weight	800 kg/m^3
NorSand		***Drucker-Prager Cap***	
* Critical Stress Ratio, *M*	*1.2*	* Critical Friction Angle at Triaxial Compression Condition, θ_{cr}	*50.2°*
State Parameter, ψ	*-0.135*	Dilatancy Index, I_R	*2.5*
CSL slope in semi log pressure - void ratio space, λ	*0.024*	Cohesion, *d*	*2 kPa*
CSL altitude at 1 *kPa*, Γ	*0.97*	Cap Eccentricity Coefficient, *R*	*2.7*

* equivalent to $\phi' = 30°$

Table 6-3 Properties of the medium dense soil

OCR		2	
NorSand		Drucker Prager Cap	
ψ	-0.035	θ_{cr}	50.2°
M	1.2	I_R	0.5
		R	2.7

Figure 6-9 and Figure 6-12 compares the triaxial response of the NorSand and the Drucker-Prager Cap models for respectively dense and medium dense (less dense) sand. These two models have similar response for these sets of input parameters. For triaxial condition the Lode angle is constant so the Mohr-Coulomb and circular criteria yield the same results.

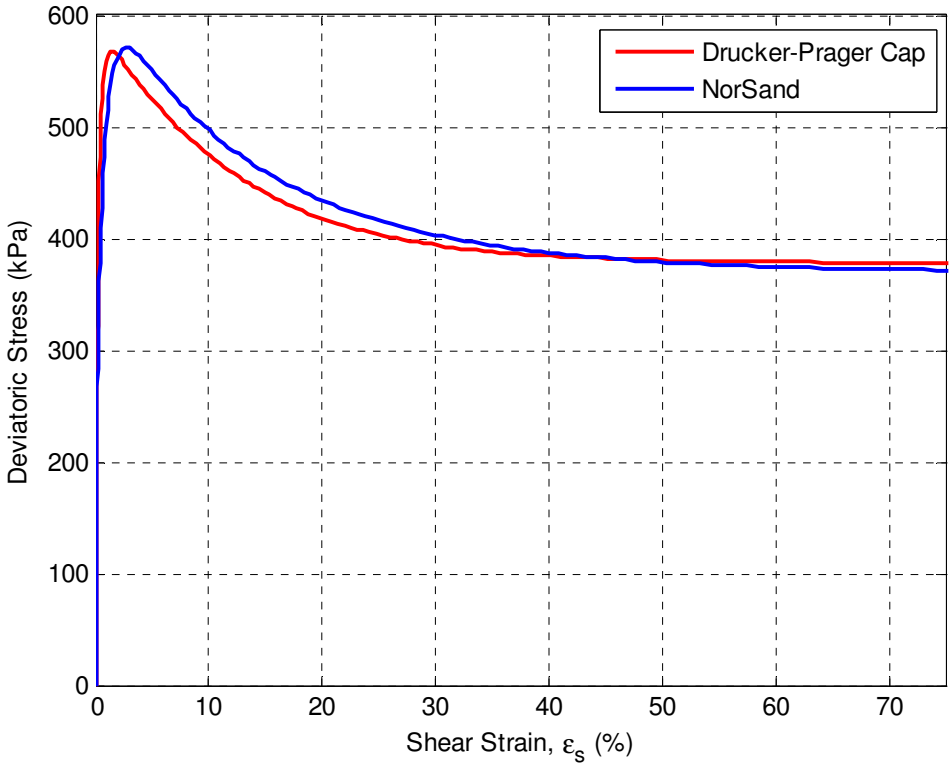

Figure 6-9 Triaxial response of the dense soil

Figure 6-10 compares the volumetric behaviour of the two models. Both these models could capture the general dilative behaviour of the dense sand. Although the Drucker-Prager Cap model ultimately achieves the same volume increase as the NorSand model does but the model captures a more dilative response prior to the materialization of the same dilation. This discrepancy could be a result of the distinct hardening mechanisms and the way the yield surfaces of the NorSand and Drucker-Prager Cap model evolve before they accommodate the maximum dilation rates which are intended to be equal in both triaxial analyses using these models.

The volumetric behaviours of the two models for less dense soil are compared in Figure 6-13. This confirms the same trend as explained for dense case.

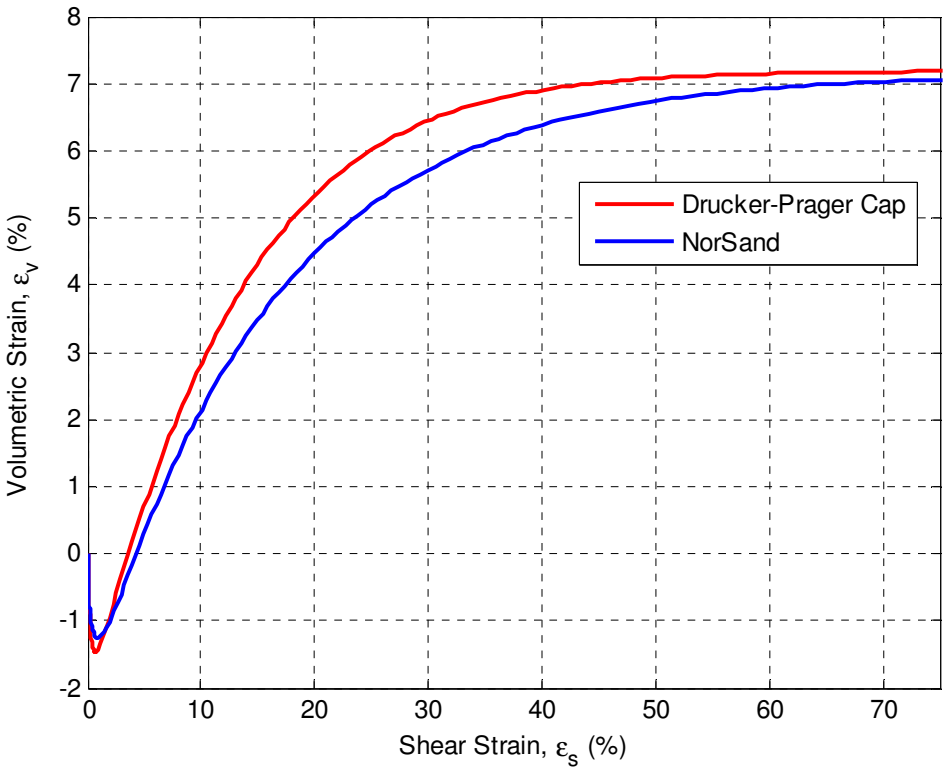

Figure 6-10 Comparison of the volumetric strain in NorSand and Drucker-Prager Cap

Figure 6-11 shows how the two analyses approach to the steady sate. The dilatancy index, which is a measurement of the soil state in the implemented model, evolves toward zero with continuous shearing. The NorSand model exhibits similar behaviour through the state parameter. Both Drucker-Prager Cap model and the critical state NorSand model achieve the steady state at about 70% of shear strain for the adopted set of input parameters.

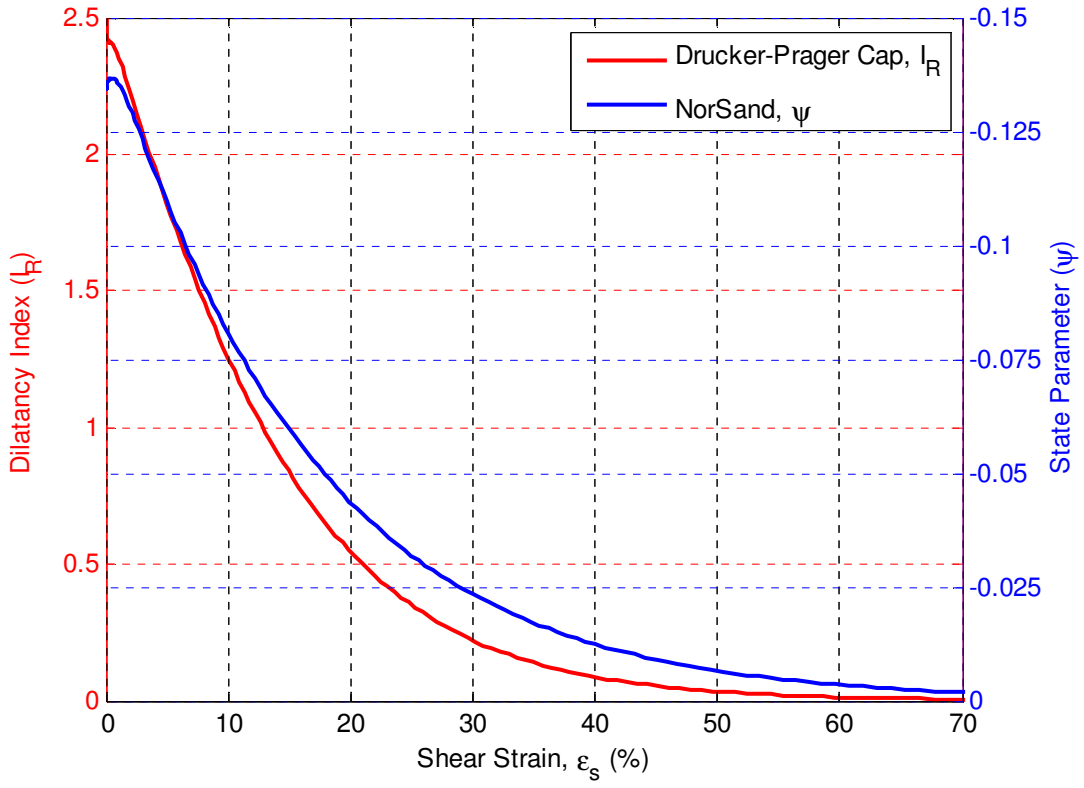

Figure 6-11 Comparison of the development of the steady state in NorSand and Drucker-Prager Cap

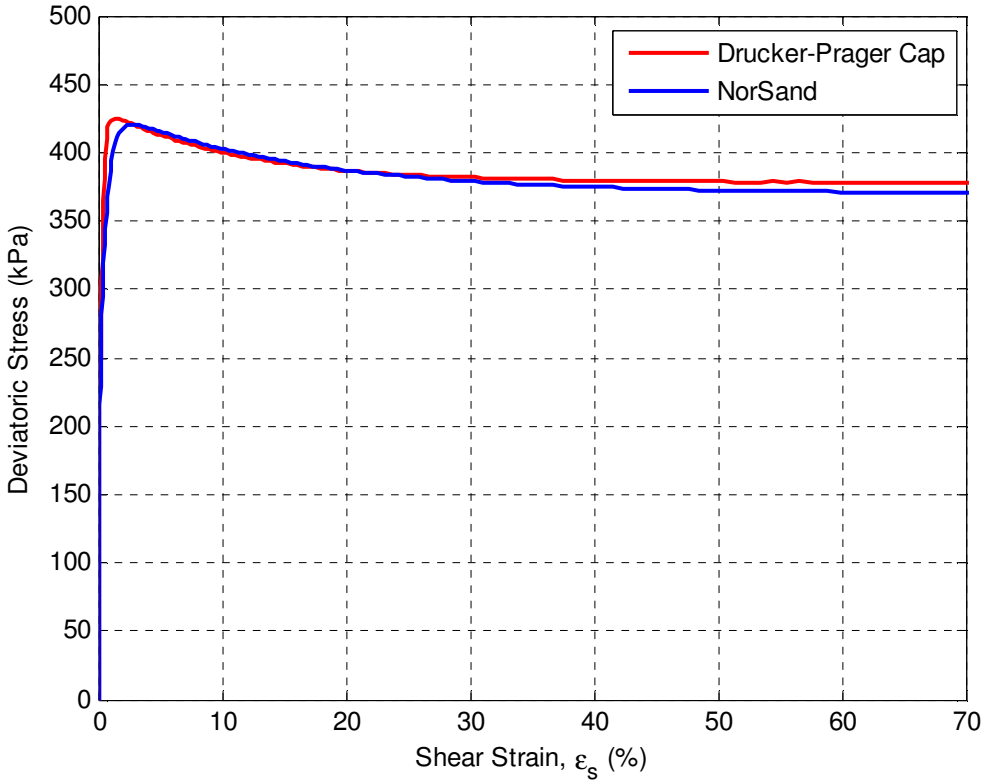

Figure 6-12 Triaxial responses of the loose soil using Drucker-Prager Cap and NorSand

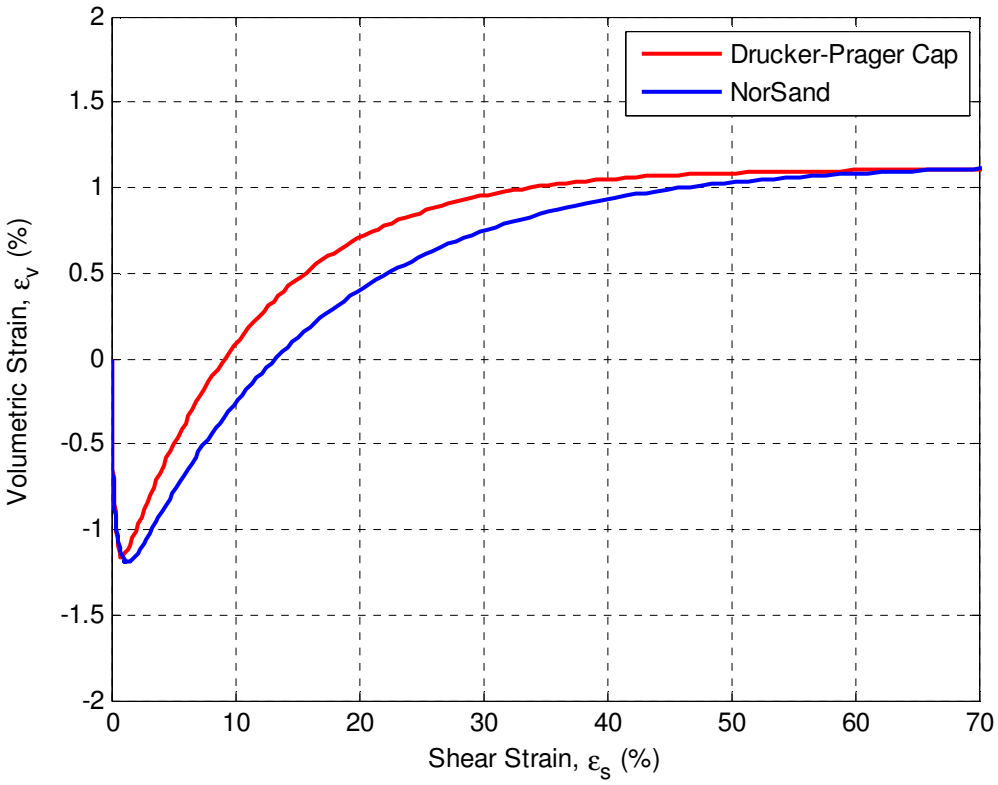

Figure 6-13 Comparison of the volumetric strain in NorSand and Drucker-Prager Cap

Figure 6-9 to Figure 6-13 show that the two constitutive models exhibit relatively similar responses under triaxial compression condition for the selected input parameters.

In the following these models with the selected input parameters, as shown in Table 6-1 and Table 6-2, are applied in the three-dimensional finite element ice gouging model.

6.2.1. VUMAT for the Ice Gouging Analyses

This section studies the effect of the third stress invariant in different implementations of the developed numerical models of the soil. This section examines all the developed models and compares their behaviour as a function of how the third stress invariant is considered.

Figure 6-14 shows three approaches to model the yield surface in the π plane applied in this study. The NorSand model (Jefferies & Shuttle, 2005) uses Matsuoka-Nakai criterion. The developed Drucker-Prager Cap model could either use a Mohr-Coulomb criterion or have circular shape. In the latter case the angle of internal friction at triaxial extension condition is the same value of friction angle under triaxial compression condition and regardless of the intermediate principal stress it is kept constant through the analysis (the small green circle in Figure 6-14). The soil is then let to harden according to Bolton dilation formula. The maximum friction angle predicted by Bolton formula is also adopted based on the triaxial condition regardless of the Lode angle.

The third approach is to use the Mohr-Coulomb criterion as shown in Figure 6-14 instead of the conventional Drucker-Prager circle in π plane. In this case the maximum friction angle due to dilation which is predicted by Bolton's dilatancy formula is also converted to correspond with current lode angle.

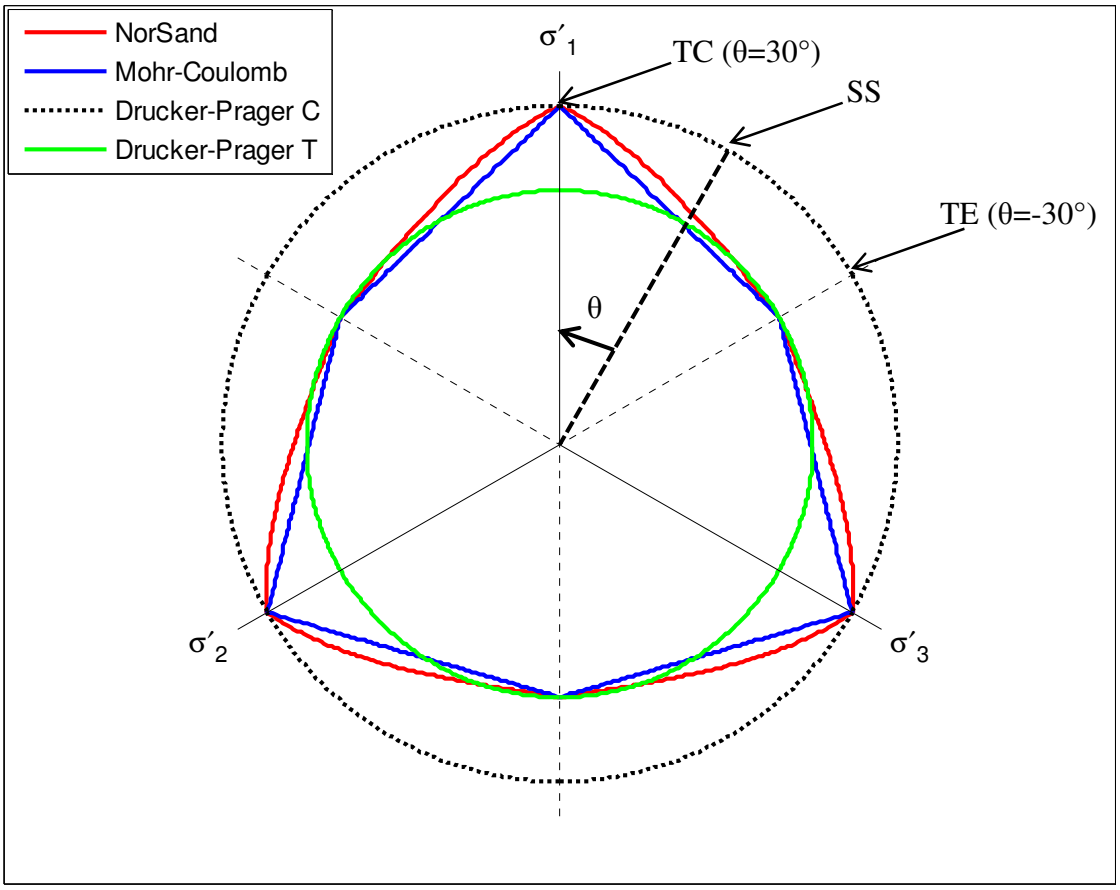

Figure 6-14 The applied yield surfaces in the developed user materials.

Based on the calibrated triaxial compression analyses it is expected that the ice gouging models also yield similar behaviour. It should be reminded that the NorSand model employs the Mohr-Coulomb and the Matsuoka-Nakai criteria in order to correlate the critical stress ratio to the Lode angle. This correlation is essential to capture realistic behaviour in numerical modeling of the soil.

The size of the yield surface of NorSand model changes in the π plane based on the Lode angle. Figure 6-15 shows how the critical stress ratio, M, varies depending on the stress state, or in other word the Lode angle, of every region of the soil domain. The critical stress ratio from triaxial compression test is M = 1.2.The mobilised stress ratio is usually

less than the critical stress value of 1.2 which is associated to the triaxial compression condition.

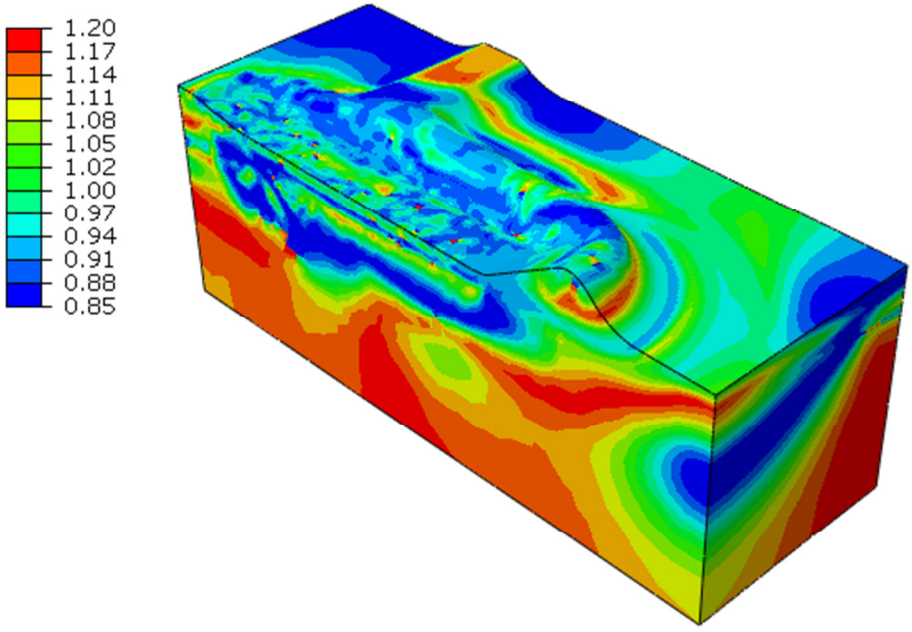

Figure 6-15 Variation of the critical stress ratio

However, Figure 6-14 also shows that the mentioned feature is not available in the Drucker-Prager Cap (circular) model implemented in this study. Since the three-dimensional ice gouging mostly occurs under plane strain condition rather than triaxial condition the internal friction angle, θ_{cr}, in Table 6-1 is reduced to 39.8° to compensate for this discrepancy. This conversion is based on the Mohr-Coulomb criterion.

The mobilised friction angle and the dilatancy of sand which contribute to the soil strength are the main factors to determine the sub-gouge deformation magnitude. However, these factors could affect the sub-gouge deformation under ice gouging event in different ways. On one hand during the steady state ice gouging higher shear forces are transferred deeper into the soil when it is more frictional and mobilises a larger angle of

internal friction as expected based on the passive pressure of the Rankine's theory. On the other hand when the soil is more dilative it could gain more strength if sheared due to the dilation and therefore resists better against yielding and producing plastic strains or in other word being highly deformed. Although, as it is anticipated, high shear strength soil tend to deform less compared with a low strength soil but a higher stress field is spread through the depth of the soil under an ice gouging scenario which would not have been experienced otherwise if less frictional strength is mobilized in the soil. The deeper extension of the stress field deforms the soil. This accumulated deformation is amplified at upper levels of the soil due to the relative displacement of the underlying layers of the soil.

Figure 6-16 to Figure 6-18 shows the three models, Drucker-Prager Cap with Mohr Coulomb yield surface in π plane, NorSand and Drucker-Prager Cap with circular yield surface, consistently result in less near surface sub-gouge deformation for dense soils (red plots). The reason is that the more dense sands have the potential to harden more due to dilation and as the results yield less plastic deformation. Would no hardening law be used, as was the case in the built in model, the impose load to the soil resulted in higher plastic deformation.

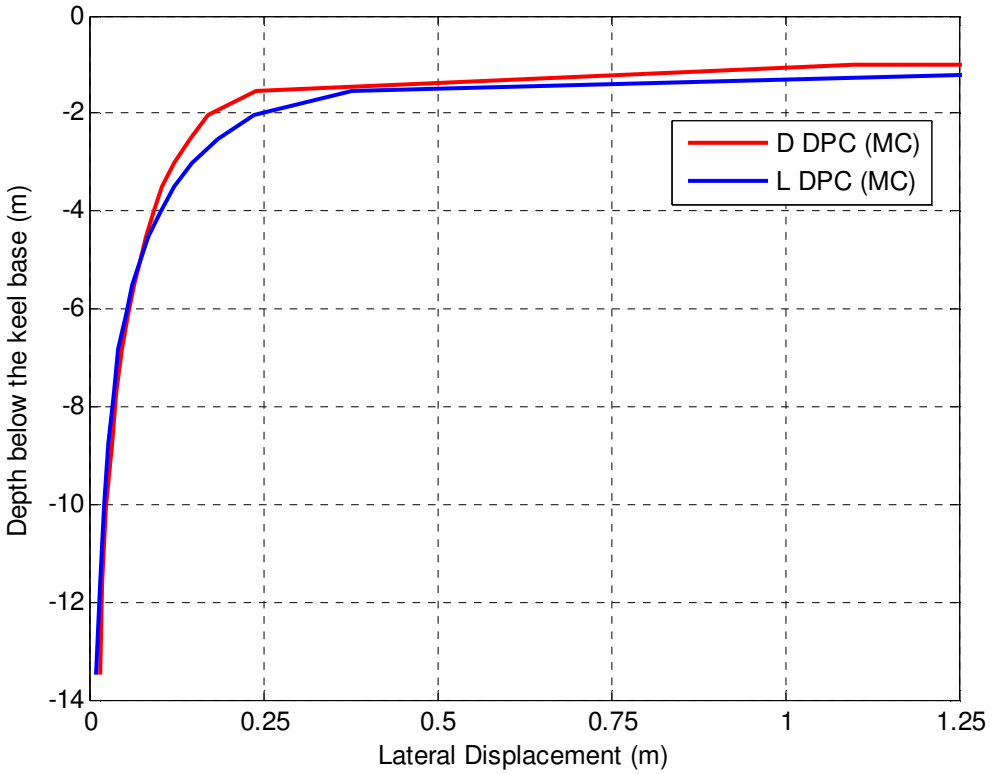

Figure 6-16 Subgouge deformations for dense and loose sand modelled by Drucker Prager Cap (MC)

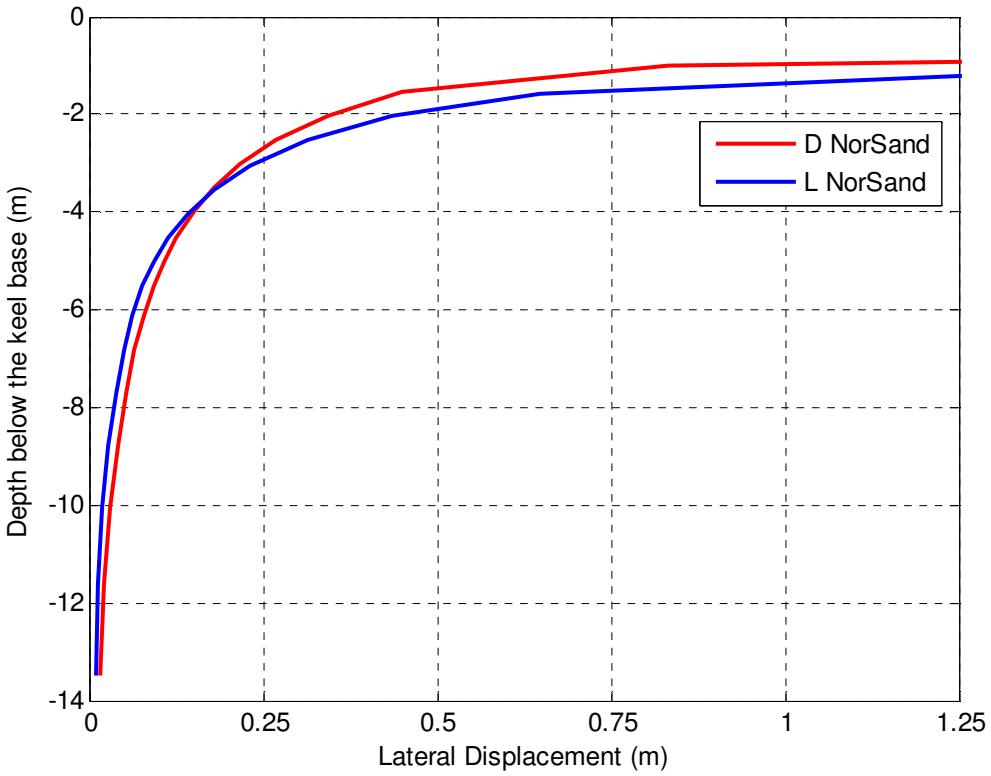

Figure 6-17 Subgouge deformations for dense and loose sand modelled by NorSand

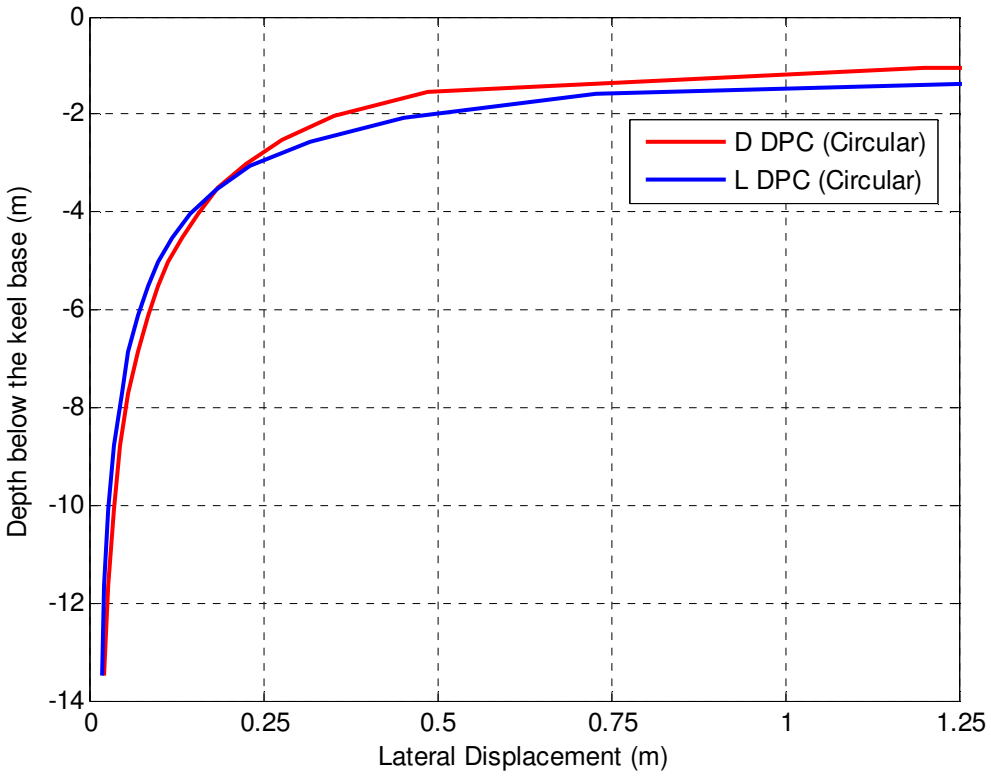

Figure 6-18 Subgouge deformations for dense and loose sand modelled by DP Cap (Circular)

Figure 6-19 to Figure 6-21 shows the gouging response for dense sand using the three models. These responses are the same except for the sub-gouge deformation which is less for the Drucker-Prager with the MC criterion as shown in Figure 6-21.

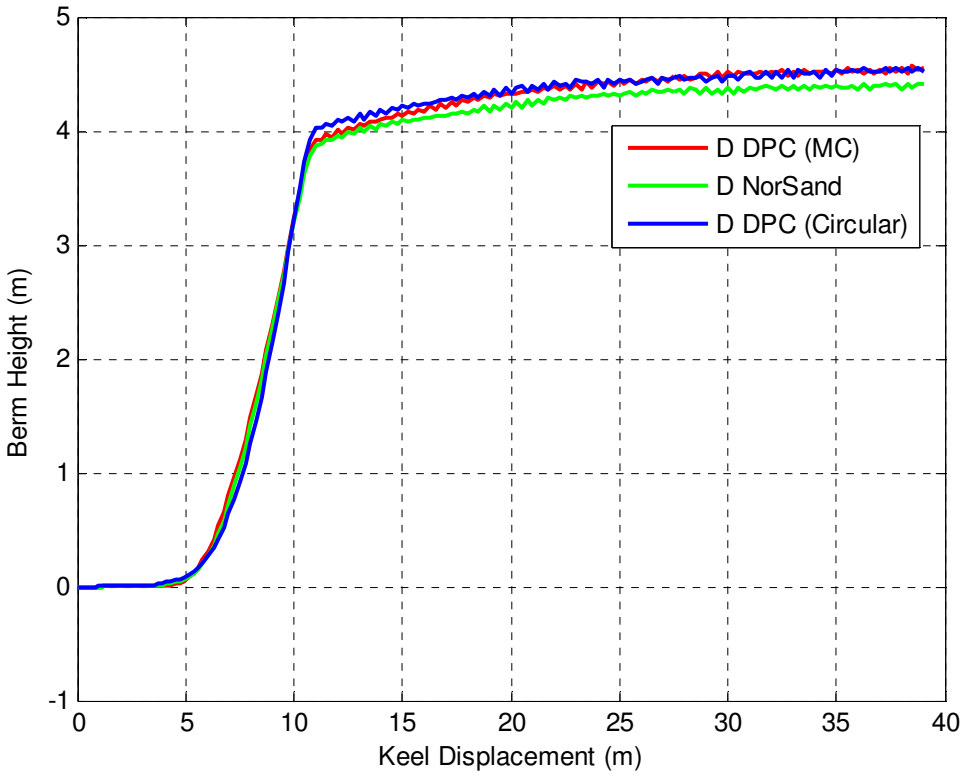

Figure 6-19 Comparison of frontal berm height development using the three models for dense sand

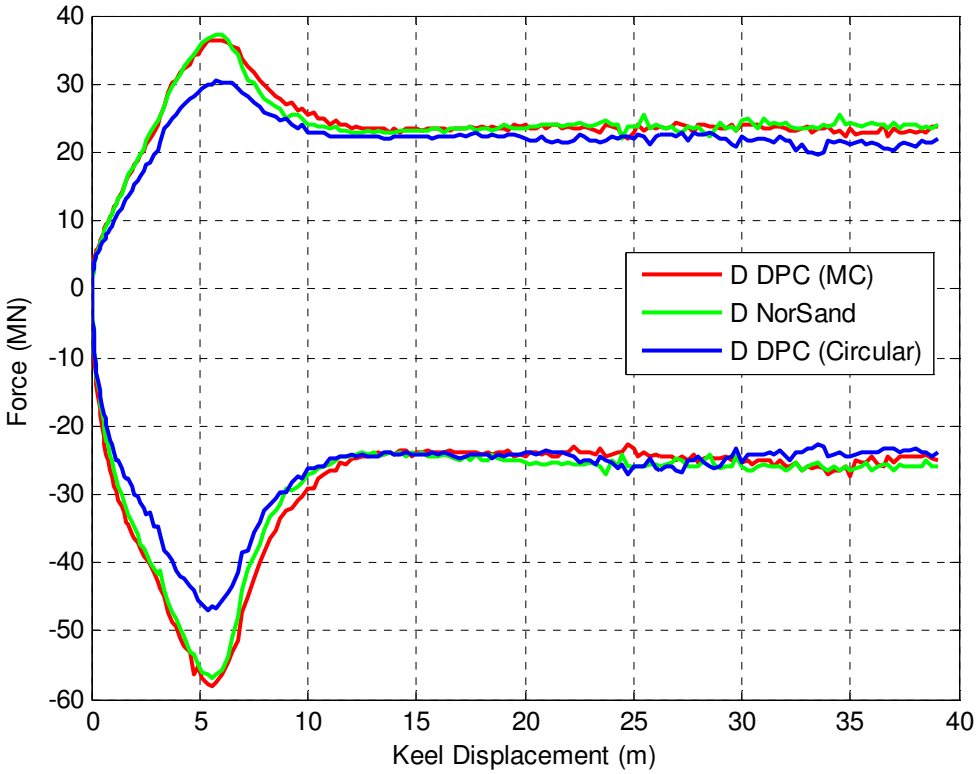

Figure 6-20 Comparison of keel reaction forces using the three models for dense sand

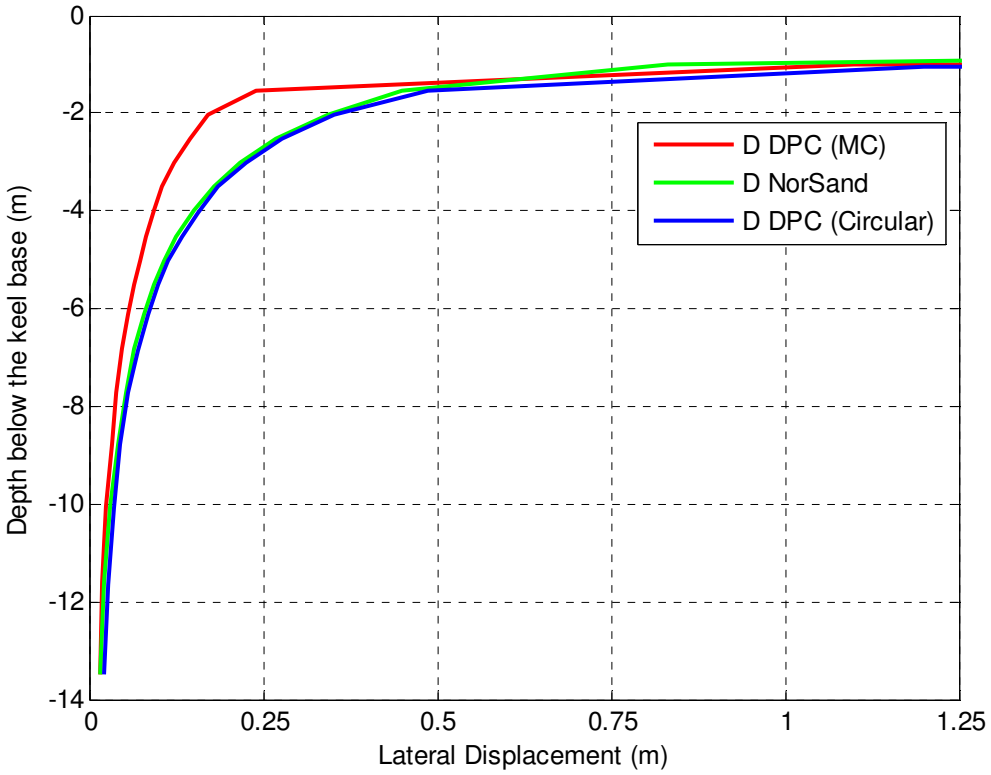

Figure 6-21 Comparison of sub-gouge deformations using the three models for dense sand

The results of the analyses for the medium dense sand (Table 6-3) draws the same conclusion as presented for the dense sand. These results are shown in Figure 6-22 to Figure 6-24.

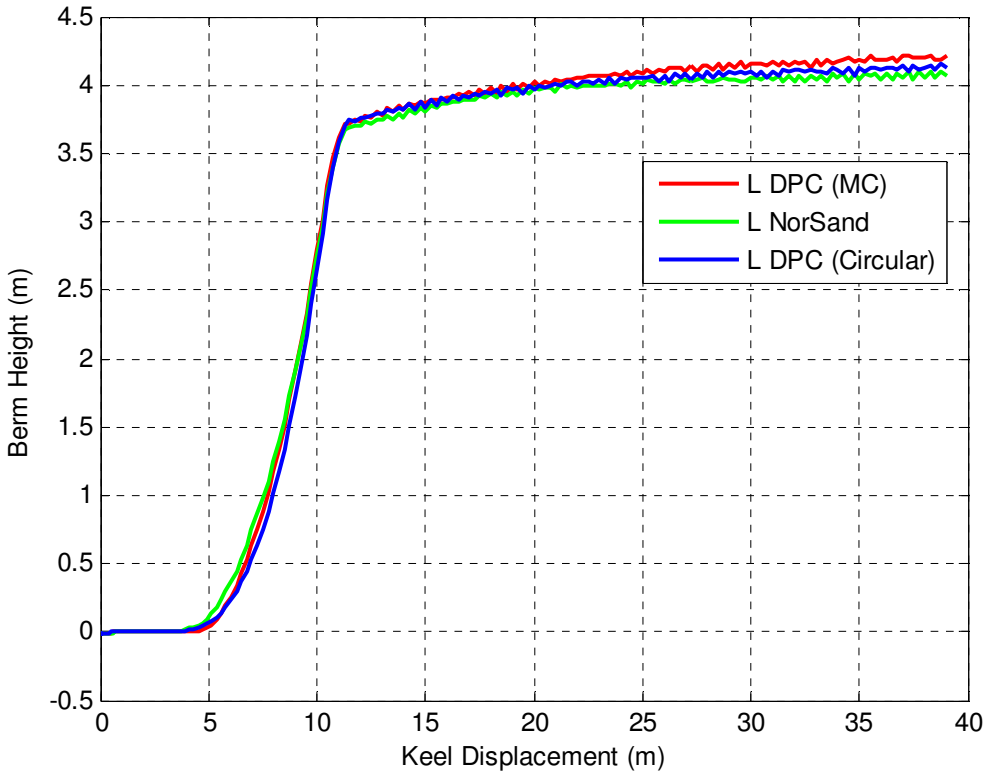

Figure 6-22 Comparison of frontal berm height development using the three models for loose sand

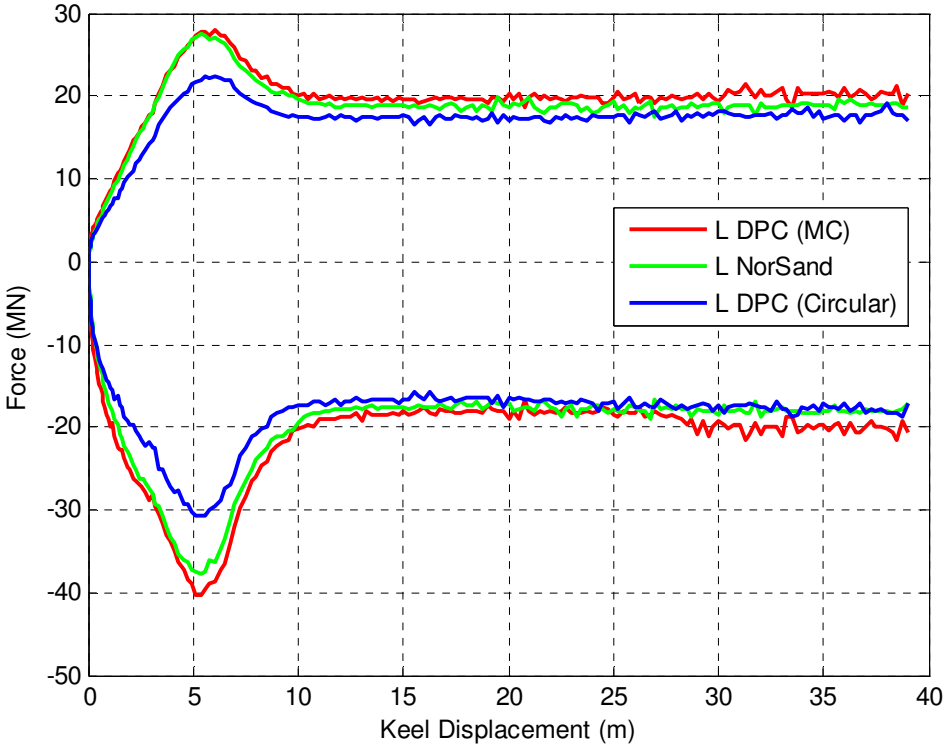

Figure 6-23 Comparison of keel reaction forces using the three models for loose sand

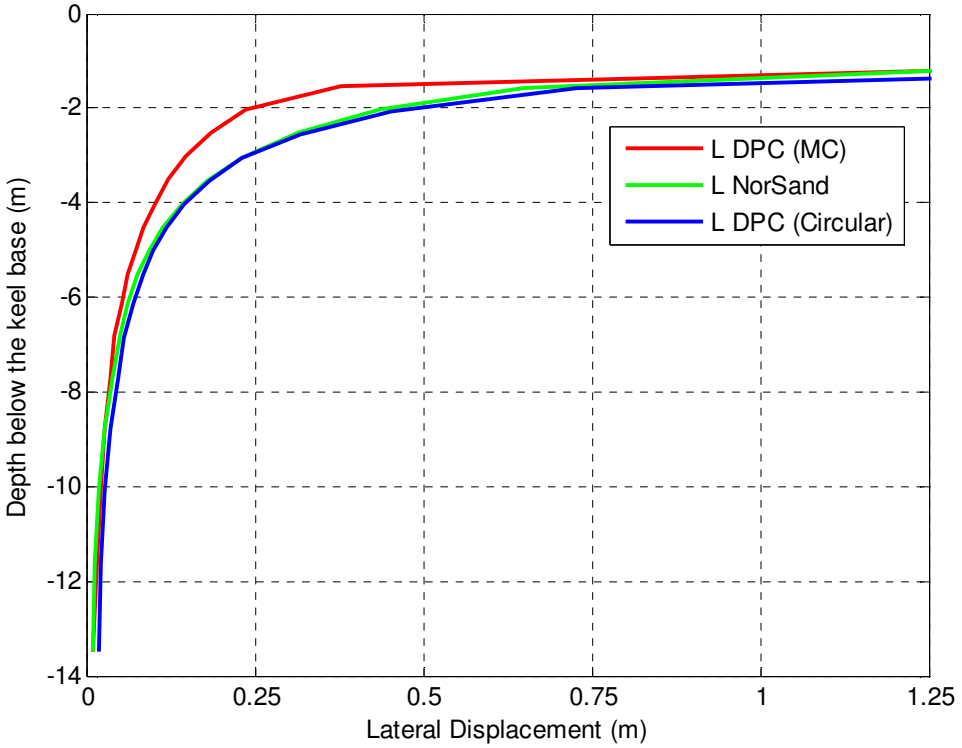

Figure 6-24 Comparison of sub-gouge deformations using the three models for loose sand

In the same way Figure 6-25 to Figure 6-27 shows that all three models result in similar plastic equivalent strains however in Drucker-Prager Cap (MC) the equivalent plastic strains are smaller beneath the front of the keel. The soil deforms in a consistent way in all three models. The strains shown in Figure 6-25 to Figure 6-27 are true strains in logarithmic scale, i.e. these figure cover strains of magnitude of 3500%.

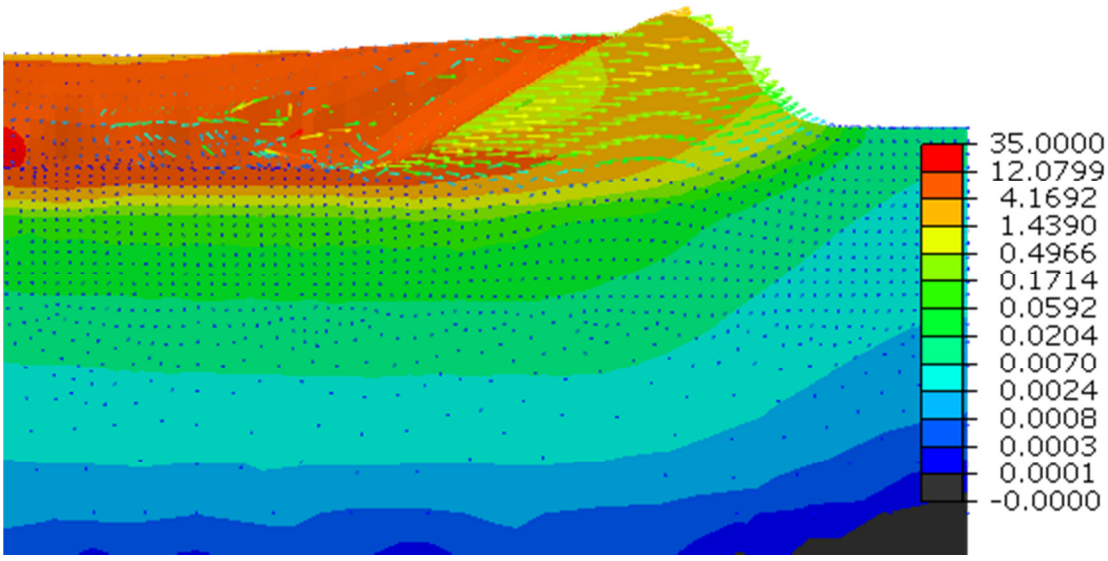

Figure 6-25 Plastic equivalent strains and soil movement paths in NorSand

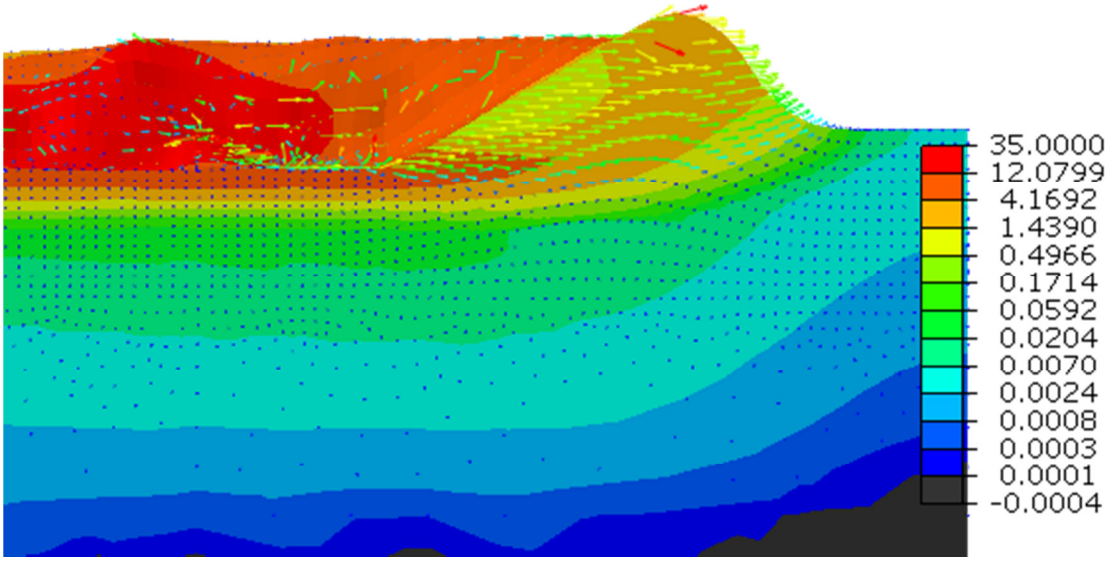

Figure 6-26 Plastic equivalent strains and soil movement paths in Drucker-Prager Cap (MC)

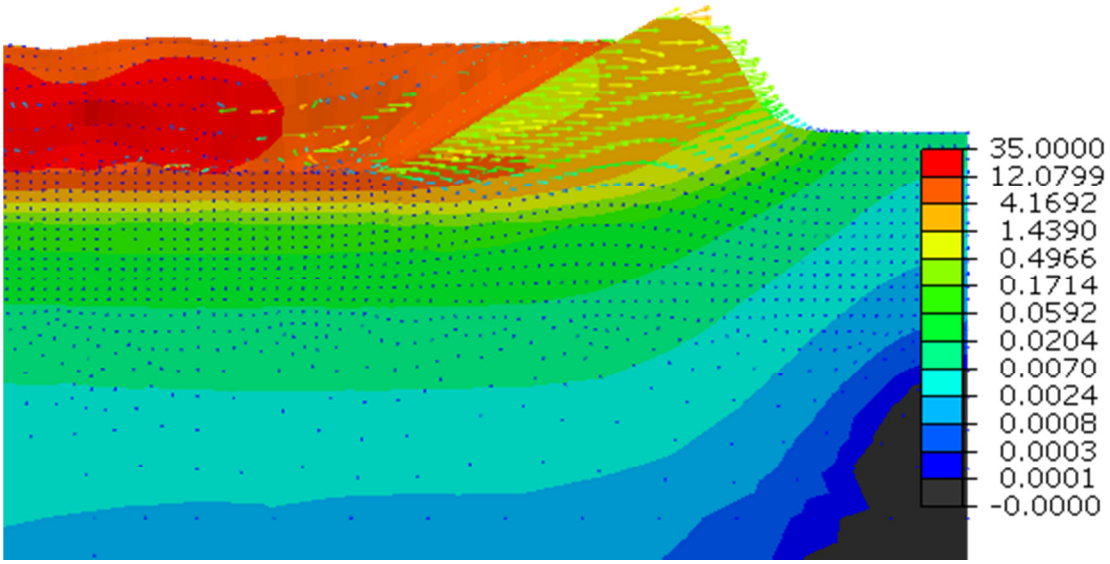

Figure 6-27 Plastic equivalent strains and soil movement paths in Drucker-Prager Cap (circular)

Figure 6-28 and Figure 6-29 shows the variation of Lode angle in Drucker-Prager Cap (MC) and Drucker-Prager Cap (circular) respectively. A Lode angle of 30° represents triaxial compression condition and Lode angle of -30° indicates the triaxial extension condition. Both these models have relatively similar responses in this regard. As the keel approaches a certain portion of the soil that portion becomes more confined and experience a compression-like condition therefore the lode angle rises up compared to the next portion of the soil.

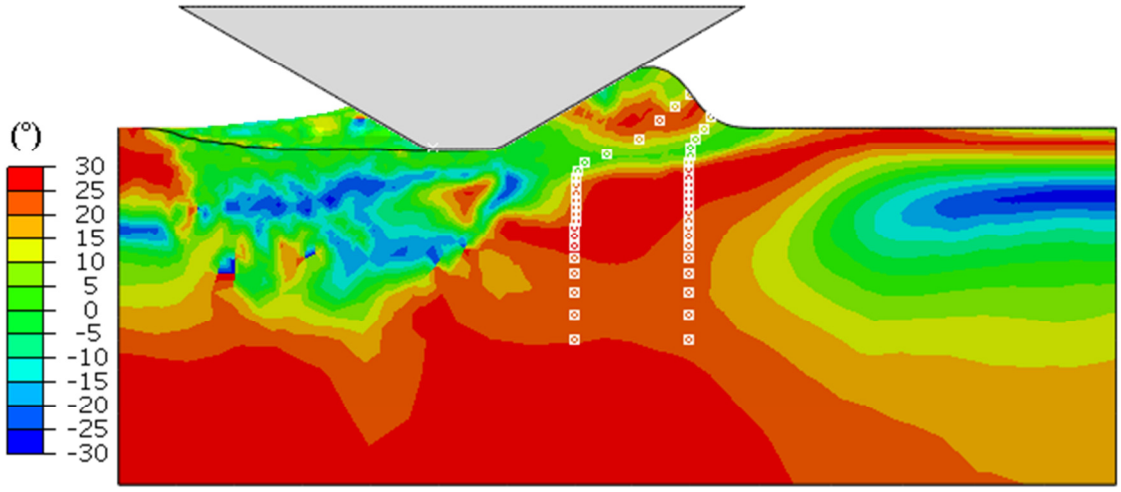

Figure 6-28 Lode Angle in DPC (MC)

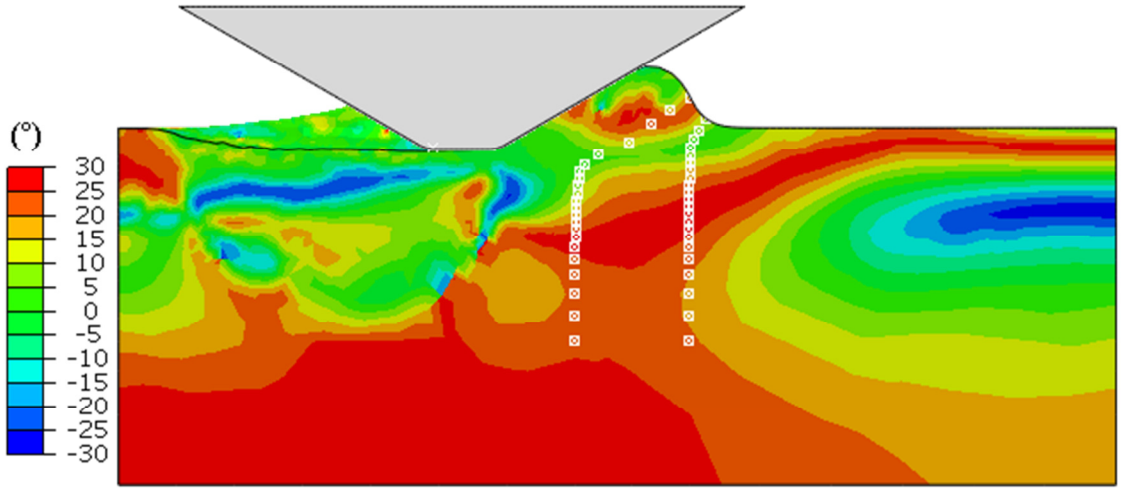

Figure 6-29 Lode Angle in DPC(circular)

Figure 6-30 shows the variation of Lode Angle in NorSand model and confirms the same pattern. In NorSand higher critical stress ratio will be mobilised when the lode angle is higher.

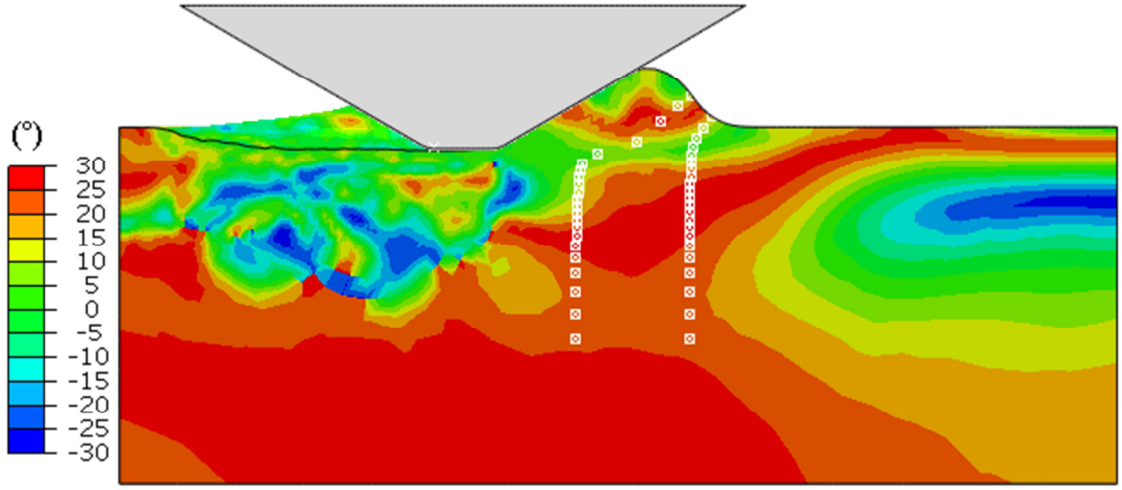

Figure 6-30 Lode Angle in NorSand

Figure 6-28 and Figure 6-29 could explain why the Drucker-Prager Cap (MC) model exhibits less sub-gouge deformation compared with the Drucker-Prager (circular). As the tracer particles shown in these figure are about to experience the effect of the gouging and respond to it by yielding plastically the increase in the lode angle could act as secondary source of hardening by increasing the mobilised friction angle. Figure 6-31 shows how the Drucker-Prager Cap with the Mohr-Coulomb criterion mobilises higher frictional properties through the depth of the soil. The increase in lode angle has no effect if the circular yield surface in the π plane is used.

There is a similar effect in NorSand, i.e. the critical stress ratio increase with the increase of the Lode angle, however, in NorSand the image pressure directly governs the hardening whereas in Drucker-Prager model the increase in θ directly enlarges the yield surface.

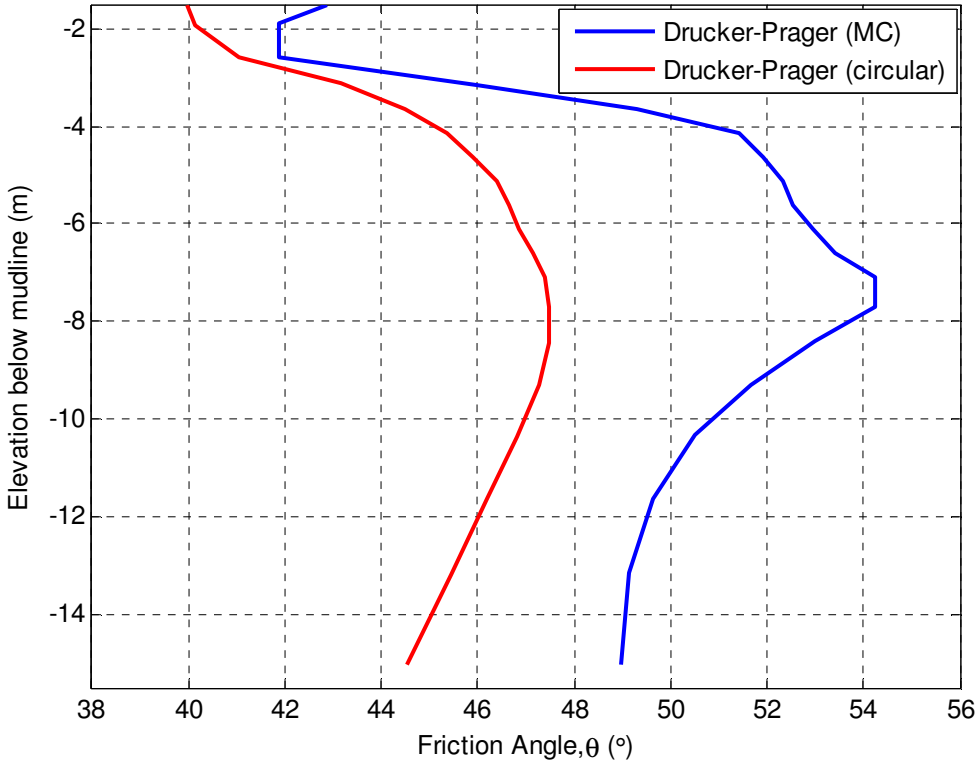

Figure 6-31 Variation of the friction angle, θ, through the depth of the soil in the two DPC models

6.3. Improvement of the analyses using the developed models

Figure 6-32 to Figure 6-34 compare the results of the user subroutines and the built in Drucker-Prager model. Depending on the density of the sand the developed model could simulate a range of responses. While a steady frontal berm is achieved using the developed models, it is possible to reach to realistic sub-gouge deformation and keep the keel reaction forces at expected levels. Figure 6-32 shows that the built-in model and the developed constitutive models exhibit similar keel reaction forces under the same gouging event. On the other hand, significant differences in sub-gouge deformations are observed between ABAQUS built-in model and the implemented user material models in Figure 6-34. An advantage of using the implemented user material model is avoiding

overestimation of sub-gouge deformations. In addition, Figure 6-32 to Figure 6-34 show how the implemented user material models could discriminate between different state of the same soil, whether it is loose or dense. It must be mention that one of the goals of developing a soil constitutive model is to be able to cover the different behaviour of the same soil with varying states.

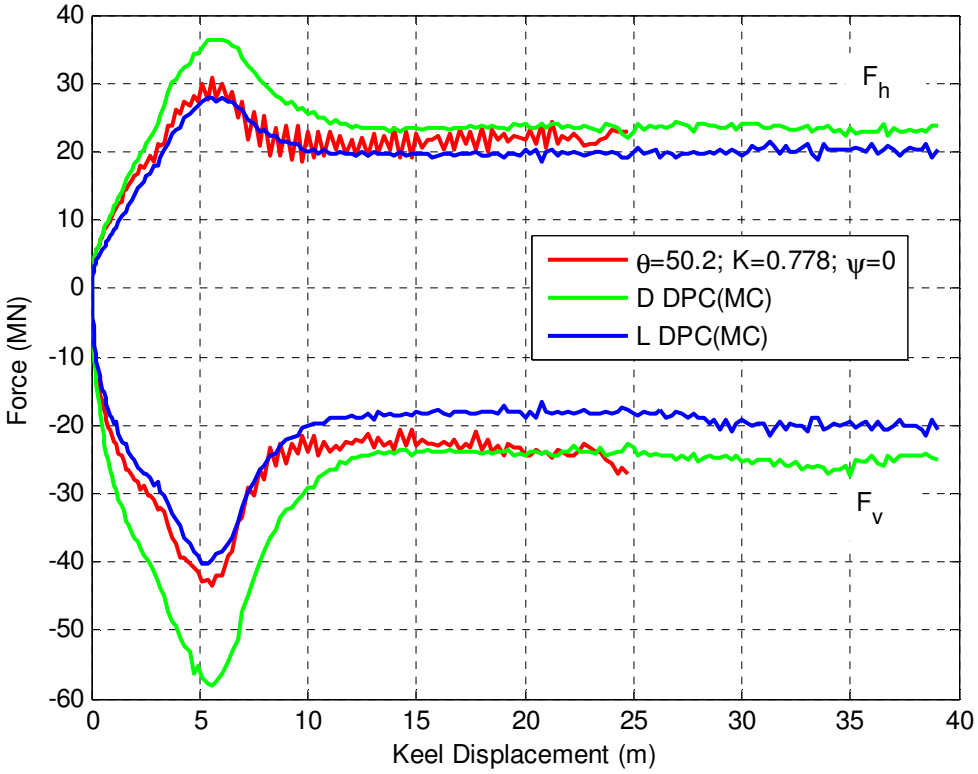

Figure 6-32 Comparison of keel reaction forces using built in model and the developed models

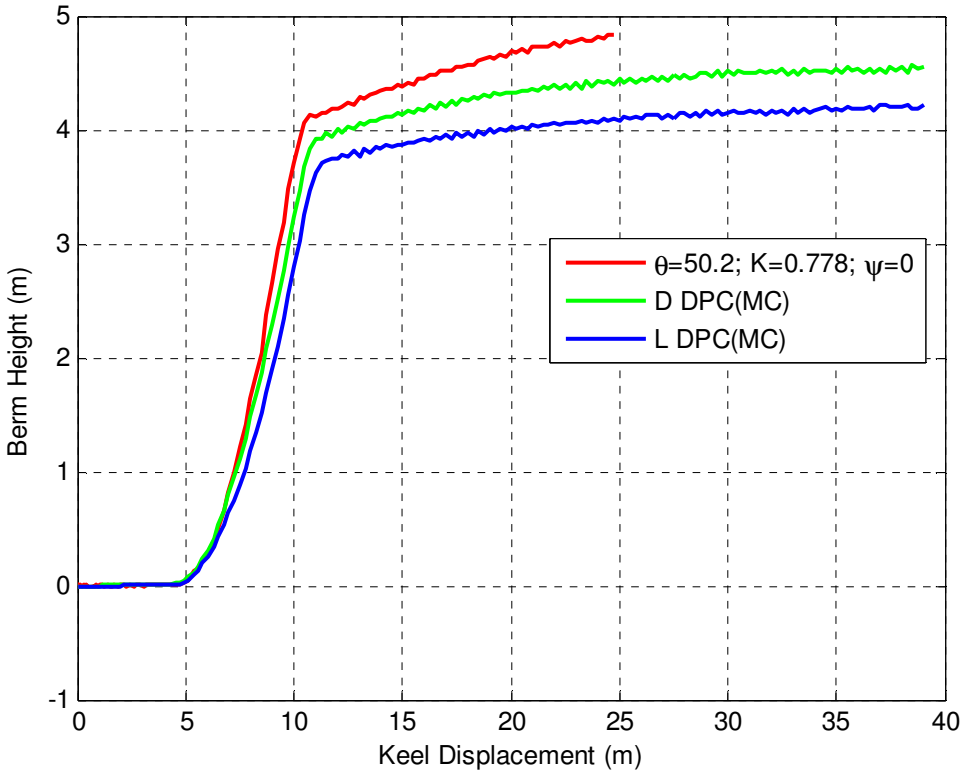

Figure 6-33 Comparison of frontal berm heights using built in model and the developed models

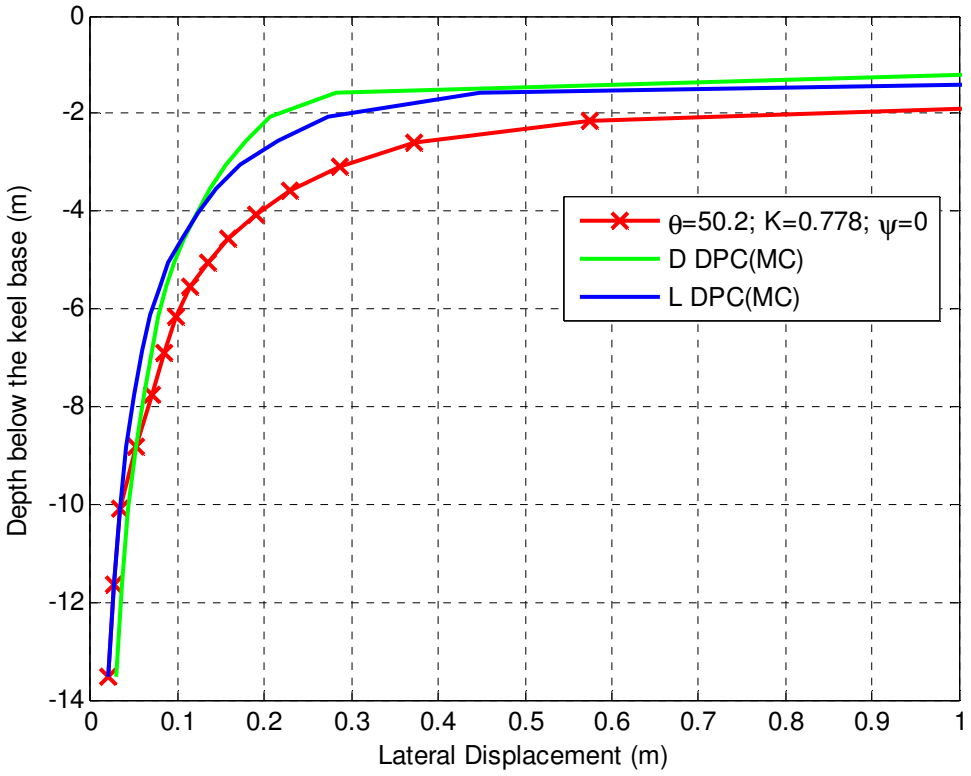

Figure 6-34 Comparison of sub-gouge deformations using built in model and the developed models

6.4. Model Validation Using Centrifuge Test Data

To validate the implemented critical state NorSand model some of the available physical tests are simulated in this section.

6.4.1. Issues and Limitations in Centrifuge Modeling of Soil

Since the soil self-weight is a significant factor in the mechanical soil behaviour and extremely affects its material strength, it is not possible to examine large scale problems based on the response of small laboratory models under earth gravity loads (g). Therefore, the centrifuge tests are very suitable for materials such as soils that are pressure dependent.

However, centrifuge tests involve time dependency and strain rate issues that might influence the results. Model boundaries can affect the results as well.

Based on scaling laws, stress and pressure and density in the model, which are actually coupled in soil, are equal to those in prototype. This helps to prepare the centrifuge tests to represent the actual soil behaviour as much as possible. However, there are specific characteristics of soil that jeopardize the similarity of model and prototype in centrifuge tests. One of which is size effects at shear interfaces. During the shearing process, the breakout friction between the granular soil material and structural surfaces embedded in the soil will mobilize as a function of relative displacement. It is then necessary to determine the dependency of the mobilization displacement on the grain sizes and the dimensions of the contact surfaces.

The scaling in centrifuge could be problematic when pore pressure issues involve. This is more critical when the soil is unsaturated or shear bands form. It is usually very difficult to maintain the same scale for all parameters or to use same material in both model and prototype. Therefore, the parameters that should be scaled have to be prioritized. There are also occasions that time scaling leads to some conflicts between the parameters. For example in a dynamic problem, ice gouging for example, the time scaling due to model size and pore fluid dissipation may conflict. These conflicts can be resolve by modifying the pore fluid (viscosity) or modifying the particle sizes. It should be noted that as implied earlier these conflicts may be neglected in some cases. For example if tests are performed in fully drained condition or fully undrained condition in a dynamic event (e.g. ice gouging) then it is expected that the inaccuracy due to time scaling is minimum.

The formation of shear bands in a centrifuge may have some issues. It is known that the thickness of shear bands in soil is a function of the particle sizes. If both the model and prototype consist of the same grain sizes then the formed shear bands in centrifuge may not be representative of the shear bands in the real ice gouging events. Therefore, in order to be able to assume soil as a continuum material in centrifuge tests it should be ensured that enough number of particles are placed around different parts of model such as boundaries of the keel or pipe in case of ice gouging tests. This can be achieved by adjusting the soil particle sizes. However, to develop similar contact stresses the prototype and model grain sizes should match. Usually it is not practical to adjust the grain sizes based on the scaling laws. The grain size in centrifuge tests represents much larger grain sizes compared with the actual soil that is modeled. Therefore, scaling sand grains may require using silt or clay in centrifuge which are significantly different in term of strength and behaviour. Different researchers have studied the grain size effect and have developed relations to limit the ratio of grain size to model dimensions (e.g. footing) in order to minimize the grain size errors.

Another issue that can affect the accuracy of the centrifuge tests is the boundary or container effect. The side frictions are important in the centrifuge models. It is advised to use container that its width is larger than its height and the side wall frictions should be minimized as much as possible. The structures, e.g. the keel, should be kept away from the boundaries as far as possible.

6.4.2. Numerical Analyses of Centrifuge Tests

These physical tests performed in a centrifuge are described by W. Yang (2010). In this section a total of 3 tests are examined.

The equivalent physical properties of the gouges in each test are summarized in Table 6-4.

Table 6-4 Gouging properties in the centrifuge tests (prototype scale)

	Attack Angle (degree)	*Gouging Depth* D_s *(m)*	*Gouging Width* W *(m)*	*Velocity* (cm/s)
PIRAM P03	*30*	*1.43*	*10*	*5*
PIRAM P06	*30*	*2.3*	*14.4*	*11*
PIRAM P07	*30*	*2.4*	*14.4*	*55*

Table 6-5 summarizes the soil properties that are used in the numerical analyses of the PIRAM tests. These properties include the input parameters for both NorSand and Drucker-Prager Cap models. The submerged density is assumed to be 800 kg/m^3.

Table 6-5 Soil properties used in numerical analyses

E	ν		OCR
26 *MPa*	0.32		2
	NorSand		
Γ	0.91	M_{tc}	1.2
λ	0.03	χ_{tc}	3.8
	PIRAM P03	*PIRAM P06*	*PIRAM P07*
ψ	-0.1	-0.065	-0.025
H	250	225	200
	Drucker-Prager Cap		
d	θ		R
2 kPa	50.2°		2.7
	PIRAM P03	*PIRAM P06*	*PIRAM P07*

I_R	1.5	0.97	0.6

To simulate these centrifuge test a meshing size of 0.5 m by 0.5 m by 0.25m (length by width by depth) is used. The previous ice gouging analyses have shown that the adopted meshing size provides mesh independent numerical models in which the soil is adequately discretized (Eskandari et al., 2012).

Figure 6-35 and Figure 6-37 compare the keel reaction forces for test 3 and test 6 of PIRAM, respectively. In centrifuge tests the keel is initially indented into the soil at the gouging depth and begins to advance horizontally. However, in the numerical analyses presented in this study the keel is initially at mudline and penetrates the soil vertically until it reaches the gouging depth. This process includes a small period of the analyses and the keel then only moves horizontally. This discrepancy is the reason why the keel reaction forces initially respond differently in Figure 6-35, Figure 6-37 or Figure 6-39. The steady state keel reactions, approximately after 15m keel displacement, are close to the centrifuge results. Figure 6-36 and Figure 6-38 show the sub-gouge deformations for test 3 and test 6 respectively. As mentioned before the Drucker-Prager Cap with Mohr-Coulomb criterion has the lowest sub-gouge deformation.

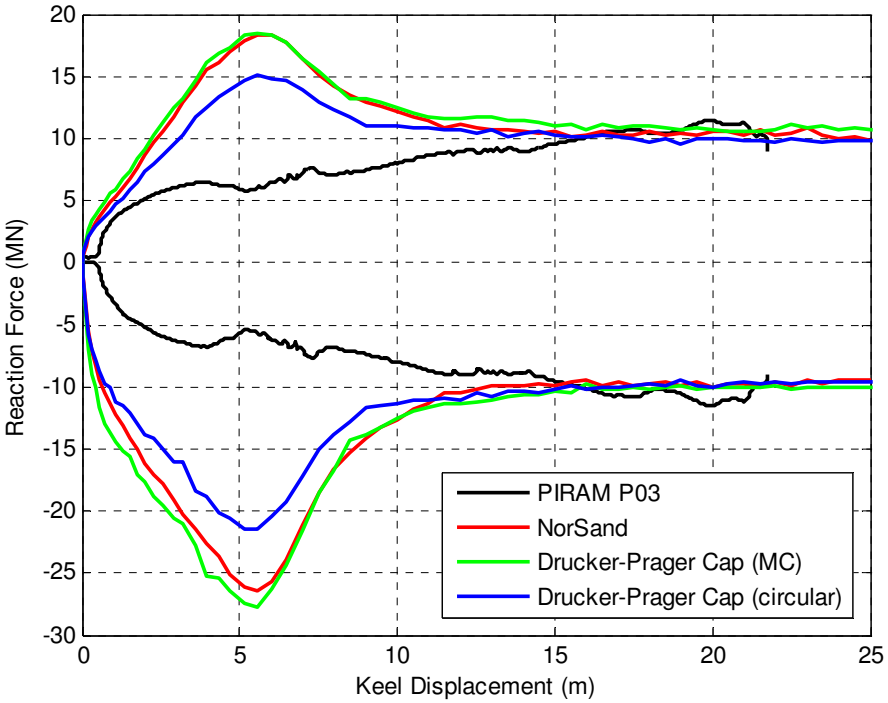

Figure 6-35 Comparison of the reaction forces in PIRAM P03

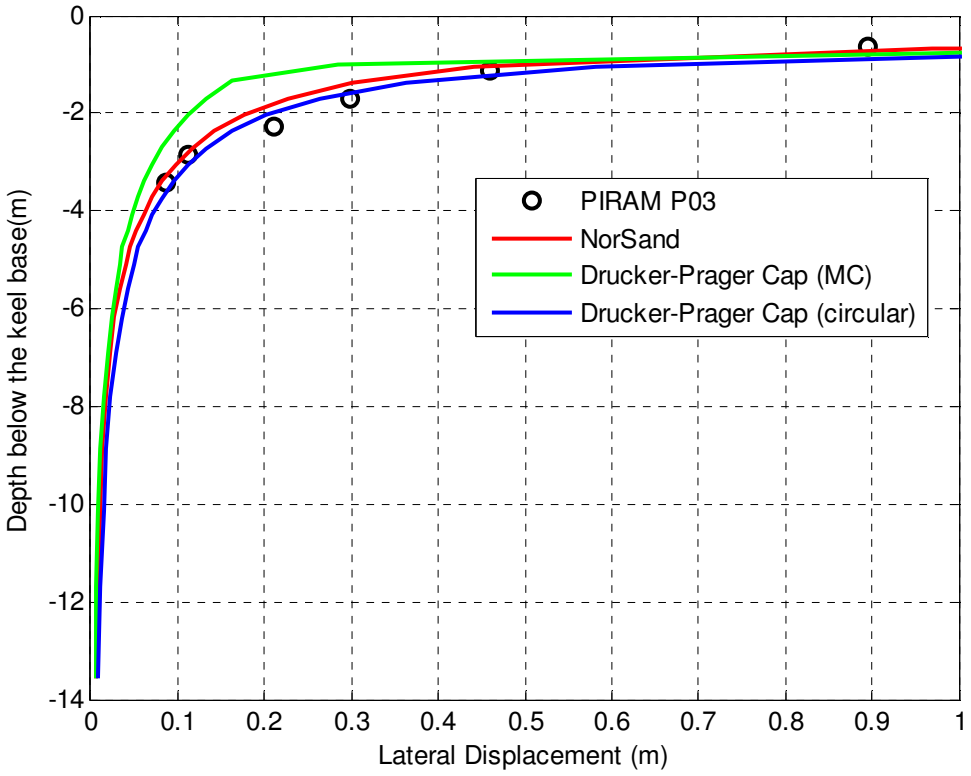

Figure 6-36 Comparison of the sub-gouge deformation for PIRAM P03

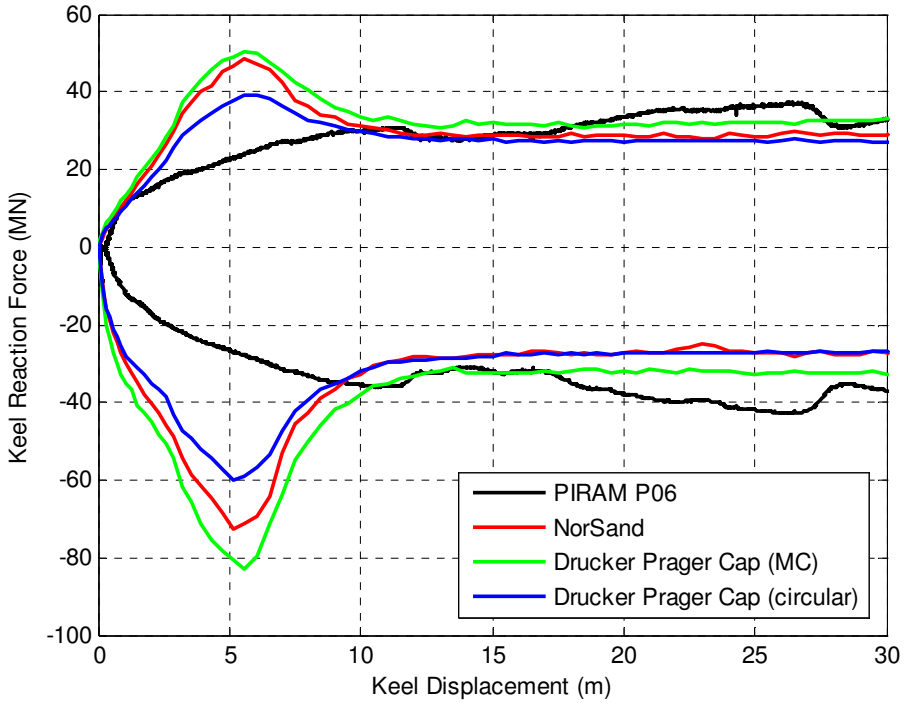

Figure 6-37 Comparison of the reaction forces in PIRAM P06

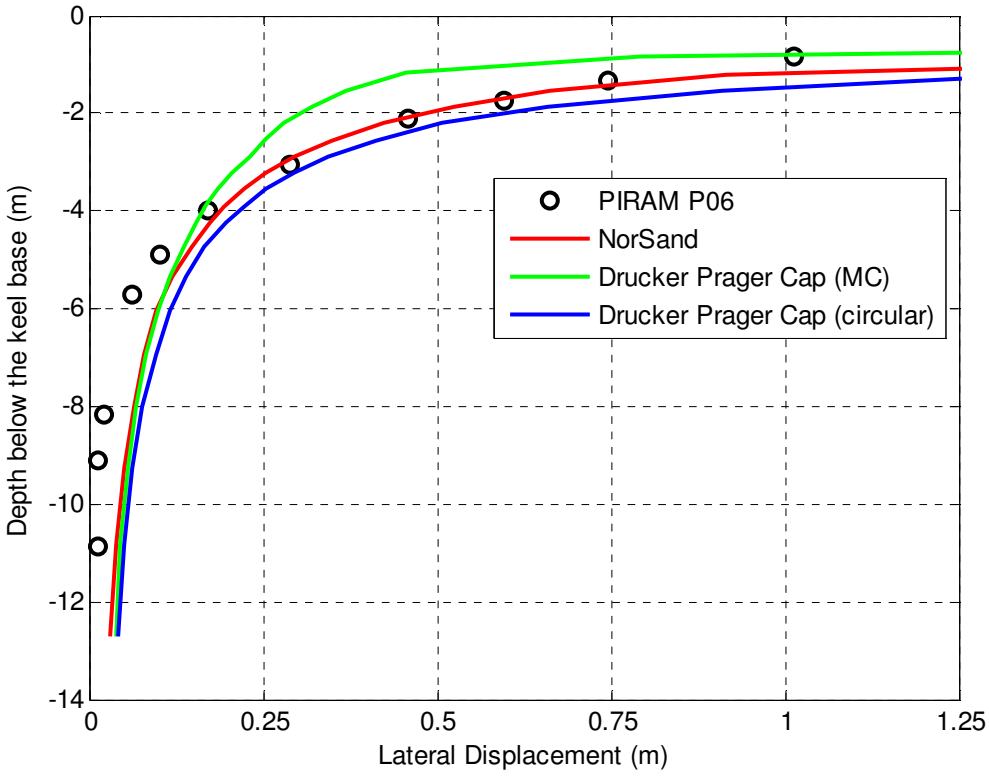

Figure 6-38 Comparison of the sub-gouge deformation for PIRAM P06

Figure 6-39 compares the keel reaction forces for test 7 and Figure 6-40 shows the sub-gouge deformations for the same centrifuge test,

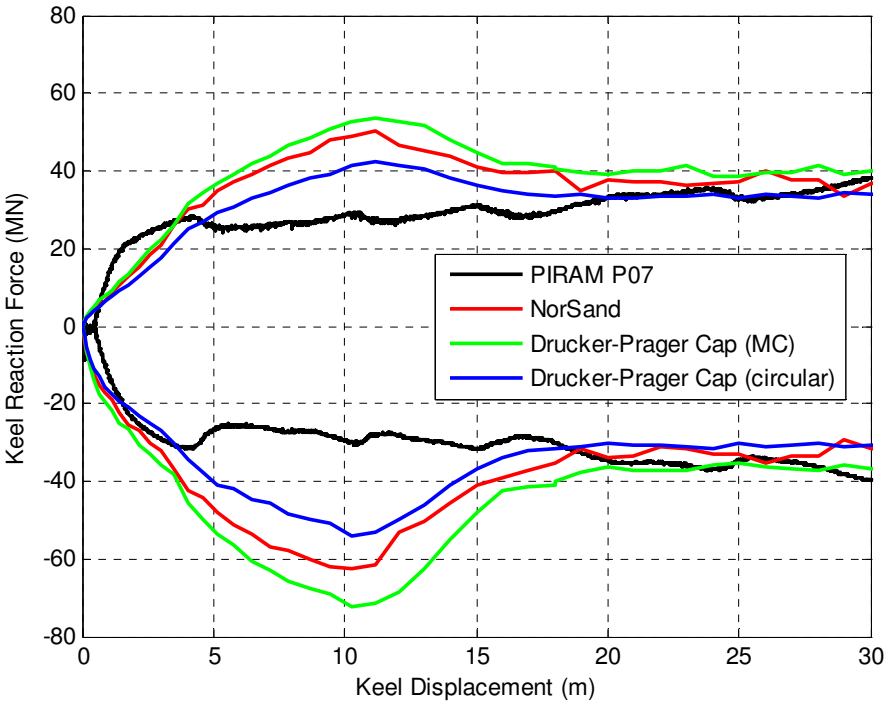

Figure 6-39 Comparison of the reaction forces in PIRAM P07

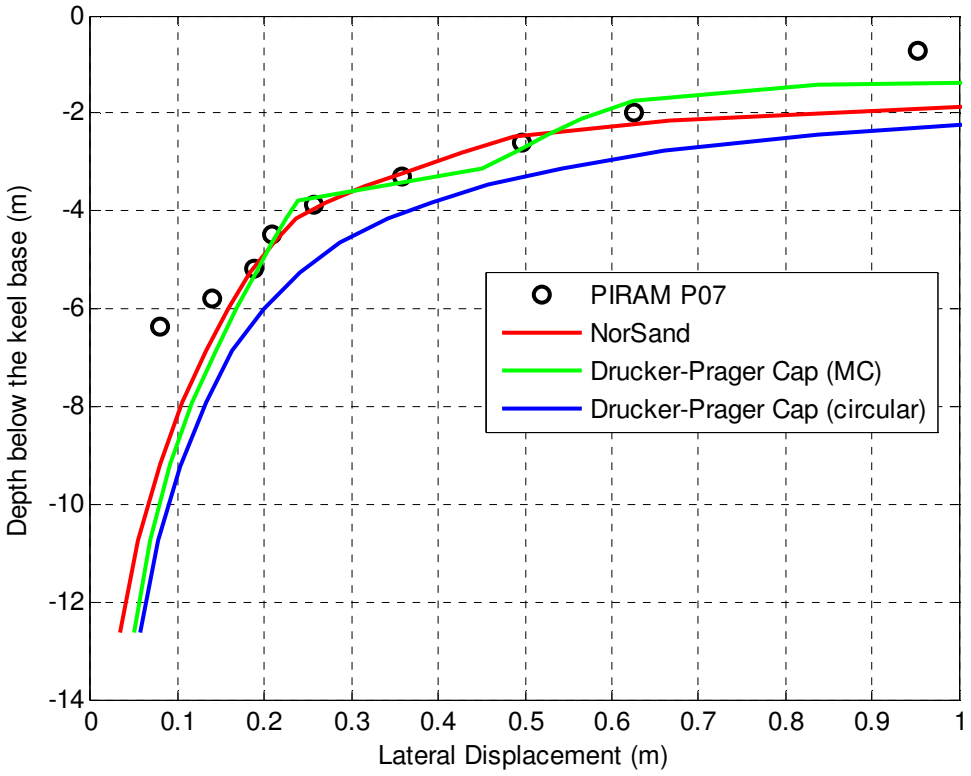

Figure 6-40 Comparison of the sub-gouge deformation for PIRAM P07

Figure 6-41 shows the sub-gouge deformation for all three centrifuge tests and compares them with the results that are obtained from numerical analyses based on the NorSand model. The predicted sub-gouge deformations match the test results well.

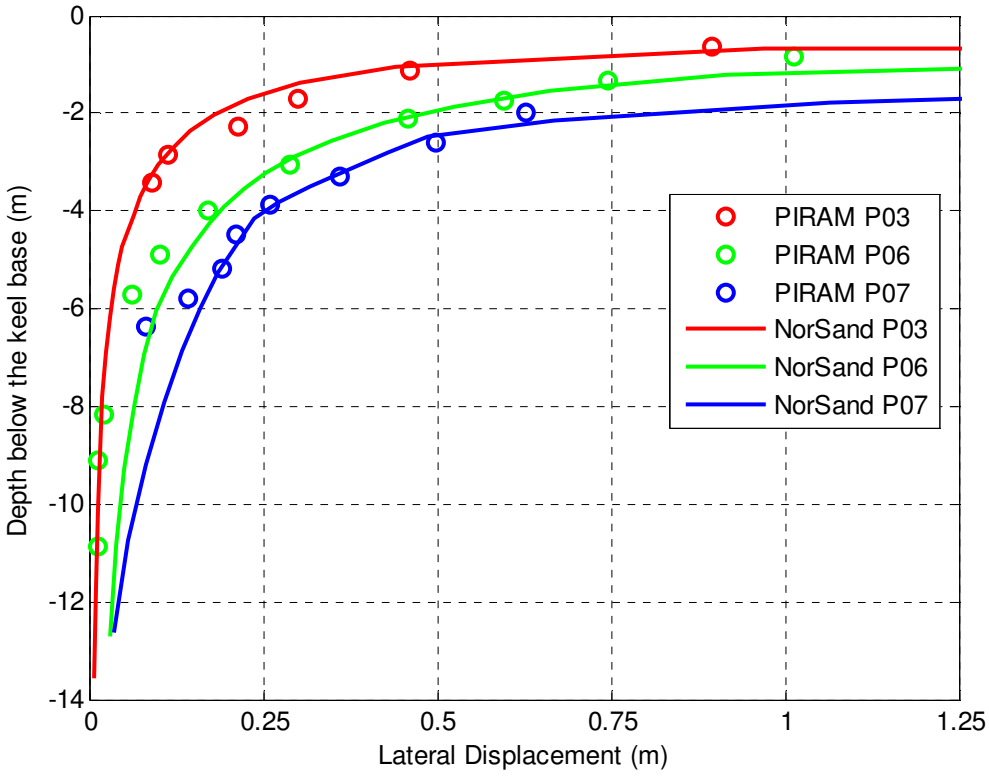

Figure 6-41 Simulation of sub-gouge deformations of PIRAM tests 3, 6 and 7

6.5. Contribution of the study

Numerical analyses are powerful tools to study the ice gouging problems. The finite elements models that are used to study the ice gouging are either Winkler based models or continuum models. The current state of practice in offshore Arctic pipeline design for ice gouging is to use the structural soil/spring models integrated with some empirical functions to simulate uncoupled ice/soil and soil/pipe interaction.

The structural models are easy to implement but usually they are not accurate. More complex structural models are proposed but it is very difficult to determine realistic input parameters for these models. On the other hand, the continuum models are more accurate for soil modelling and geotechnical engineers have relatively reliable methods to evaluate

their parameters. The soil spring models represent the soil as independent linear springs which differ from the real soil behaviour. Different researches has shown that if directional coupling of soil spring models are considered, the conservatism of the soil/spring models could be reduced by 30%. Another issue with soil/spring models is that they do not consider the slice to slice coupling either. This means that the spring forces, i.e. soil strength, at one point only depends on the displacement at the same location and the adjacent region has no effect on the soil strength. In reality the ice loads affect the soil resistance and reduce its strength. Therefore the soil resistance on pipe is decreased.

Different sub-gouge deformation functions are proposed in a number of projects such as PRISE, PIRAM or Kashigan to use in soil/spring analyses of ice gouging.

Figure 6-42 and Figure 6-43 compares the results of an ice gouge analyses based on the PRISE, PIRAM and Kashigan sub-gouge deformations formulas and compare them with results obtained from a similar coupled analyses using the constitutive models that are implemented in this research, specifically the NorSand model. The results shown in Figure 6-42 pertain to the outer side of the pipeline.

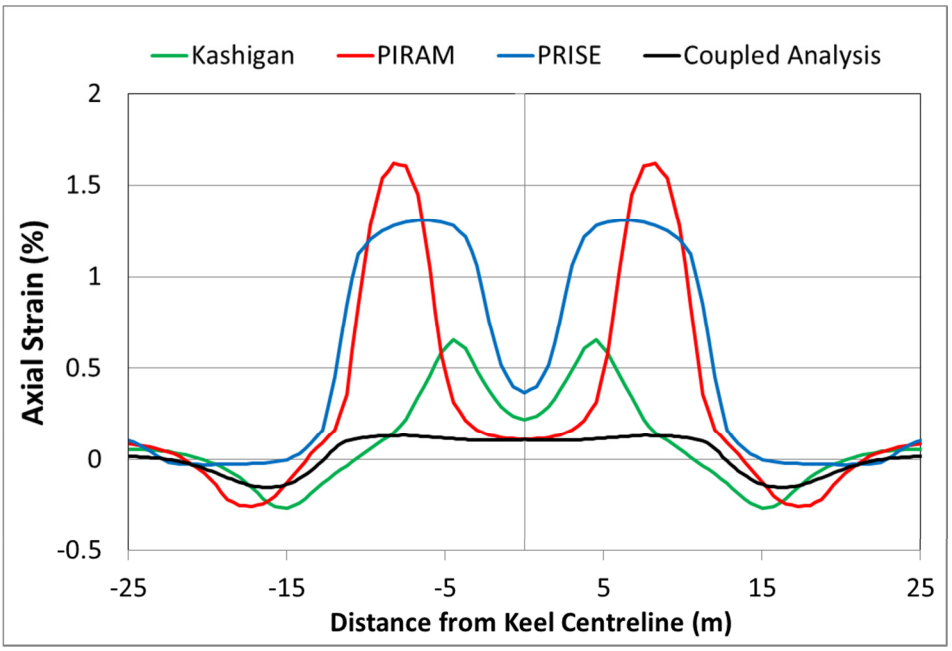

Figure 6-42 Axial strain at extrados

The same comparison for the inner side of the pipe is shown in Figure 6-43. As these two figures show, the soil spring analyses regardless of which function for sub-gouge deformations is used, results in more conservative strains.

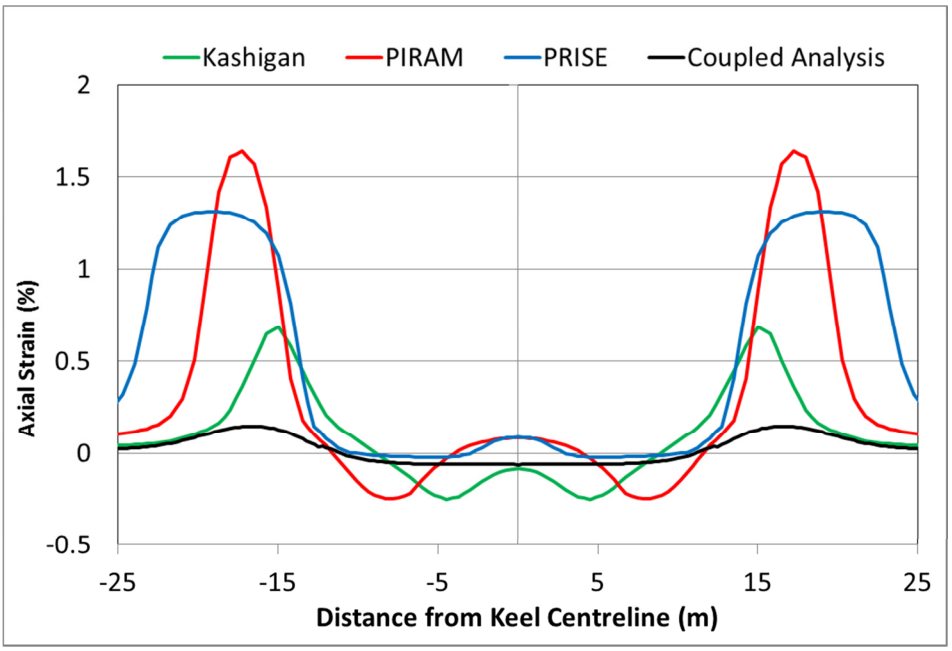

Figure 6-43 Axial strain at intrados

The unnecessarily over conservative results that are obtained based on soil/spring models could rise the cost of the project dramatically to the extent that it might deemed as uneconomical or unfeasible. Additionally, the soil/spring analyses are enable to adequately capture a number of important aspects of ice gouging problem such as soil failure mechanism, non-uniform pressure field in the soil, soil pipeline strain discontinuity, pipeline seciton ovalization and wrinkling and finally local buckling or failure.

Most of the shortcomings of the soil/spring analyses can be addressed by the coupled continuum models. These models are usually complicated. The complexity of these models doubles when they are applied to the geotechnical problems because the soil behaviour cannot be accurately captured using simple constitute models that may work well for other materials such as metals.

The Mohr-Coulomb criterion is one the most popular constitutive theories in geotechnical engineering. However, this model has some disadvantages that limit its broader use in geotechnical numerical simulations. One issue with the Mohr-Coulomb model is that it does appropriately consider the intermediate principal stress in the yield surface which leads to inconsistency with laboratory test results. In addition, this model has an irregular yield surface in deviatoric plane which makes it unsuitable for implementation in numerical methods because the sharp corners of the model may prevent convergence. The Drucker-Prager model is widely used in geotechnical problems. The yield surface of Drucker-Prager is matched with Mohr-Coulomb criterion. However, the Drucker-Prager model takes the effect of the intermediate stress into account.

Abaqus Explicit offers two versions of Drucker Prager model which are usually employed in the analyses of geotechnical problems 1) Drucker-Prager and 2) Plasticity Cap models. The conventional Drucker-Prager yield surface in Abaqus Explicit features a non-associated flow rule in which the potential surface is defined based on the dilation angle as an input parameter. The dilation angle in this model is defined as a constant variable, therefore, the soil under continued shear dilates indefinitely. As a result, the soil volume increases unrealistically. The plasticity Cap model features an associated flow rule. The Cap helps realize more realistic behaviour in modeling geotechnical problems. However, the normality rule and the associated flow rule cause excessive volume increase at lower pressure. Low pressure is a common situation of soil and an appropriate soil constitutive model should be able to handle this situation adequately. Figure 6-44 shows how the plasticity Cap model could result in unrealistic excessive volume increase in the soil.

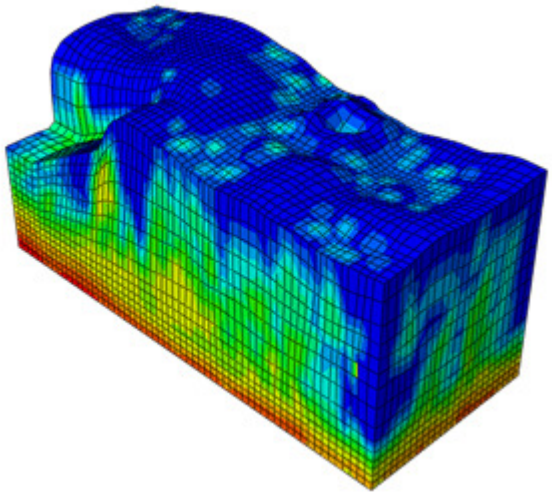

Figure 6-44 Excessive volume increase using the plasticity Cap model

There are fairly good models for clay that can relatively adequately simulate the clay behaviour in geotechnical problems. One of the main issues with sand is that dilate when they shear. The dilation rate of sand determines how the sand deforms. In the ice gouging problem, the dilation rate influence how deep the sub-gouge deformations can extend and how large is the magnitude of sub-gouge deformations. This has direct implication on the buried pipeline response and strain levels and therefore governs the required burial depth which has direct impact on the economics of a project. As the result a numerical model that can capture dilation is significantly needed to improve the current state of practice of the ice gouging analyses and the design of buried pipelines. This research seek a solution to this problem by developing constitutive models that limit the dilation rate and base the dilative behaviour of the soil on the empirical relations. The critical state theory, as discussed in this research, is the framework in which the soil behaviour is defined. Modifying the dilation ratio and following the critical state theory principals to outline the

soil behaviour will significantly improve the performance of the finite element ice gouging models.

6.6. Summary

In this chapter the three-dimensional finite element model which was developed using ABAQUS Explicit is applied to simulate the ice gouging events in the sandy subsea. This section highlighted some of the inherent limitations of the common built in numerical models in finite element packages. It was shown how the developed constitutive models could improve the numerical simulation of the seabed gouging event.

The developed three-dimensional finite element model integrated with the improved constitutive models is validated by simulating the gouging results of physical tests. The results of the ice gouging analyses were relatively well in agreement with results obtained from centrifuge tests.

The analyses in this chapter show that the NorSand model is capable of predicting ice gouging behaviour. The results presented in this section are satisfactorily close to the gouging data obtained from centrifuge test for drained (slow gouging) conditions.

7. Conclusion

7.1. Summary

The work outlined in this thesis was conducted to improve the numerical analysis of sandy seabed response to ice gouging.

In this thesis, the Drucker-Prager Cap model was improved to capture the different responses of sands, depending on the density and stress level. These improvements include the modification of the plastic potential function in the shear zone to control the dilation rate at lower stress levels, and a proposition of a hardening law based on critical state theory. The result is a simple model that can relatively accurately predict the strain-stress behaviour of sands. This constitutive model resolves the issue of excessive dilation which the basic Drucker-Prager Cap model suffers from. The shear hardening model, which is based on soil state and a maximum allowable dilation, enables the model to predict some aspects of dense sand behaviour, such as softening. The proposed model has been validated for behaviour of loose to dense drained sand under triaxial loading conditions. The model has been implemented in ABAQUS finite element software with a user defined subroutine, VUMAT, that was developed as part of this study to simulate large strain behaviour of sand during ice gouging events.

A second model, the NorSand model has been implemented in ABAQUS Explicit as well to analyze seabed response to ice gouging. This model has shown good performance in modeling various laboratory tests for sand. Both models are extended to capture the undrained behaviour of the soil through the application of volume constraint method.

A three-dimensional finite element model is created to model the ice gouging event. The steps of the numerical modeling are explained. The implemented user defined material models are applied in the finite element software to simulate the ice gouging process. The developed three-dimensional finite element model integrated with the improved constitutive models is validated by simulating the gouging results of physical tests.

Some of the inherent limitations of the common built-in soil constitutive models in the ABAQUS finite element package are highlighted. It is shown how the advanced constitutive models developed in this study could improve the numerical simulation of the seabed gouging event.

7.2. Results

The built-in Drucker-Prager model or Drucker-Prager Cap model in ABAQUS has some limitations in the analyses of large deformation ice gouging events. In this thesis it is illustrated that it is important that a soil model can capture different states of the soil, i.e. whether it is loose or dense, as it influences the stress-strain behaviour of the soil. Based on the numerical analyses performed in this research it is also shown that use of these built-in models could reduce the accuracy and stability of numerical analyses due to excessive dilation. The modified Drucker-Prager Cap model developed in this thesis mitigates these shortcomings of the built-in models (i.e. the excessive dilation and inability to model soil state). The empirical hardening law of the modified Drucker-Prager Cap model made it possible to simulate more realistic behaviour (in term of dilation rate and hardening/softening behaviour) of the soil under an ice gouging event which is consistent with the results obtained from physical tests. The NorSand model

however, performed better in the simulation of both the triaxial tests and the ice gouging events. This model could predict the keel induced sub-gouge deformations well.

Using the NorSand model some of the significant factors in gouging mechanism are studied in this thesis. It is shown how basic properties influence the seabed behaviour under a gouging event. Through the numerical analyses it is demonstrated that:

- The critical stress friction ratio of soil directly correlates with the keel reaction forces;
- In sand at a denser state (i.e. more dilative), larger keel reaction forces are required in order to reach the steady state condition;
- Higher keel attack angles result in lower keel reactions forces;
- Deeper gouges yield larger keel reaction forces;
- It is possible to normalize the keel reaction forces based on the keel geometry and soil material properties;
- The developed frontal berm height consistently increases with the increasing shear strength of the soil;
- A larger frontal berm is developed in denser soil at steady state;
- An increase of keel attack angle and gouging depth results in larger frontal berm height. Variation of the attack angle modifies the mechanism of the frontal berm development;
- Smaller sub-gouge deformations are observed in denser soil;
- The sub-gouge deformation increases in soils with higher shear strength. The critical stress ratio is more influential for denser soils compared with the loose soils;

- The increase of the attack angle reduces the vertical extension of the sub-gouge deformation and
- The increase of the gouging depth extends the sub-gouge deformations deeper into the seabed.

These results are confirmed through comparisons with physical tests published in the literature. Further it was shown that the horizontal keel reaction forces could be correlated with gouging depths, frontal berm height and soil properties for a specific attack angle.

The results of the ice gouging analyses were in reasonable agreement with results obtained from centrifuge tests. The analyses in this thesis show that the NorSand model is capable of predicting ice gouging behaviour. This model show better performance compared with the modified Drucker-Prager Cap model. The results presented in this thesis are satisfactory for drained (slow gouging) conditions.

7.3. Future Studies

In this section some of the topics that could be potentially interesting subjects for continuation of this research are discussed. Ice gouging is a complicated event and different aspect of this phenomenon beyond the suggestions in this section could be investigated. The proposed subjects are exclusively pertained to the development of soil user defined materials which was the main focus of this study.

- Improvement of Numerical Models
  - This can involve improving the hardening/softening law, elasticity rule, critical state line locus and etc.
- Undrained Analyses of Ice Gouging

  - More rigorous implementation of undrained analysis can be applied using more complex structures in Abaqus.

- Coupled Eulerian Lagrangian Analyses
  - The developed VUMAT subroutines were tested in ALE framework in this thesis. Implementation of these subroutines in CEL framework in which very large deformation can be handled is very beneficial for soil analysis.

- Ice/Soil/Pipe Interaction
  - By using the developed VUMAT subroutines in the coupled ice/soil/pipe analyses the current state of practice in pipeline design can be improved and the mechanism of pipeline deformation under ice gouging can be better understood.

For more information on these subjects see appendix A.

Bibliography

Abdalla, B., Jukes, P., Eltaher, A., & Duron, B. (2008). *The technical challenges of designing oil and gas pipelines in the arctic.* Paper presented at the OCEANS'08 MTS/IEEE, Quebec City.

Abdalla, B., Pike, K., Eltaher, A., & Jukes, P. (2009). *A Coupled Eulerian Lagrangian Finite Element Model of Ice-Soil-Pipe Interaction.* Paper presented at the Proceedings of the Nineteenth (2009) International Offshore and Polar Engineering Conference, Osaka, Japan.

Abdelnour, R., Lapp, D., Haider, S., Shinde, S. B., & Wright, B. (1981). *Model test of sea bottom scouring*. Paper presented at the Proceedings of the 6th International Conference on Port and Ocean Engineering under Arctic Conditions (POAC), Quebec City, Canada.

Allersma, H. G., & Schoonbeek, I. S. (2005). *Centrifuge modeling of scouring ice keels.* Paper presented at the Proceedings of the 15th International Conference on Offshore Mechanics and Arctic Engineering (OMAE), Halkidiki, Greece.

Atkinson, J. H. (2000). Non-linear soil stiffness in routine design. *Geotechnique, 50*(5), 487-508.

Banneyake, R., Hossain, M. K., Eltaher, A., Nguyen, T., & Jukes, P. (2011). *Ice-Soil-Pipeline Interactions Using Coupled Eulerian-Lagrangian (CEL) Ice Gouge Simulations - Extracts from Ice Pipe JIP*. Paper presented at the OTC Arctic Technology Conference, Houston, Texas, USA.

Barker, A., & Timco, G. (2002). Laboratory experiments of ice scour processes: rigid indentor. *Cold Regions Science and Technology, 35*(3), 195–206.

Barker, A., & Timco, G. (2003). Laboratory experiments of ice scour processes: buoyant ice model. *Cold Regions Science and Technology, 36*(1-3), 103-114. doi: 10.1016/s0165-232x(02)00096-4

Barrette, J., & Phillips, R. (2011). *Ice Keel-Seabed Interaction: Numerical Modelling for Sands.* Paper presented at the Conference on Ports and Ocean Engineering Under Arctic Conditions (POAC).

Barrette, P. (2011). Offshore pipeline protection against seabed gouging by ice: An overview. *Cold Regions Science and Technology, 69*(1), 3-20. doi: 10.1016/j.coldregions.2011.06.007

Barrette, P., & Timco, G. (2008). *Ice scouring in a large flume: Test set-up and preliminary observations.* Paper presented at the Proceedings of ICETECH'08, ICETECH08-133-RF, Banff, Canada.

Barrette, P. D., & Sudom, D. (2014). *Ice-Soil-Pipeline Interaction during Seabed Gouging in Physical Tests: Database Analysis and Outstanding Issues*.

Been, K., & Jefferies, M. G. (1985). A state parameter for sands. *Geotechnique, 35*(2), 99-112.

Been, K., & Jefferies, M. G. (1986). Discussion on "A State Parameter for Sands", by Been and Jefferies (1985). *Geotechnique, 36*(1), 127-132.

Been, K., Jefferies, M. G., & Hachey, J. (1991). The critical state of sands. *Geotechnique, 41*(3), 365-381.

Been, K., K., C., I., J., & P., V. (2013). *Practice for Pipeline Design in Ice Scoured Environments: Application to the Kashagan Project.* Paper presented at the POAC, Montreal.

Been, K., Peek, R., Croasdale, K., & Verlaan, P. (2013). *Subscour displacements for pipeline design: state of practice for Kashagan project.* Paper presented at the POAC 2013, Montreal.

Been, K., Sancio, R. B., Ahrabian, D., van Kesteren, W., Croasdale, K., & Palmer, A. (2008). Subscour Displacement in Clays From Physical Model Tests. *ASME Conference Proceedings, 2008*(48609), 239-245. doi: 10.1115/ipc2008-64186

Bird, K. J., Charpentier, R. R., Gautier, D. L., Houseknecht, D. W., Klett, T. R., Pitman, J. K., . . . Wandrey, C. J. (2008). Circum-Arctic Resource Appraisal estimates of undiscovered oil and gas north of the Arctic Circle, from http://pubs.usgs.gov/fs/2008/3049/

Bishop, A. W. (1966). The strength of soils as engineering materials. *Geotechnique, 16*(2), 89-13.

Bolton, M. D. (1986). The strength and dilatancy of sands. *Geotechnique, 36*(1), 65-78.

Britto, A. M., & Gunn, M. J. (1987). *Critical State Soil Mechanics via Finite Elements*: Ellis Horwood LImited.

Casagrande, A. (1936). Characteristics of cohesionless soils affecting the stability of earth fills. *J. Boston Sot. Civ. Engrs*, Reprinted in Contributions to soil mechanics 1925-1940. Boston Society of Civil Engineers.

Castro, G. (1969). *Liquefaction of sands.* Harvard University, Harvard Soil Mechanics Series. (81)

Chari, T. R. (1979). Geotechnical aspects of iceberg scours on ocean floors. *Canadian Geotechnical Journal, 16*(2), 379– 390.

Chari, T. R., & Green, H. P. (1981). *Iceberg Scour Studies in Medium Dense Sands.* Paper presented at the Proceedings of the 6th International Conference on Port and Ocean Engineering under Arctic Conditions (POAC), Quebec City, Canada.

Chu, J. (1995). An experimental examination of the critical state and other similar concepts for granular soils. *Canadian geotechnical journal. Revue canadienne de géotechnique., 32*(6), 1065.

Clark, J. I., Paulin, M. J., Lach, P. R., Yang, Q. S., & Poorooshasb, H. (1994). *Development of a design methodology for pipelines in ice scoured seabeds.* Paper presented at the Proceedings of the International Conference on Offshore Mechanics and Arctic Engineering - OMAE, Houston, USA.

Clark, J. I., Paulin, M. J., & Poorooshasb, F. (1990). *Pipeline Stability in an Ice-Scoured Seabed.* Paper presented at the 1st European Offshore Mechanics Symposium EUROMs 90, Trondheim, Norway.

Croasdale, K., Bruneau, S., Christian, D., Crocker, G., English, J., Metge, M., & Ritch, R. (2001). *In-Situ Measurements on the Strength of First-Year Ice Ridge Keels.* Paper presented at the 16th International Conference on Port and Ocean Engineering Under Arctic Conditions, Ottawa, Canada.

Croasdale, K., Comfort, G., & Been, K. (2005). *Investigation of ice limits to ice gouging.* Paper presented at the 18th International Conference on Port and Ocean

Engineering Under Arctic Conditions, POAC '05, Clarkson University, Potsdam, NY.

Daiyan, N., Kenny, S., Phillips, R., & Popescu, R. (2010). Numerical Investigation of Oblique Pipeline/Soil Interaction in Sand. *ASME Conference Proceedings, 2010*(44212), 157-164.

Davies, G., Marley, M., & Mork, K. (2011). *Limit State Design Methodology for Offshore Pipelines against Ice Gouging-Industry Guidelines from the ICEPIPE JIP.* Paper presented at the OTC Arctic Technology Conference.

DiMaggio, F. L., & Sandler, I. S. (1971). *Material model for granular soils.* Paper presented at the Proc. Am. Soc. Civ. Engrs. 97, Em3.

DNV. (2007). *Submarine pipeline systems*. Hovik, NO: Det Norske Veritas.

Drucker, D. C. (1957). A definition of stable inelastic material: BROWN UNIV PROVIDENCE RI.

Drucker, D. C., Gibson, R. E., & Henkel, D. J. (1957). Soil mechanics and work hardening theories of plasticity. *J. Soil Mech. Fdn Engng Div. Am. Sot. Civ., 122*, 338-346.

El-Gebaly, S., Paulin, M., Lanan, G., & Cooper, P. (2012). *Ice Gouge Interaction with Buried Pipelines Assessment Using Advanced Coupled Eulerian Lagrangian*.

Eltaher, A. (2014). *Gaps in Knowledge and Analysis Technology of Ice-gouge – Pipeline Interaction*.

Eskandari, F., Phillips, R., & Hawlader, B. (2012). *Finite Element Analyses of Seabed Response to Ice Keel Gouging.* Paper presented at the Canadian Geotechnical Conference, Winnipeg, MB.

Evgin, E., & Fu, Z. (2008). *Numerical Analysis of Soil Response to Ice Scouring.* Paper presented at the 27th International Conference on Offshore Mechanics and Arctic Engineering, OMAE2008.

Fuglem, M., Parr, G., Jordaan, I., Verlaan, P., & Peek, R. (2013). *Sea ice scour depth and width parameters for design of pipelines in the Caspian sea.* Paper presented at the POAC 2013.

Grass, J. (1984). *Ice scour and ice ridging studies in Lake Erie.* Paper presented at the Proc International Symp. on Ice.

Green, H. P., & Chari, T. R. (1981). *Sediment compaction below iceberg furrows.* Paper presented at the Proceedings of Oceans '81 IEEE/MTS, Boston, USA.

Green, H. P., Reddy, A. S., & Chari, T. R. (1983). *Iceberg scouring and pipeline burial depth.* Paper presented at the Proceedings of the 7th International Conference on Port and Ocean Engineering under Arctic Conditions (POAC), Espoo, Finland.

Griffiths, D. V. (1985). *Numerical modeling of interfaces using conventional finite elements.* Paper presented at the Proc. 5th Int. Conf. Num. Meth. Geomech., Nagoya.

Gustajtis, K. A. (1979). Iceberg Scouring on the Labrador Shelf, Saglek Bank: C-CORE.

Hird, C., & Hassona, F. (1990). Some factors affecting the liquefaction and flow of saturated sands in laboratory tests. *Engineering Geology Engineering Geology, 28*(1-2), 149-170.

Hodge, P. G. (1957). A new method of analyzing stresses and strains in work hardening plastic solids. *J. Appl. Mech, 24*, 482–483.

Hodgson, G. J., Lever, J. H., Woodworth-Lynas, C. M., & Lewis, C. F. M. (1988). *The Dynamics of Iceberg Grounding and Scouring (DIGS) Experiment and Repetitive Mapping of the Eastern Canadian Continental Shelf. Volume 1 - the Field Experiment*. Ottawa: Environmental Studies Research Funds.

Ishihara, K. (1993). Liquefaction and flow failure during earthquakes. *Géotechnique, 43*(3), 351-415.

Ishihara, K., Tatsuoka, F., & Tasuda, S. (1975). Undrained deformation and liquefaction of sand under cyclic stresses. *Soils and Foundations, 15*(1), 29-44.

Jefferies, M. G. (1993). NorSand: a simple critical state model for sand. *Geotechnique, 43*, 91-103.

Jefferies, M. G., & Been, K. (2006). *Soil Liquefaction*: Taylor & Francis.

Jefferies, M. G., & Shuttle, D. A. (2002). Dilatancy in general Cambridge-type models. *Géotechniquec, 52*(9), 625 –638.

Jefferies, M. G., & Shuttle, D. A. (2005). Norsand, features, calibration, and use. *Soil constitutive models: evaluation, selection and calibration. Edited by J. A. Yamamuro and V. N. Kaliakin. ASCE Geotechnical Special Publication 128*, 204-236.

Jukes, P., Eltaher, A., Abdalla, B., & Duron, B. (2008). *The Design and Simulation of Arctic Subsea Pipelines.* Paper presented at the DNV Conference on Arctic activities.

Kenny, S., McKenna, R., Bruce, J., Nobahar, A., King, T., & Phillips, R. (2004). *Probabilistic design methodology to mitigate ice gouge hazards for offshore pipelines.* Paper presented at the Proc., Biennial Int. Pipeline Conf.,IPC04-0527, Calgary, Alta., Canada.

Kenny, S., Palmer, A. C., & Been, K. (2007). Design challenges for offshore pipelines in arctic environments. *Proc., Offshore Oil and Gas in Arctic and Cold Waters, 15p*.

Kenny, S., Phillips, R., Clark, J., & Nobahar, A. (2005). *PRISE numerical studies on subgouge deformations and pipeline/soil interaction analysis.* Paper presented at the Proceedings of the 18th Conference on Ports and Ocean Engineering Under Arctic Conditions (POAC), Potsdam, NY, USA,.

King, T. (2011). Protection of pipelines from ice gouging. *Journal of Pipeline Engineering, 10*(2), 115.

King, T., Phillips, R., Barrett, J., & Sonnichsen, G. (2009). Probabilistic pipeline burial analysis for protection against ice scour. *Cold regions science and technology., 59*(1), 58-64.

Kioka, S., Abe, S., Sasaki, H., & Saeki, H. (1999). *Mechanical model of ice scour.* Paper presented at the Proceedings of the 15th International Conference on Port and Ocean Engineering under Arctic Conditions (POAC), Helsinki, Finland.

Kioka, S., Kubouchi, A., Ishikawa, R., & Saeki, H. (2004). *Application of the mechanical model for ice scour to a field site and simulation method of scour depths.* Paper presented at the Proceedings of the 14th International Offshore and Polar Engineering Conference (ISOPE), Toulon, France.

Kioka, S., Yasunaga, Y., Watanaba, Y., & Saeki, H. (2000). *Evaluation of ice forces acting on sea bed due to ice scouring.* Paper presented at the Proceedings of the

10th International Offshore and Polar Engineering Conference (ISOPE), Seattle, WA, USA.

Konuk, I., & Gracie, R. (2004). *A 3-Dimensional Eulerian Finite Element Model for Ice Scour.* Paper presented at the IPC 2004 International Pipeline Conference, Calgary.

Konuk, I., Liferov, P., & Loset, S. (2007). *Challenges in Modelling Ice Gouge and Pipeline Response.* Paper presented at the POAC-07, Dalian, China.

Konuk, I., Yu, S., & Gracie, R. (2005). *A 3-dimensional continuum ALE model for ice scour-study of trench effects.* Paper presented at the Proceedings of the 24th International Conference on Offshore Mechanics and Arctic Engineering (OMAE), Halkidiki, Greece.

Lach, P. R. (1996). *Centrifuge Modeling of Large Soil Deformation due to Ice Scour*: Doctoral Thesis , Memorial University of Newfoundland.

Lanan, G. A., & Ennis, J. O. (2001). *Northstar Offshore Arctic Pipeline Project.* Paper presented at the Proceedings.

Lele, S. P., Hamilton, J. M., Panico, M., & Arslan, H. (2011). Advanced Continuum Modeling to Determine Pipeline Strain Demand Due to Ice-Gouging.

Lever, J. H. (2000). *Assessment of Millennium Pipeline Project, Lake Erie Crossing: Ice Scour, Sediment Sampling, and Turbidity Modeling*: US Army Corps of Engineers, Engineer Research and Development Center.

Lever, J. H., Bass, D. W., Lewis, C. F. M., Klein, K., Diemand, D., & Dyke, M. (1991). Iceberg/Seabed Interaction Events Observed During the DIGS Experiment. *J. Offshore Mech. Arct. Eng. Journal of Offshore Mechanics and Arctic Engineering, 113*(1).

Liferov, P. (2005). *First-year Ice Ridge Scour and Some Aspects of Ice Rubble Behaviour*: Norwegian University of Science and Technology, Doctoral Theses.

Liferov, P., Løset, S., Moslet, P., Bonnemaire, B., & Høyland, K. (2002). Medium scale modelling of ice ridge scouring of the seabed, Part I: Experimental set-up and basic results.

Liferov, P., Nes, H., Asklund, J., Shkhinek, K., & Jilenkov, A. (2014). *Ice Gouging and Its Effect on Pipelines*.

Liferov, P., Shkhinek, K. N., Vitali, L., & Serre, N. (2007). *Ice Gouging Study - Actions and Action Effects.* Paper presented at the Recent Development of Offshore Engineering in Cold Regions, POAC-07, Dalian, China.

Mahdavi, H., Kenny, S., Phillips, R., & Popescu, R. (2008). Influence of Geotechnical Loads on Local Buckling Behavior of Buried Pipelines. *ASME Conference Proceedings, 2008*(48593), 543-551.

Matsuoka, H., & Nakai, T. (1974). *Stress-deformation and strength characteristics of soil under three different principal stresses.* Paper presented at the Proc. JSCE.

McKenna, R., Crocker, G., & Paulin, M. J. (1999). *Modelling iceberg scour processes on the Northeast Grand Banks.* Paper presented at the International Conference on Offshore Mechanics and Arctic Engineering, St. John's, NL.

Naylor, D. J. (1974). Stresses in nearly incompressible materials by finite elements with application to calculation of excess pore water pressure. *Int. Jnl. Num. Meth. Eng., 8*, 443-460.

Nilsen, R. (2003). *Geotechnical aspects of first-year ridge scouring on a seabed*. Trondheim, Norway: Norwegian University of Science and Technology (NTNU), Geotechnical Division.

Nobahar, A., Kenny, S., King, T., McKenna, R., & Phillips, R. (2007). Analysis and Design of Buried Pipelines for Ice Gouging Hazard: A Probabilistic Approach. *Journal of Offshore Mechanics and Arctic Engineering, 129*.

Nobahar, A., Kenny, S., & Phillips, R. (2007). Buried Pipelines Subject to Subgouge Deformations. *INTERNATIONAL JOURNAL OF GEOMECHANICS, 7*(3), 206-216.

Noble, P., & Comfort, G. (1980). *Damage to an underwater pipeline by ice ridges.* Paper presented at the proceedings NRC Symposium on Ice Ridging, Calgary.

Nova, R. (1982). A constitutive model for soil under monotonic and cyclic loading. *Soil mechanics-transient and cyclic loads, 343*.

Palmer, A. C. (1999). Speed effects in cutting and ploughing. *Geotechnique, 49*(3), 285–294.

Palmer, A. C., & King, R. A. (2008). Subsea pipeline engineering, from http://www.knovel.com/knovel2/Toc.jsp?BookID=3610

Palmer, A. C., Konuk, I., Comfort, G., & Been, K. (1990). *Ice Gouging and the Safety of Marine Pipelines.* Paper presented at the 22nd Annual OTC, Houston.

Palmer, A. C., & Niedoroda, A. (2005). *Ice gouging and pipelines: unresolved questions.* Paper presented at the Proceedings of the 18th Conference on Ports and Ocean Engineering Under Arctic Conditions (POAC), Potsdam, NY, USA.

Palmer, A. C., White, D. J., Baumgard, A. J., Bolton, M. D., Barefoot, A. J., Finch, M., . . . Baldry, J. A. (2003). Uplift resistance of buried submarine pipelines: Comparison between centrifuge modelling and full-scale tests. *Geotechnique, 53*(10), 877-883.

Pastor, M., & Zienkiewicz, O. (1986). *A generalized plasticity hierarchical model for sand under monotonic and cyclic loading.* Paper presented at the Proc., 2nd Int. Symp. on Numerical Models in Geomechanics.

Pastor, M., Zienkiewicz, O. C., & Chan, A. H. C. (1990). Generalized plasticity and the modelling of soil behaviour. *International Journal for Numerical and Analytical Methods in Geomechanics, 14*(3), 151-190. doi: 10.1002/nag.1610140302

Paulin, M. J., Lach, P. R., Poorooshasb, F., & Clark, J. I. (1991). *Preliminary results of physical model tests of ice scour.* Paper presented at the Proceedings of the 11th International Conference on Port and Ocean Engineering under Arctic Conditions (POAC), St. John's, Canada.

Peek, R., Been, K., Bouwman, V., Nobahar, A., Sancio, R., & Schalkwijk, R. v. (2013, June 9-13, 2013). *Buried Pipeline Response to Ice Gouging on a Clay Seabed Large Scale Tests and Finite Element Analysis.* Paper presented at the Proceedings of the 22nd International Conference on Port and Ocean Engineering under Arctic Conditions, Espoo, Finland.

Peek, R., & Nobahar, A. (2012). Ice Gouging over a Buried Pipeline: Superposition Error of Simple Beam-and-Spring Models. *International Journal of Geomechanics, 12*(4), 508-516. doi: doi:10.1061/(ASCE)GM.1943-5622.0000150

Phillips, R., & Barrett, J. (2011). *Ice Keel-Seabed Interaction: Numerical Modelling for Sands.* Paper presented at the Port and Ocean Engineering under Arctic Conditions, Montreal.

Phillips, R., & Barrett, J. (2012). *PIRAM: Pipeline Response to Ice Gouging*.

Phillips, R., Clark, J. I., & Kenny, S. (2005). *PRISE studies on gouge forces and subgouge deformations.* Paper presented at the Proceedings of the 18th International Conference on Port and Ocean Engineering under Arctic Conditions (POAC), Potsdam, U.S.A.

Phillips, R., King, T., & Bruce, J. (2012). *PIRAM:Pipeline Risk Assessment & Mitigation Oveview.* Paper presented at the 9th International Pipeline Conference. IPC2012-90423.

Phillips, R., & Popescu, R. (1998). Safety and Integrity of Arctic Marine Pipelines: C-CORE Publication 98-C15.

Pike, K., & Kenny, S. (2014). *Numerical Pipe/Soil Interaction Modelling: Sensitivity Study and Extension to Ice Gouging*.

Pike, K., Kenny, S., Kavanagh, K., & Jukes, P. (2014). *Pipeline Engineering Solutions for Harsh Arctic Environments: Technology Challenges and Constraints for Advanced Numerical Simulations*.

Poorooshasb, F., & Clark, J. I. (1990). On Small Scale Ice Scour Modelling (pp. 193-236): In Clark.

Potts, D. M., & Zdravkovic, L. (1999). *Finite element analysis in geotechnical engineering : theory*. London; Reston, VA: Telford ; Distributed by ASCE Press.

Poulos, S. J., Castro, G., & France, J. W. (1988). Closure to Liquefaction Evaluation Procedure by Steve J. Poulos, Gonzalo Castro, and John W. France (June, 1985, Vol. 111, No. 6). *J. Geotech. Engrg. Journal of Geotechnical Engineering, 114*(2).

Rearic, D. M., & McHendrie, A. G. (1983). *Ice Gouge Data Sets from the Alaskan Beaufort Sea: Magnetic Tape and Documentation for Computer Assisted Analyses and Correlation*: US Department of the Interior, Geological Survey.

Reynolds, O. (1885). On the dilatancy of media composed of rigid particles in contact, with experimental illustrations,. *Philosophical Magazine, 5*(20), 469–481.

Roscoe, K. H., & Burland, J. B. (1968). On the generalized stress-strain behavior of 'wet' clay. *In Engineering Plasticity (eds J. Heyman and F. A, Leckie),*, 535-609.

Roscoe, K. H., & Poorooshasb, H. B. (1963). *A fundamental principle of similarity in model tests for earth pressure problems.* Paper presented at the 2nd Asian Conference on Soil Mechanics.

Roscoe, K. H., Schofield, A. N., & Wroth, C. P. (1958). On The Yielding of Soils. *Geotechnique, 8*(1), 22-53.

Rowe, P. W. (1962). The Stress-Dilatancy Relation for Static Equilibrium of an Assembly of Particles in Contact. *Proceedings of the Royal Society of London. Series A, Mathematical and Physical Sciences, 269*(1339), 500-527.

Sancio, R. B., Been, K., & Lopez, J. (2011). *Large Scale Indenter Test Program to Measure Sub Gouge Displacements.* Paper presented at the International Conference on Ports and Ocean Engineering under Arctic Conditions, Montreal.

Sayed, M., & Timco, G. W. (2009). A numerical model of iceberg scour. *Cold Regions Science and Technology, 55*(1), 103-110.

Schofield, A. N., & Wroth, C. P. (1968). *Critical state soil mechanics*. London: McGraw-Hill.

Schoonbeek, I. S., & Allersma, H. (2006). *Centrifuge modelling of scouring ice keels in clay.* Paper presented at the Proceedings of the 6th International Conference on Physical Modelling in Geotechnics – 6th ICPMG, Hong Kong, China.

Schoonbeek, I. S., Xin, M. X., van Kesteren, W. G., & Been, K. (2006). *Slip line field solutions as an approach to understand ice subgouge deformation patterns.* Paper presented at the Proceedings of the 16th International Offshore and Polar Engineering Conference (ISOPE), San Francisco, CA, USA.

Stava, I., Nystrom, P. R., Vikse, N., Gudmestad, O. T., Liferov, P., & Gronli, J. (2008). Small Scale Model Tests of Ice Gouge in Soft Sandy Silt. *ASME Conference Proceedings, 2008*(48203), 891-900. doi: 10.1115/omae2008-57086

Stroud, M. A. (1971). *The behaviour of sand at low stress levels in the simple shear apparatus*: PhD thesis, University of Cambridge, UK.

Vaid, Y. P., Chung, E. K. F., & Kuerbis, R. H. (1990). Stress path and steady state. *Can. Geotech. J. Canadian Geotechnical Journal, 27*(1), 1-7.

Vaid, Y. P., & Sasitharan, S. (1992). The strength and dilatancy of sand. *Canadian Geotechnical Journal, 29*(3), 522-526.

Verdugo, R. (1992). *Characterization of sandy soil behavior under large deformation*: Ph.D. thesis, University of Tokyo, Tokyo, Japan.

Verdugo, R., & Ishihara, K. (1996). The Steady State of Sandy Soils. *Soils and foundations., 36*(2), 81.

Vershinin, S., Truskov, P., & Liferov, P. (2008). Ice Action on Seabed and Subsea Structures. *IPK, Moscow*.

Vikse, Normann, Gudmstad, Ove, T., Nystrom, Per, R., . . . Pavel. (2007). *Small Scale Model Tests on Subgouge Soil Deformations.* Paper presented at the 26th International Conference on Offshore Mechanics and Arctic Engineering OMAE2007, San Diego.

Walter, D. J., & Phillips, R. (1998). Prise - Force Models for Drained and Undrained Steady State Ice Scouring: C-CORE Publication 98-C33.

Woodworth-Lynas, C. M. (1998). *Sub-scour Deformations and the Development of Ideas from the Field Work in the Last Decade.* Paper presented at the Proceedings of Ice Scour and Arctic Marine Pipeline Workshop, 13th Okhotsk Sea and Sea Ice Symposium, Hokkaido, Japan.

Woodworth-Lynas, C. M., Josenhans, H. W., Barrie, J. V., Lewis, C. F. M., & Parrott, D. R. (1991). The physical processes of seabed disturbance during iceberg grounding and scouring. *Continental Shelf Research, 11*(8), 939-961.

Woodworth-Lynas, C. M., Nixon, D., Phillips, R., & Palmer, A. (1996). *Subgouge deformations and the security of Arctic marine pipelines.* Paper presented at the Proceedings of the 28th Offshore Technology Conference, Offshore Technology Conference (OTC), Houston, USA.

Woodworth-Lynas, C. M., Phillips, R., Clark, J., Hynes, F., & Xiao, X. (1998). *Verification of centrifuge model results against field data: results from the Pressure Ridge Ice Scour Experiment (PRISE)*: C-CORE.

Wroth, C. P., & Basset, R. H. (1965). A stress-strain relationship for the shearing behaviour of a sand. *Geotechnique, 15*(1), 32-56.

Yamamuro, J. A., & Lade, P. V. (1998). Steady-state concepts and static liquefaction of silty sands. *Journal of geotechnical and geoenvironmental engineering, 124*(9), 868-877.

Yang, Q. S., Poorooshasb, F., & Poorooshasb, H. (1993). *Analysis of subscour deformation by finite element method.* Paper presented at the 4th Canadian Conference on Marine Geotechnical Engineering.

Yang, Q. S., Poorooshasb, H. B., & Lach, P. R. (1996). Centrifuge Modeling and Numerical Simulation of Ice Scour. *Soils and foundations., 36*(1), 85.

Yang, W. (2010). *Physical modelling of subgouge deformations in sand.* M. Eng., Memorial University of Newfoundland.

Yoshimine, M., & Ishihara, K. (1998). Flow Potential of Sand during Liquefaction. *Soils and foundations., 38*(3), 189.

Zienkiewicz, O. C., & Naylor, D. J. (1972). *The adaptation of critical state soil mechanics for use in finite elements.* Paper presented at the Proc. Roscoe Memorial Symposium, Cambridge.

Appendix A

A.1. Improvement of Numerical Models

In this research a variant of Drucker-Prager Cap model was developed with a proposed hardening/softening law and a modified yield surface over the shear zone in order to supress excessive dilation. These modifications improved the performance of the Drucker-Prager Cap model. However, there are a lot of simplifications associated with a constitutive soil model that if replaced with a more realistic representation of the soil behaviour the accuracy of the model could be enhanced. One of these simplifications is the assumption of the linear elasticity based on Hooke's law in the Drucker Prager Cap model. Other elasticity relationships based on the mean effective stress have been proposed in the literature. It is recommended that one of these elasticity models be employed in the framework of the Drucker Prager Cap.

The hardening law in the Drucker Prager Model is a simple relationship in compliance with CSSM. Further studies on this relationship could improve the performance of the model to capture more realistic behaviour of the soil. Although the liquefaction is not a significant issue in ice gouging studies but it should be noted that the current hardening law of the Drucker Prager Cap model which is based on dilatancy index is not suitable for sand liquefaction.

A.2. Undrained Analyses of Ice Gouging

This research essentially focused on the drained behaviour of the soil during the ice gouging event of the sandy seabed. Although a reasonable performance was achieved in analyses of slow gouging events modeled in centrifuge tests but it should be noted that in

reality the ice gouging phenomenon in sand is behaves partially as drained and partially as undrained condition. As the result it is highly important to be able to both analyze the gouging process both in drained and undrained condition to have a clearer understanding of the whole mechanism.

Unfortunately, as of version 6.12, there is no element in the ABAQUS Explicit library in which the pore water pressure is coupled with the displacement degrees of freedom, i.e it is not possible to perform undrained analyses. During the course of this study it was attempted to investigate the undrained gouging scenario by improving the ABAQUS Explicit capabilities. These efforts were challenged by time and resources and a solid outcome was never achieved. Nonetheless, a brief explanation of the undertaken steps will follow.

A.2.1. Volume Constraint Method

In section 0 the extension of a user material model to capture the undrained behaviour of the soil is explained. In this research the implemented user defined materials (VUMAT) apply the volume constraint method to perform the undrained analyses. The volume constraint method produced reasonable results in triaxial analyses performed earlier in chapter 4. However the first challenge encountered when this method is used in a gouging problem is the inefficiency of the analysis. This is due to the fact that this method introduces an equivalent bulk modulus which is many times larger than the bulk modulus of the soil skeleton alone. Therefore the explicit solver requires highly smaller stable time increments compared with an equivalent drained analysis. This problem imposed using relatively much coarser meshing schemes in the undrained analyses. In the following the performance of the undrained gouging analyses is compared with the same gouging

analysis but under drained condition. In these analyses the gouging depth is 1.2 meters, the gouging width is 16 meters (prototype scale) and the attack angle is 15 degrees. The critical stress ratio is 1.2 and the state parameter is -0.05. Other parameters are chosen the same as the parameters selected for analysis in chapter 1.

Figure A-1 shows the stress paths of a particular point in the soil under drained and undrained condition. In undrained analysis the effective stress remains constant until the soil yields. This implies, as anticipated, that all excess pressure are carried by the uncompressible liquid phase while the stress path is in elastic zone. By the commencement of the yielding, and onward, the yield surface in the undrained analyses does not harden as much as it does in the drained analyses. Since the excess pressure is carried by the pore water in the elastic zone and the effective mean stress remains constant, in this undrained analysis the soil yields at an effective mean stress smaller than the limit imposed by NorSand model due to the maximum dilatancy. As the result the soil begins to soften. This could be the reason why the undrained analysis results in smaller shear stress field and less hardening. The total stress path behaves more erratically. Although further examinations and improvements are necessary but in absence of additional investigations it seems that coarse mesh has a considerable attribution on this behaviour. For future undrained analysis the initial soil stress condition should be adopted more precisely.

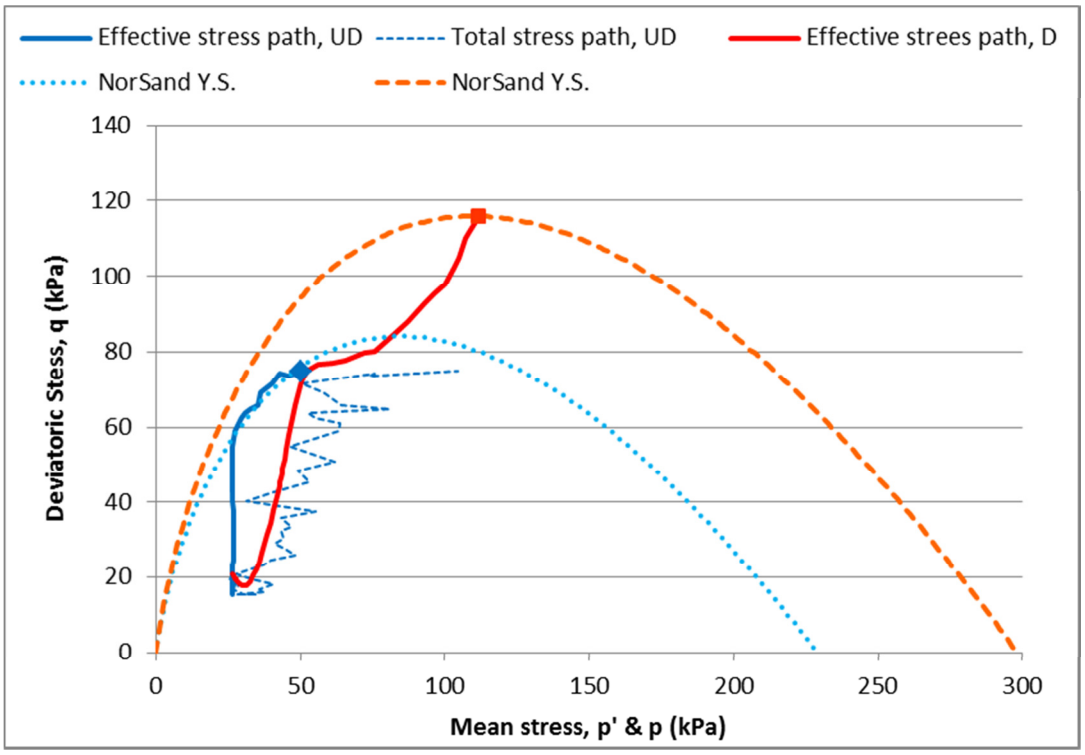

Figure A-1 Stress paths for undrained and drained gouging analyses

Figure A-2 show the development of pore water pressure, effective mean stress and total mean stress for the same soil particle discussed earlier in Figure A-1. The way the user defined materials are formulated in this research assigns negative pore water pressure for compression and positive pore water pressure for extension.

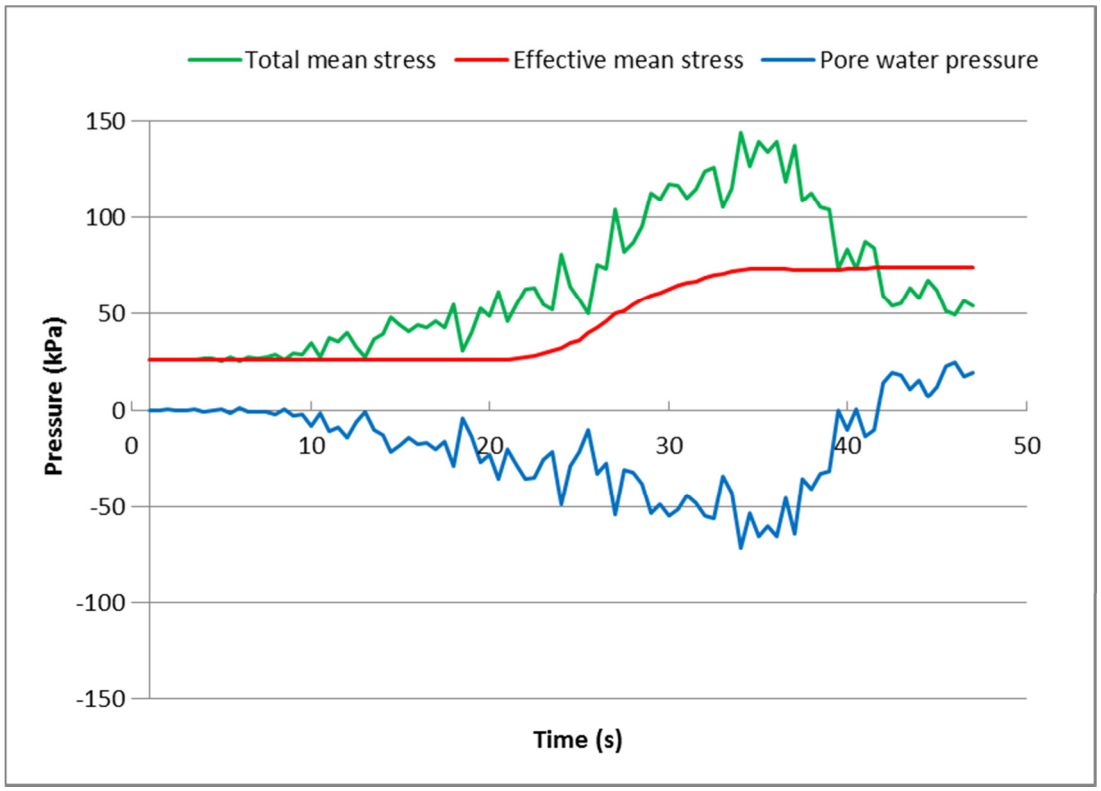

Figure A-2 Development of the pore water pressure, effective and total pressures for a specific soil particle during the gouging event

The sub-gouge deformations for both drained gouging analysis and undrained gouging analysis are compared in Figure A-3.

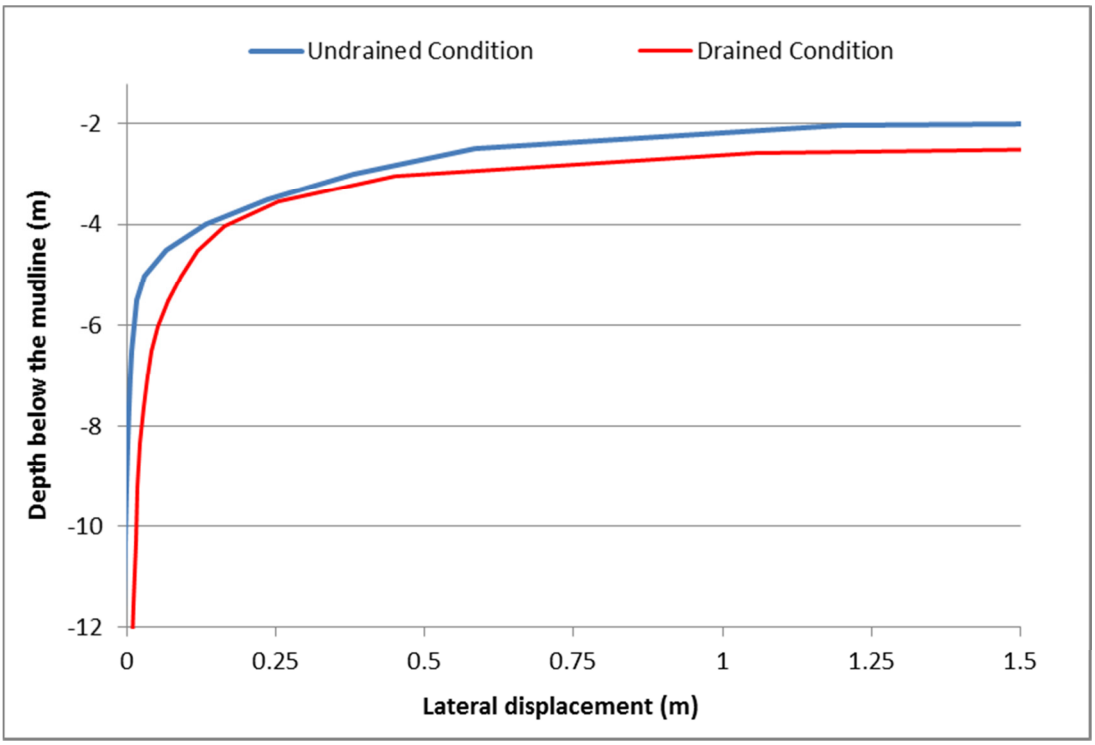

Figure A-3 Comparison of undrained and drained sub-gouge deformation

The shear stress contours in Figure A-4 and Figure A-5, respectively for drained and undrained analyses, reaffirms an earlier point that higher shear stress field are observed in drained analysis.

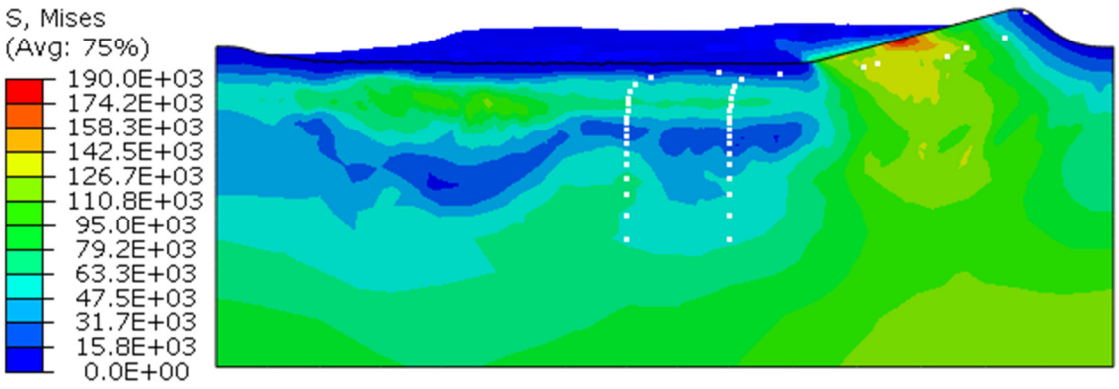

Figure A-4 The shear stress field in a drained gouging analysis

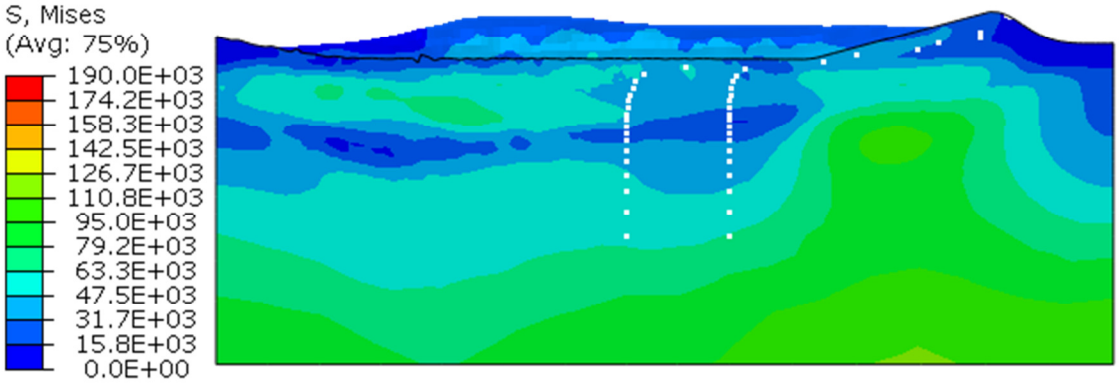

Figure A-5 The shear stress field in an undrained gouging analysis

The results of the analyses show that a smaller frontal berm is developed in undrained analysis compared with the drained analysis (2.5 m vs 3.0 m for this particular gouging event).

Figure A-6 shows the contours of the developed pore water pressures in the undrained analysis. For this specific analysis generally the soil in front of the keel has negative pore water pressure and the soil behind the keel has positive pore pressure. Figure A-2 already showed how for a specific soil particle pore water pressure becomes positive in this analysis as the keel passes that point. Assuming the soil behind the keel unloads elastically it is acceptable to observe constant effective mean pressure and decreasing pore water pressure (from high negative values to positive values).

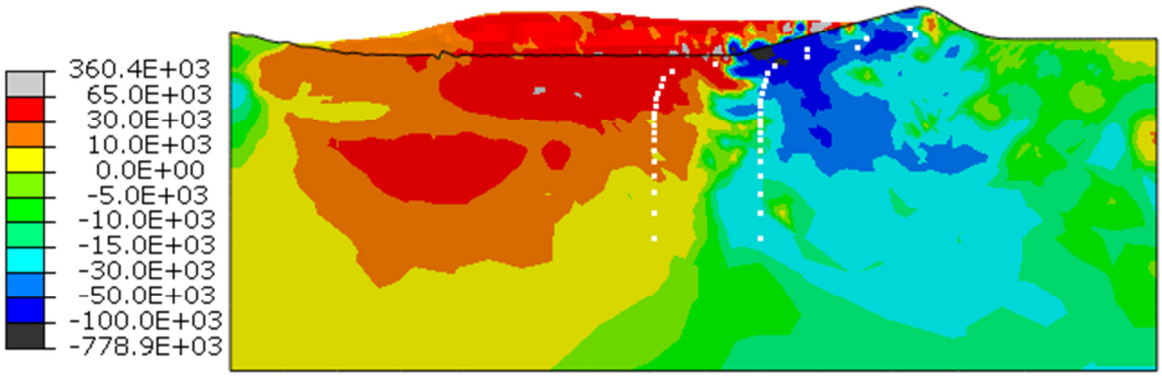

Figure A-6 Development of the pore water pressure in an undrained gouging analysis

For comparison the plastic shear strains are also shown in Figure A-7 and Figure A-8 respectively for undrained and drained analyses.

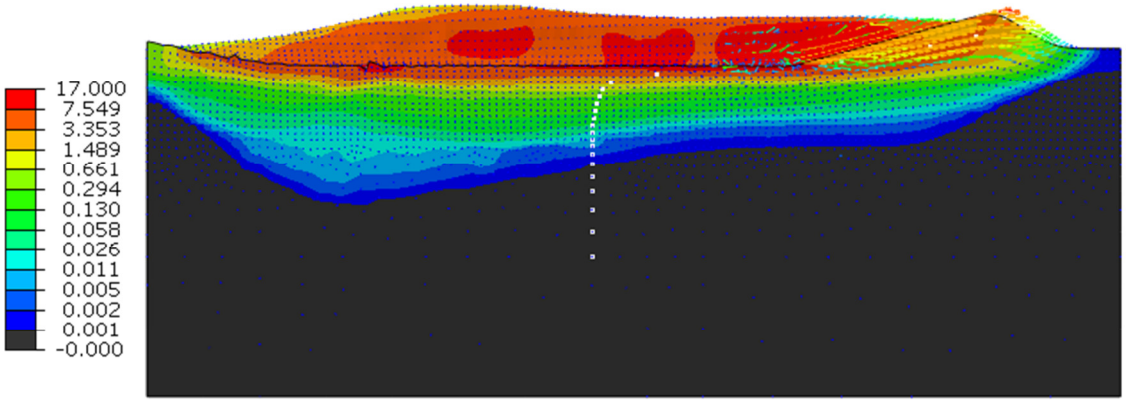

Figure A-7 Plastic shear strain in undrained analysis (log scale)

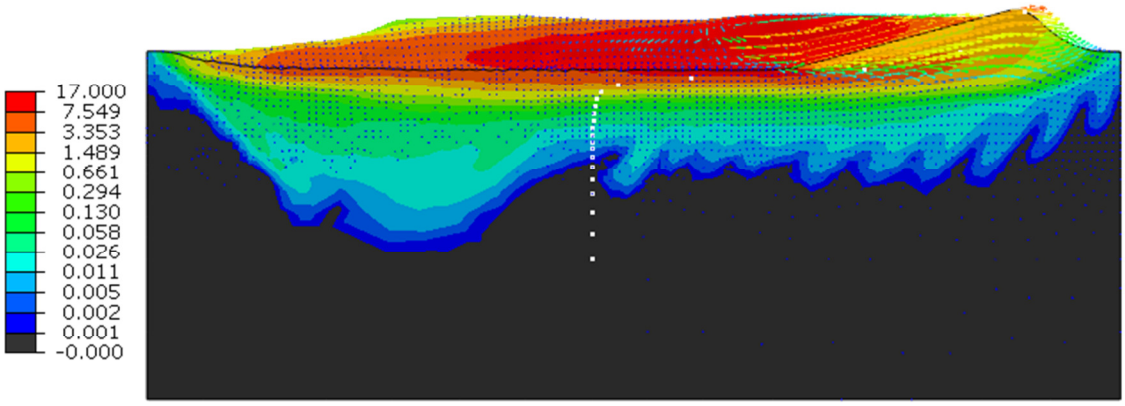

Figure A-8 Plastic shear strain in drained analysis (log scale)

A.2.2. Coupled Explicit Method

To overcome the lack of an ABAQUS Explicit built-in element that can model the effect of pore water pressure it is possible to develop a user defined element which couples the pore pressure and displacement governing equations. In ABAQUS Explicit the user defined element is implemented through VUEL subroutine. The development of the user defined element also includes an implementation of the material constitutive model. In addition, the subroutine should perform all the required calculations in the element level such as equivalent internal or external nodal forces and mass matrix of element. As the result writing a VUEL is more demanding but it should be more efficient since there is no need to change the bulk modulus of the soil. Considering the importance of the development of pore water pressure in the geotechnical problems the implementation of a user defined element as described seems to be good subject for an interested researcher.

A.3. Coupled Eulerian Lagrangian Analyses

The Arbitrary Lagrangian Eulerian (ALE) formulation in ABAQUS Explicit can well manage the soil deformation in a wide range of geotechnical problem. However, this method could fail where extreme soil deformation happens in the analysis. Large soil deformation result in excessively distorted elements that force the numerical analysis to be terminated prematurely. In this research more realistic soil numerical model were implemented in ABAQUS Explicit and the seabed ice gouging event was successfully modeled within the ALE framework. The attempts to extend the analyses to the Coupled Eulerian Lagrangian framework (CEL) in the current study encountered numerical problems.

Figure A-9 shows a typical ice gouging model in the CEL framework. The keel is modeled as a Lagrangian body and the soil is modeled as an Eulerian domain. The soil elements could be empty or either partially or completely filled with material as illustrated.

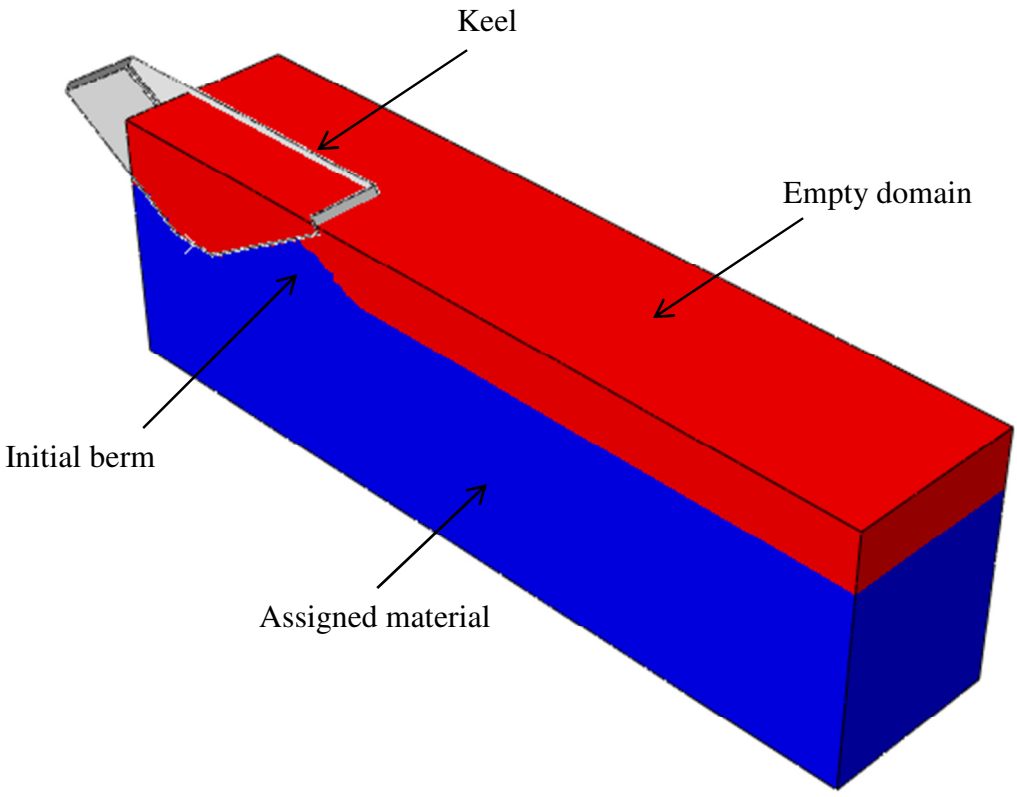

Figure A-9 Configuration of a CEL ice gouging analysis

During the course of this research simpler user defined models were successfully implemented and applied in CEL framework. Figure A-10 compares the keel reaction forces for two analyses based on the built-in Drucker-Prager model with zero dilation angle and the same constitutive model implemented through VUMAT subroutine. The reaction forces obtained from built-in model and the VUMAT user defined material for this simple constitutive material model, Drucker-Prager, are basically the same. As indicated in this figure keel in these analyses has advanced a long distance that the effect of the end wall of the soil domain is visible.

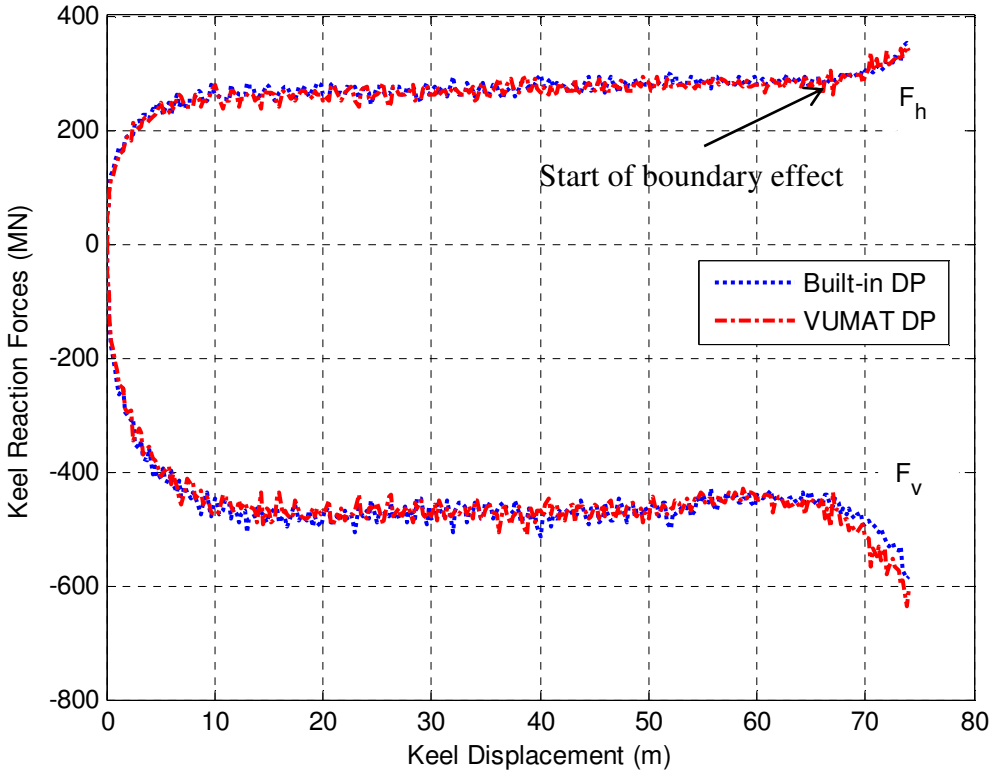

Figure A-10 Compression of keel reaction forces in CEL analysis based ABAQUS built-in model and VUMAT

For more complicated models such as NorSand or the proposed Drucker-Prager Cap the research to complete an analysis in CEL framework is yet incomplete.

Basically it is recommended to use a Lagrangian framework unless the problem involves such high deformations that only coupled Eulerian Lagrangian framework could handle them. In geotechnical problems, specifically ice gouging, it is very likely to be have to address the large deformation of the soil. Especially if the soil interacts with another structure such as pipeline or a subsea caisson the CEL framework could be the only way to solve the problem. Therefore a research to extend a more advanced soil constitutive

model in CEL is very rewarding and recommended. The application of the developed user material models in CEL framework will be pursued in future studies.

A.4. Ice/Soil/Pipe Interaction

In this thesis the ice/soil interaction has been studied. The purpose of the research is to improve the calculation of permanent soil deformation under the gouging forces in the ice-infested waters. The permanent soil deformation could have serious effect on the buried pipelines and should be investigated in every pipeline design. In the current state of practice in engineering guidelines the pipeline/soil interaction is modeled using structural springs in three longitudinal, lateral and vertical directions to represent the soil behaviour. These springs function independently however the interaction of effects in different axial, lateral or vertical directions are known to be significant.

The pipeline/soil interaction has been studied by many researches (Daiyan et al., 2010; Mahdavi et al., 2008). For future studies it is suggested to use the developed soil constitutive models and simulate the coupled interaction of ice/soil/pipeline. Enough number of coupled ice/soil/pipe analyses could provide sufficient data to investigate the required burial depths under different gouging scenarios. The burial assessment could be based on maximum stress or displacement allowance in the pipe.

Figure A-11 shows the configuration of a finite element model in which the interaction of ice keel, soil and pipeline is integrated.

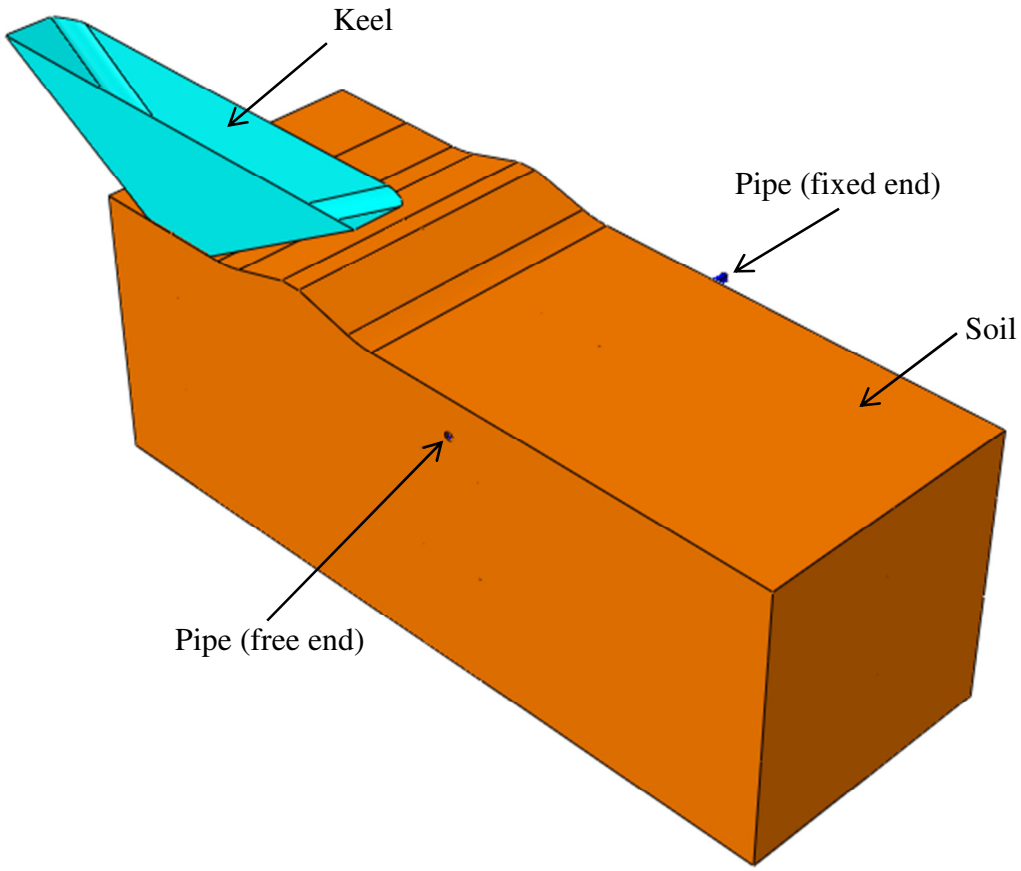

Figure A-11 Integrated Ice/Soil/Pipe model

In this model the gouging keel displaces the seabed soil. The displaced soil interacts with the pipeline upon which the gouging loads are eventually imposed. Based on serviceability limit state, ultimate limit state or any other appropriate criteria the integrity of the pipeline under the gouging event could be assessed.

Further investigation of ice/soil/pipe interaction is left for future studies. In this section however, some of the results of a typical coupled analysis is presented. With the new technology and the reducing cost of the production of higher grade steels the trend in offshore pipeline projects is to use high grade carbon steels. However, in this sample

analysis the elasticity modulus of the pipe is chosen about tenth of the steel to reduce the analysis time.

Figure A-12 shows the strain profile at a specific point in the pipe (Figure A-13). There are two peaks identified in the lateral strain profile each of which pertain to relative location of the keel.

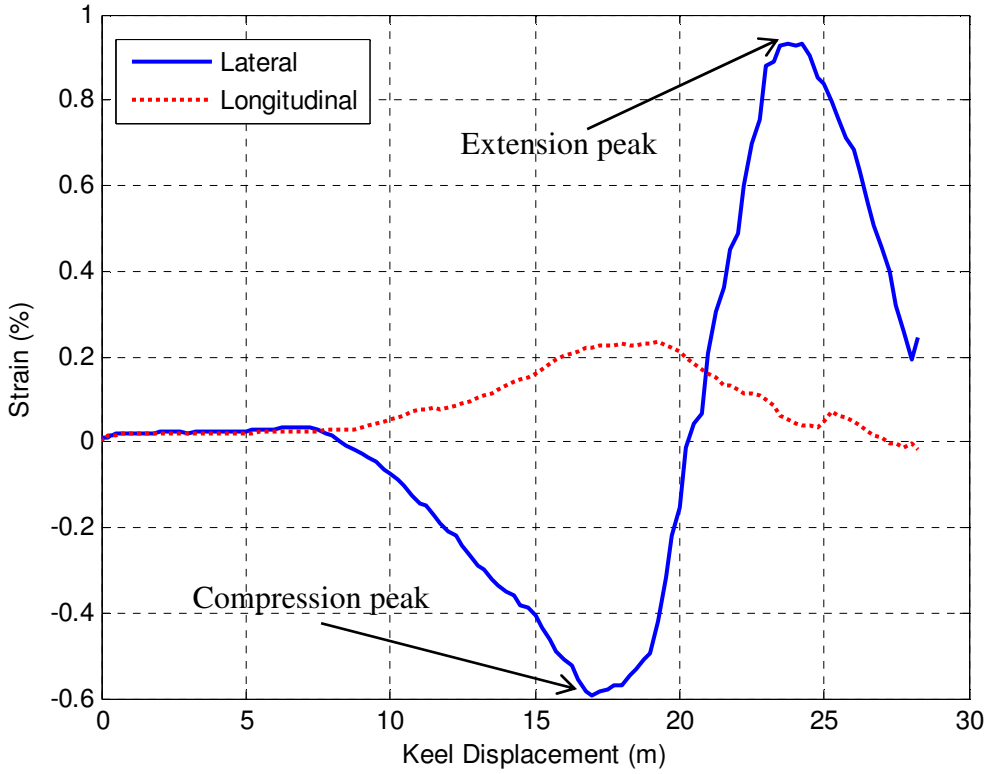

Figure A-12 Typical strain profile in the pipe

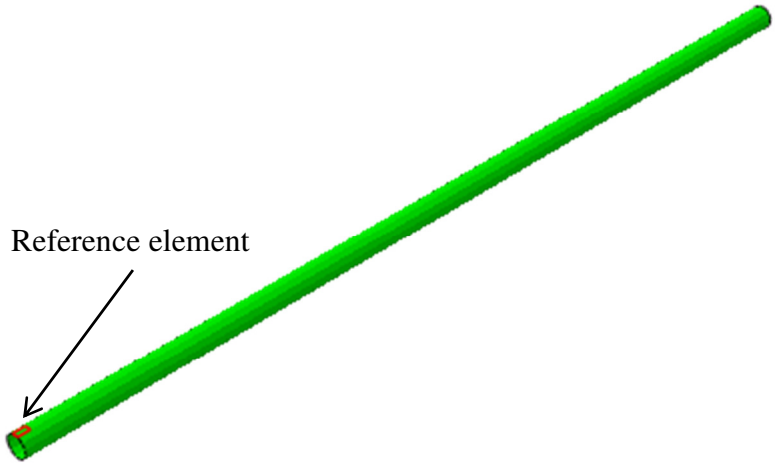

Figure A-13 Location of the reference element in Figure

The shear strain field and soil deformation vectors are shown in Figure A-14 and Figure A-15 for respectively the first and second peak lateral strains in Figure A-12. The effect of the existence of the pipe could be seen on the soil deformation under the gouging. Especially Figure A-14 shows that the existence of the pipe initially reduces the soil plastic yielding in front of the pipe.

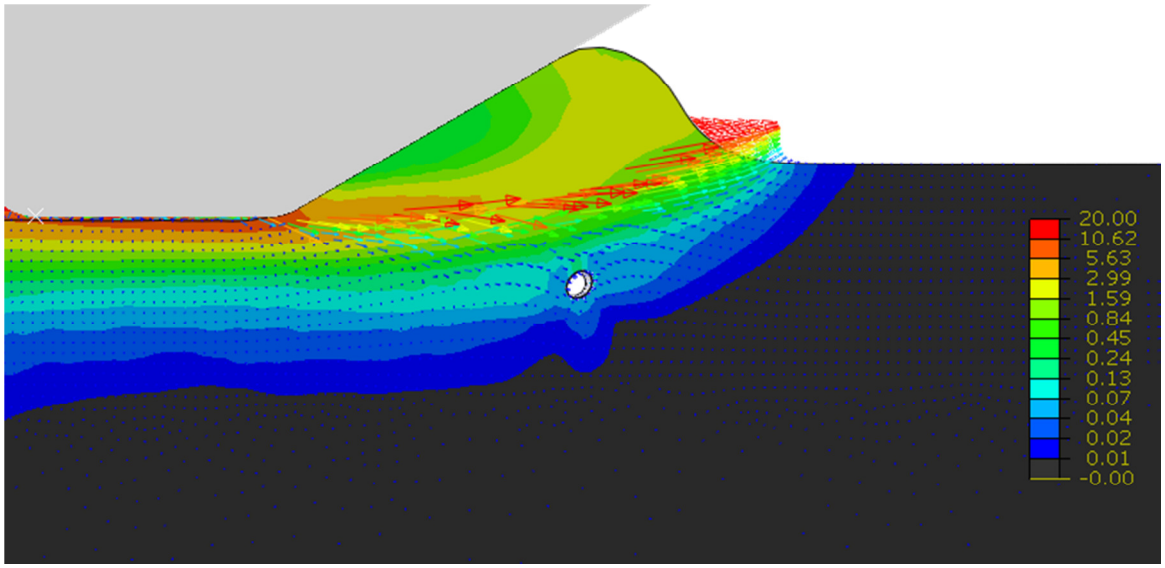

Figure A-14 Shear strain field in the soil and around pipe (compression peak in Figure A-12)

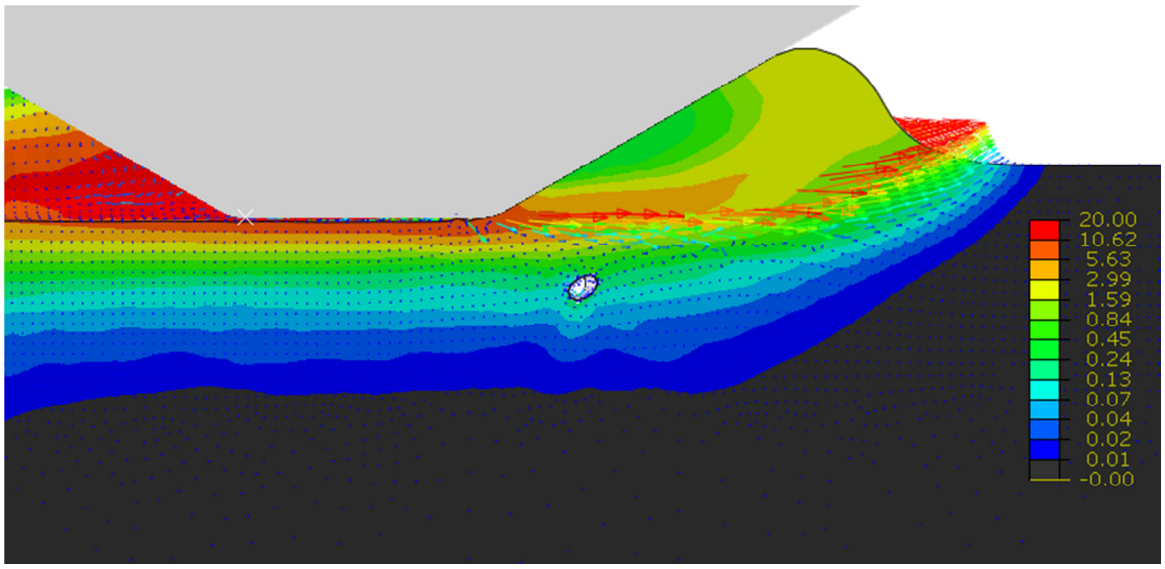

Figure A-15 Shear strain field in the soil and around pipe (extension peak in Figure A-12)

Figure A-16 illustrates the pipe deformation for the two peak states identified in Figure A-12. The pipe in this analysis has total magnitude of about 40 cm of deformation.

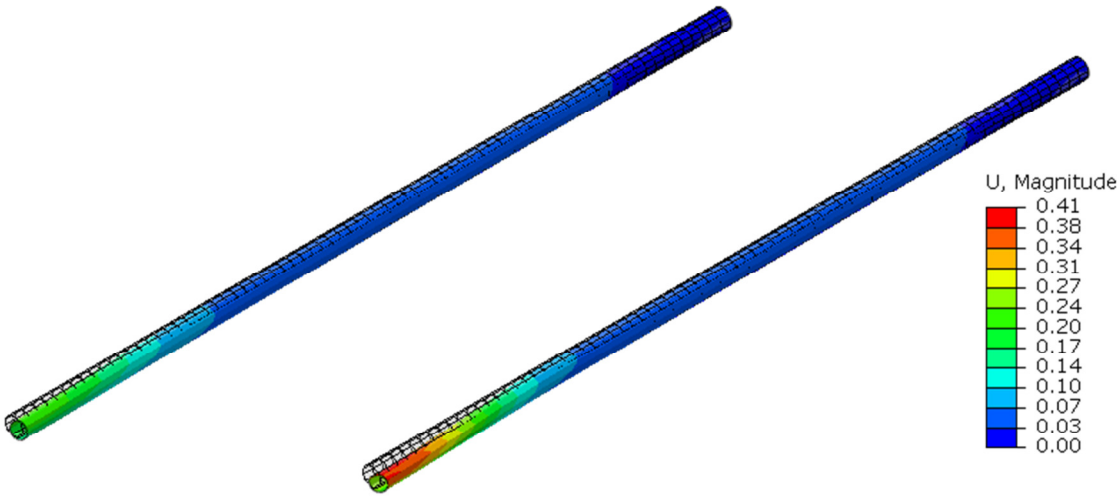

Figure A-16 Relative deformed pipe shape (left: at peak compression state in Figure A-14; right: at peak extension state in Figure A-15)